SPECTROSCOPIC AND KINETIC STUDIES

OF HIGHLY EXCITED DIATOMIC SPECIES

by

Gary Gilbert

A thesis presented for the degree of

Doctor of Philosophy in the

Faculty of Science at the

University of Edinburgh, 1986

UNIV. EDINBURGH.

To Nahad

DECLARATION

I hereby declare that this thesis has been composed by me, and that the work described in it is my own and was carried out at the University of Edinburgh, except where due acknowledgement is made. The thesis has not been submitted previously for any other degree.

Signed

Date 27th November 1986

ACKNOWLEDGEMENTS

First and foremost I would like to thank Professor R J Donovan for his help and guidance during the course of this work. His enthusiastic approach did much to maintain the momentum during the less inspired hours. I would also like to thank the other members of the research group for their many constructive comments, and in particular Dr M A MacDonald with whom I collaborated on some of the work, and Dr C Nokes who took the time to explain computing to me. Thanks also go to all in the mechanical and electrical workshops at Edinburgh and to Mr J Broom (glassblower).

I also thank Drs M C Gower and J Szechi for their help and advice during work at the Rutherford Appleton Laboratory, and Drs I Munro, D Show, and G R Mant for their help and advice at the Daresbury Laboratory.

Thanks are also due to Ann Gillies for typing, and to my wife Nahad for helping with the figures.

Finally, I would like to thank the SERC for making this thesis possible through their financial support.

ABSTRACT

There are at least two ion-pair states of IBr which are accessible by single photon absorption in the region 160-200nm. The lowest of these, the DO^+ state, gives rise to two bound-free fluorescence systems in the UV/visible. This state is efficiently collisionally transferred by CF_4, SF_6 and N_2 to the D'2 state which lies ca. 640cm^{-1} lower.

The excitation spectrum of I_2 in the region 175-215nm shows that a wide range of vibrational levels of the DO_u+ state fluoresce, and that the state is not predissociated. The reaction of $I_2(DO_u+)$ with Xe to form $XeI(B^2\Sigma^+)$ occurs for excitation at $\lambda \leq 190nm$, implying that there is little or no activation barrier.

Values of 27 ± 4, 11 ± 2, 7.25 ± 0.2 and 8.57ns were obtained for the pure radiative lifetimes of $IBr(DO^+)$, IBr(D'2), $I_2(D'2_g)$ and $XeI(B^2\Sigma^+)$ respectively. The D and D' states of IBr are removed extremely efficiently by the reactive gases CH_4, CH_3Cl, C_2H_6, CH_3Cl and O_2. The non-reactive gases CF_4, SF_6 and N_2 do not remove IBr(D'2) but do remove $IBr(DO^+)$ efficiently through interstate transfer to IBr(D'2). The various processes are rationalised in terms of a curve-crossing mechanism, where an ionic intermediate curve couples the entrance and exit channels.

$CH(A^2\Delta)$ was produced from CH_3Br, $CHBr_3$, CH_3OH, $(CH_3)_2CO$, CH_2I_2 and C_2H_2 via multiphoton fragmentation processes. The dominant

mechanism for the unsaturated precursor molecules involves secondary photolysis of primary photofragments. Rotationally hot $CH(A^2\Delta)$ radicals are relaxed more efficiently by H_2, Ar and SF_6 (collision numbers = 3.5, 4 & 5 respectively) than they are by He (collision number = 8). The removal rates determined for $CH(A^2\Delta)$ with CH_4, H_2, O_2 and N_2 are all slower than those with ground state CH radicals.

CONTENTS

CHAPTER 1 - INTRODUCTION

GENERAL INTRODUCTION

The work presented herein comprises spectroscopic and kinetic observations of processes involving highly excited electronic states of diatomic molecules. The species studied include ion-pair states of halogen molecules, $I_2(DO_u^+)$, $I_2(D'2_g)$, $IBr(DO^+)$, IBr(D'2) and the $A^2\Delta$ state of the CH radical. The unusual chemical and physical properties of the halogen ion-pair states merit attention, particularly with reference to the development of UV lasers, while study of the CH radical is necessary if we are to develop our understanding of such diverse chemical and physical environments as those of flames and comets.

The ion-pair states were produced by single photon absorption in the far ultraviolet. When excited in the presence of a foreign gas, one or more of the following processes resulted:

1. Radiative decay to a (lower) valence state;
2. Physical quenching to the ground state or a lower valence state;
3. Chemical reaction;
4. Collisional transfer to another ion-pair state.

When step 4 was operative, the resultant ion-pair state subsequently underwent some combination of steps 1, 2 and 3.

The $CH(A^2\Delta)$ radical was produced in the fragmentation of multiphoton excited parent molecules (ie molecules excited by the absorption of two or more photons), and monitored via the $A^2\Delta \rightarrow X^2\Pi$ emission band centred at 431nm. Quenching and reactive processes were studied by the addition of foreign gases.

In the past, limitations imposed by instrumentation have greatly hindered detailed studies of such highly excited species. However, recent technological advances have opened up many new fields of research. The range of molecular states and phenomena under study is expanding, with observations increasingly being made on individual rovibronic levels. Pulsed UV lasers and synchrotron radiation (two major developments from the photochemists point of view) were utilised as excitation sources for most of the work reported here. Both of these have several features which make them ideal tools for spectroscopic and kinetic studies (see Table 1.1)

The excimer laser produces extremely powerful pulses of UV radiation at a fixed wavelength in a narrow bandwidth. The pulse duration is short and the beam divergence is small. As a result of the high intensity, multiphoton processes can compete with single photon absorption, and the production of highly excited states lying in the vacuum UV ($\lambda \leq$ 200nm) by this means eliminates the need to use VUV transmitting optical materials and high vacuum techniques.

Using synchrotron radiation it is possible to tune through wide regions of the electromagnetic spectrum. The light beam is highly polarised, and has a well defined time structure of extremely short pulses. Although the beam is much lower in intensity, a very high repetition rate enables rapid data acquisition in certain types of experiments.

TABLE 1.1 : Comparison between some features of a typical excimer laser operating on the ArF transition, and those of the Synchrotron Radiation Source at Daresbury.

	ArF Laser	Synchrotron Radiation Source
Wavelength	193 nm	Tunable from X-rays to IR
Bandwidth (nm)	1	0.004 - 3
Pulse energy (mJ)	100 - 400	
Pulse duration (S)	1.5×10^{-8}	1.2×10^{-10}
Repetition rate (Hz)	0.25 - 20	5×10^{8} in multi-bunch mode 3.125×10^{6} in single bunch mode

1.2 ELECTRONIC STATES OF HALOGEN MOLECULES

The electronic states of halogen molecules fall into three categories : the valence states, the ion-pair states, and the Rydberg states. The potential energy curves for some of these are represented in Figure 1.1.

The low lying electronically excited states ($E \approx 20000\ cm^{-1}$ in the case of I_2) are of valence character, ie. in the dissociation limit they give atoms in either their ground state ($^2P_{3/2}$) or spin-orbit excited state ($^2P_{1/2}$). These valence states, and particularly the BO_u^+ state of I_2, have been extensively studied providing a good understanding of their spectroscopic [1-6] and collisional quenching[7-10] properties.

Over 70 years ago McLennan[11,12] first identified the I_2 absorption in the UV at λ = 180-200nm using various light sources and filters. This absorption has been assigned[13] to the $DO_u^+ \longleftarrow XO_g^+$ transition. Some years later Duschinsky and Pringsheim[14], while conducting a similar experiment, noted that the addition of He or Ne to the I_2 sample gave rise to a strong fluorescence near 340nm. This emission band is known to originate from the D'2g $\longrightarrow$ A'2u transition. The D and D' states are examples of ion-pair states, however it is only recently that these and other similar higher lying electronic states have received much attention. Much of the impetus for recent studies has come from rapidly advancing technology, particularly that associated with lasers operating in the UV and visible.

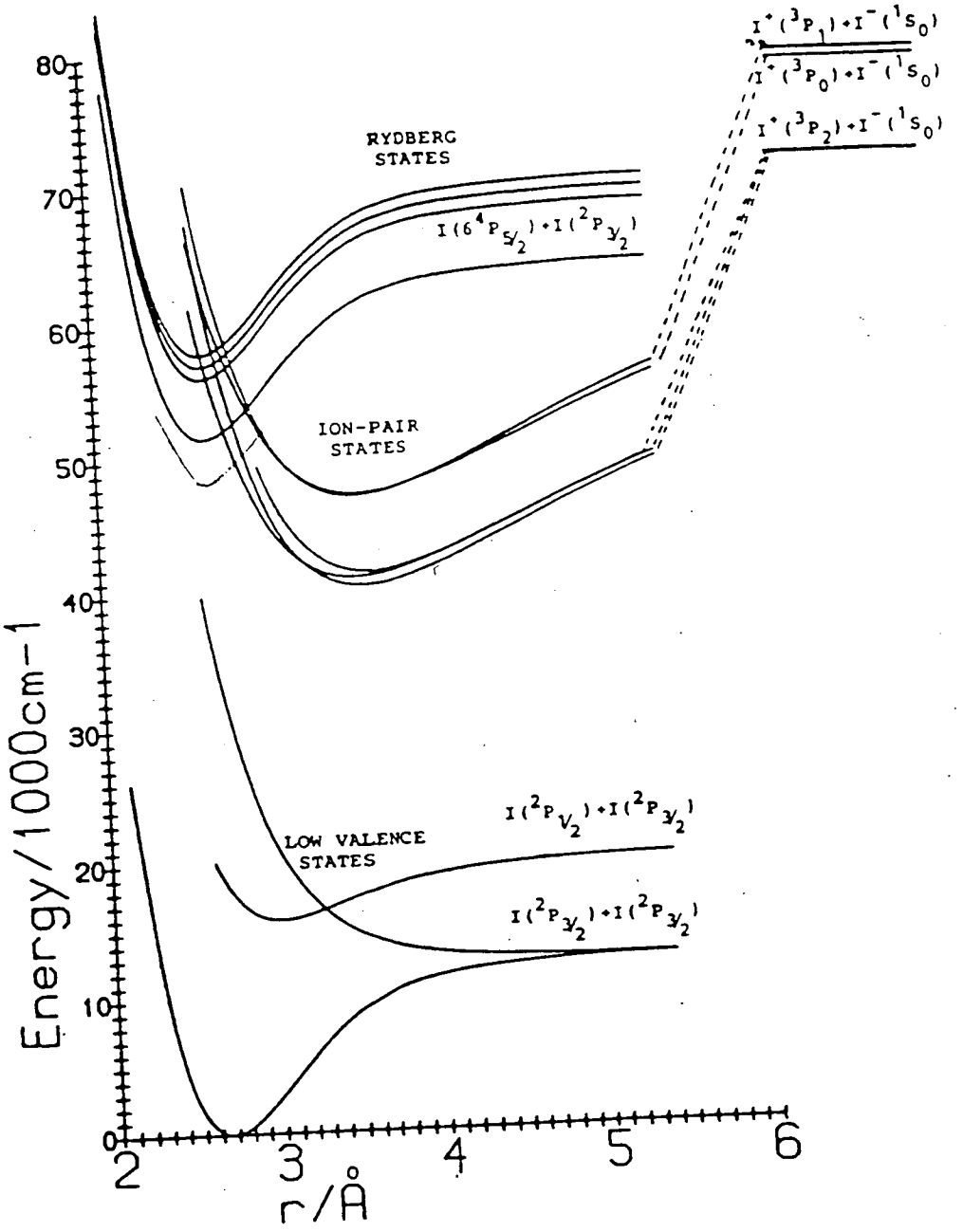

Figure 1.1 : **Selected electronic states of I_2**

(Taken from M A MacDonald, Ph.D. thesis, 1984)

As these states ($E \geq 40000\ cm^{-1}$) are ion-pair in character[13] (ie they correlate with $X^+ + X(Y)^-$ in the diabatic dissociation limit), they are expected to exhibit behaviour which differs markedly from their valence counterparts. An example which bears this out is the efficiency of the reaction of $I_2(DO_u+)$ with CH_4 and CH_3Cl[17,18], in sharp contrast to $I_2(BO_u+)$. In fact $I_2(DO_u+)$ is so reactive that it can break extremely strong C - F bonds[19] (Bond Energy $\simeq 485 KJmol^{-1}$) to form radicals.

One of the areas of great interest in the ion-pair states stems from the possible development of halogen lasers. A decade ago several groups demonstrated the possibility of an I_2 laser operating on the D'2g $\longrightarrow$ A'2u transition at 342nm using electron beam excitation[20-22]. Using the same technique the analogous Br_2 laser[23,24] (operating at 291nm) and a range of interhalogen lasers[25,26] have been investigated. Figure 1.2 shows the potential energy curves for an interhalogen laser. More recently the possibility of an efficient optically pumped I_2 laser has been investigated[27,28]. This 4-level laser system is represented schematically in Figure 1.3. Optical excitation of the DO_u+ state is very efficient for $180nm < \lambda < 200nm$ making the ArF excimer laser (operating at 193nm) a suitable pump source. The DO_u+ state is coupled by rapid collisional relaxation to the D'2g state, which is believed to be the lowest of the ion-pair states[15,29]. Relaxation is efficiently accomplished by the addition of moderate pressures of inert gases. The D'2g state is vibrationally and rotationally relaxed by inert gases, but only very weakly quenched[30-32].

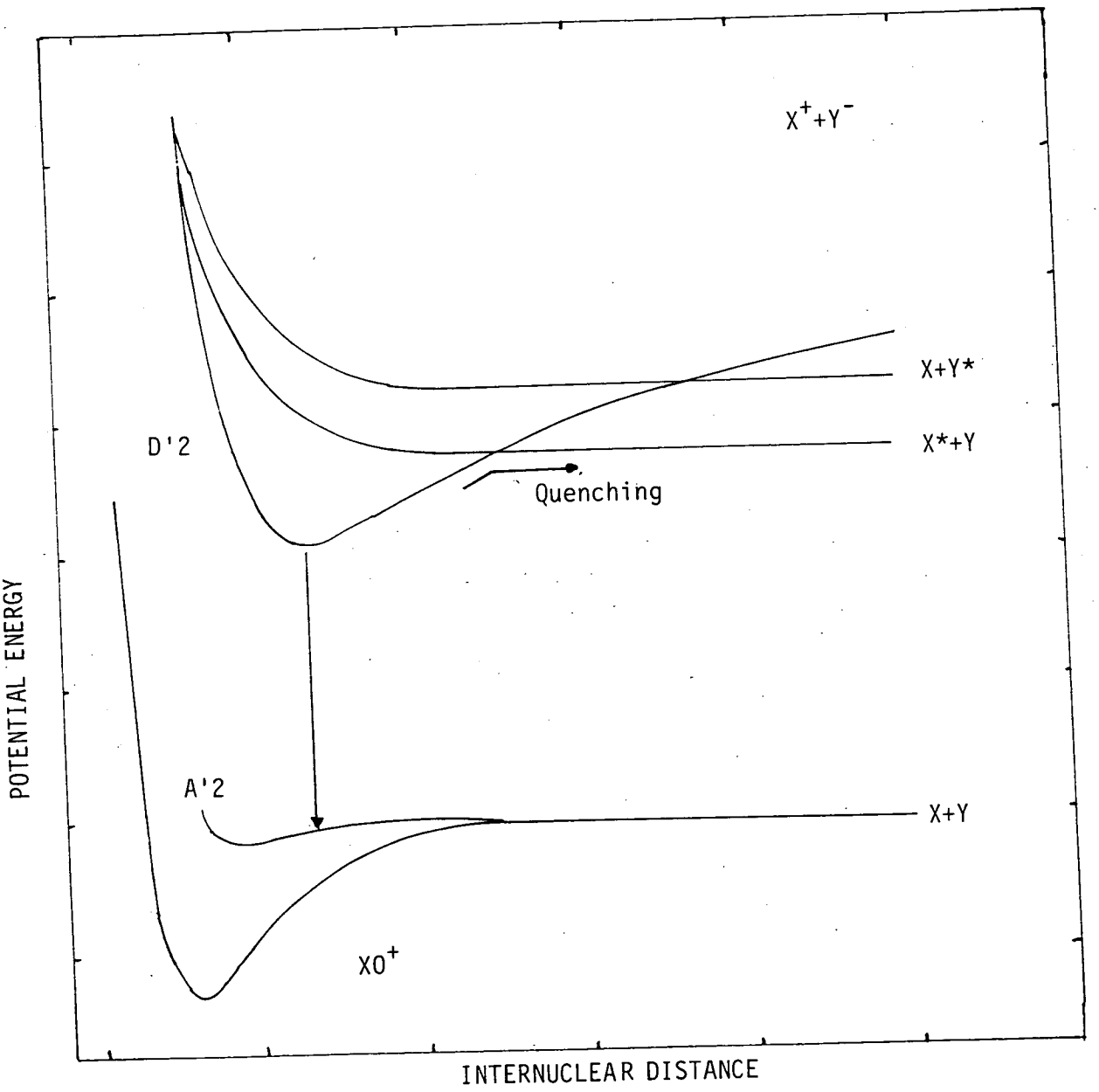

Figure 1.2 : **Potential curve diagram of an interhalogen laser molecule, XY**

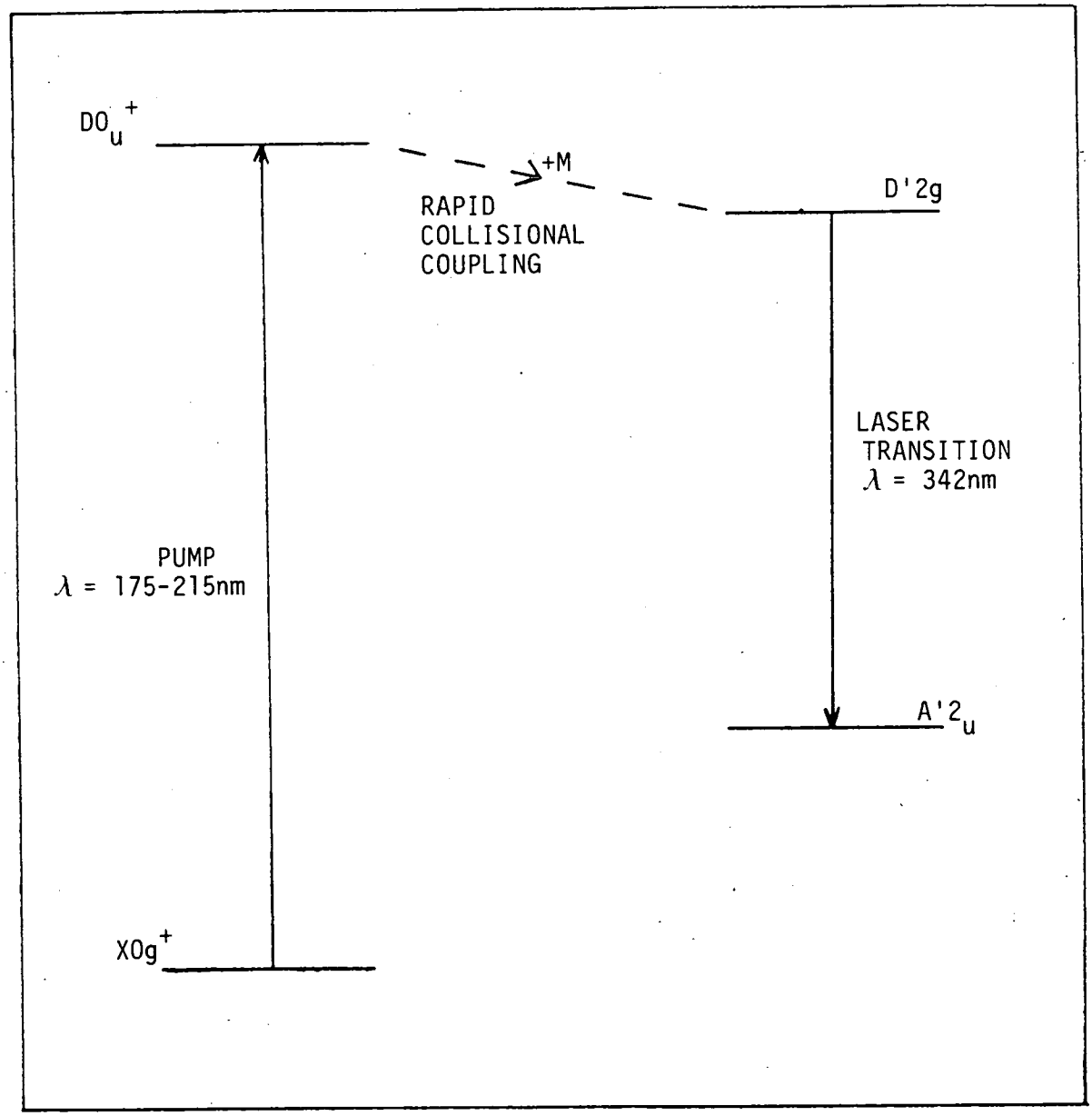

Figure 1.3 : **Optically pumped I_2 laser (schematic)**

In some cases excitation of halogen ion-pair states in the presence of rare gases can provide an alternative route in the production of rare gas-halide exciplexes, which are important in the development of pulsed UV laser systems. The pathway involving an electronically excited rare gas atom (RG*) and a ground state halogen molecule or halogen containing molecule, eg.

$$RG^* + X_2 \longrightarrow RG - X^* + X \qquad -(1.1)$$

has been studied extensively[33-38] and is the basis of commercially available excimer laser systems. However, the complementary pathway may prove to be a viable alternative for some systems ; the reaction

$$IBr(D) + Xe \longrightarrow XeBr(B) + I \qquad -(1.2)$$

has been shown to produce XeBr* efficiently[39] (quantum yield ≈ 30%).

The electronic configuration of the ion-pair states correspond to the promotion of one or two electrons in the filled orbitals of the ground state ($.....(5p\,\sigma_g)^2(5p\,\pi_u)^4(5p\,\pi_g)^4$ for I_2) to a vacant σ^* orbital (the $5p\,\sigma_u^*$ orbital in the case of I_2).[40] As previously mentioned, the behaviour of these states differs greatly from that of the lower valence states. This is mainly due to the potentials (see Figure 1.1): the two charges in the

ion-pair attract each other electrostatically and so the attractive part of the potential is of the form r^{-1} ($e^2 / 4\pi\epsilon_o r$), c.f. r^{-6} for the lower valence states. This results in a deeply bound potential with a gently sloping attractive limb reaching the dissociation limit at a large separation. The vibrational spacings are small, compared with the valence states, and converge very slowly towards the dissociation limit due to the uniformity of the gradient of the potential in the attractive and replusive limbs. For comparison, typical values of some parameters are given in Table 1.2, taking I_2 as an example.

TABLE 1.2 : Some parameters for $I_2(X0_g+)$ compared to typical values for the ion-pair states correlating with $I^-(^1S)+I^+(^3P_2)$. Data taken from KP Huber and G Herzberg, "Molecular structure and molecular spectra Vol. 4, Constants of diatomic molecules" (Van Nostrand, Princeton, 1979).

	$I_2(X0_g+)$	I_2(Ion-pair state)
r_e (Å)	2.67	~3.6
D_o (eV)	1.542	~3.8
ω_e (cm^{-1})	214	~100
$\omega_e x_e$ (cm^{-1})	0.614	~0.24

As the predominant ionic attraction term, $e^2/4\pi\epsilon_o r$, does not discriminate between the different ion-pair states they all have virtually identical shapes and are nested within one another (the only crossings that need be considered are those with neighbouring Rydberg states). Another consequence of this is that the members of any group of ion-pair states (ie. states correlating in the diabatic dissociation limit with a particular pair of ions such as $X^-(^1S)+X^+(^3P_2)$) will have similar term values. The close (energetic) proximity of the lowest group of I_2 ion-pair states coupled with the small vibrational spacings within the states facilitiates the extremely efficient collisional transfer process:

$$I_2(DO_u^+,v')+M \longrightarrow I_2(D'2g,\text{thermalised } v'')+M \qquad -(1.3)$$

which creates the necessary population inversion for the I_2 laser.

In fact it is reasonable to assume that all the states within the lowest group will be collisionally coupled to each other, but will only be very weakly quenched (ie. transferred to lower valence states). Thus in the presence of a large excess of inert gas the lowest state within the group should be dominantly populated, provided that its term value is lowest by a margin greater than kT. This, together with the fact that all of the ion-pair states are expected to have at least one strong transition to the valence states[13], supports the assertion that the D'2g state is lowest. This is borne out experimentally and a term value of 40388 cm^{-1} has been determined for the D'2g state[16,41], while one of 40821 cm^{-1} has been determined for the next lowest $\beta 1g$ state[42] of I_2.

Provided that the selection rules permit single-photon transitions from the ground state, the large equilibrium bond lengths of the ion-pair states dictate that the resultant excited species will be highly vibrationally excited (eg $v' \simeq 140$ for $I_2(DO_u+)$ excited at 193nm). Single-photon studies have been largely restricted to the $DO_u+(DO^+)$ state (and states collisionally populated therefrom) in the case of I_2 [17,18,28,32,43-45] and IBr[39,46].

Restrictions imposed by the selection rules and Franck-Condon factors can be overcome by probing the states in two-step multiphoton transitions through an intermediate state (usually BO_u+/BO^+). A variety of multiphoton processes have been devised, giving access to many of the other ion-pair states. Thus, for I_2, gerade states have been accessed via two-photon processes[47-50], while the $F'O_u+$ state has been accessed via a three-photon process[51]. A summary of the spectroscopic investigations of I_2 ion-pair states has been given by Tellinghuisen[52]. By comparison the ion-pair states of IBr, excepting the DO^+ and D'2 states, have received little attention[53,54].

Finally, the Rydberg states lie above the minima of the ion-pair states ($E \geq 50000$ cm^{-1} for I_2) and are similar to the lower valence states but with an (essentially) non-bonding electron excited into an orbital with a higher principal quantum number. Their interactions with the ion-pair states give rise to complex spectra, but they are not expected to be efficiently collisionally coupled with the ion-pair states due to their different character.

1.3 ELECTRONIC STATES OF HALOGENS : NOMENCLATURE

In diatomic molecules composed of two light atoms, spin-orbit coupling is small and the conventional (Λ , Σ) notation scheme provides a valid description of the molecular electronic states. Under this scheme a molecule is described by three main quantum numbers in the format $^{2\Sigma+1}\Lambda_{\Omega}$ where $(2\Sigma+1)$ is the electron spin multiplicity, Λ is the orbital angular momentum, and Ω is the total electronic angular momentum ($\Omega = |\Lambda + \Sigma|$, $|\Lambda + \Sigma| - 1, \ldots\ldots, |\Lambda - \Sigma|$).

A further small splitting occurs between pairs of 'degenerate' $\Omega = 0$ states when symmetry is taken into consideration: reflection in a plane which contains the nuclei will either leave the electronic wave function unchanged (denoted +) or produce a sign inversion (denoted -) giving, for example Σ^+ / Σ^-, Π_{0^+} / Π_{0^-} states. For degenerate states with $\Omega > 0$, no such distinction arises. Finally, electronic states of homonuclear diatomics can be further characterised according to whether or not the sign of the wavefunction is changed upon inversion through the centre of symmetry. The electronic wavefunction can be either even (no change of sign, denoted by subscript g) or odd (change of sign, denoted by subscript u) with respect to this operation.

In diatomic molecules composed of heavy atoms (eg Br_2, I_2, IBr), electrons experience a greater magnetic field due to their presence in greater numbers, giving rise to considerable spin-orbit coupling. In these cases Ω is the only meaningful

quantum number with Σ and Λ becoming redundant, and the designation of electronic states takes the format $\Omega^{+/-}_{g/u}$ (or $\Omega^{+/-}$ in the case of heteronuclear diatomics).

The ion-pair states of the halogen molecules correlate with $X^+ + X^-$ ($X^+ + Y^-$ in the case of interhalogens) in the dissociation limit. By considering the combination of the two ions to form a molecule, the electronic states which arise can be deduced.

1.4 THE ION-PAIR STATES OF I_2

The ion-pair states of I_2 dissociate to $I^+([Kr]\,5s^2 4d^{10} 5p^4)$ plus $I^-([Kr]\,5s^2 4d^{10} 5p^6)$. In order of increasing energy, the electronic states of I^+ will be ^3P_J, ^1D and ^1S (cf. Group VI atoms), while I^- will be produced in a ^1S state (cf. rare gas atoms). 20 ion-pair states can be formed by taking all the possible combinations of the angular momentum quantum numbers of the ions, ie. $\Omega = |J_1 + J_2|$. Figure 1.4 illustrates the construction of the various states, which can be roughly divided (energetically) into four groups in accordance with the energies of the various I^+ states.

The ^3P_J state has three spin-orbit components, corresponding to J=0,1,2 (in order of decreasing energy). The six states ($0_u^+(D)$, $0_g^+(E)$, $1_u(\gamma)$, $1_g(\beta)$, $2_u(\delta)$ and $2_g(D')$) from $I^+(^3P_2)$ should be lowest. Tellinghuisen et al[15] have suggested that this group begins at around 40000 cm^{-1}, and this view is supported by

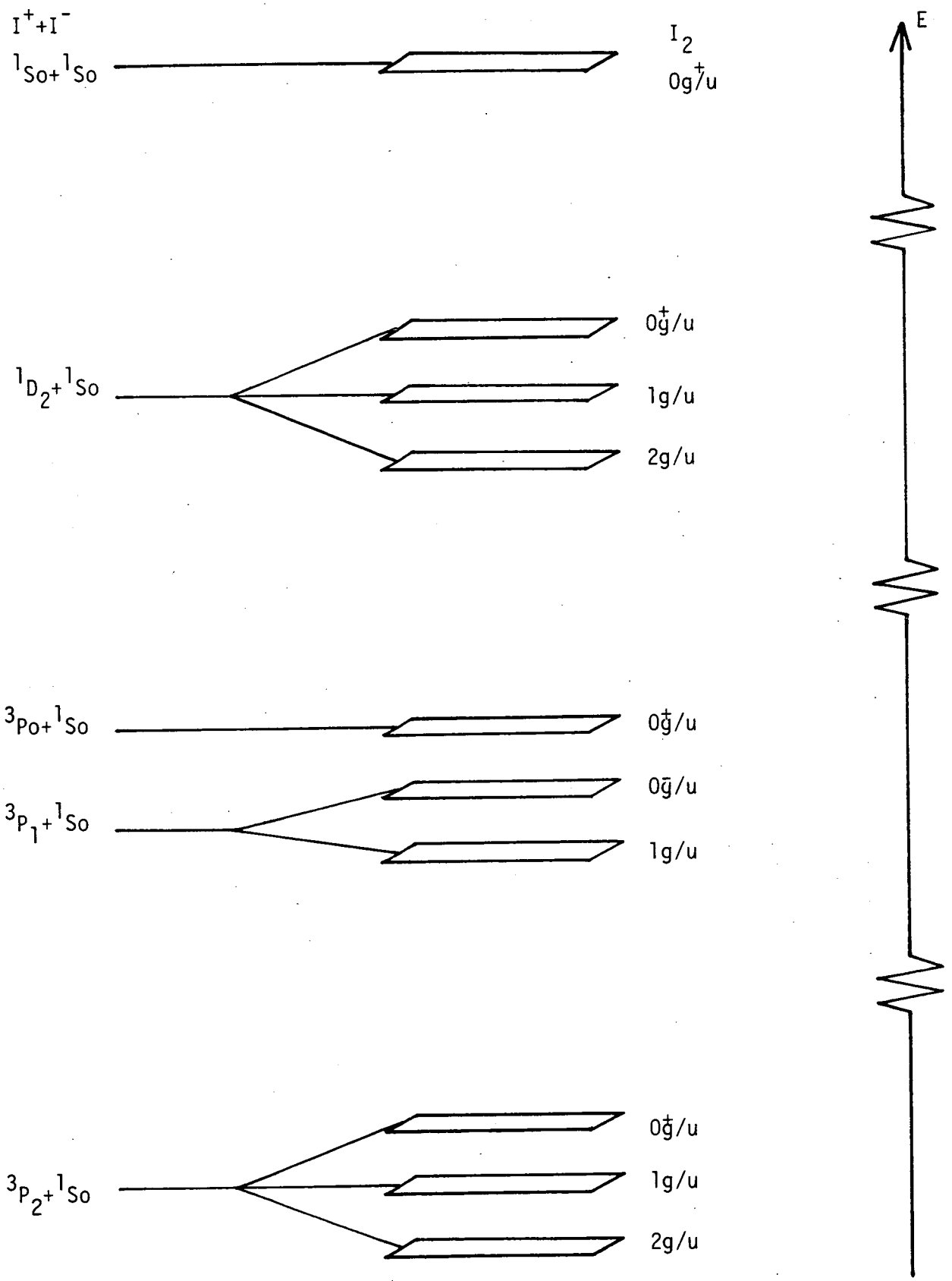

Figure 1.4 : **Relative energetic ordering of I_2 ion-pair states (not to scale)**

theoretical calculations[55] as well as by experimental results[56].

The four states (0_u^-,0_g^-(g),1_u and 1_g(G)) from $I^+(^3P_1)$ and the two (0_u^+(F) and 0_g^+(f)) from $I^+(^3P_0)$ should by higher by about 7000cm^{-1}, and the six states (0_u^+(F'),0_g^+,1_u,1_g,2_u and 2_g) from $I^+(^1D_2)$ still higher by about 7000cm^{-1}. The two remaining states from $I^+(^1S_0)$ lie at much higher energy (approximately 17500 cm^{-1} higher still than the states from $I^+(^1D_2)$).

1.5 THE ION-PAIR STATES OF IBr

The ion-pair states of IBr dissociate to either $I^+([Kr]5s^24d^{10}5p^4)$ plus $Br^-([Ar]4s^23d^{10}4p^6)$ or $Br^+([Ar]4s^23d^{10}4p^4)$ plus $I^-([Kr]5s^24d^{10}5p^6)$. Of the 20 ion-pair states which can be thus formed, half dissociate to $I^+ + Br^-$ and half to $Br^+ + I^-$. The relative energetic orderings within these two groups are determined by the energies of the various X^+ states ($^3P_2$, $^3P_1$, $^3P_0$, $^1D_2$ and $^1S_0$), while all states dissociating to $Br^+ + I^-$ will be displaced to higher energy by approximately $9000cm^{-1}$ relative to the states dissociating to $I^+ + Br^-$. This displacement can be calculated, using equation 1.4, from the ionization potentials and electron affinities of I and Br atoms:

$$-\Delta = \text{I.P.(I)}+\text{E.A.(Br)}-\text{I.P.(Br)}-\text{E.A.(I)} \qquad -(1.4)$$

Figure 1.5 illustrates the construction of the various states, which can be roughly divided (in theory) into six groups of three plus two individual states. The lowest group lies in the region 37840 - 49490 cm^{-1} above the ground state (see section 3.1).

The vertical axis on Figure 1.5 is not to scale : Table 1.3 gives approximate, theoretical energy gaps between the term values of the lowest states in each successive group. A gap of 3000 cm^{-1} may not be significant compared with the spread of term values within a group, in which case two or three of the groups may merge.

Figure 1.5 : **Relative energetic ordering of ion-pair states of IBr**
(not to scale)

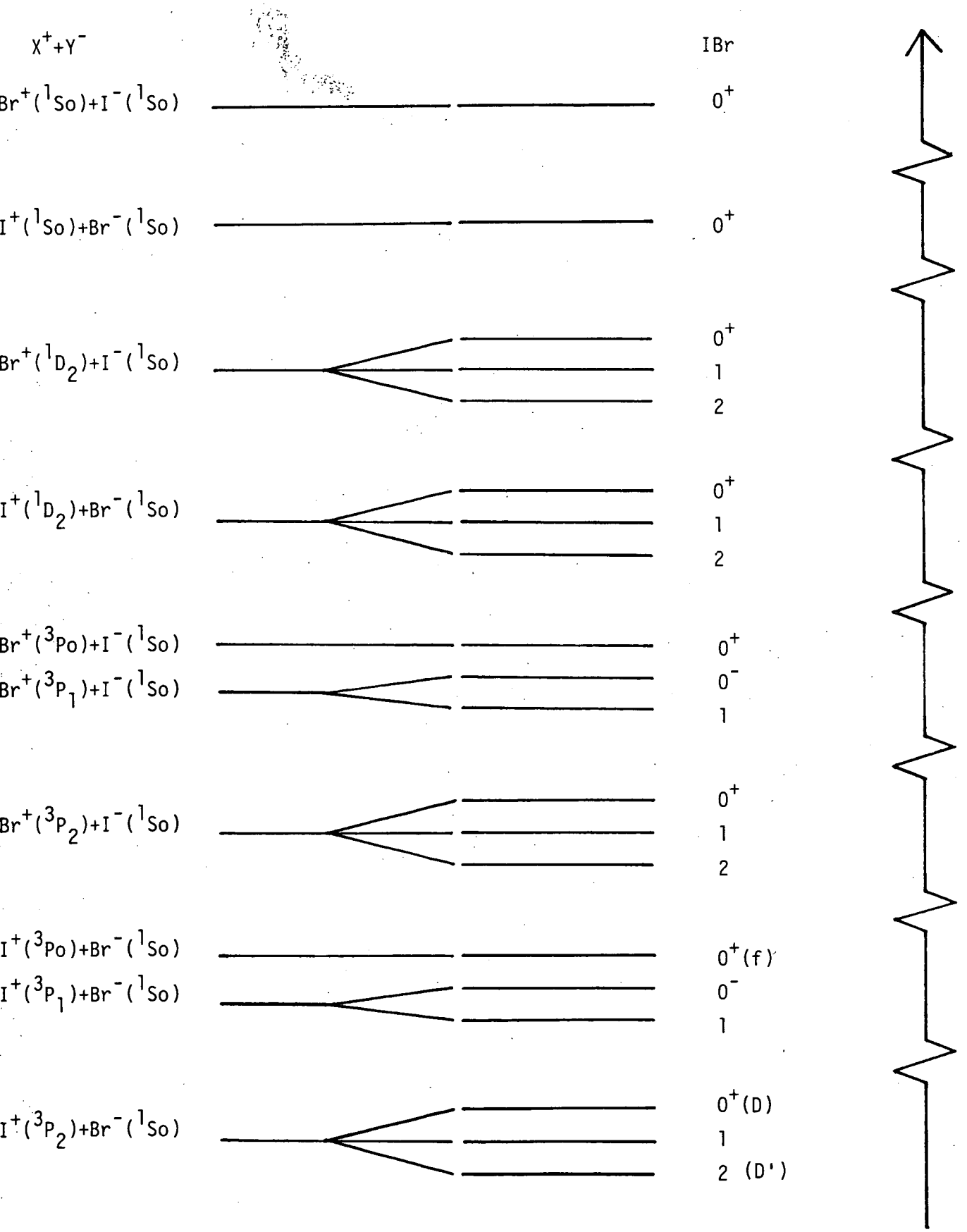

TABLE 1.3 : Approximate theoretical energy gaps between successive groups of ion pair states of IBr.

PAIR OF IONS PRODUCED IN THE DISSOCIATION LIMIT	NO OF STATES IN THE GROUP	APPROXIMATE ENERGY GAP (cm^{-1})
$Br^+(^1S_0)+I^-(^1S_0)$	1	
		10000
$I^+(^1S_0)+Br^-(^1S_0)$	1	
		11000
$Br^+(^1D_2)+I^-(^1S_0)$	3	
		8000
$I^+(^1D_2)+Br^-(^1S_0)$	3	
		3000
$Br^+(^3P_{0,1})+I^-(^1S_0)$	3	
		3000
$Br^+(^3P_2)+I^-(^1S_0)$	3	
		3000
$I^+(^3P_{0,1})+Br^-(^1S_0)$	3	
		6000
$I^+(^3P_2)+Br^-(^1S_0)$	3	

1.6 OSCILLATORY CONTINUUM FLUORESCENCE FROM I_2

I_2 gives rise to oscillatory continuum fluorescence[13,57] when excited at $170 \leq \lambda \leq 200$nm, in the absence of a buffer gas. Figure 1.6 shows a low resolution fluorescence spectrum of I_2 in the region 200-500 nm following 193 nm excitation (taken from M. Martin et al[28]). Figure 1.7 shows the potential curves of the $X(0_g+)$ and $D(0_u+)$ states, with the difference potential above the ground state curve (dashed line) representing the locus of points to which transitions can occur (classically) from the high vibrational level of the $D(0_u+)$ state while conserving kinetic energy. Since single photon absorption from the ground state at $170 \leq \lambda \leq 200$nm populates very high vibrational levels of the upper state, there is a large range of r from which transitions can occur, and it is evident from Figure 1.7 that a large fraction of such transitions will terminate in unbound levels of the ground state. In addition to intensity maxima corresponding to transitions from the two turning points on the upper potential, there will be a third, long-wavelength maximum corresponding to transitions at intermediate r to the (maximum) turning point on the difference potential. This 'accumulated' intensity (at 322 nm) results from the very flat gradient of the difference potential in the region of its turning point, ie. isoenergetic transitions can occur over a relatively large range of internuclear separation.

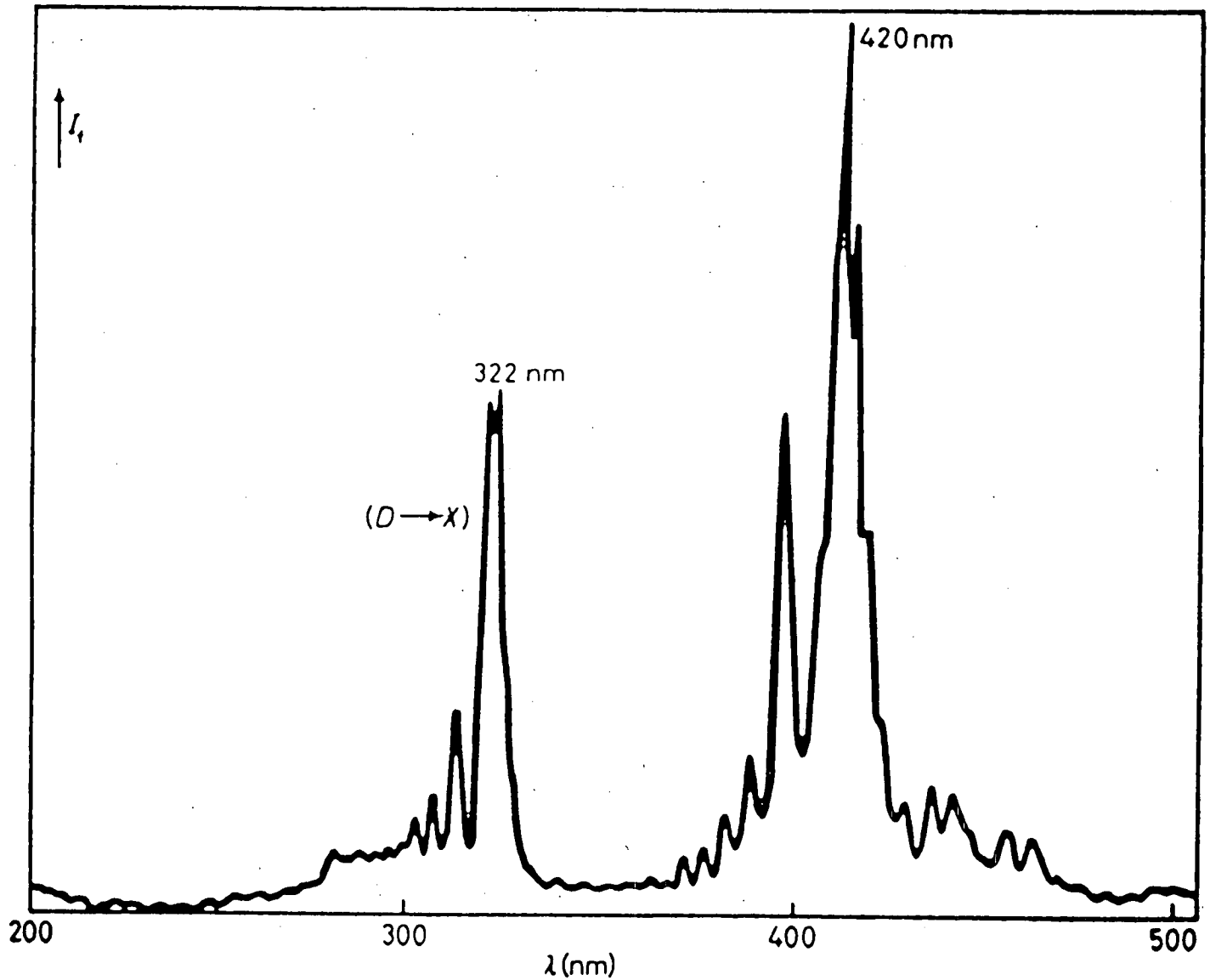

Figure 1.6 : **Low resolution fluorescence spectrum of I_2(10Nm^{-2}), following excitation at 193nm**

(Taken from M Martin et al, Nouvo Cimento 63B, 300 (1981))

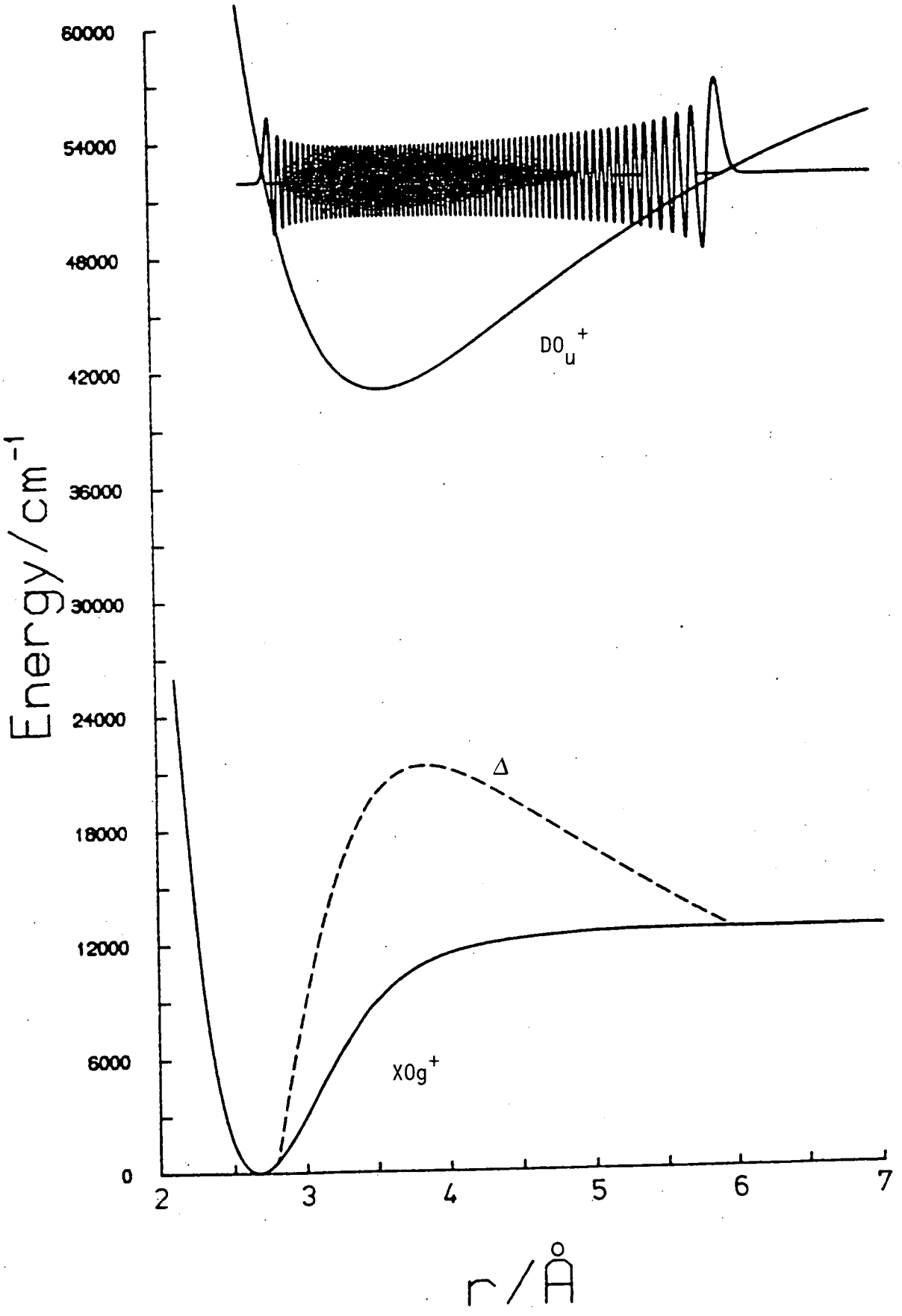

Figure 1.7 : **The difference potential (Δ) for fluorescence from $I_2(DO_u^+, v^1)$ to $I_2(XOg^+)$.**

Taken from M A MacDonald, Ph.D. Thesis (1984)

On either side of this maximum turning point there are pairs of values of r with identical vertical transition energies. Depending on the phase of the wavefunctions of these pairs of points, constructive or destructive interference will result. The oscillations in the continuum emission are the manifestation of this interference. At higher resolution, a high frequency interference structure can be observed superimposed upon the low frequency structure. This high frequency structure results from the changing phase difference between the upper and lower state wavefunctions.

Similar considerations apply to the second oscillatory continuum system with maximum intensity at 420 nm. Transitions to a difference potential above the lower state (in this case purely repulsive), with associated constructive and detructive interference, give rise to the intensity oscillations in this long wavelength band.

For a rigorous treatment of this phenomenon, see RS Mulliken[13] and J Tellinghuisen[57].

1.7 THE CH RADICAL

The CH radical is an important radical in hydrocarbon combustion systems. Its chemiluminescence at λ = 420-440 nm (from the $A^2\Delta \longrightarrow X^2\Pi$ transition) has been observed in various high temperature hydrocarbon flames[58-61], and in atomic oxygen

reactions with hydrocarbons[62,63] (particularly unsaturated hydrocarbons). CH radicals have also been produced in electron bombardment of organic molecules[64], in compression ignition of petrol in combusion engines[65], and in ion-molecule reactions of N^+ [66], O^+ [67], He^+ [68] and Ar^+ [69] with hydrocarbons.

Figure 1.8 is an energy level diagram showing potential curves for some of the experimentally observed electronic states of the radical : the $A^2\Delta$, $B^2\Sigma^-$ and $C^2\Sigma^+$ states have been observed in emission to the $X^2\Pi$ ground state[70]. These emission spectra (along with the spectra of other small radicals such as CN, OH, NH, C_2 and C_3) are observed from many stars and comets[71-73], and from interstellar space[74-78]. These radicals are produced either by the absorption of far-UV solar radiation by certain parent molecules or by chemical reactions, their fluorescence being subsequently excited by sunlight of longer wavelengths.

The CH radical is also important as a precursor to other radicals, for example the $OH(A^2\Sigma^+ \longrightarrow X^2\Pi)$ emission has been observed in many hydrocarbon flames and has been attributed in part to the reaction[79]:

$$CH(X^2\Pi) + O_2(X^3\Sigma_g^-) \longrightarrow CO(X^1\Sigma^+) + OH(A^2\Sigma^+) \qquad -(1.5)$$

while electronically excited CH radicals are believed to promote chemi-ionization in flames through their reaction with atomic oxygen[80,81], viz:

$$CH^* + O \longrightarrow HCO^+ + e^- \qquad -(1.6)$$

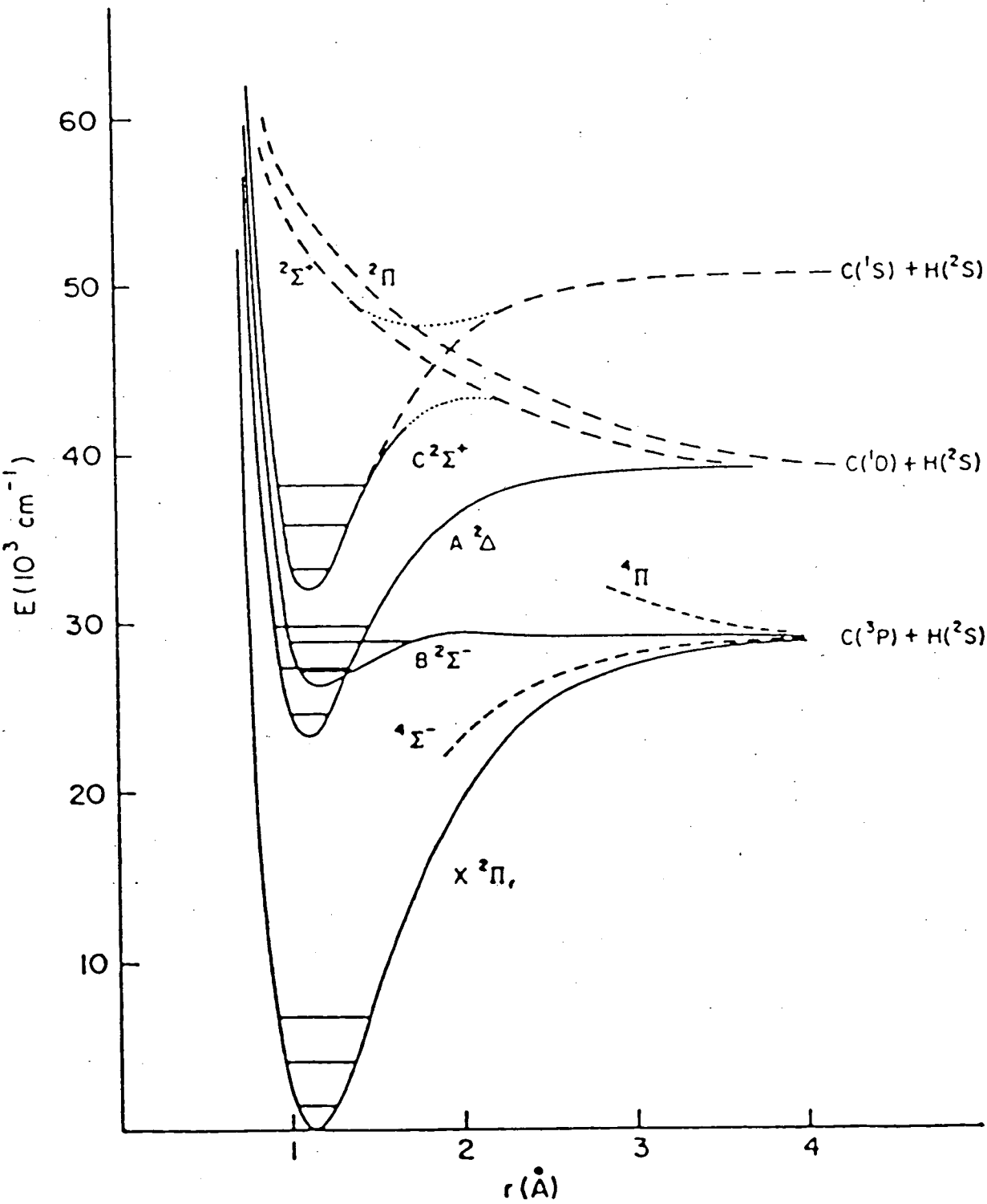

Figure 1.8 : **Potential curves of the lower electronic states of CH.**

(Adapted from G Herzberg and JWC Johns, Astrophys.J., 158, 399 (1969))

Our understanding of the extreme physical/chemical environments of hydrocarbon flames and interstellar space will benefit from any information that we can obtain on small free radicals in the laboratory. However, a reasonable understanding of the kinetics and mechanics of CH formation and reaction has only recently been established. This stems partly from the complexity of hydrocarbon combustion chemistry in general, and partly from the difficulty in the past of producing high enough concentrations of the highly reactive radical, making direct measurements very difficult. The second of these problems has been greatly alleviated by the advent of high-power UV excimer lasers, as a result of which several detailed studies have been carried out in the last few years. These include kinetic studies[62,82-87], and studies of photodissociation processes leading to CH formation[88-96] which yeild information on excited state dynamics and fragmentation. In these experiments multiphoton processes are responsible for CH production.

1.8 MULTIPHOTON PROCESSES

The probability, P, of the absorption of photons is given by the relation:

$$P \propto \alpha_1 I + \alpha_2 I^1 + \alpha_3 I^3 + \ldots \qquad -(1.7)$$

Where α_n is the cross-section for the absorption of n photons and I is the radiation intensity. From equation 1.7 it can be seen that a high radiation intensity favours the higher order terms, ie. multiphoton processes become more feasible. These processes can be divided into three categories : sequential (resonant) multiphoton excitation (MPE), simultaneous (non-resonant) MPE, and secondary photolysis of photofragements formed in the primary step. The first two are illustrated in Figure 1.9 for a 2-photon process, the same principles being extendable to higher order processes.

In sequential MPE (see figure 1.9a) the first photon excites the parent molecule, A, to a real intermediate state, A*, which is further excited by a second photon to a super-excited state, A**. The intermediate state is said to resonantly enhance the process. Super-excited states produced by UVMPE usually have energies near or above the ionization potentials of the parent molecules, and can subsequently ionize, dissociate (often producing electronically excited fragments), fluoresce, react with other species present, or undergo collisional quenching. Fluorescence is seldom observed, and if desired the reaction and quenching pathways can be precluded by working with sufficiently low gas pressures.

In simultaneous MPE (see Figure 1.9b) there is no real intermediate state involved : instead the electric field of the first photon interacts with the parent molecule to produce a 'virtual' state with a lifetime of about 10^{-15} seconds (the photon

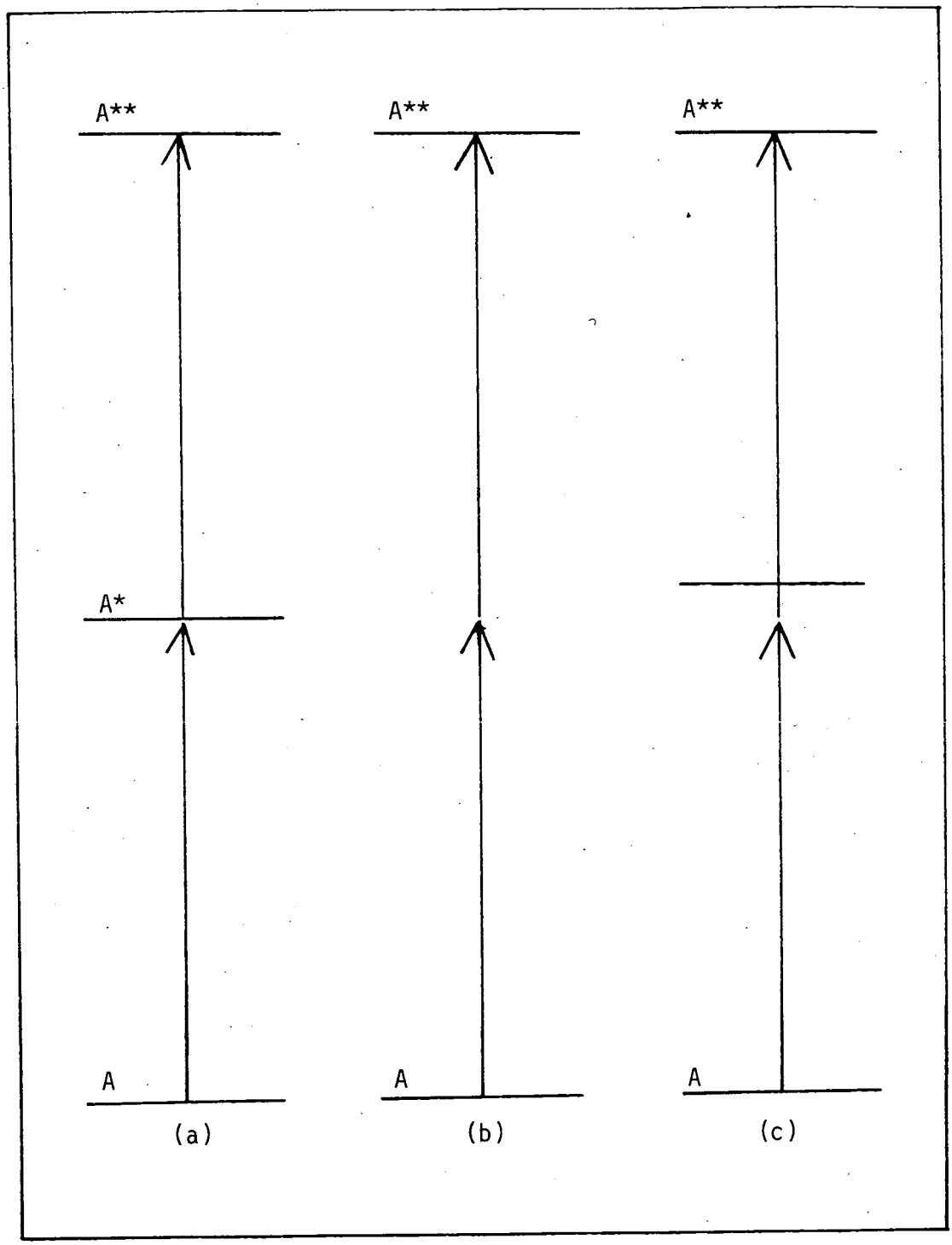

Figure 1.9 : **Schematic representation of 2-photon MPE processes - (a) sequential, (b) simultaneous (non-resonant), (c) simultaneous (near-resonant)**

fly-by time). If a second photon arrives during this time the molecule can simultaneously absorb them both. The presence of a nearby off-resonant state (or states) can increase the probability of absorption of the two photons (see Figure 1.9c).

Secondary excitation of primary photofragments can be represented schematically as follows:

$$A + (n)h\nu \longrightarrow A^* \qquad -(1.8a)$$

$$A^* \longrightarrow B + C \qquad -(1.8b)$$

$$B \text{ (or } C) + (n)h\nu \longrightarrow B^* \text{ (or } C^*) \qquad -(1.8c)$$

After absorption of the first photon(s) the parent molecule fragments. The second photon(s) is then absorbed by one of the photofragments taking it into an excited state. The overall process must occur during a single laser pulse (typically 15ns for an ArF excimer laser).

When a fluorescent species is produced in MPE, a lower limit to the order of the process can be determined from the dependence of the fluorescence intensity upon the laser energy. However, excepting the case of simultaneous MPE, this will be less than the true order if one of the transitions becomes saturated.

For processes involving an odd number of photons the parity selection rule is the same as that for single-photon absorption, ie $g \longleftrightarrow u$, $g \not\longleftrightarrow g$, $u \not\longleftrightarrow u$, but the reverse applies to processes involving an even number of photons where the selection rule is $g \longleftrightarrow g$, $u \longleftrightarrow u$, $g \not\longleftrightarrow u$.

An interesting feature of MPE is that it is possible to form doubly excited states, ie states in which two separate electrons are excited. This has been proposed[88], for the ArF laser photolysis of CH_3I:

$$CH_3I + 2h\nu \xrightarrow{\text{SIMULTANEOUS}} CH_3^*I^* \qquad -(1.9a)$$

$$CH_3^*I^* \longrightarrow CH^* + H_2 + I \qquad -(1.9b)$$

where $CH_3^*I^*$ has one electron excited into a C-I antibonding orbital and another into a CH_3 antibonding orbital.

1.9 QUENCHING MECHANISMS

Since much of the work to be reported here involves collisional quenching processes, a resumé of the various models used in the past to explain these processes will now be given. These models evolved initially in order to rationalise processes involving electronically excited atoms, and have since been extended to molecular systems.

Electronic quenching processes have been studies since the 1920's[97-100], but it is only recently that a reasonably complete understanding of the mechanisms governing them has been obtained. This is due to the difficulties involved in the theoretical treatment of excited state potentials. Three classes of mechanisms will be considered : (a) near-resonant (long-range) electronic energy transfer, (b) curve-crossing, and (c) collision complex formation.

(a) Near-resonant Electronic Energy Transfer

Electronic relaxation may be strongly influenced by this mechanism where near resonances are involved, and where strongly allowed electric dipole or electric quadrupole transisitions are involved. In atom-atom systems this necessitates a small energy mismatch, ΔE, between the inital and final states involved. In atom-molecule (or molecule-molecule) systems some of the internal energy can be 'soaked up' by the rovibrational degrees of freedom, thus giving more nearly resonant conditions.

An example of an atom-atom system in which this mechanism is operative involves electronic energy transfer between the multiplet levels of alkali metals induced by collisions with rare gas atoms. The experimental results have been reviewed by Krause[101], and exhibit a logarithmic decrease in transfer probability with increasing ΔE. This behaviour is characteristic of the near-resonant electronic relaxation mechanism. When the long-range dipole-dipole mechanism is operative (ie when the electronic states involved for both atoms are connected by dipole matrix elements), the resonant energy transfer probability is given by

$$P_{if} = \sin^2(2C/\hbar b^2 v) \qquad -(1.10)$$

assuming a straight line trajectory, where b is the impact parameter, v is the relative velocity and C is given by

$$C = \mu_{1if}\,\mu_{2if} \times \text{angular matrix elements} \qquad -(1.11)$$

where the μ_{if} are the transition moments. Such interactions can give rise to extremely large cross-sections, of the order 10^3 - 10^4Å, and thus resonant electronic energy transfer for dipole-allowed transitions is very efficient.

In atom-molecule (or molecule-molecule) systems the situation is less straight-forward as complications arise due to the internal degrees of freedom of the collision partners. Resonant energy transfer usually involves excitation of rovibrational motion in the collision partner, either exclusively ($E \longrightarrow V,R$), or in addition to electronic excitation ($E \rightarrow E,V,R$). Expressions for calculating the transfer probabilities for the various types of electrostatic interactions are given by Yardley[102].

There are several sets of experimental results which provide good tests for this theory. The results of Fink and co-workers[103] indicate that energy is resonantly transferred in collisions of optically excited Ar* with H_2, HD and D_2. Observations of the resulting light emission from individual rovibronic levels of the $B^1\Sigma_u^+$ state of $H_2/HD/D_2$ show that the largest cross-sections occur for transitions which are electric dipole-allowed and for which $\Delta E < 200cm^{-1}$. Relaxation of Ar* is also dipole allowed, and cross-sections calculated on the basis of the long-range dipole-dipole mechanism gave excellent agreement with experiment in the case of $\Delta E \lesssim 20cm^{-1}$. Poor agreement was obtained for larger values of ΔE as another mechanism(s) becomes predominant.

Examples of dipole-quadrupole[104,105] and quadrupole-quadrupole[106]

near-resonant energy transfer processes can also be found in the literature.

(b) Curve-Crossing Mechanism

In this model quenching proceeds by transfer from the diabatic curve of the initial state (X*+Q) to one or more diabatic potential surfaces leading to the final state(s) $(X + Q^{\ddagger})$[107-117].

When the entrance and exit channels are coupled directly and the collision energy is sufficient to reach the crossing point, σ_Q is obtained classically by averaging the Landau-Zener transfer probability over impact parameter and the Boltzmann velocity distribution. A large σ_Q results if the entrance channel crosses a large number of exit channels. Reactive quenching, with the entrance channel adiabatically converted to a product chanel, may also have a large σ_Q. For small crossing probabilities, P_x, the quenching cross section is given approximately by[109,114]

$$\sigma_Q = 2\pi r_x^2 P_x \exp[-\Delta E/kT] \qquad -(1.12)$$

where ΔE is the energy defect between the curves.

The entrance and exit channels may be coupled by an intermediate potential, which is frequently an ion-pair curve[107]. Figure 1.10 illustrates this type of coupling, which was first suggested by

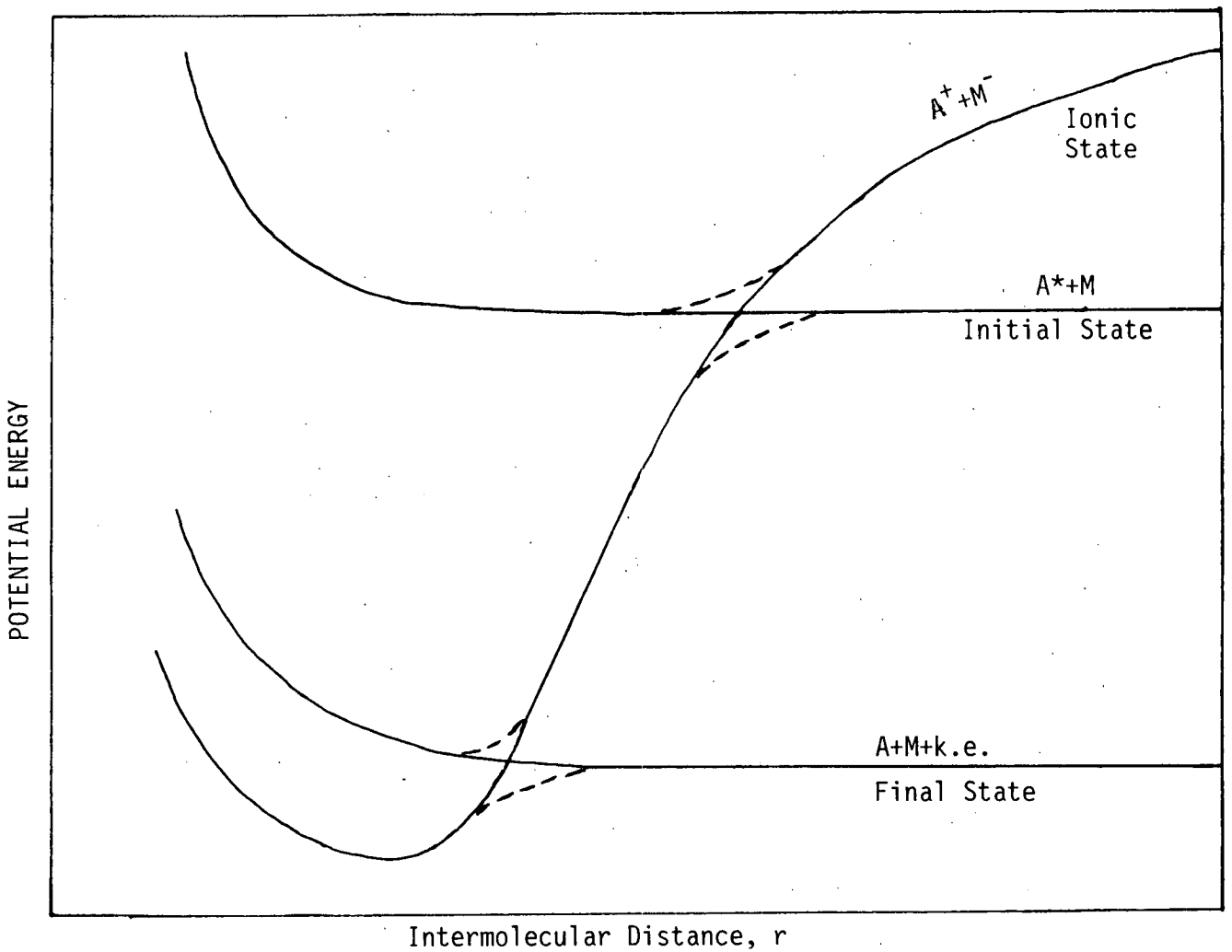

Figure 1.10 : **Potential energy curves illustrating the quenching of an excited species, A*, by a collision partner, M, via an ionic intermediate state, $A^+ + M^-$**

Laidler in 1942[118]. If the entrance channel is nearly flat up to the crossing point r_x, its value can be estimated from the condition

$$e^2/r_x = IP(A^*) - EA(M) \qquad -(1.13)$$

where IP is the ionization potential and EA the electron affinity.

If the collision pair transfers to the ionic curve a variety of exit channels may become accessible as the steeply attractive curve crosses them, and the distribution of products will be determined by the relative strength of the couplings between the ionic curve and the various product channels. Ultimately the ion-pair will dissociate either back into the initial elastic channel, or into some other neutral channel due to a crossing of the ionic curve with a lower energy neutral curve. In the special case for which a second strong coupling does not occur, either because the interactions are very weak or because no exit channel exists, the collision pair follows the ionic potential and reactive quenching can result[33,34,119].

The electron transfer model has been successfully applied to E-V transfer in the Na^*-N_2 system[120,121], however the model is not generally applicable to E-V transfer processes.

c. Collision Complex Theory

In an atom-molecule or molecule-molecule encounter it is

possible for a long-lived collision complex to form provided that there is a sufficiently strong attraction between the species. This entails a partitioning of the available energy between the various degrees of freedom of the complex (ie. inter- and intra-molecular). When such a complex is formed a curve-crossing point may be crossed several times during its lifetime, thus enhancing the energy transfer rate. Statistical theories can be used to predict the probability of decomposition of the complex.

Collision complex formation has been proposed for a number of systems. Polanyi and co-workers[122] have suggested that an Hg-CO complex is produced in the interaction of Hg* with CO, while Levine and Bernstein[123] have argued a similar case in the interaction of Na* with CO. By applying a collision complex model to the quenching of $O(^1D)$ by N_2, Tully[124] was able to calculate a rate constant of $7\times10^{-11}cm^3molec^{-1}s^{-1}$, which agrees well with the experimental value of $(6.9\pm0.6)\times10^{-11}cm^3molec^{-1}s^{-1}$.[125] Tully also calculated that $(30\pm10)\%$ of the available energy will appear as vibrational excitation, c.f. the experimental value of 33%[126].

CHAPTER 2 : EXPERIMENTAL

2.1 THE SYNCHROTRON RADIATION SOURCE

The synchrotron radiation source (SRS) used is located at the SERC Daresbury Laboratory, and consists of an evacuated ($p \approx 10^{-8}Nm^{-2}$) storage ring around which bunches of electrons are accelerated at close to the speed of light. Radiation, covering the entire electromagnetic spectrum, is produced at each of 16 magnets which steer the electrons in a near circular path. Beams of this radiation are collected at several experimental ports where the desired wavelength can be selected by an appropriate means, eg a monochromator when working in the UV.

The SRS can be run in either of two modes. In 'multibunch' mode, 160 discrete bunches of electrons (each 3.6cm in length) are accelerated around the ring. This produces light pulses of ~120ps duration at 2ns intervals. In 'single-bunch' mode as the name suggests, only one bunch of electrons is accelerated around the ring, producing 120ps pulses at intervals of 320ns. The beam energy was 1.8-2.0 GeV and the current was normally $\lesssim$ 180mA (multibunch) or $\lesssim$ 20mA (single-bunch).

2.2 ABSORPTION SPECTRA (PORT VUV3)

The absorption spectrum of IBr in the region 160-200nm was recorded on port VUV3 of the SRS (operating in multibunch mode). The synchrotron radiation was dispersed using a McPherson 5m monochromator (dispersion 0.16nm/mm), and then directed along the axis of a cylindrical pyrex cell containing the gas sample. The

cell, path length 10cm, was fitted with front and rear LiF windows. The rear (exit) window was coated externally with sodium salicylate to allow monitoring of transmitted light with a conventional photomultiplier detector (EMI 62565). The photomultiplier output was fed via a current integrator to a PDP 11/04 minicomputer, which recorded the wavelength setting simultaneously. The stepping of the monochromator grating was also controlled by the minicomputer. Digitised spectra were then transferred to an AS7000 mainframe computer for plotting.

The monochromator wavelength setting was calibrated before commencement and after completion of the experiments by recording the Schumann-Runge absorption bands of O_2.

2.3 EXCITATION AND ABSORPTION SPECTRA (PORT HA12)

Excitation and absorption spectra were recorded simultaneously using beam line HA12 of the SRS (operating in multibunch mode). The radiation from the ring was dispersed using a Spex 1500 SP Czerny-Turner monochromator. The beam was then directed along the axis of a 10cm spectrosil fluorescence cell containing the sample, which was mounted in an evacuable box fitted with two photomultiplier detectors (see Figure 2.1). The box could be pumped down to a pressure of $\sim 0.5 Nm^{-2}$. Absorption was monitored using a conventional photomultiplier detector (EMI 62565) which was bolted in position, in direct line with the excitation beam, behind a sodium salicylate coated screen. Undispersed fluorescence was monitored using a quartz windowed photomultiplier

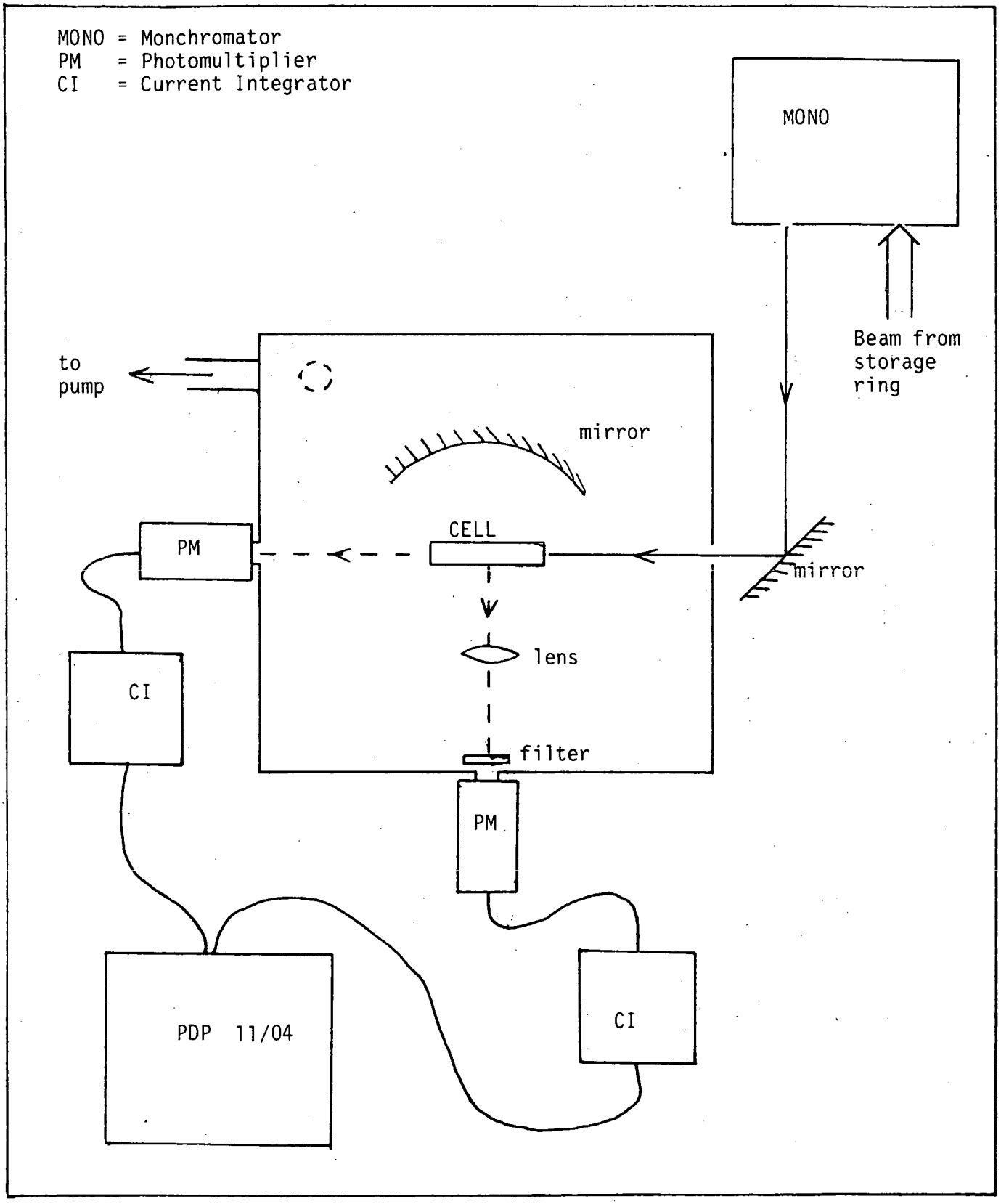

Figure 2.1 : **Schematic diagram of experimental set-up employed to record excitation/absorption spectra on SRS port HA12**

(Mullard PM2020Q), which was bolted in position, opposite the cell, at right angles to the beam. A concave mirror and focussing lens were utilised to maximise the fluorescence signal, and a filter (cut-off below 280nm) was positioned in front of the photmultiplier to exclude scattered light. Thus fluorescence was detected for $280 \leq \lambda \leq 650$nm.

Outputs from the photomultipliers were sent via current integrators to a PDP 11/04 minicomputer, which also recorded the wavelengths and controlled the stepping motor of the monochromator grating during scans. Digitised spectra were then transferred to an AS7000 mainframe computer for plotting.

The monochromator was calibrated before and after runs using the O_2 Schumann-Runge band system, which was recorded in the region 188-200nm with the box full of air.

2.4 FLUORESCENCE SPECTRA RECORDED WITH A SPECTROFLUORIMETER

Fluorescence spectra were recorded on a Perkin-Elmer 650-40 spectrofluorimeter, using an excitation wavelength of 200nm with various bandpasses. The samples were contained in standard $1cm^2$ quartz spectrofluorimeter cells. The use of a 280nm cut-off pyrex filter prevented scattered light from the excitation lamp reaching the detection photomultiplier. All spectra were recorded in 'ratio' mode, whereby the fluorescence intensity is automatically scaled to compensate for random fluctuations in the excitation lamp intensity.

2.5 LIFETIME STUDIES (PORT HA12)

Lifetime studies on ion-pair states of IBr and I_2 were carried out on port HA12 of the SRS, operating in single bunch mode. Radiation from the storage ring was dispersed by a Spex 1500 SP Czerny-Turner monochromator, then passed through a $1cm^2$ spectrosil fluorescence cell containing the gas sample. The cell was mounted in a blacked-out chamber to exclude light from the surroundings. Fluorescence at right angles to the excitation beam was passed through a filter (usually LF30, $\lambda > 300nm$), then detected by a Mullard XP2020Q photomultiplier. Fluorescence lifetimes were determined by measuring successive time intervals between photomultiplier pulses (after constant fraction discrimination) and the zero time reference signal from the storage ring, using a time-to-amplitude converter (TAC). Output pulses from the TAC were accumulated in a multichannel analyser. Lifetime spectra were recorded on a PDP 11/04 minicomputer, from which they were transferred to an AS7000 mainframe computer for data analysis and plotting. This arrangement is represented schematically in Figure 2.2. This time-resolved work was carried out with my colleague, Dr M MacDonald.

2.6 SPECTRALLY RESOLVED CH($A^2\Delta \rightarrow X^2\Pi$) EMISSION RECORDED AT EDINBURGH

The focussed output of a Lambda Physik EMG500 excimer laser operating at 193nm (ArF laser) was passed axially through a large cross-shaped cell (fitted with specrosil windows) containing the gas samples. Typically the laser energy was ~6mJ, with a pulse

Figure 2.2 : **Schematic diagram of experimental set-up employed in lifetime studies on SRS port HA12**

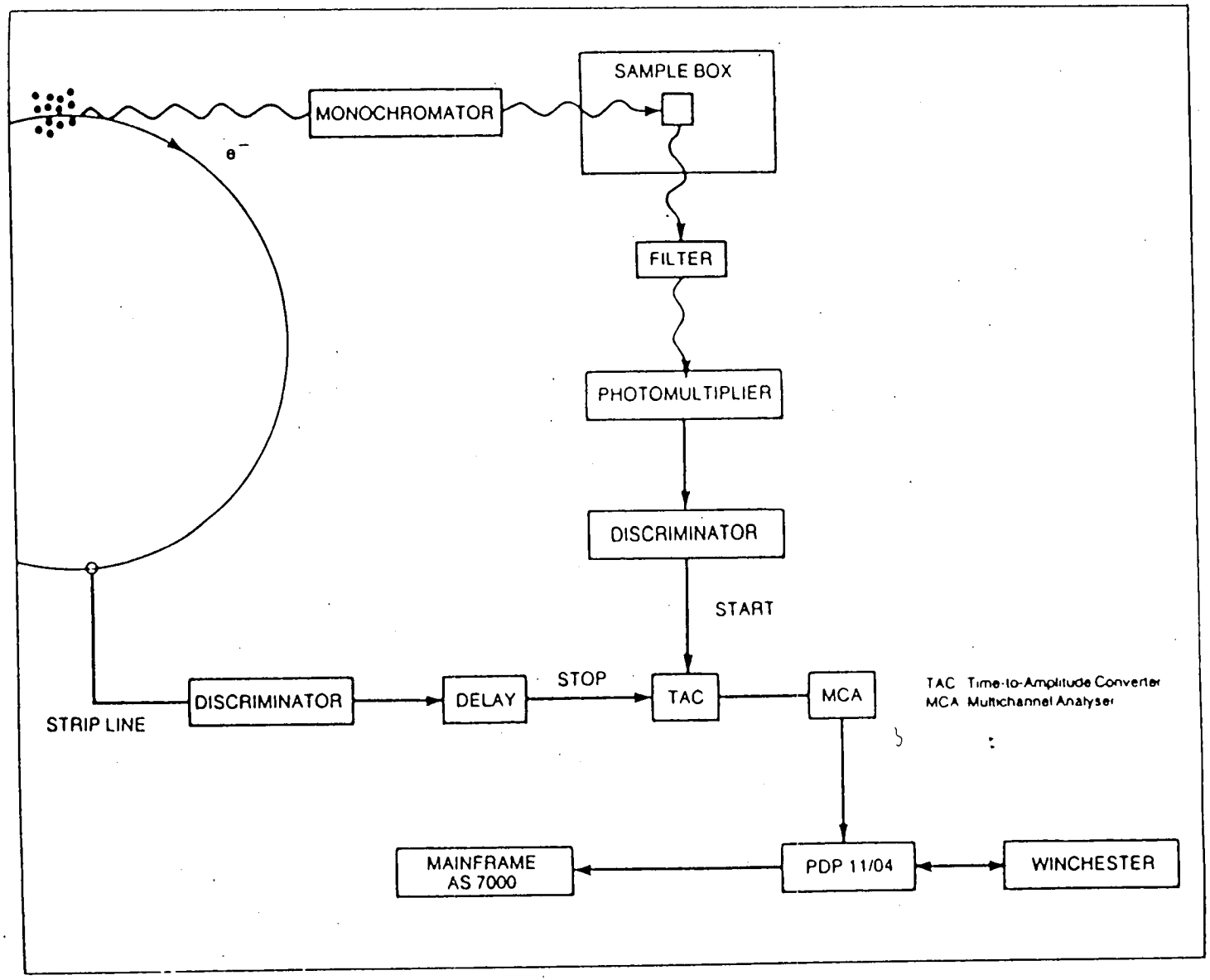

duration of 14ns, a repetition rate of 2Hz, and a bandwith of 1nm. The resulting focussed output intensity was of the order of 5 $MWcm^{-2}$. Photofragment fluorescence was observed at right angles to the laser beam. The fluorescence was dispersed by means of a monochromator (McKee-Pederson MP1018B or Jobin-Yvon HRS2) prior to detection by a photomultiplier (EMI 9661B or Hamamatsu R928). The signal from the photomultiplier was processed by a gated integrator (Brookdeal 9415), and the output of the integrator was recorded on a strip chart. The resultant spectra were not corrected for the spectral response of the system.

2.7 SPECTRALLY RESOLVED CH($A^2\Delta \longrightarrow X^2\Pi$) EMISSION RECORDED AT THE RUTHERFORD APPLETON LABORATORY

The focussed output of a Lambda Physik EMG201 excimer laser operating at 193nm (ArF laser) was passed through a large cross-shaped cell (fitted with spectrosil windows) containing the gas samples. Laser energies as high at 200mJ were obtained, with a pulse duration of 14ns and $\Delta\lambda \approx 0.5$nm. Photofragment fluorescence was observed at right angles to the laser beam. The fluorescence was dispersed using a Jobin Yvon 0.3m monochromator fitted with a medium-resolution grating (resolution $\Delta\lambda \approx 0.35$nm). Light was detected at the exit port of the monochromator with an optical multichannel analyser (Princeton Applied Research/EG+G OMA2 with silicon intensified vidicon). In this way fluorescence spectra covering the region 400-460nm were recorded using a single laser pulse.

2.8 KINETIC STUDIES ON CH($A^2\Delta$)

Time-resolved studies of CH($A^2\Delta \longrightarrow X^2\Pi$) emission were carried out at the Rutherford Appleton Laboratory. The focussed output of a Lambda Physik EMG201 excimer laser operating at 193nm was passed through a large cross-shaped cell, fitted with spectrosil windows, containing the gas samples (precursor plus quenching gas). The CH($A^2\Delta \longrightarrow X^2\Pi$) fluorescence at 431.5nm was viewed using a monochromator (Monospek 600) plus photomultiplier (NPAG334) combination. The photomultiplier output signal was taken via a $50\,\Omega$ termination to a fast storage oscillocope (Tektronix 466). The oscilloscope trace was photographed for subsequent measurement and least squares analysis.

Helium buffer gas ($1.3\times10^3 Nm^{-2}$) was added to the photolysis mixtures to minimuse the rate at which the CH($A^2\Delta$) fragments moved out of the viewing region.

2.9 GAS HANDLING AND CHEMICALS USED

Gas samples were introduced to the cells via a conventional pyrex vacuum line. All of the cells were fitted, by means of black wax, with greasless taps. Ampoules containing solid/liquid substances and bulbs containing gaseous substances were also fitted for the most part with greaseless taps. To facilitate degassing, bulbs with 'cold fingers' were used for condensable gases.

IBr samples were prepared by filling a bulb with a 3:1 mixture of

Br_2:I_2, in order to completely supress I_2. After degassing, the mixture was left for several days to allow equilibration : $I_2 + Br_2 \rightleftharpoons 2IBr$.

The reagent pressures used in the experiments were measured with a capacitance manometer (MKS Baratron).

The chemicals used were as follows : I_2 (BDH, Analar grade, 99.9% purity), Br_2 (Fisons, SLR grade, 99% purity), SF_6 (Matheson, CP grade), Xe (BOC, Spectroscopic grade), CF_4 (BOC), CH_4 (BOC, Spectroscopic grade, 99% purity), N_2 (BOC, oxygen free), CH_3Cl (BDH), C_2H_6, CF_3Cl (Matheson), O_2 (BOC, 'Zero' grade), CH_3Br, $CHBr_3$, C_2H_2 (BOC), CH_3OH (May + Baker, AR grade), $(CH_3)_2CO$ (Fisons, AR grade), CH_2I_2, He (BOC, 'A' grade), Ar (BOC, high purity), H_2 (BOC, CP grade).

CHAPTER 3 - SPECTROSCOPIC STUDIES OF IBr

3.1 INTRODUCTION

The spectroscopic studies outlined in this chapter were carried out in order to elucidate the ion-pair states of IBr in the region 160-200nm. Aside from the intrinsic value of such studies, the excitation spectra were useful in the selection of excitation wavelengths for lifetime experiments (see Chapter 5).

Figure 3.1 shows approximate potential energy curves for some electronic states of IBr. Most of the purely repulsive states have been omitted.

Spectroscopic studies of the ion-pair states (three of which are shown in Figure 3.1) have been scarce to date. Diegelmann and co-workers[26] observed the D'(2) A'(2) emission following electron bombardment of IBr, and have estimated the spectroscopic constants for the (lowest) D'(2) state (see Table 3.1). Brand and co-workers[54] have probed the other two states which dissociate to $I^+(^3P_2)+Br^-(^1S)$, the "E" (0^+) and the $1(^3P_2)$ state ($\Omega=1$), and the $f(0^+)$ state which dissociates to $I^+(^3P_0)+Br^-(^1S)$. A 2-photon pump-probe technique was used, giving access to the lower vibrational levels ($v < 31$) for these states. The derived spectroscopic constants are given in Table 3.1 where the "E" state is renamed $D(0^+)$. There are two reasons for renaming it : (1) the "E" designation was adopted in analogy to the $E(0g^+)$ state of I_2 which can only be probed by 2-photon excitation from the ground state, however the parity selection rule in not applicable to IBr.

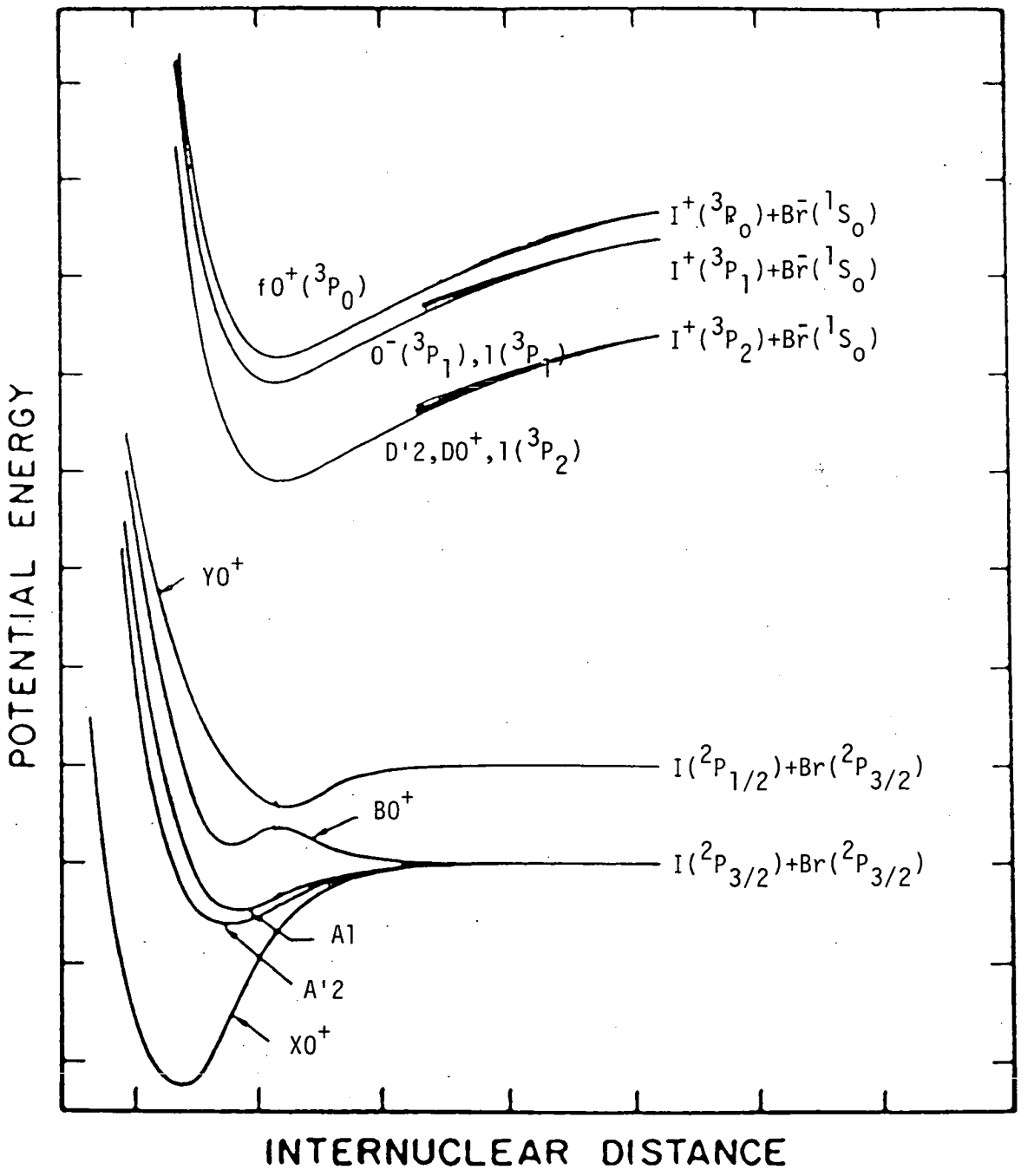

Figure 3.1: Approximate potential energy curves for selected valence states plus three of the six lowest ion-pair states of IBr.

TABLE 3.1 Spectroscopic constants for some ion-pair states of IBr.

STATE	DIABATIC DISSOCIATION PRODUCTS	T_e/cm^{-1}	$r_e/Å$	ω_e/cm^{-1}	$\omega_e x_e/cm^{-1}$
D'(2)	$I^+(^3P_2)+Br^-(^1S)$	~37840[a]	~3.105[a]	154[a]	
$D(0^+)$	$I^+(^3P_2)+Br^-(^1S)$	39487 39491.35[b]	3.42 3.360[b]	119.5 119.518[b]	0.211 0.2063[b]
$_1(^3P_2)$	$I^+(^3P_2)+Br^-(^1S)$	≤39520	~3.4	~120	
$f(0^+)$	$I^+(^3P_o)+Br^-(^1S)$	45383	3.40	128.8	0.363

Data from Brand et al[54], except when marked

a : Diegelmann et al[26]

b : King et al[53]

(2) the first Rydberg state (energy $\simeq$51200 cm^{-1}) has already been designated "E"[127] and this could confuse matters. Therefore the lowest 0^+ state shall be referred to as $D(0^+)$, in analogy to the $D(0_u+)$ state of I_2. ($I_2D(0_u+)$ lies below $I_2E(0_g+)$ by ~400 cm^{-1}). This 0^+ state has also been probed by King and co-workers[53] using a similar 2-photon absorption technique. The spectroscopic constants derived by them are also given in Table 3.1.

3.2 THE IBr ABSORPTION SPECTRUM

RESULTS

The absorption spectrum of IBr, recorded at a resolution of 0.064nm, is shown in the region 160-200nm in Figure 3.2 (for experimental details see section 2.2). The pressure of IBr in the cell was reduced by expansion until the strongest peak gave less than total absorption. Figure 3.3 shows the instrument response which was measured with the cell evacuated. A comparable spectrum of I_2 is also presented (Figure 3.4) as it exists in equilibrium with IBr, viz:

$$I_2 + Br_2 \rightleftharpoons 2IBr \quad , K_{eq} \qquad -(3.1)$$

for which K_{eq} has been measured as 480[128]. None of the I_2 absorption features are evident in Figure 3.2, indicating that the 3:1 mixture of Br_2 :I_2 is sufficient to reduce I_2 absorption below the noise level. As the onset of Br_2 absorption in the UV is at ~165nm, contamination of the spectrum due to the excess Br_2 will

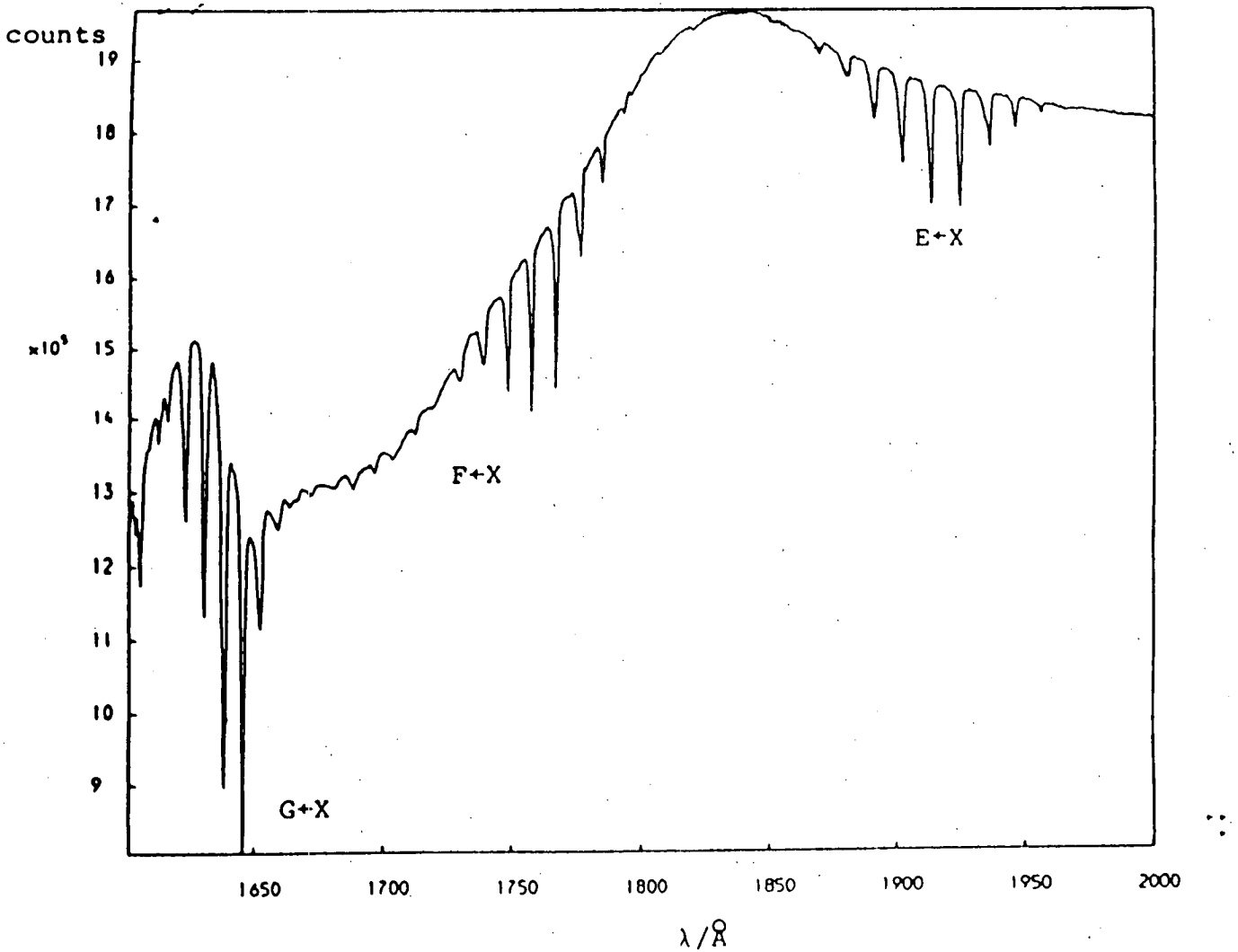

Figure 3.2: The absorption spectrum of IBr recorded at 0.064nm resolution. (NB: the scale reads high by 2.8Å)

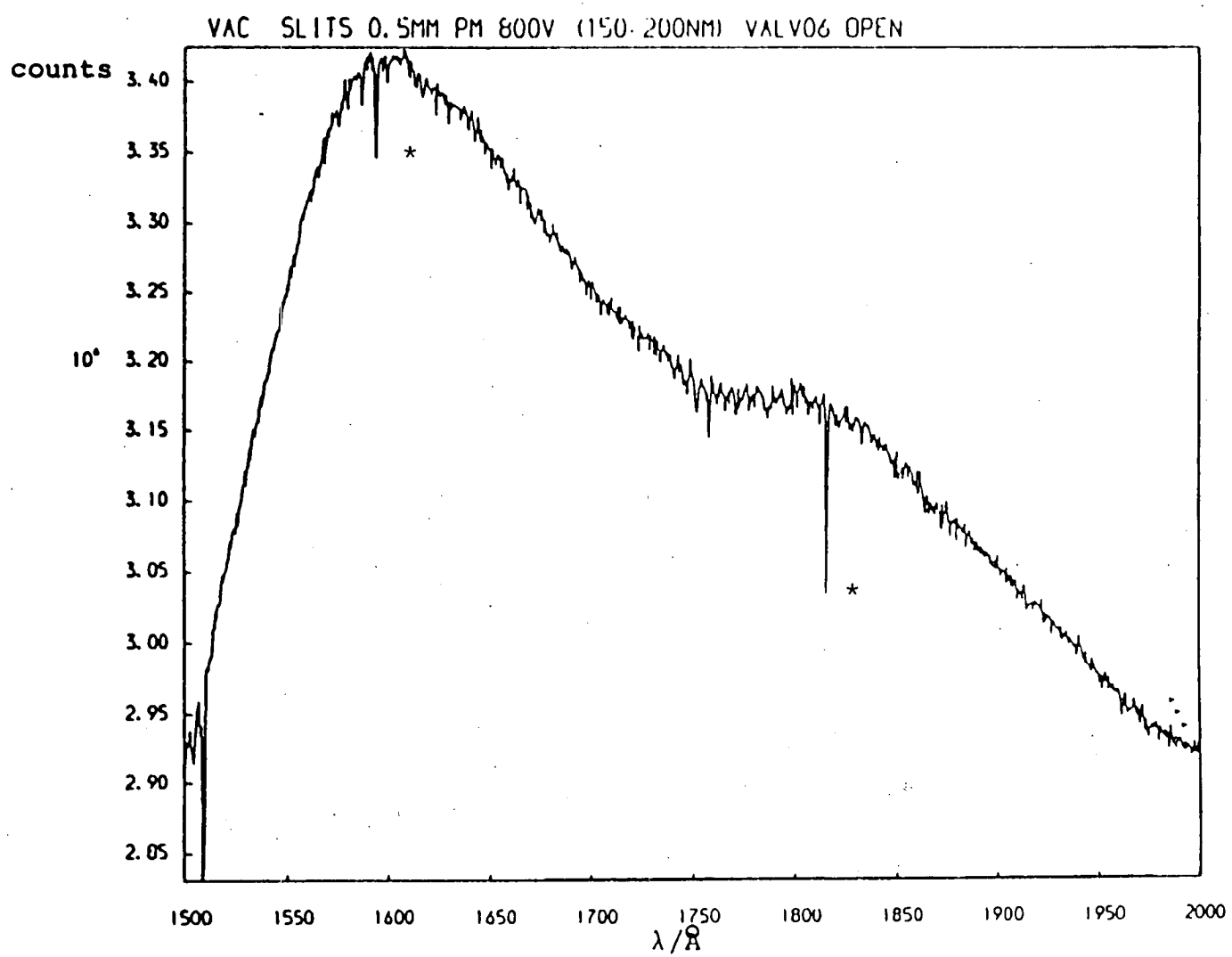

Figure 3.3: Instrument response of SRS port VUV3, recorded with the cell evacuated. (* : these features are noise spikes)

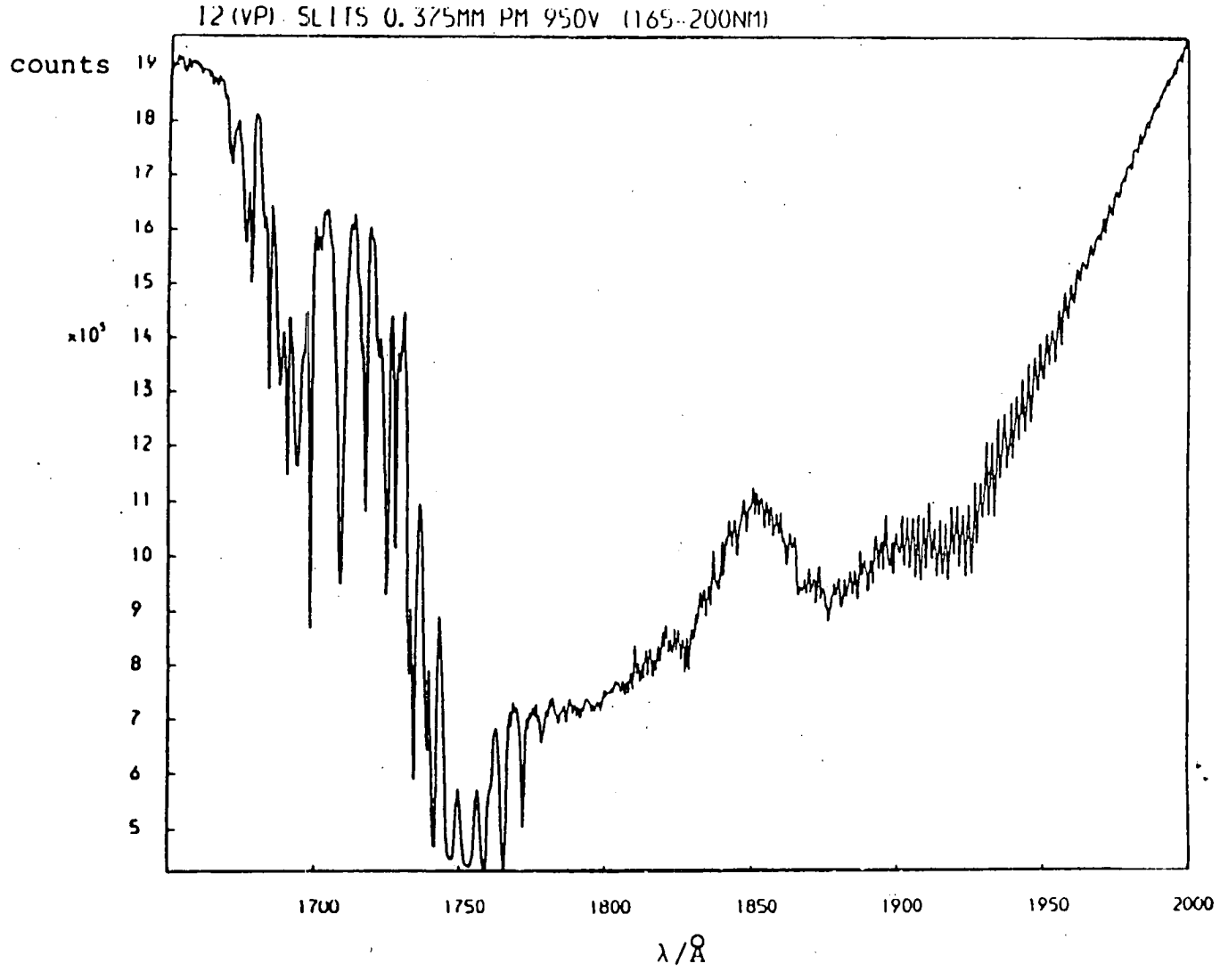

Figure 3.4: The absorption spectrum of I_2 (27 Nm^{-2}) recorded at 0.064nm resolution (NB: the scale reads high by 2.8Å)
Taken from M A MacDonald, PHD Thesis, 1984.

be minimal.

The most prominent features in the spectrum are due to three previously assigned Rydberg systems[129], ie $E \leftarrow X(\nu_{00} \approx 51200cm^{-1})$, $F \leftarrow X(\nu_{00} \approx 54900cm^{-1})$ and $G \leftarrow X(\nu_{00} \approx 60900cm^{-1})$. The spacings between the peaks in the structured region at 166-173nm are ~ 0.9nm($\equiv 300cm^{-1}$), indicating that they also form part of the Rydberg series. Other than this there is a broad continuous absorption extending from ~163-180nm, and possibly another less intense absorption underlying the $E \leftarrow X$ Rydberg system. Higher frequency structure, if found, would be indicative of the ion-pair states, which are expected to have vibrational spacings of $\leq 70cm^{-1}$ at levels accessible by single photon absorption. Therefore higher resolution spectra were recorded in a search for such structure.

A high resolution (0.016nm) spectrum of the region 190-195nm is presented in Figure 3.5. Although there is possible structure between the Rydberg peaks, it is not clearly resolved and thus gives no information on any underlying state(s). The region 185-190nm is shown under even higher resolution (0.008nm) in Figure 3.6. Very small peaks are barely discernible between the Rydberg peaks, with spacings of ~0.21nm ($\equiv 60cm^{-1}$). This suggests that they belong to an ion-pair system.

The region 180-185nm was found to be completely devoid of resolvable features. In sharp contrast, the broad absorption at $\lambda < 180nm$ which underlies the $F \leftarrow X$ Rydberg system clearly shows high frequency structure (see Figure 3.7). A resolved series of

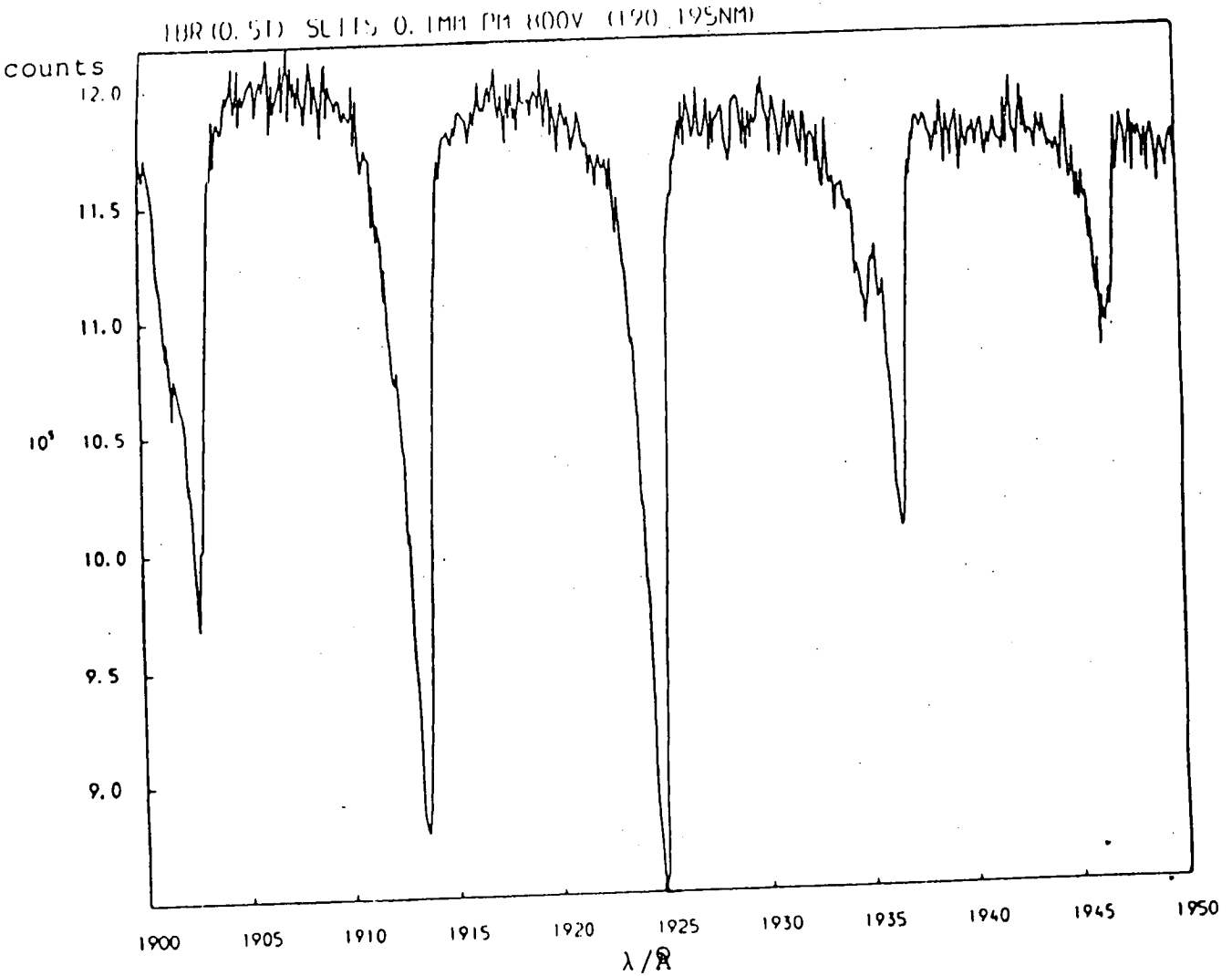

Figure 3.5: The absorption spectrum of IBr in the region 190-195nm, recorded at 0.016nm resolution. (NB: the scale reads high by 2.8Å)

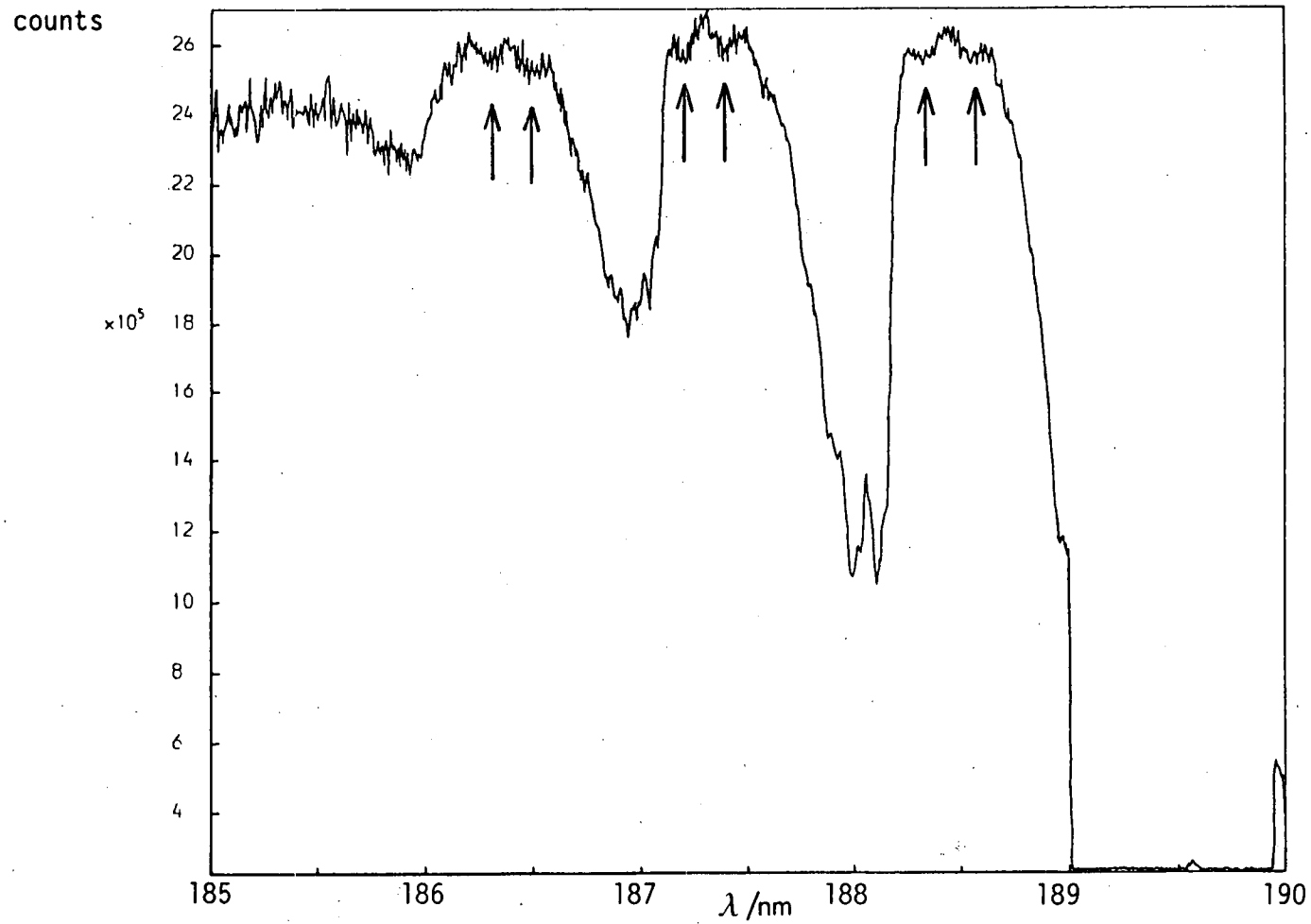

Figure 3.6: Absorption spectrum of IBr in the region 185-190nm, recorded at 0.008nm resolution. The arrows show peaks due to an ion-pair state absorption. (NB: the scale reads high by 0.28nm)

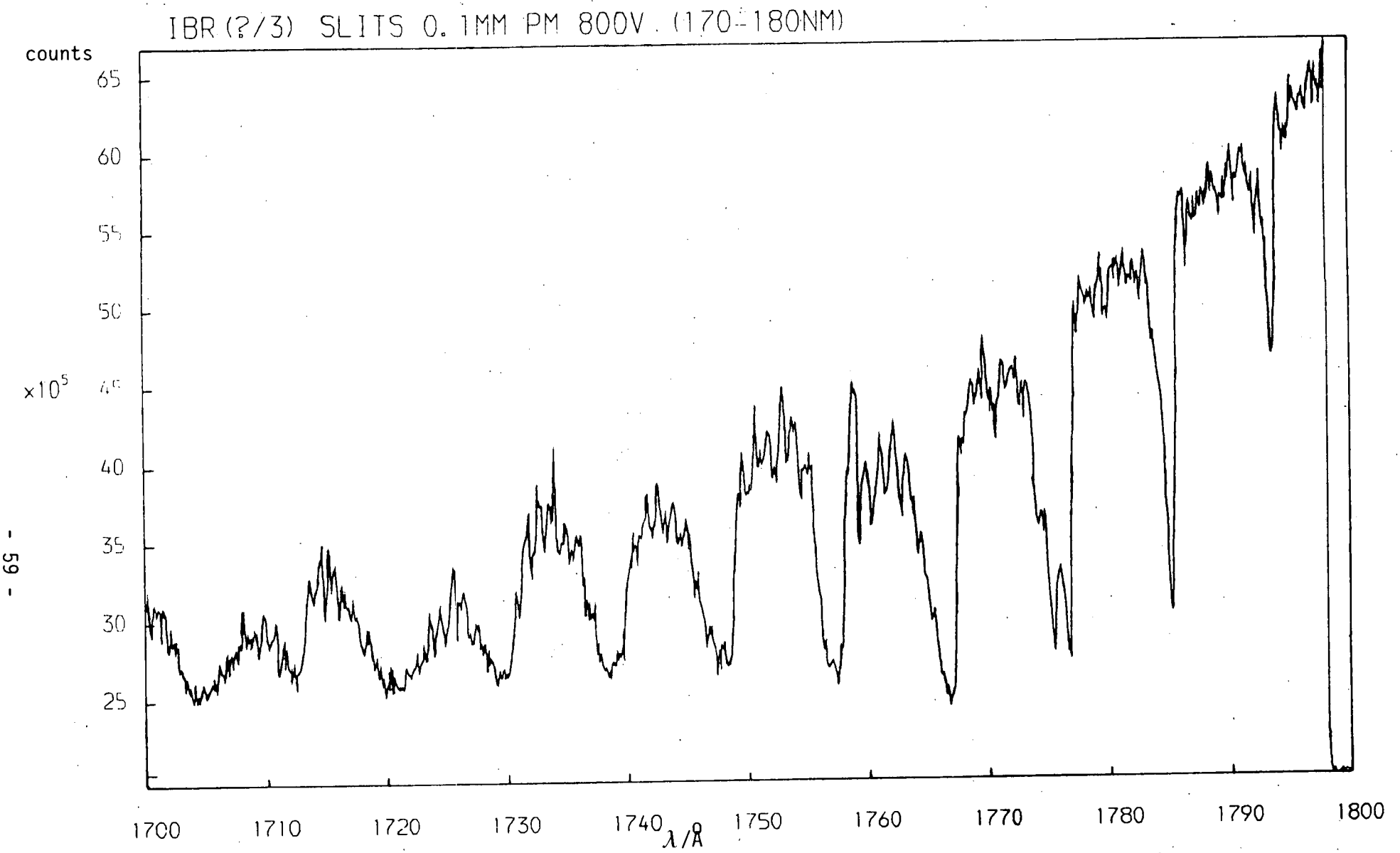

Figure 3.7: Absorption spectrum of IBr in the region 170-180nm, recorded at 0.016nm resolution. (NB: the scale reads high by 2.8Å)

peaks forming a single progression can be seen extending from ~171-179nm. The small peak spacings and the very gradual convergence are both symptomatic of an ion-pair state ($\Delta\nu$ =45+5cm^{-1} at 171nm). As the room temperature population of IBrX(v"=0) is approximately four times that of IBrX(v"=1) this progression is likely to be dominantly v'$\longleftarrow$v"=0. (If the Franck-Condon factors are favourable, it is possible that this is a v"=1 progression).

In the region below 170nm any high frequency structure, if present, is below the noise level.

DISCUSSION

Any ion-pair states observed must have total angular momentum, Ω=0 or 1. The state detected in the region 185-190nm will almost certainly belong to the lowest grouping of these states (correlating with $Br^-(^1S)+I^+(^3P_2)$ in the diabatic dissociation limit), and this being the case it must be either the $D(0^+)$ state or the $1(^3P_2)$ state previously observed using sequential 2-photon absorption[54]. The vibrational spacing of 60±5cm^{-1} at 188.5nm (marked with arrows on Figure 3.6) is possibly an extrapolation of the trend in $\Delta\nu$ from ~30$\longrightarrow$~45cm^{-1} noted in the progression at shorter wavelengths. If this is the case it is most likely that a single ion-pair state is (at least partially) responsible for the absorption underlying the E$\leftarrow$X and F$\leftarrow$X Rydberg systems. (The lack of structure in the intermediate region does not affect this argument : a contribution from a v'$\longleftarrow$v"=1 progression or from absorption to another ion-pair state could obscure any structure).

To test this the vibrational quantum numbers and expected vibrational spacings were calculated at the relative wavelengths, using the spectroscopic constants derived for the $D(0^+)$ state in references **54** and **53** (see Table 3.1). The results of these calculations are set out in Table 3.2. (Insufficient information is available to perform similar calculations for the $1(^3P_2)$ state which lies $\leq 30cm^{-1}$ above the $D(0^+)$ state and is believed to have an almost identical potential.) There is good agreement at 188.5nm between the observed vibrational spacings and those calculated from the constants in reference **53**, given that these were derived from the analysis of data for the lowest vibrational levels ($v < 21$) of the $D(0^+)$ state. However, due to the limitations imposed by this (their RKR analysis only extended to r=3.999Å in the attractive limb) they did not derive any higher order terms, and this deficiency is illustrated by the rapid convergence of the peaks (the limit being reached at a wavelength longer than 171nm). The pairs of values obtained for ω_e and $\omega_e x_e$ are in excellent agreement (see Table 3.1). In addition, Brand and co-workers obtained a value of $-2.34 \times 10^{-4} cm^{-1}$ for $\omega_e y_e$ in their analysis which extended to v'=30.[54] When this term is included in the calculations it overcompenstates, slowing down the rate of convergence. (In the absence of higher oder terms, ie $v^n (n \geq 4)$, the series would start diverging at higher v', never reaching a convergence limit.) The agreement in the vibrational spacings at 188.5nm suggests that the ion-pair state observed is in fact the $D(0^+)$ state. The disagreement at shorter wavelengths results from the inaccuracy of

TABLE 3.2 : Calculated values of v and $\Delta\nu$ for $IBrD(O^+)$ at selected wavelengths, using the spectrocopic constants from Table 3.1 (Reference **54** gives $\omega_e y_e = 2.34 \times 10^{-4} cm^{-1}$).

Reference	λ = 188.5nm		λ = 179nm		λ = 171nm	
	v'	$\Delta\nu/cm^{-1}$	v'	$\Delta\nu/cm^{-1}$	v'	$\Delta\nu/cm^{-1}$
54	145	72.9	185	65.3	227	59.8
53	156	54.4	227	25.1	---	---
Experimental Observation		60		45		30

the value of $\omega_e y_e$: it can be seen from Table 3.2 that the term in v^3 has a marked effect at $v' \geq 150$.

A more accurate value for $\omega_e y_e$ was obtained by imposing the restriction that v'(170.21nm)-v'(174.29nm)=41 (see Figure 3.8). Using values of ω_e=119.518cm^{-1} and $\omega_e x_e$=0.2109cm^{-1}, a value of $\omega_e y_e$=-1.13x10^{-4}cm^{-1} was obtained by iteration. This value was then used to calculate the vibrational levels and spacings at various wavelengths (see Table 3.3). These spectroscopic constants provide a good fit to the observations in both spectral regions where high frequency structure was resolved. However, the vibrational levels are predicted to converge at v'=436, which corresponds to a well depth of 21384cm^{-1}. The actual well depth of the D(0$^+$) state can be calculated as

$$E = D_e(IBrX \rightarrow Br^-(^1S) + I^+(^3P_2)) - T_e(IBrD) \qquad -(3.2)$$

which yields a value of 32557cm^{-1}. This implies that higher order terms (v^n,$n \geq 4$) must dominate at very high v'.

There are two other possible explanations for these results : (1) the absorption discussed above may be due to the transition $1(^3P_2) \leftarrow X(0^+)$ rather than $D(0^+) \longleftarrow X(0^+)$, or (2) there may be contributions from both of these transitions. The second possibility would provide a feasible explanation for the absence of structure in the region 180-185nm,

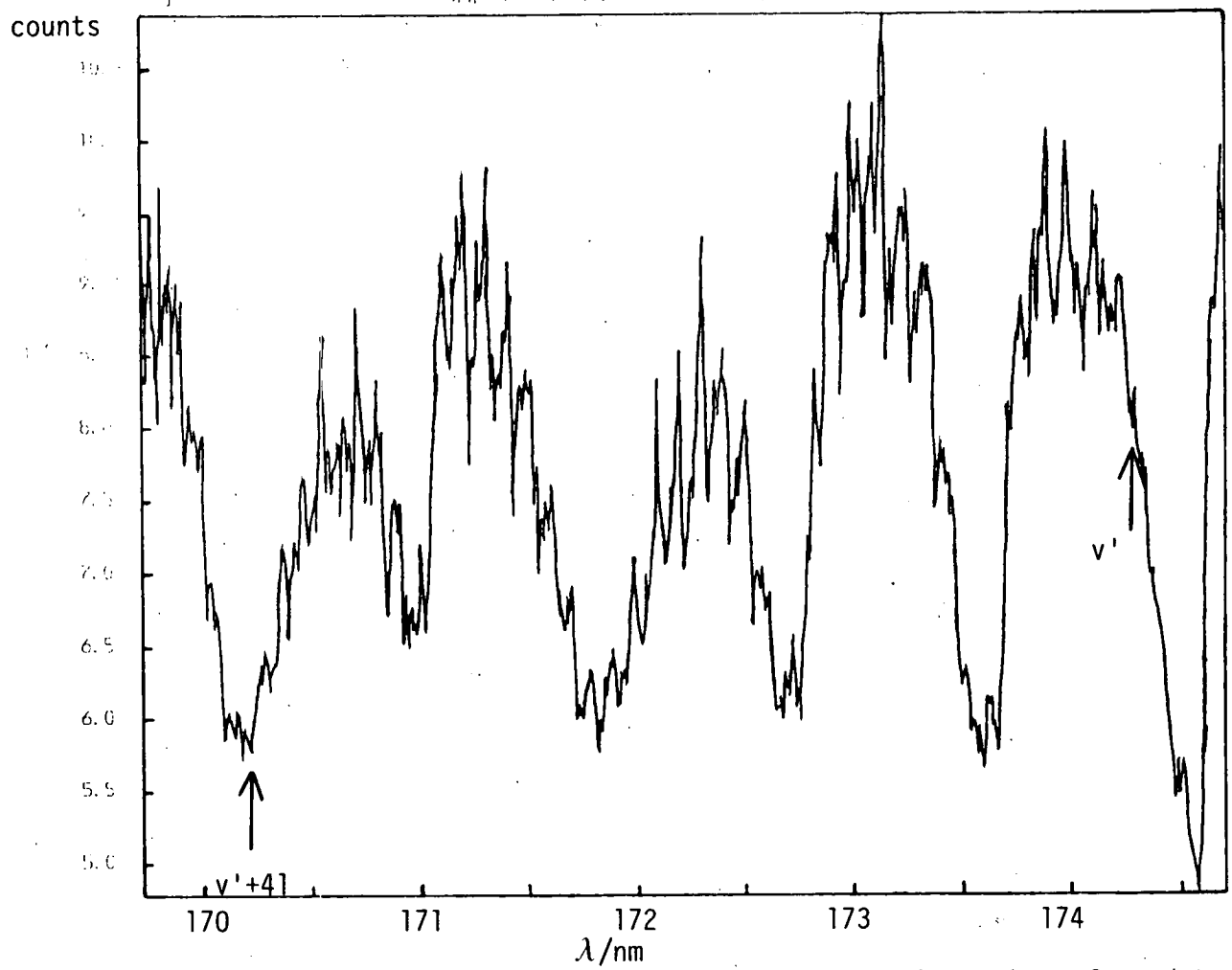

Figure 3.8: Absorption spectrum of IBr recorded at 0.008nm. The peaks referred to in the text are marked ↑ .

TABLE 3.3 : Values of v' and Δv ((v'+1)-v') of $IBrD(0^+)$ for selected wavelengths calculated using

$\omega_e = 119.518 cm^{-1}$,

$\omega_e x_e = 0.2109 cm^{-1}$,

$\omega_e y_e = -1.13 \times 10^{-4} cm^{-1}$.

λ/nm	v'	VIBRATIONAL SPACING/cm^{-1}
200	107	~80
195	124	~72
190	144	~66
185	167	~58
180	194	~50
175	230	~40
170	279	~28
164.43	436	0

NB In reality the v' levels will not converge as a Coulombic potential contains an infinite number of vibrational levels.

ie. it being due to overlap of transitions to the two states (rather than overlap of v"=0 and v"=1 progressions). However both of these possibilities are unlikely as they involve a perpendicular transition, $\Delta\Omega = +1$, which is expected to be very weak.

The loss of ion-pair vibrational structure at $\lambda \geq 190$nm and $\lambda \leq 171$nm will be largely due to diminishing Franck-Condon factors for transitions to these vibrational levels (ie $v' \leq 140$ and $v' \geq 280$). The possibility of absorption to the higher group of ion-pair states correlating with $Br^-(^1S) + I^+(^3P_1$ or $^3P_0)$ also exists. For example the $f(0^+)$ state (correlating with $Br^-(^1S)+I^+(^3P_0)$) which lies 5896cm^{-1} above the $D(0^+)$ state has a comparable equilibrium bond length. As the potentials of these two states will be similar it seems reasonable to assume that the Franck-Condon factors will favour transitions to vibrational levels lying ~5900cm^{-1} above the accessible levels of the $D(0^+)$ state. This translates to appreciable absorption setting in at 170.9nm, taking 190nm as the onset for the $D(0^+)$ state, which corresponds roughly to the short wavelength limit of the resolved (ion-pair) vibrational progression. Absorption to a higher ion-pair state of IBr is therefore a distinct possibility at shorter wavelengths.

3.3 EXCITATION/ABSORPTION SPECTRUM OF IBr

RESULTS

The excitation and absorption spectra of IBr in the region 155-200nm were recorded simultaneously on SRS port HA12 (for experimental details see section 2.3). Figure 3.9 shows the variation of the light throughput with wavelength, with the box

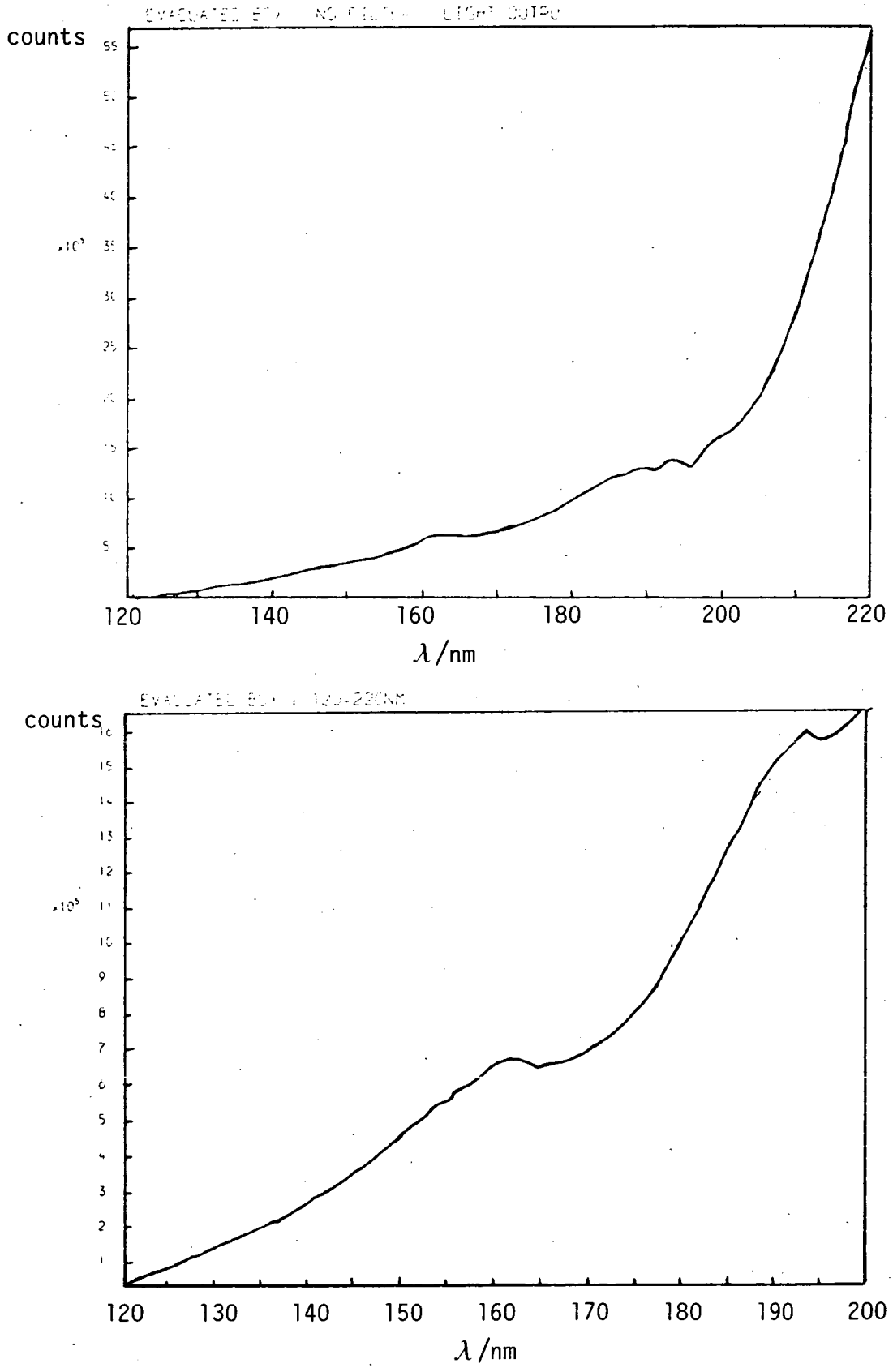

Figure 3.9: The light throughput of SRS port HA12 under the conditions employed in experiments as a function of wavelength.

evacuated. The intensity falls off appreciably toward shorter wavelenghts, and this will be reflected in the excitation fluorescence spectrum. (The fall in throughput was mainly due to the monochromator grating, which was blazed at 350nm.)

Figure 3.10 shows a superimposition of medium resolution excitation/absorption spectra in the region 169-197nm (bandpass = 0.5nm). The sample contained a large excess of Br_2 (Br_2/I_2=5/1) in order to completely suppress I_2 which has a very intense fluorescence spectrum when excited in this wavelength region (see Chapter 4). The total pressure in the cell was $1kNm^{-2}$. Although the E$\longleftarrow$X Rydberg system can be clearly seen in the absorption spectrum, there is no sign of the F$\longleftarrow$X system (cf Figure 3.2). The apparent absence of the F$\longleftarrow$X Rydberg bands is due to the poor sensitivity which results from a low beam intensity at shorter wavelengths. The fluorescence excitation spectrum consists of a broad feature extending from ~175-195nm, with a banded structure superimposed. This structure (spacings ≈ 1.2nm corresponding to $\Delta E \approx 300cm^{-1}$) is due to the high optical density of the sample, ie, absorption to the Rydberg states reduces the beam intensity before it reaches the region of the cell from which fluorescence is observed, and is not related to the fluorescence. This is verified by the exact coincidence of the E$\longleftarrow$X Rydberg absorption peaks with the series of dips in the excitation spectrum at $\lambda \geq$ 186nm. This structure continues to shorter wavelengths, extending beyond the F$\longleftarrow$X Rydberg system. While the structure in the excitation spectrum at $173 \leq \lambda \leq$ 179nm corresponds to the F$\longleftarrow$X Rydberg absorption spectrum (see Figure 3.2), the origin of the structure

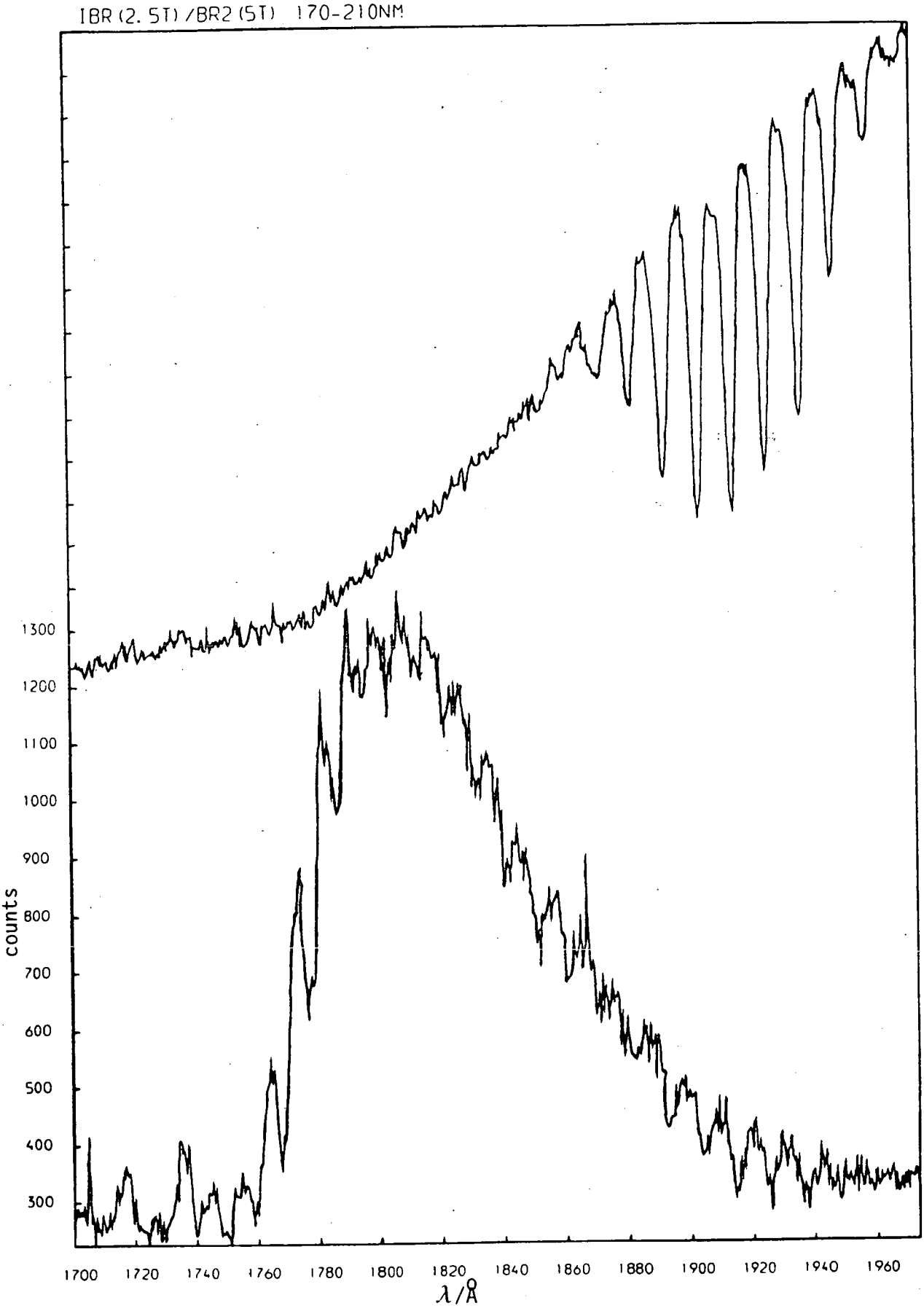

Figure 3.10: Simultaneously recorded absorption (top) and excitation (bottom) spectra of IBr : P_{IBr}=333Nm^{-2}, P_{Br_2}=667Nm^{-2}, excitation bandpass =0.5nm. (NB scale reads high by 7 Å)

in the intermediate region and at $\lambda < 173$nm is unclear.

Higher resolution excitation spectra of the most intense area near 180nm were recorded. However, due to very low signal levels no fine structure was discernible above the noise.

Medium resolution excitation/absorption spectra extending down to 153nm are shown in Figures 3.11 and 3.12. These were recorded when the SRS was carrying a very large current (~200mA), giving a more intense beam. The improved resolution is a result of the increased signal : noise ratio. The absorption spectrum shows traces of the F$\longleftarrow$X Rydberg system in addition to the E$\longleftarrow$X system. The excitation fluorescence spectrum shows two new broad features in addition to the one previously noted, with an extensive banded structure imposed throughout. This structure, due to the high optical density of the sample, can be largely accounted for by transitions to the E, F and G Rydberg systems. The onsets of the latter two systems are marked on Figure 3.11. (Comparison of Figure 3.12 with Figure 3.2 illustrates the inferior sensitivity of this experimental set-up at shorter wavelengths.)

DISCUSSION

The broad feature in the excitation fluorescence spectrum at $\lambda \geq 171$nm corresponds to the ion-pair state identified in the high resolution absorption spectrum and provisionally designated $D(O^+)$. In fact this observation lends support to the assignment, as the

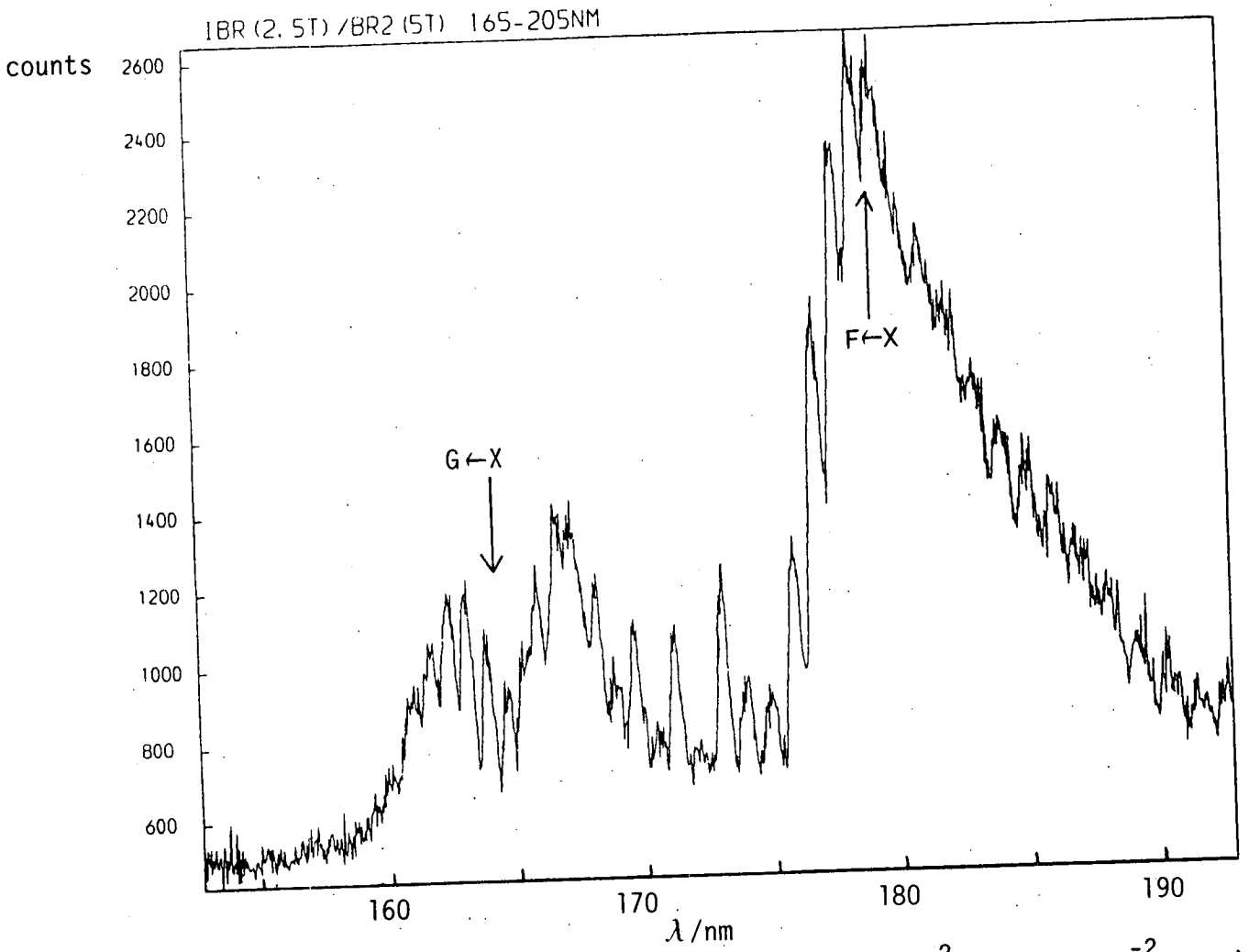

Figure 3.11: Excitation spectrum of IBr. Conditions used : P_{IBr}= 333Nm^{-2}, P_{Br_2}=667Nm^{-2}, excitation bandpass = 0.5nm. The wavelengths of the 0-0 transitions are marked for the F← X and G ← X Rydberg systems.

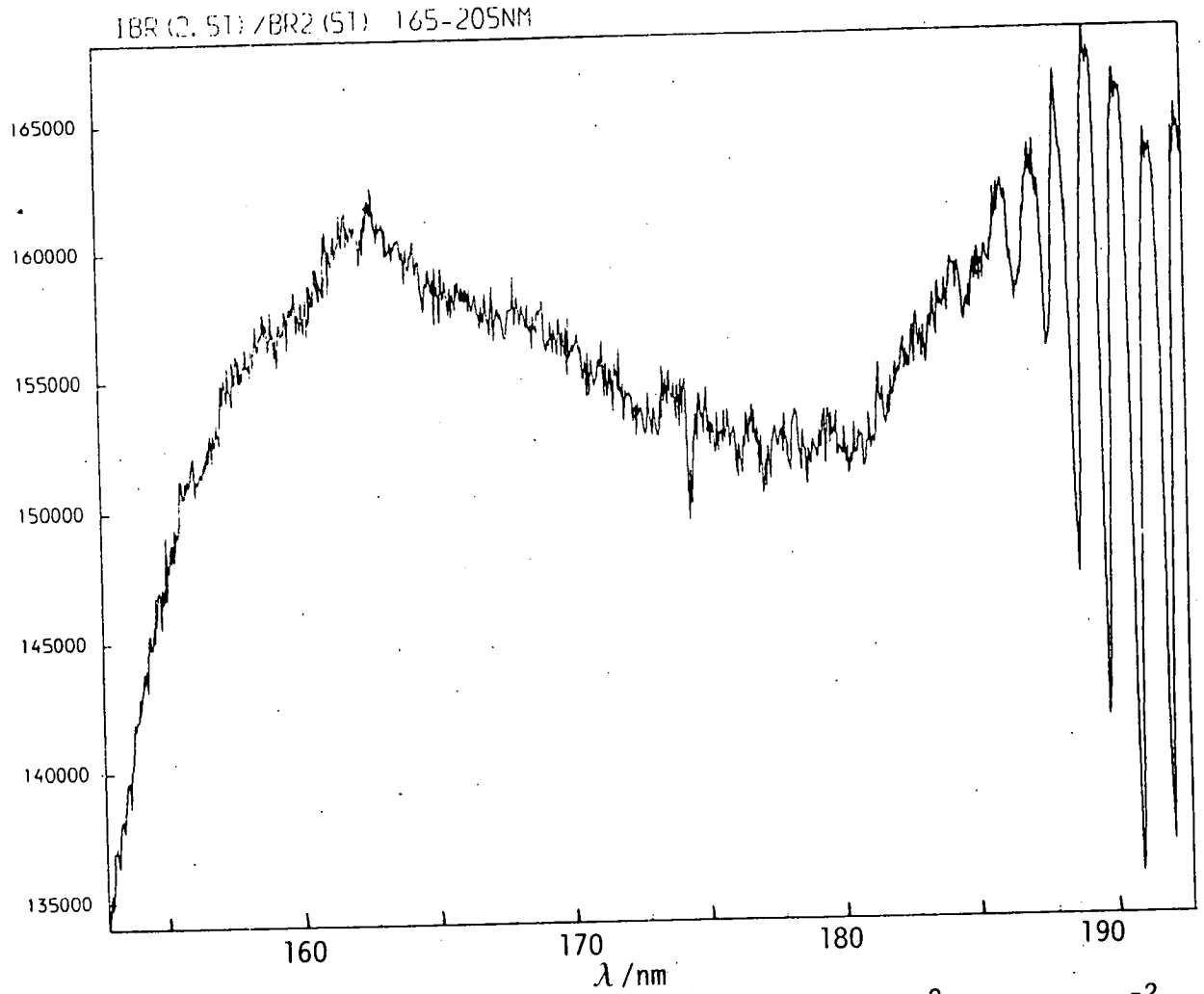

Figure 3.12: Absorption spectrum of IBr. Conditions used : P_{IBr}= 333 Nm^{-2}, P_{Br_2}=667Nm^{-2}, excitation bandpass =0.5nm. The F←X Rydberg absorption is discernible in this spectrum.

analogous $I_2D(0_u^+)$ state also fluoresces in the UV/visible when excited in this wavelength region (see Chapter 4).

The broad feature with maximum intensity at ~167nm would be increased in height by ~50% relative to the maximum at ~179nm if a correction was made for the decreased excitation beam intensity at the shorter wavelength. This feature must also be the result of fluorescence from an ion-pair state of IBr, which, taking energetic considerations into account, is likely to be a member of the next ion-pair grouping. The group of states correlating with $Br^-(^1S)+I^+(^3P_{0,1})$ lies ~5400-5900cm^{-1} above the $D(0^+)$ state, while the separation between the maxima (167-179nm) translates to an energy gap of ~4000cm^{-1}. This discrepancy is tolerable in view of the following facts : (1) the potentials are not identical in shape and may be slightly displaced relative to the lower ion-pair grouping, and (2) the beam intensity falls off markedly toward shorter wavelengths and thus the true maximum of the second system may lie at a higher energy. To date there have been no experimental observations of the $0^-(^3P_1)$ or $1(^3P_1)$ states which correlate with $Br^-(^1S)+I^+(^3P_1)$, so the most logical assignment of the second ion-pair system is to the $f(0^+)$ state. (The analogous $F(0_u^+)$ state of I_2, correlating with $I^-(^1S)+I^+(^3P_0)$, has previously been observed in single-photon excitation.[130])

The remaining broad feature, with maximum intensity at 163nm, can be reasonably confidently assigned to fluorescence from the "K" state of Br_2. The reasons for this are three-fold. Firstly, Br_2

gives rise to intense emission from this state in the region 210-440nm when excited at 157.8nm with a F_2 laser.[131] Secondly, Br_2 "K"$\longleftarrow X(0_g+)$ absorption occurs at $\lambda \leq 166nm$[132]. And finally, there was a large excess of Br_2 present in the sample cell. On the basis of this, the feature would be expected to extend to shorter excitation wavelengths then 160nm if it were not for the cut-off of the spectrosil fluorescence cell. (The "K" state of Br_2 has recently been established as the $D(0_u+)$ state, corresponding to the $D(0_u+)$ state of I_2 [133].)

3.4 THE FLUORESCENCE SPECTRUM OF IBr EXCITED AT 200nm

RESULTS

The dispersed fluorescence from IBr excited at 200nm was recorded on a Perkin-Elmer 650-40 spectrofluorimeter, in the region 280-510nm (see section 2.4 for additional experimental details). The spectrum, recorded with an excitation monochromator slit width of 10nm and a detection monochromator slit width of 2nm, is shown in Figure 3.13. The IBr sample, total pressure $280Nm^{-1}$, was composed of equal pressures of IBr and Br_2 (ie $[Br]/[I] = 3/1$). A greater ratio of Br_2/I_2 would be required to completely suppress I_2 fluorescence (see Figure 3.13), but the Br_2 pressure can only be increased at the expense of the fluorescence intensity, which it quenches extremely efficiently (see Chapter 5). As the fluorescence is already weak, a small contamination due to I_2 was tolerated. On scanning the detection monochromator out to 850nm,

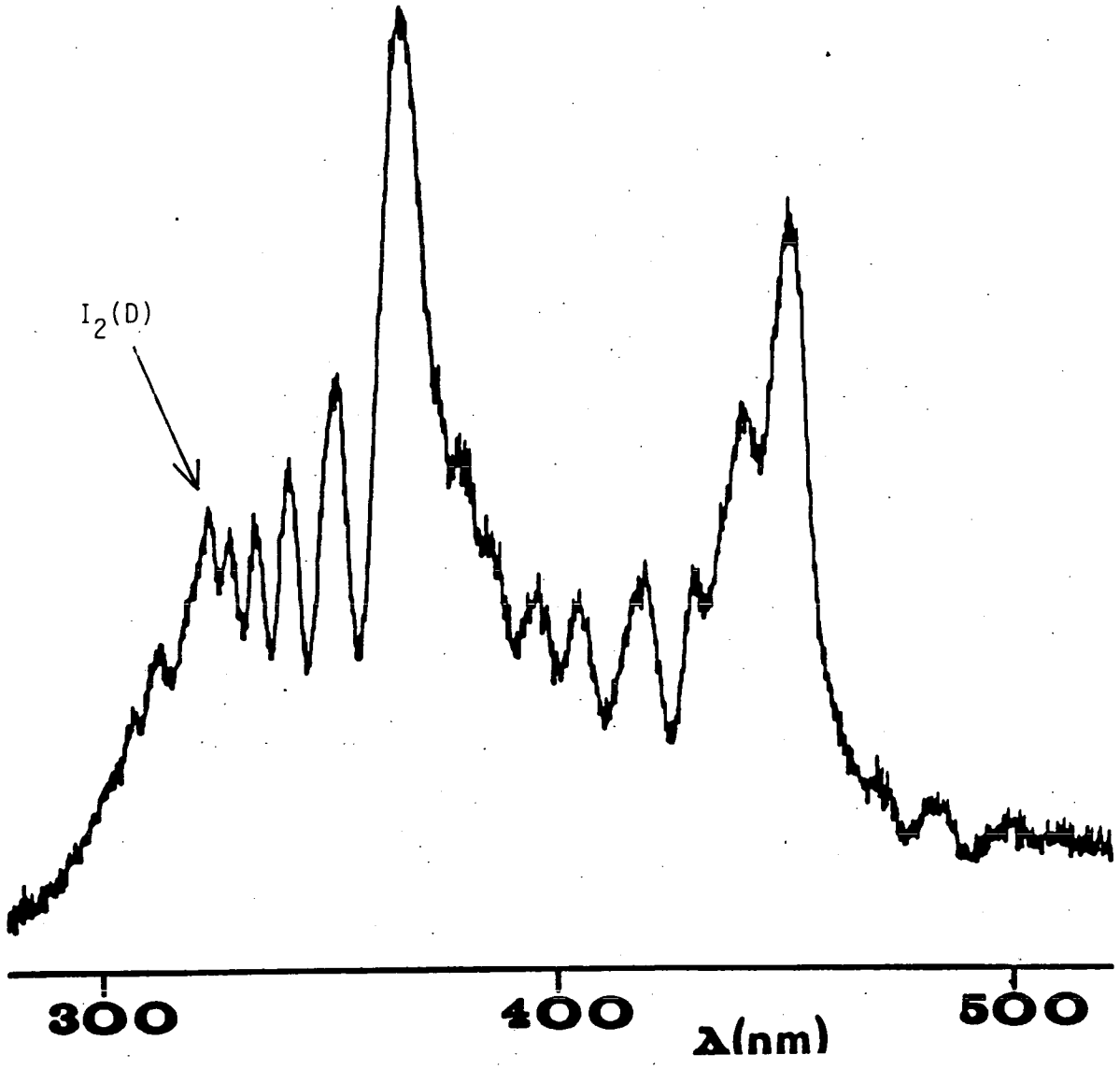

Figure 3.13: Fluorescence spectrum of IBr excited at 200nm. The conditions used were as follows : excitation monochromator slit width = 10nm, fluorescence monochromator slit width = 2nm, $P_{IBr}=P_{Br_2}=$ $140Nm^{-2}$.

no additional fluorescence was found.

The spectrum is seen to consist of two oscillatory continua[57,134,135] ranging between 300-380 and 390-460nm. The interference structure associated with bound-free emission of this type has been observed previously for diatomic halogen molecules,[45,131,136] and the two systems in Figure 3.13 have been noted in IBr fluorescence following 193nm laser excitation.[46] The IBr oscillatory continua are similar to those previously observed from $I_2D(0_u+)$,[28,45,57] and have therefore been assigned to bound-free emission from $IBrD(0^+)$.[46] (Bound-bound emission, $D(0^+) \longrightarrow X(0^+)$, can only occur at $\lambda \leq 270$nm, which is below the filter cut-off.)

A second fluorescence spectrum of IBr was recorded under similar conditions, except for the addition of a large pressure ($14.26 KNm^{-2}$) of SF_6 to the sample, and is reproduced in Figure 3.14. (The vertical scale is approximately 4x that in Figure 3.13.) The use of alternative inert buffer gases, such as CF_4, N_2 and the lighter noble gases, produced a similar result. This spectrum is virtually entirely composed of new features, and is dominated by two narrow peaks at 342 and 385nm. Two other less intense features at 410 and 490nm are also now present, while the feature at 447nm is greatly diminished. The intensities of the four new features increase in parallel, upon raising the buffer gas pressure, and the peak at 385nm also narrows down and shifts slightly to the red.

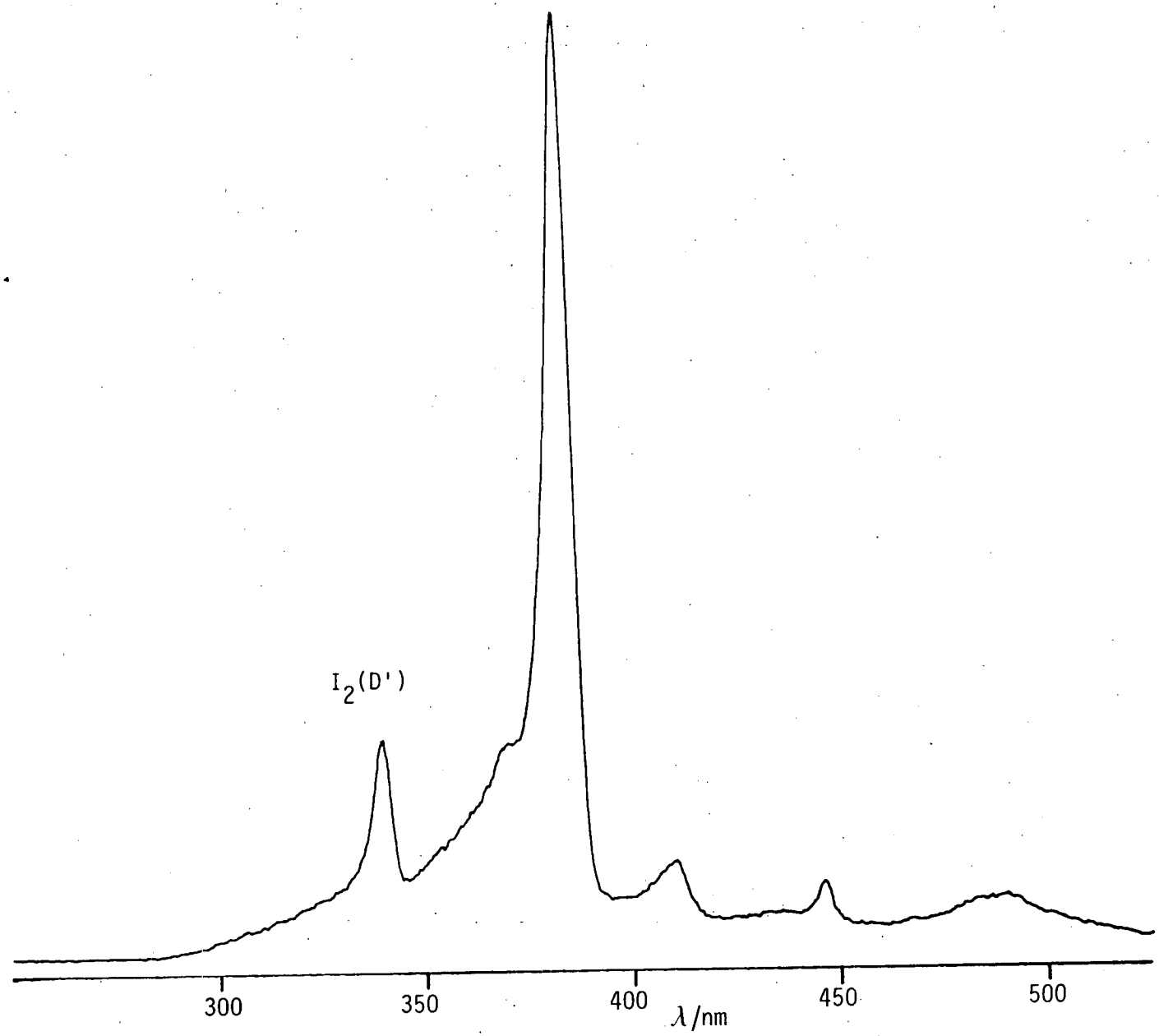

Figure 3.14: Fluorescence spectrum of $IBr+SF_6$ excited at 200nm. The conditions used were as follows: excitation monochromator slit width = 10nm, fluorescence monochromator slitwidth = 2nm, $P_{IBr}=P_{Br_2}$ =140Nm^{-2}, P_{SF_6} = 14.26kNm^{-2}.

DISCUSSION

In the absence of buffer gas the IBr fluorescence spectrum originates entirely from the initially populated upper state. Apart from analogy to $I_2D(0_u^+)$, the assignment to the $D(0^+)$ state is supported by the fact that the spectrum is very weak compared to I_2 excited under similar conditions - this is to be expected as 200nm excitation only accesses the tail of the D-state absorption, populating $v' \approx 107$ (see preceeding sections). In view of this a shorter excitation wavelength would have been desirable (see Figure 3.10), but this was restricted to $\lambda \geq 200$nm by the instrument. The fluorescence in the region 300-380nm results from transitions terminating in unbound levels of the ground state, while the fluorescence at 390-460nm is due to a transition which terminates on an unbound lower state. In analogy to Tellinghuisen's[57] tentative assignment for I_2, this repulsive state is probably 0^+, correlating with two ground state atoms.

In the presence of a large excess of inert buffer gas the oscillatory continuum emission is virtually completely quenched, leaving only a weak peak at 447nm and a shoulder on the short wavelength side of the 385nm peak. The D-state emission at 447nm is relatively narrow, indicating that it has been vibrationally relaxed by the SF_6.

The emission at 342nm can be readily assigned to the $I_2D'(2_g) \longrightarrow A'(2_u)$ emission[28,43], which results from the residual I_2 pressure in the sample cell. The strong peak at 385nm is the IBr analogue, ie. the $D'(2) \longrightarrow A'(2)$ emission,[26] which has

previously been observed following 193nm laser excitation of IBr in the presence of excess Ar buffer gas[39]. The narrowing and red shift of this peak at high SF_6 pressures indicates efficient vibrational relaxation of the D'-state, however physical quenching of this state is extremely inefficient, corroborating the assertion that it is the lowest of the ion-pair states.

The most likely assignment of the broad feature at 490nm is to a $D'(2) \longrightarrow \Omega=2$ transition in which the lower state is repulsive, and correlates with $I(^2P_{1/2})+Br(^2P_{3/2})$ in the dissociation limit (cf. the 505nm emission peak of I_2 which has been assigned $D'(2_g) \rightarrow 2_u(^3\Delta)$[15]). Given that the D'(2) state is vibrationally relaxed, the breadth of this feature can only be explained if the lower state is repulsive.

The feature at 410nm in Figure 3.14 is most likely to originate from the D'(2) state also, since it gains intensity in tandem with the 385 and 490nm peaks. It is quite broad so the lower state must again be repulsive. Of the several possible contenders for the lower state (there is no parity selection rule for IBr), the counterpart of the lower state in the 490nm emission is the most obvious choice. This repulsive state, $\Omega=2$, will correlate with $I(^2P_{3/2}) + Br(^2P_{1/2})$ in the dissociation limit, and will lie below the previously mentioned $\Omega=2$ repulsive state since the spin splitting in $Br(^2P_J)$ is less than in $I(^2P_J)$.

However, the possibility of the 410nm peak originating from the $I(^3P_2)$ state of IBr cannot be completely discounted. There are

two reasons for this. Firstly, it is extremely likely that the interstate transfer process involves a cascade down the vibronic levels of all three ion-pair states in the lowest grouping (cf I_2 collisional transfer[18]), in which case the $I(^3P_2)$ state will at least have a transient population. Secondly, by analogy with I_2, all of these states should have at least one allowed transition to a valence state[13]. (As this peak gains in intensity at the expense of the oscillatory continuum emission, the D(O+) state can be excluded.)

The effect of adding inert gases is thus to promote collisional transfer between the ion-pair states in this (lowest) grouping, with concomitant vibrational relaxation of the individual states. When a high enough pressure of inert gas is used, this cascading process will terminate in a Boltzmann distribution over the vibronic levels of the states. A general characteristic of the halogen ion-pair states is that they are efficiently transferred collisionally to the lowest state in the manifold[15], which lends further support to the above assignments. This process is facilitated by the very high density of states within the manifold, and it may well be the case that interstate transfer is more rapid than intrastate vibrational deactivation.

A rough estimate of the difference in the term energies of the $D(O^+)$ and D'(2) states can be obtained using the Boltzmann relation and the relative peak areas at 385 and 447nm. This can only be very approximate due to several factors: (1) the instrument response varies with the fluorescence wavelength, (2)

the entire emission from a state is not confined to a single wavelength, and (3) the transition probability will be different for each of the states. The ratio of the areas at 447/385nm tends to 0.0234 at high buffer gas pressures. Taking the degeneracies of the two states into account (1 for $D(0^+)$, 2 for D'(2)), this gives $T_e(D) \approx T_e(D')+640cm^{-1}$. The term energy of the $D(0^+)$ state is known accurately to be $39487cm^{-1}$ (see Table 3.1), and so an absolute value of $T_e(D') \approx 38850cm^{-1}$ is obtained.

It will be noted that this value differs markedly from that of Diegelmann et al[26] who calculated $T_e(D') \approx 37840cm^{-1}$. However, their value is also subject to a degree of uncertainty, which is introduced in the computation of the D'(2) and A'(2) potential curves. Both curves, and particularly that of the D'(2) state, are poorly characterized. Their model predicts that the $D'(2) \longrightarrow A'(2)$ emission will occur at 395.8nm rather than 385nm. This discrepancy can be rectified by taking $T_e(D') \approx 38550cm^{-1}$. Given the uncertainties involved in the calculation of $T_e(D')$ from spectrofluorimeter data, the value of $38850cm^{-1}$ is credible.

3.5 CONCLUSION

There are at least two ion-pair states of IBr which are accessible by single photon absorption in the region 160-200nm, as well as three Rydberg systems. The lowest of these ion-pair states is the $D(0^+)$ state which correlates with $Br^-(^1S)+I^+(^3P_2)$ in the diabatic

dissociation limit. This state is populated by excitation at $170 \leq \lambda \leq 200$nm, and gives rise to two fluorescence systems in the UV/visible which are of the bound-free type. The vibrational band structure in the absorption spectrum gives a reasonable fit to the equation:

$$\nu_v = \nu_{oo} + (v+1/2)\omega_e - (v+1/2)^2 \omega_e x_e - (v+1/2)^3 \omega_e y_e$$

using the spectroscopic constants $\nu_{oo}=39432cm^{-1}$, $\omega_e=119.518cm^{-1}$, $\omega_e x_e=0.2109cm^{-1}$ and $\omega_e y_e=-1.13x10^{-4}cm^{-1}$. Maximum fluorescence intensity is obtained for excitation at ~179nm, which corresponds to $v' \simeq 199 \longleftarrow v''=0$.

The second of the ion-pair states gives rise to fluorescence at $\lambda \geq 280$nm when excited at $165 \leq \lambda \leq 170$nm. This is possibly the $f(0^+)$ state which should lie $\sim 5900cm^{-1}$ above the $D(0^+)$ state, and correlates with $Br^-(^1S)+I^+(^3P_0)$ in the diabatic dissociation limit. The possibility of absorption to other ion-pair states cannot be excluded.

Finally, the $D(0^+)$ state undergoes rapid collisional interstate transfer to the D'(2) state in the presence of an inert buffer gas. This state in turn is vibrationally relaxed, but not physically quenched, by excess buffer gas. The overall process probably proceeds in part via levels of all three ion-pair states in the group correlating with $Br^-(^1S)+I^+(^3P_2)$ in the diabatic dissociation limit. The D'(2) state is the lowest ion-pair state of IBr, probably lying $\sim 640cm^{-1}$ below the $D(0^+)$ state. In the

absence of a reactive gas it decays spontaneously, giving rise to a sharp emission band at 385nm.

CHAPTER 4 - SPECTROSCOPIC STUDIES OF I_2

4.1 INTRODUCTION

The absorption and fluorescence spectra of I_2 excited at $180 \leq \lambda \leq 210$nm have been extensively studied and are well characterised. The transition responsible for the strong absorption in this region (see Figure 3.4) is $D(0_u+) \longleftarrow X(0_g+)$[13,57]. Very high vibrational levels of the upper stated (v' > 100) are populated in single photon absorption due to the large difference in the equilibrium bond lengths of the two states ($r_e(X)=2.67\text{Å}$[127], $r_e(D)=3.60\text{Å}$[137].)

The fluorescence spectrum following excitation in this wavelength range (see for example Figure 1.6) consists of a typical resonance series at short wavelengths, followed by two groups of diffuse bands at longer wavelengths. These diffuse bands, or "oscillatory continua", are the manifestation of transitions from the $D(0_u+)$ state to unbound lower levels[13,57]. (For a brief description of this phenomenon, see section 1.6). In the presence of an inert buffer gas the $D(0_u+)$ state is efficiently transferred collisionally to the $D'(2_g)$ state[13,18,28], which is the lowest ion-pair state of I_2. This state is not efficiently quenched, and decays spontaneously giving rise to a strong peak at 342nm and a weaker one at 505nm[15].

In this chapter, the complementary I_2 excitation spectrum

will be reported on. This will substantiate some of the comparisons and analogies drawn between IBr and I_2 in Chapter 3, and serve as a pointer for excitation wavelengths in the lifetime studies that follow (Chapter 5). The possibility of XeI* formation from the reaction:

$$I_2(DO_u^+) + Xe \longrightarrow XeI(B^2\Sigma^+) + I \qquad -(4.1)$$

will also be examined. XeI* exciplex formation has previously been observed in the complementary reaction of metastable Xe atoms with iodine-containing molecules[138-140].

4.2 THE EXCITATION/ABSORPTION SPECTRUM OF I_2

The fluorescence excitation and absorption spectra of I_2 in the region 165-215nm were recorded simultaneously on SRS port HA12 (for experimental details refer to section 2.3). The 10cm spectrosil fluorescence cell contained a few crystals of I_2 which were thoroughly degassed, so an I_2 pressure of ~ 30mTorr (ie the vapour pressure at room temperature) was present. Figure 4.1 shows the fluorescence excitation spectrum, recorded with a bandpass of 0.3nm. The corresponding absorption spectrum showed no features (for an absorption spectrum in this region refer to Figure 3.4).

Absorption to the $D(O_u^+)$ state ranges from 175-215nm, with maximum intensity at ~188nm excitation. The only regular

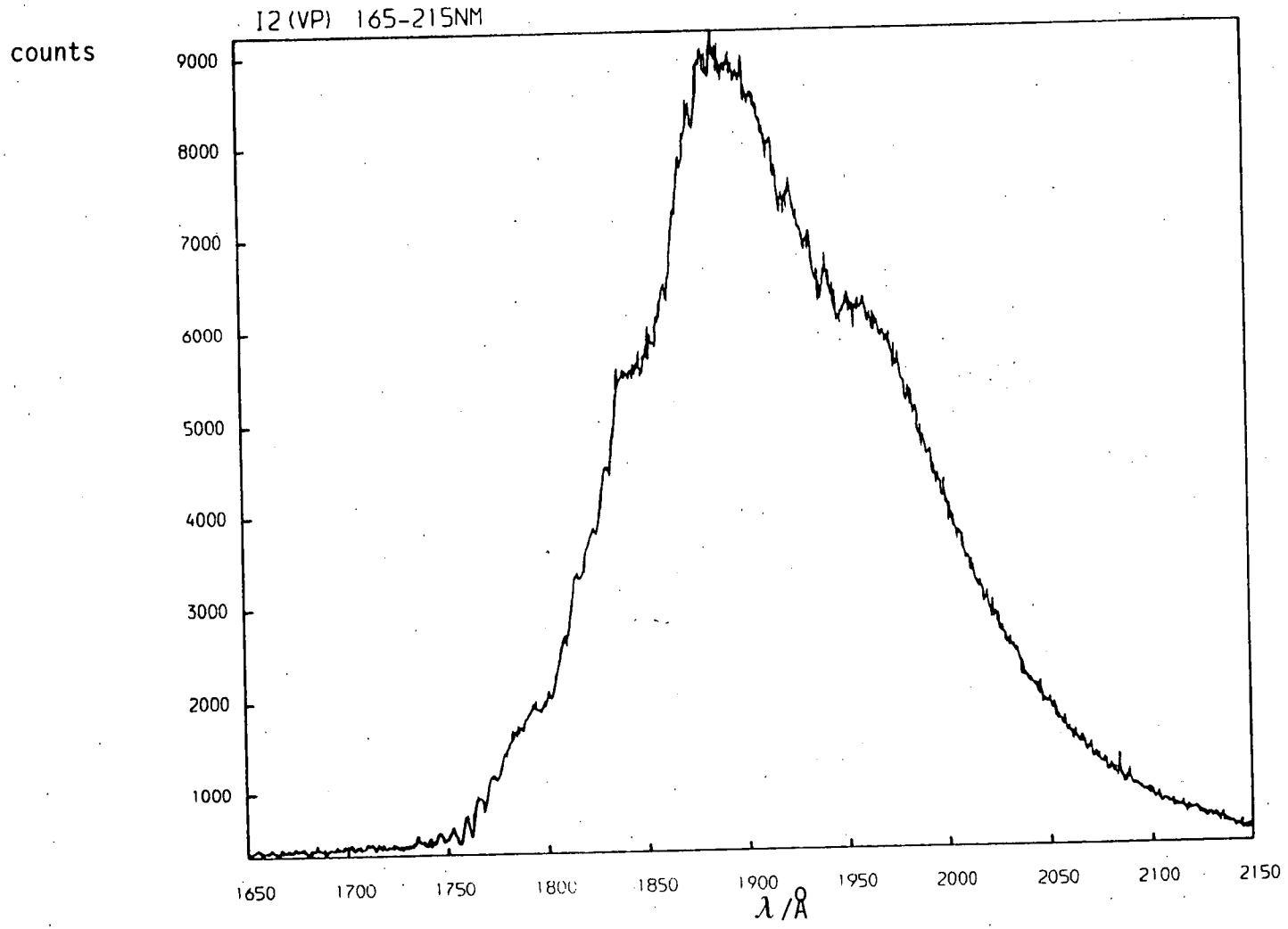

Figure 4.1: Excitation spectrum of I_2 (27 Nm^{-2}). Excitation bandpass = 0.3nm (NB: scale reads high by 6.2Å).

structure occurs at 175-177nm, where there are a few peaks with spacings of ~ 0.65nm ($\equiv 210 cm^{-1}$). In fact, this structure is not related to the excitation spectrum, but results from the high optical density of the sample : the dips in this region correspond to the removal of beam intensity through absorption to the Rydberg series of I_2. These bands have previously been analysed[141].

Higher resolution spectra were recorded, covering the whole of the above region. Figure 4.2 shows a superimposition of the excitation and absorption spectra in the region 185-195nm, recorded with an excitation bandpass of 0.075nm. Both spectra display high frequency structure (spacings $\simeq$ 0.19nm), with exact coincidence between the peaks in the excitation spectrum and the peaks in the absorption spectrum. Thus the fluorescence intensity is increased upon scanning the excitation wavelength through a vibrational peak in the absorption spectrum, and so the structure in the excitation is not simply due to self-absorption by the sample before the excitation beam crosses the region of the cell from which fluorescence is observed (ie the structure in both spectra are manifestations of the same physical process). The structure is clearly resolved from 196-189nm, in which interval the peaks converge slowly from separations of $57 \pm 5 cm^{-1}$ to $50 \pm 5 cm^{-1}$. This corroborates the assignment of both the absorption and excitation spectra to the $D(0_u+)$ ion-pair state of I_2. The lack of resolved structure at $\lambda < 189$nm and $\lambda > 196$nm is most likely due to overlap of

absorption originating from two vibrational levels of the ground state.

4.3 FORMATION OF XeI*(B) FROM I_2*(D) + Xe

The possibility of XeI($B^2\Sigma^+$) exciplex formation in the reaction of $I_2D(O_u+)$ with Xe(^1S) was investigated by recording the excitation spectrum of I_2 (175-200nm) in the presence of various pressures of Xe (see previous section for experimental details). A 254nm interference filter (bandpass $\simeq$ 15nm FWHM) was positioned in front of the fluorescence detection photomultiplier. With this arrangement, only the XeI $B^2\Sigma^+ \longrightarrow X^2\Sigma^+$ emission at 253nm plus a small fraction of the $I_2DO_u+ \longrightarrow XO_g+$ emission should be observed. Due to low signal levels, incurred through the use of a narrow bandpass filter with a maximum transmission of only ~ 50%, an excitation bandpass of 1nm had to be employed.

Figure 4.3 shows a superimposition of I_2 + Xe excitation spectra, with P_{Xe} = 0,4.75, 13.07 and 53.3kNm^{-2}. Increasing the Xe pressure to ~ 13kNm^{-2} causes a decrease in fluorescence intensity at $\lambda \geq 190$nm, has little effect on the fluorescence intensity for excitation at 184nm $\leq \lambda \leq$ 190nm, and increases the fluorescence intensity to shorter wavelengths. At very high Xe pressure the intensity is

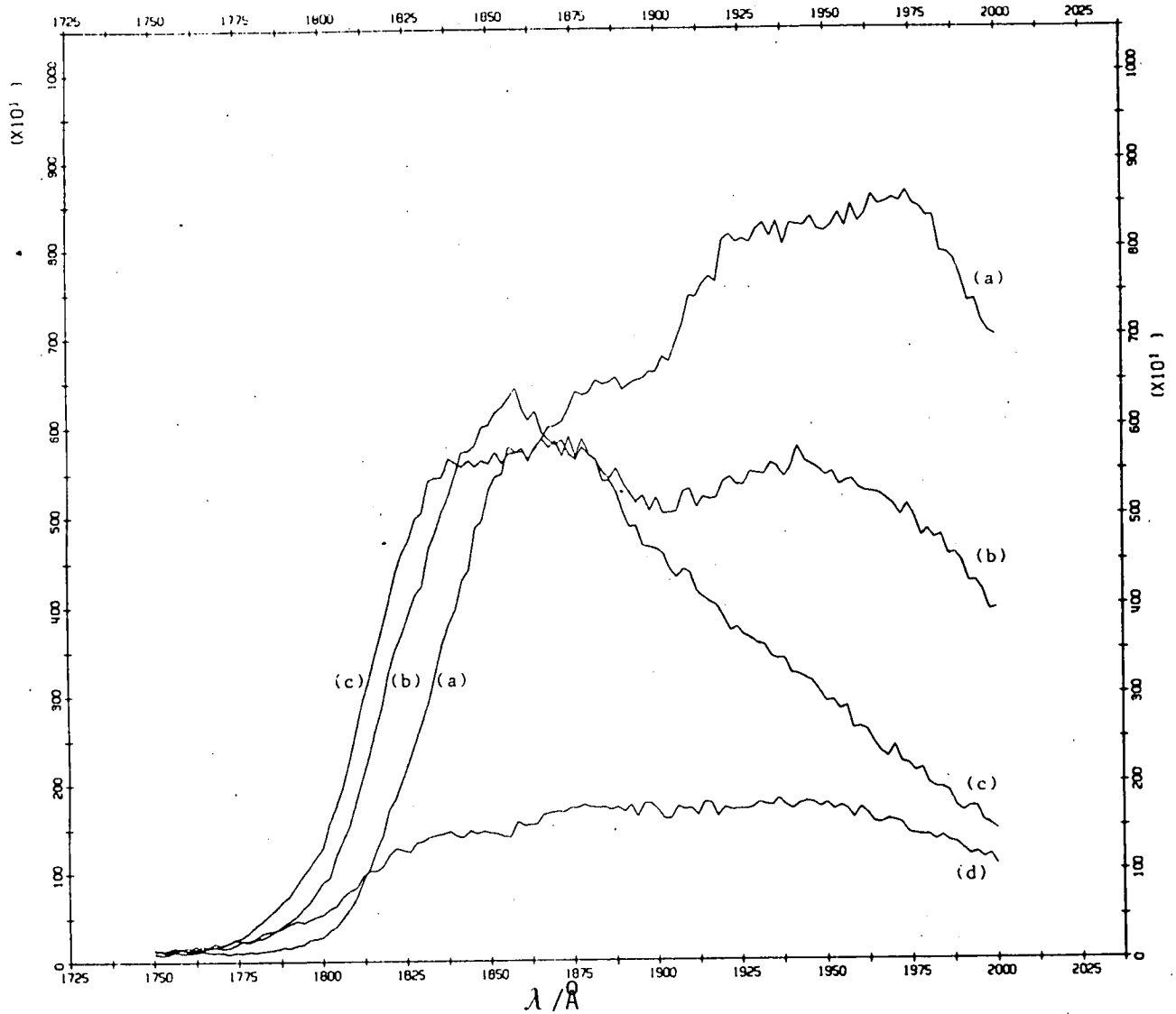

Figure 4.3: Excitation fluorescence spectra of I_2($27Nm^{-2}$) plus Xe, recorded with an excitation bandpass of 1nm. The following Xe pressures were used : (a) 0 , (b) $4.76kNm^{-2}$, (c) $13.07kNm^{-2}$, (d) $53.3kNm^{-2}$. (NB: the scale reads high by 6.2Å).

reduced over the entire range.

As a check, an excitation spectrum of I_2 plus CF_4 buffer gas ($13kNm^{-2}$) was recorded. In this case the fluorescence intensity decreased uniformly over the entire excitation range. Therefore the extra emission intensity for excitation at $\lambda \leq 190nm$ at intermediate Xe pressures is not the result of emission from another ion-pair state of I_2 populated through collisions with Xe. This implies a chemical reaction between Xe and $I_2 DO_u+$, excited at these energies, with $XeI(B^2\Sigma^+)$ responsible for the additional intensity.

At first sight it would appear that the quantum efficiency for XeI(B) production is ≈ 1 for I_2 excitation at $\lambda \leq 190nm$, since the fluorescence intensity remains effectively constant over a range of Xe pressures. However, it must be borne in mind that $I_2 DO_u+$ fluoresces over a very broad spectral range, while XeI(B) emits predominantly at 253nm. The picture is further complicated by several considerations : (1) there is likely to be a contribution from collisional transfer processes involving other ion-pair states of I_2, (2) the I_2 absorption may be pressure broadened by the added Xe (making the apparent quantum efficiency greater), and (3) XeI(B) itself appears to be quenched by Xe. Therefore dispersed fluorescence spectra would be required to determine the extent of XeI(B) production.

Energetically, the lower limit for XeI(B) production occurs

at 190.9nm. Production appears to set in at 190±1nm, implying that there is little or no activation barrier to reaction 4.1. This is highly plausible, as the reaction of IBr(D) + Xe to produce XeBr(B) has also been found to proceed under close to thermoneutral conditions[39].

The extension of the fluorescence intensity to shorter wavelengths upon increasing the Xe pressure can be explained by a contribution from the C-state of XeI. XeI(C) production becomes energetically possible for excitation at $\lambda \leq 188.4$nm. Although this state does not fluoresce in the correct spectral region, it is very efficiently collisionally transferred to the B-state[139] whence it can emit at 253nm. Thus, an indirect contribution from XeI(B) at shorter wavelengths would increase upon raising the Xe pressure.

Ultimately, the XeI(B) fluorescence is quenched by Xe (see bottom trace on Figure 4.3). However, extremely high pressures are required so the process does not appear to be very efficient.

4.4 CONCLUSION

The excitation spectrum of I_2 at $175 \leq \lambda \leq 215$nm is complementary to previously recorded absorption and fluorescence spectra in this region, as it shows that a wide

range of vibrational levels of the $D(0_u^+)$ state fluoresce. In fact, the fluorescence-excitation spectrum matches the absorption spectrum down to 185nm. Thus the $D(0_u^+)$ state is not predissociated.

The reaction of $I_2 D(0_u^+)$ with Xe to form XeI $B(^2\Sigma^+)$ occurs for excitation at $\lambda \leq 190$nm, implying that there is little or no activation barrier. It is also highly probable that XeI(C) is formed at shorter wavelengths and transferred to XeI(B) by collisions with Xe atoms.

CHAPTER 5 - KINETIC STUDIES OF ION-PAIR STATES OF IBr AND I_2

5.1 INTRODUCTION

This chapter is devoted to the kinetics of chemical and physical processes involving ion-pair states of IBr and I_2. Previous studies on the ion-pair states of I_2 [18,32,43,44] have demonstrated that such species have extremely large cross-sections for collisions with a wide range of gases, and that they can cleave strong bonds[17,19].

Initially, dispersed fluorescence spectra were obtained (with the spectrofluorimeter) for mixtures of halogen plus various pressures of foreign gases (excited at 200nm), with subsequent Stern-Volmer analysis of the plots, yielding relative removal rate constants. In order to put these data on an absolute basis, experiments were carried out on the SRS at Daresbury to obtain the lifetimes of the ion-pair states under the experimental conditions used. Pure radiative lifetimes for the states under study - $IBr(D0^+)$, IBr(D'2), $I_2(D0_u+)$ and $I_2(D'2_g)$ - were also obtained. These lifetime studies were carried out in collaboration with a colleague, Dr Michael MacDonald.

5.2 ION PAIR STATE LIFETIMES ON SRS PORT HA12

No ion-pair state lifetimes have been measured previously for

IBr, while for I_2 only three have been measured - DO_u^+(15.5ns[142]), $D'2_g$(6.7ns[31]) and EO_g^+(27ns[143]). As these states have very short lifetimes, the SRS with its well defined, pulsed time profile, proved an ideal tool for such measurements. The experimental details are set out in section 2.5.

RESULTS

(1) IBr : For work on IBr an excitation wavelength of 188nm ($\Delta\lambda$ =3nm) was exclusively used - this gave the maximum signal attainable without the sample chamber evacuated. (Although higher signal levels could be obtained at shorter wavelengths with the chamber evacuated, the time savings thus afforded were negated by the laborious process of pumping down for each run.) Figure 5.1 shows a typical decay plot, obtained in this case for IBr(DO^+) fluorescence at $\lambda \geq$ 300nm (LF30 filter). Generally the data gave an excellent fit to a single exponential decay over at least two decades, providing very precise lifetimes. The residuals, shown in the lower half of Figure 5.1, illustrate the standard deviation of the experimental points from the curve generated by computer fitting. The main source of error in these experiments therefore arose through uncertainties in the parial pressures of the various constituents of the samples, estimated to be $\pm$15%.

The relative removal rate constants for IBr(DO^+) with various

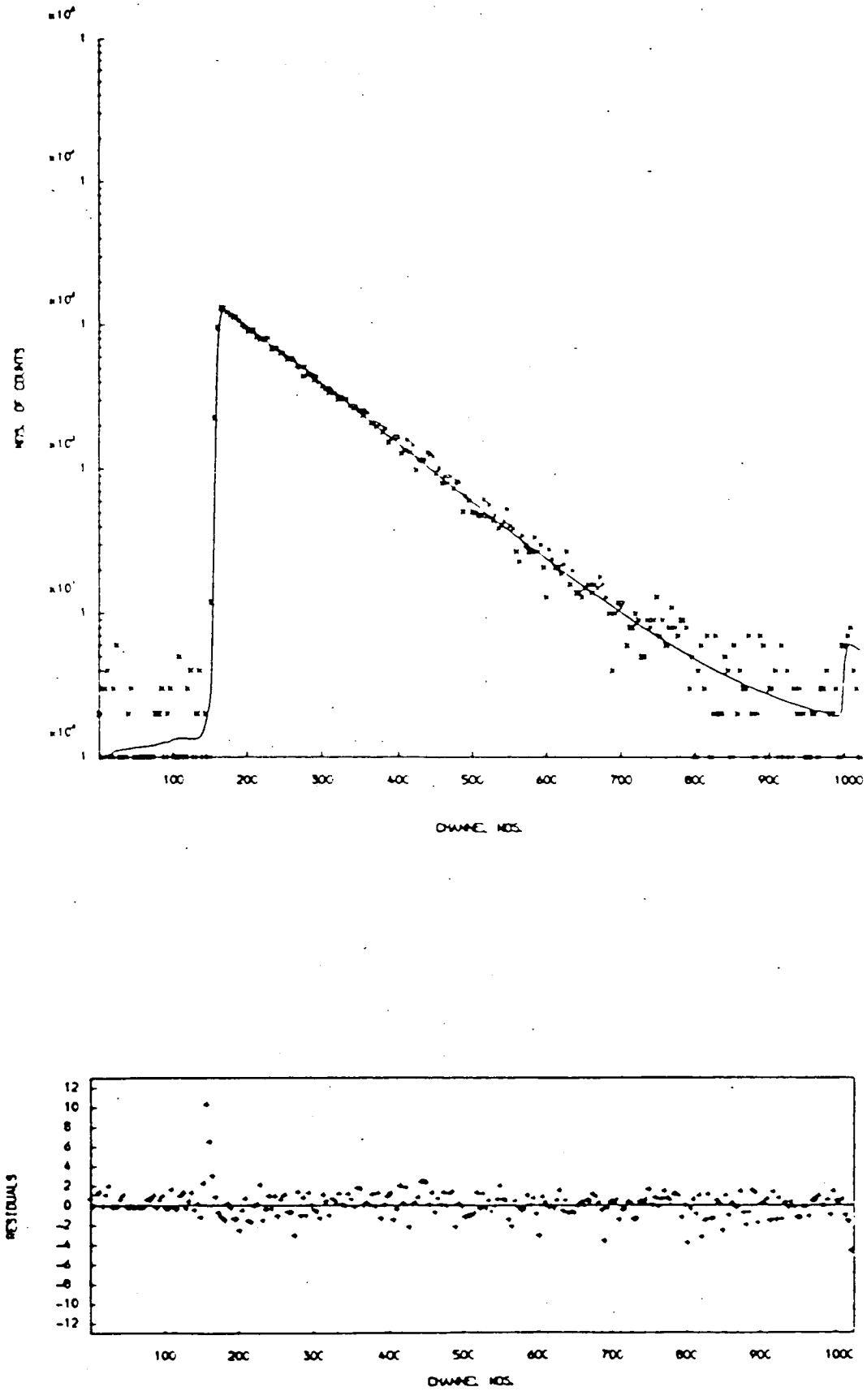

Figure 5.1 : Top trace - IBr* fluorescence decay following 188nm excitation (P_{IBr} = 133Nm^{-2}, P_{Br_2} = 266Nm^{-2}, one channel = 0.1132ns)

The bottom trace shows the residuals (see text).

foreign gases (see next section) were obtained using IBr samples comprising 2:1 of Br_2:IBr, in order to suppress I_2. The lifetime of IBr($D0^+$) under these conditions was determined by recording fluorescence decays over a range of total pressures while holding the ratio of Br_2:IBr constant at 2:1. An LF30 filter was utilised throughout, to eliminate scattered excitation light. Figure 5.2 shows a plot of the reciprocal of the fluorescence lifetime of IBr against the combined IBr + Br_2 pressure. The reciprocal of the intercept gives a value of 27 ± 4ns for the pure radiative lifetime of IBr($D0^+$), while the gradient gives a removal rate constant, $k_{REM} = (7.3\pm0.3)\times10^{-10}cm^3molec^{-1}s^{-1}$. This rate constant represents contributions to the removal process by IBr and by Br_2.

Figure 5.3 shows a plot of the reciprocal of the IBr lifetime in the presence of increasing pressures of Br_2, with the IBr pressure held constant at $133Nm^{-2}$. The slope of this plot yields a value for the rate constant for the removal of IBr($D0^+$) by Br_2, $k_{REM}(Br_2) = (6.4\pm0.4)\times10^{-10}cm^3molec^{-1}s^{-1}$. Combining this with the result from the slope of Figure 5.2 gives a value for self-quenching (ie the removal of IBr($D0^+$) by IBr), $k_{REM}(IBr) = (9.1\pm1.4)\times10^{-10}cm^3molec^{-1}s^{-1}$. These plus other rate constants are collected for ease of comparison in Table 5.1.

The effect of added buffer gas upon the fluorescence decay time profile was investigated next, using various pressures

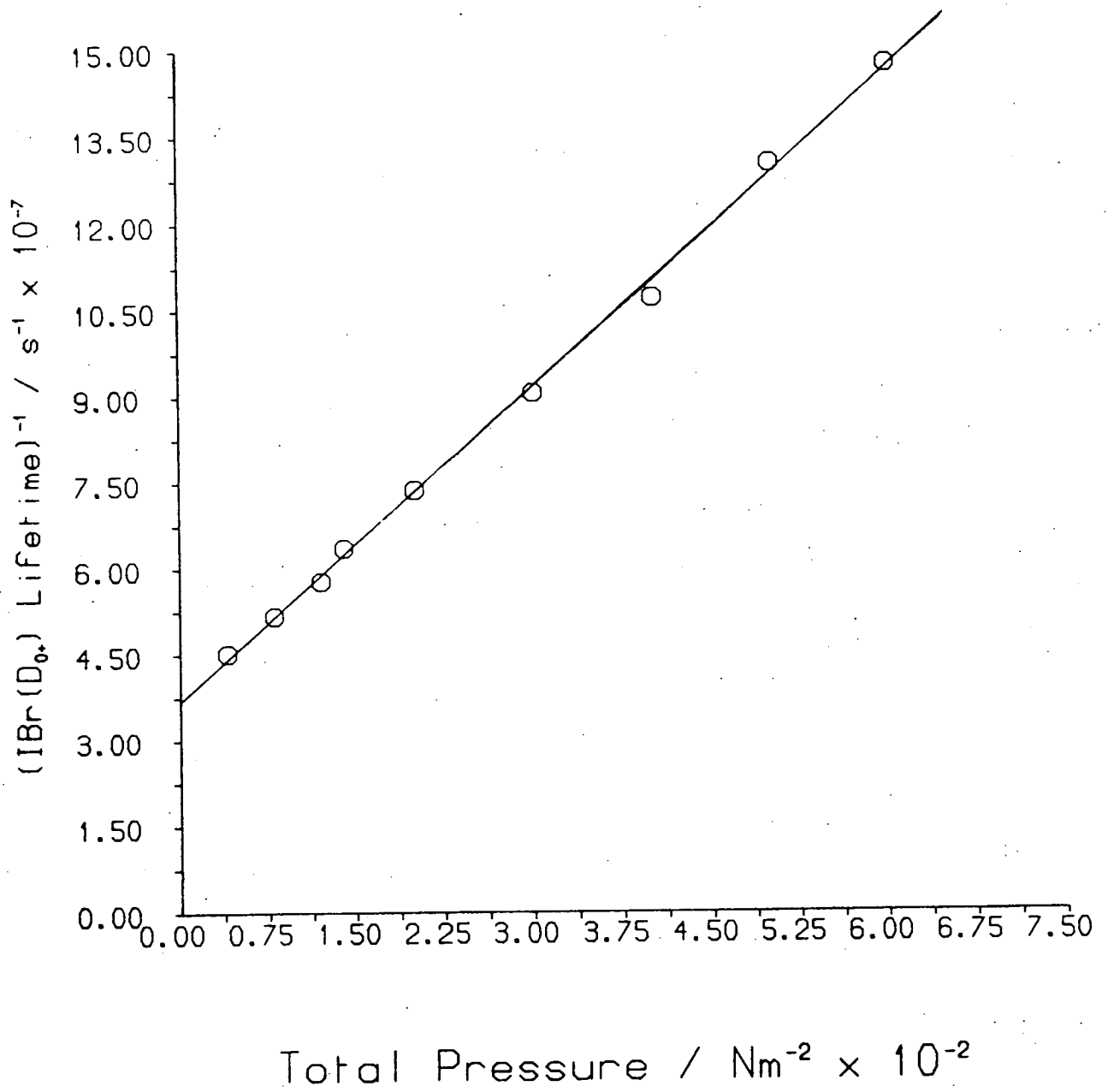

Figure 5.2 : Plot of the reciprocal of the fluorescence lifetime of IBr against the total pressure of IBr + Br_2 ($P_{Br_2}=2P_{IBr}$)

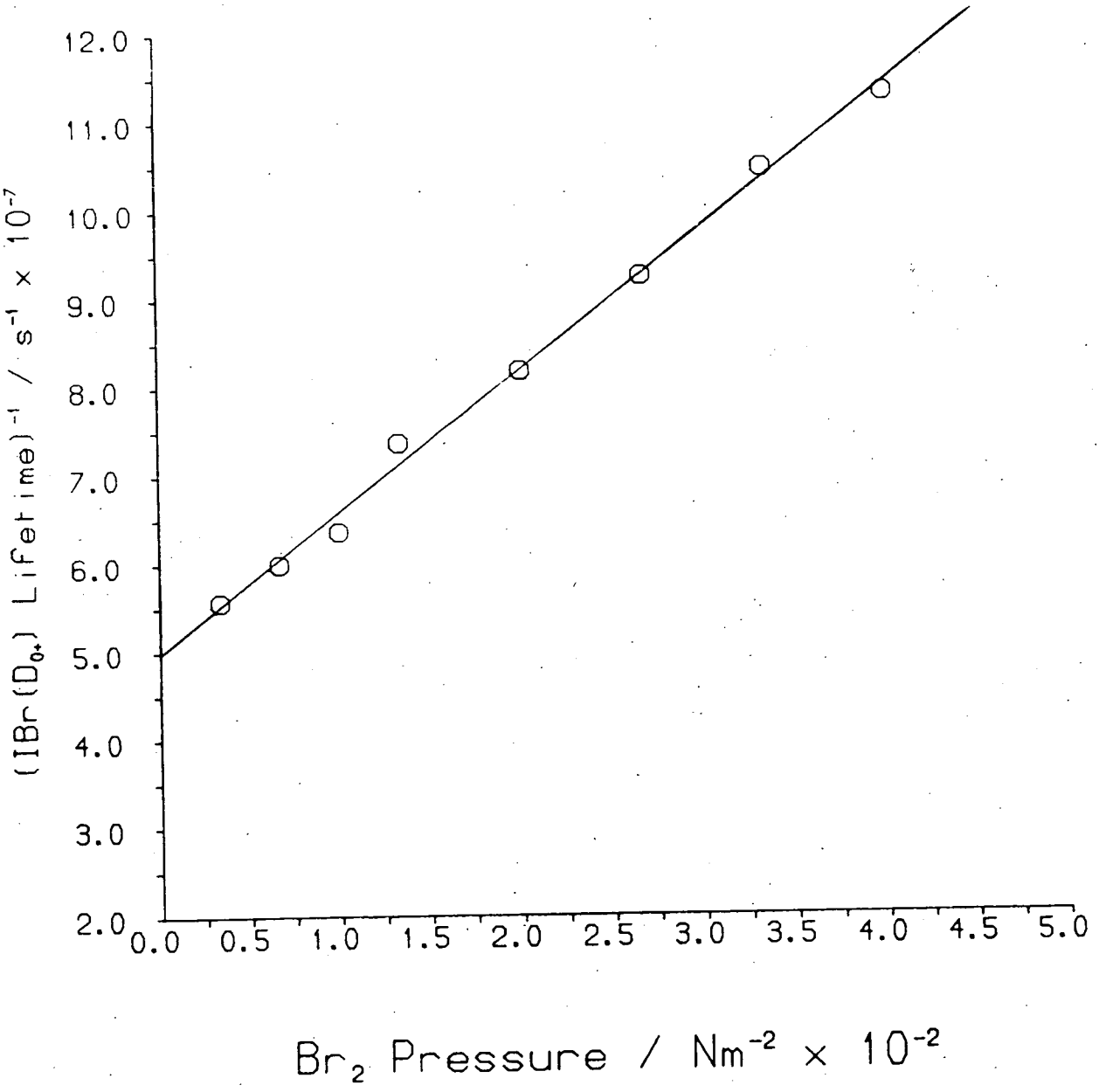

Figure 5.3 : Plot of the reciprocal of the fluorescence lifetime of IBr in the presence of increasing pressures of Br_2 (P_{IBr} = 133Nm^{-2}).

TABLE 5.1: Total removal rate constants for halogen ion-pair states with various collision partners (M).

HALOGEN STATE	M	$k_{REMOVAL}/cm^3molec^{-1}s^{-1}x10^{10}$
$IBr(DO^+)$	Br_2	6.4 ± 0.4
$IBr(DO^+)$	IBr	9.1 ± 1.4
IBr(D'2)	$IBr+Br_2$	6.5 ± 0.5
$IBr(DO^+)$	CH_4	1.9 ± 0.2
$I_2(DO_u+)$	CH_4	1.9 ± 0.2

of CF_4. Figure 5.4 shows the decay of IBr fluorescence in the presence of an intermediate pressure of CF_4 ($3kNm^{-1}$), recorded using two different filters. Using an LF30 filter (top trace), a marked risetime of ~6ns is apparent and the computer fit for a single exponetial is extremely poor. This is due to collisional transfer of IBr from the $D0^+$ to the D'2 state, which subsequently fluoresces. While the fit is improved in the case of an LF42 filter ($\lambda \geq 420nm$, bottom trace), there is still evidence of a risetime. This is further supporting evidence for the assignment of the IBr emission system at 490nm to a transition from the D'2 state. (see Figure 3.14, section 3.4). Therefore the accuracy of lifetime data obtained at intermediate buffer gas pressures is questionable as there are three processes to be deconvoluted : a risetime plus decays from two different electronic states.

On going to higher buffer gas pressures it was found that the risetime decreased, with concomitant improvement in the computer fit to the data points. For CF_4 pressures $\geq$ $50kNm^{-2}$ the accuracy of the fit and measured lifetime reach steady values, with a minimum risetime of ~1.5ns. This then is the minimum CF_4 pressure required to bring about complete collisional transfer between the $D0^+$ and D'2 state, culminating in a Boltzmann distribution over the two states.

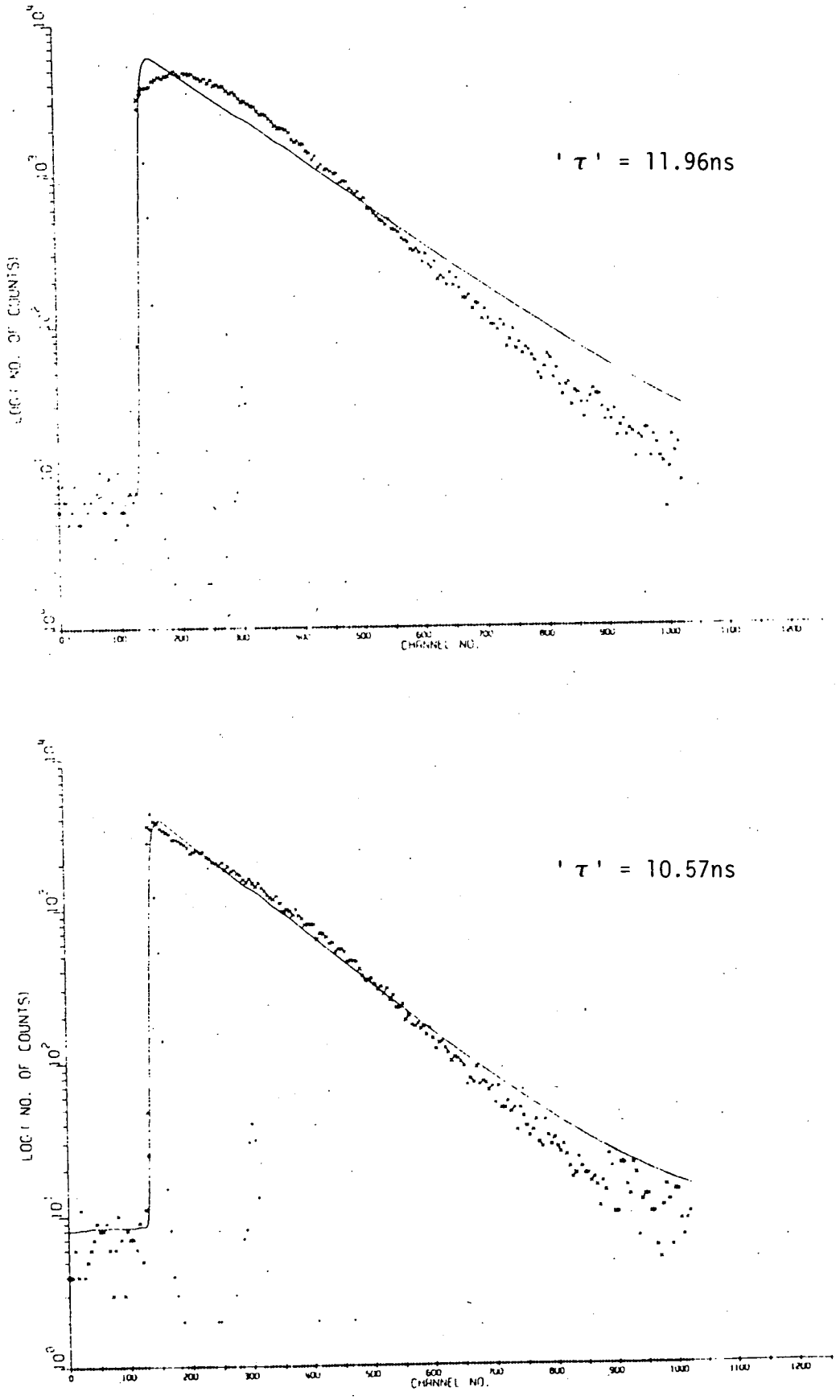

Figure 5.4 : IBr* fluorescence decay, following 188nm excitation, in the presence of $3kNm^{-2}$ of CF_4. Top trace - fluorescence at $\lambda \geq 300nm$, bottom trace - fluorescence at $\lambda \geq 420nm$. (Conditions used : $P_{IBr} = P_{Br_2} = 213Nm^{-2}$, 0.0792ns/channel).

The lifetime of IBr(D'2), under conditions used in the spectrofluorimeter experiments (see next section), could now be determined. Figure 5.5 shows a plot of the reciprocal of the IBr(D'2) fluorescence lifetime against the total pressure of $IBr+Br_2$, in the presence of a large excess of CF_4. The Br_2 : IBr ratio was held constant at 2:1. To ensure a minimum contribution from $IBr(DO^+)$, $50kNm^{-2}$ of CF_4 was added to each sample and an LF38 filter ($\lambda \geq 380nm$) was employed. (This also excluded any contribution from the residual $I_2(D'2_g \longrightarrow A'2_u)$ emission at 342nm : see Figure 3.14). Other experiments demonstrated that quenching of IBr(D'2) by CF_4 is negligible. As with $IBr(DO^+)$, relative rate constants for IBr(D'2) can be converted to absolute by taking $1/\tau$ from the best fit straight line at the required total pressure. The intercept gives the pure radiative lifetime of IBr(D'2), $\tau_{RAD} = 11 \pm 2ns$, while the gradient gives a combined ($IBr+Br_2$) rate constant for the removal of this state, $k_{REM} = 6.5 \pm 0.5 \times 10^{-10} cm^3 molec^{-1} s^{-1}$.

(2) I_2 : The fluorescence lifetime of I_2 was measured over a range of vapour pressures (temperatures = 0.7 - 27.3°C) and a range of excitation wavelengths (188 - 200nm). The lifetime remained effectively constant over the pressure range studied, while it fluctuated randomly with excitation wavelength at constant temperture giving an average value of ~ 13ns (see Table 5.2). However, excepting the runs at low temperatures, the decay plots gave very poor single exponential fits (see for example Figure 5.6, top trace), implying that the fluorescence signal originates from more

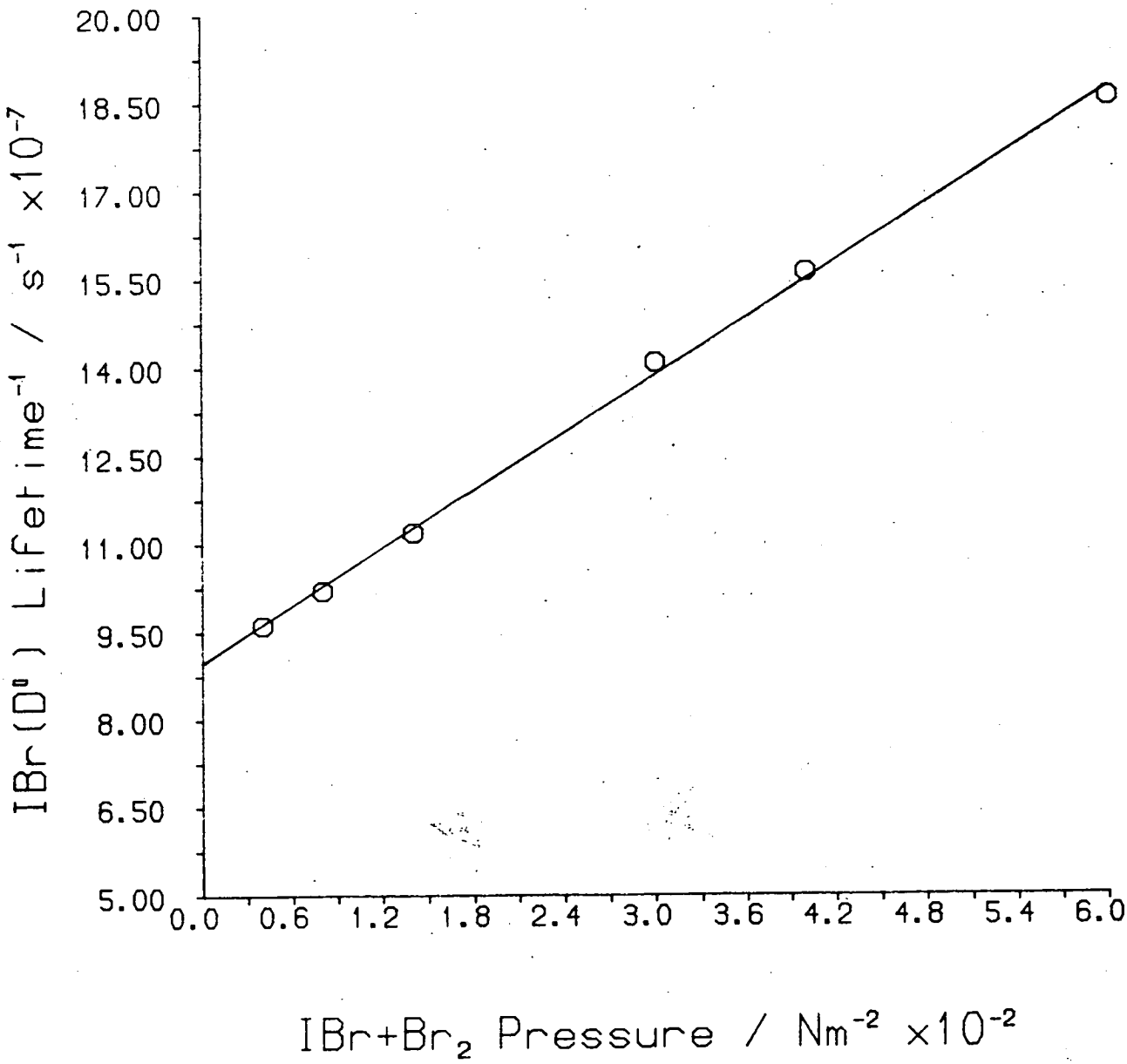

Figure 5.5 : Plot of the reciprocal of the fluorescence lifetime of IBr, in the presence of 50kNm^{-2} of CF_4, against the total pressure of IBr + Br_2 ($P_{Br_2} = 2P_{IBr}$)

TABLE 5.2 : The fluorescence lifetime of I_2 (vapour pressure at 26°C) excited at a range of wavelengths.

$\lambda_{EXC.}$/nm	τ/ns
188	14.3 $\pm$2.1
192	11.8 $\pm$1.7
194	13 $\pm$1.9
196	12.4 $\pm$1.8
198	12.8 $\pm$1.9
200	14.6 $\pm$2.2

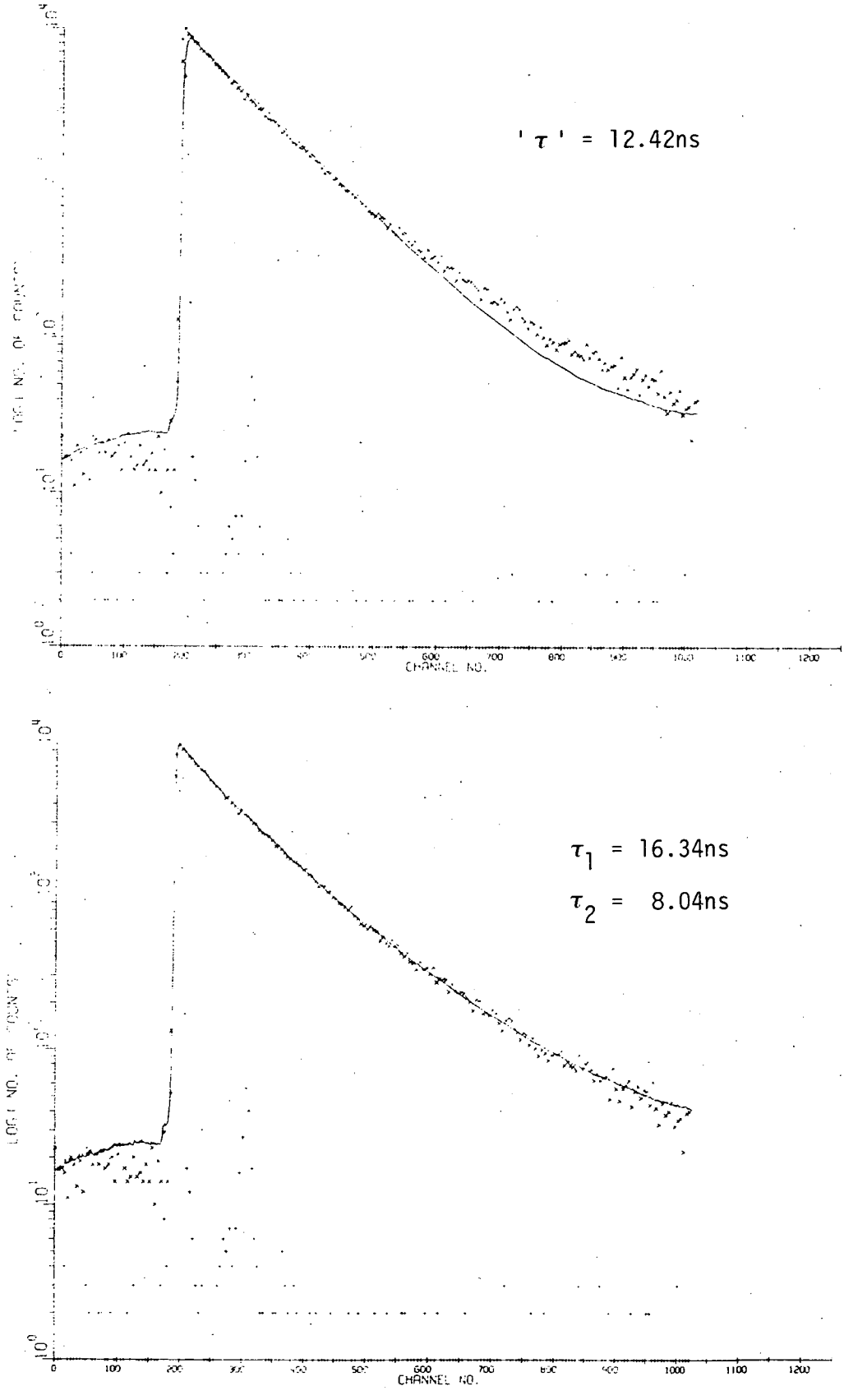

Figure 5.6 : I_2* ($27Nm^{-2}$) fluorescence decay ($\lambda \geq 300nm$) following 196nm excitation. Top trace - fitted to a single exponential decay, bottom trace - fitted to two expotential decays.

than one electronic state. When re-analysed for double exponential decays (see Figure 5.6, bottom trace), the plots gave excellent fits yielding pairs of lifetime values. Unfortunately these values were subject to huge fluctuations, varying by a factor of 2 (cf ~20% for the single exponentials). This is symptomatic of two lifetimes with similar magnitudes (the deconvolution program can only separate out two exponentials reliably if their values differ markedly). However, the ratio of the two lifetimes was virtually constant at ~1.9. Taking 15.5ns for the lifetime of $I_2(DO_u+)$[142], this implies a lifetime of ~8ns for the other electronic state involved.

The lifetime of $I_2(D'2_g)$ was ascertained from a decay plot of I_2* fluorescence, excited in the presence of $50kNm^{-1}$ of CF_4. Other experiments demonstrated that quencing of $I_2(D'2g)$ by CF_4 is negligible. This gave a value of 7.25ns for the radiative lifetime (reproducible to $\pm$0.2ns), which is in good agreement with the previously reported value of 6.7ns[31].

(3) Removal by CH_4 : The rate constants for the removal of $IBr(DO^+)$ and $I_2(DO_u+)$ by CH_4 were obtained by recording fluorescence decays in the presence of increasing CH_4 pressures. The IBr samples comprised $67Nm^{-2}$ of IBr plus $133Nm^{-2}$ of Br_2, while the I_2 samples were at room temperature vapour pressure. The reciprocals of the lifetimes for the two states were plotted against CH_4 pressure (Figures 5.7 and 5.8), and total removal rate constants were derived from the gradients. In both cases a

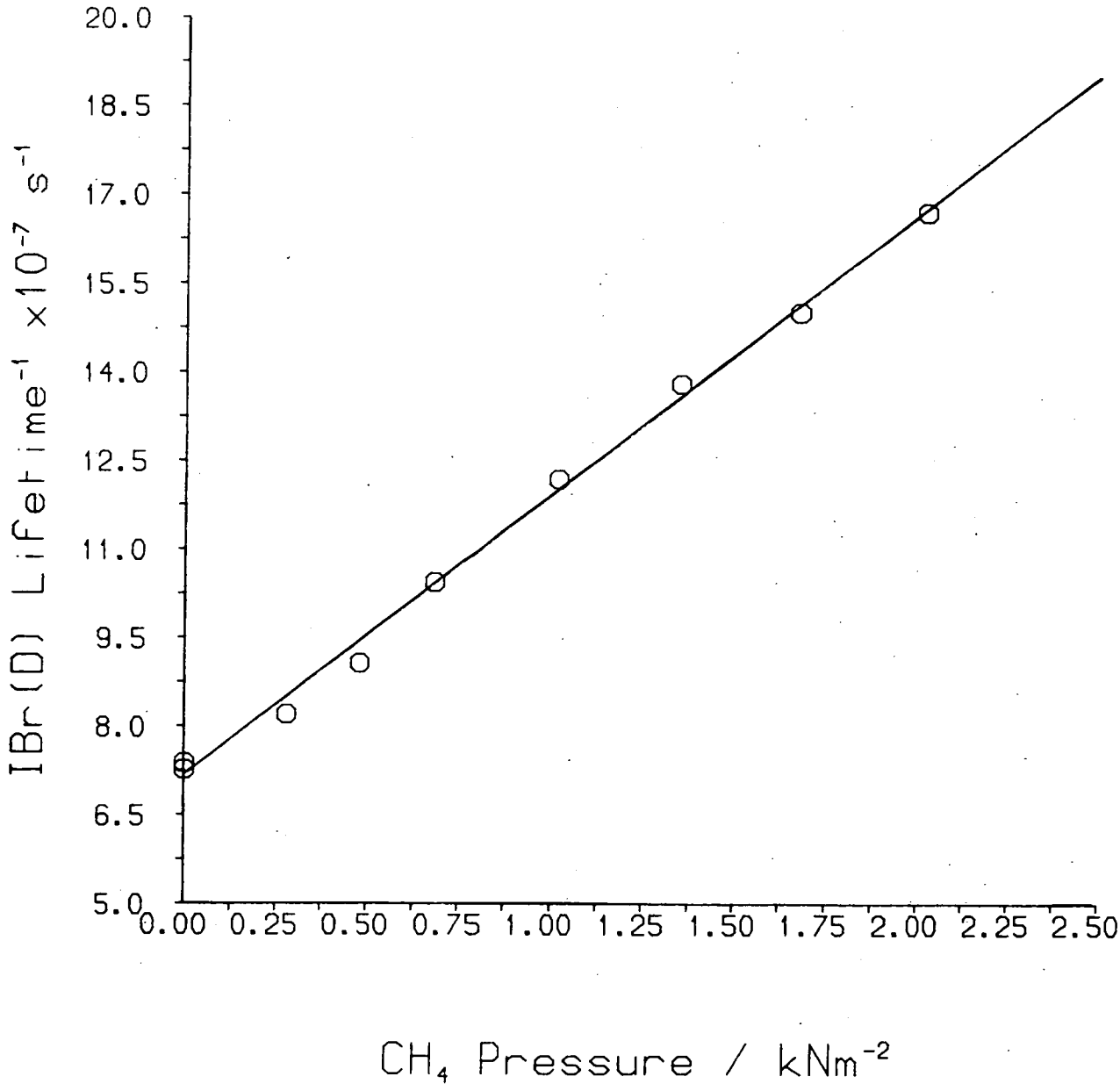

Figure 5.7 : Plot of the reciprocal of the fluorescence lifetime of IBr*, excited at 188nm, against added pressure of CH_4 (P_{IBr} = 67Nm^{-2}, P_{Br_2} = 133Nm^{-2}). The identity of IBr* is discussed in the text and states other than DO^+ may be involved.

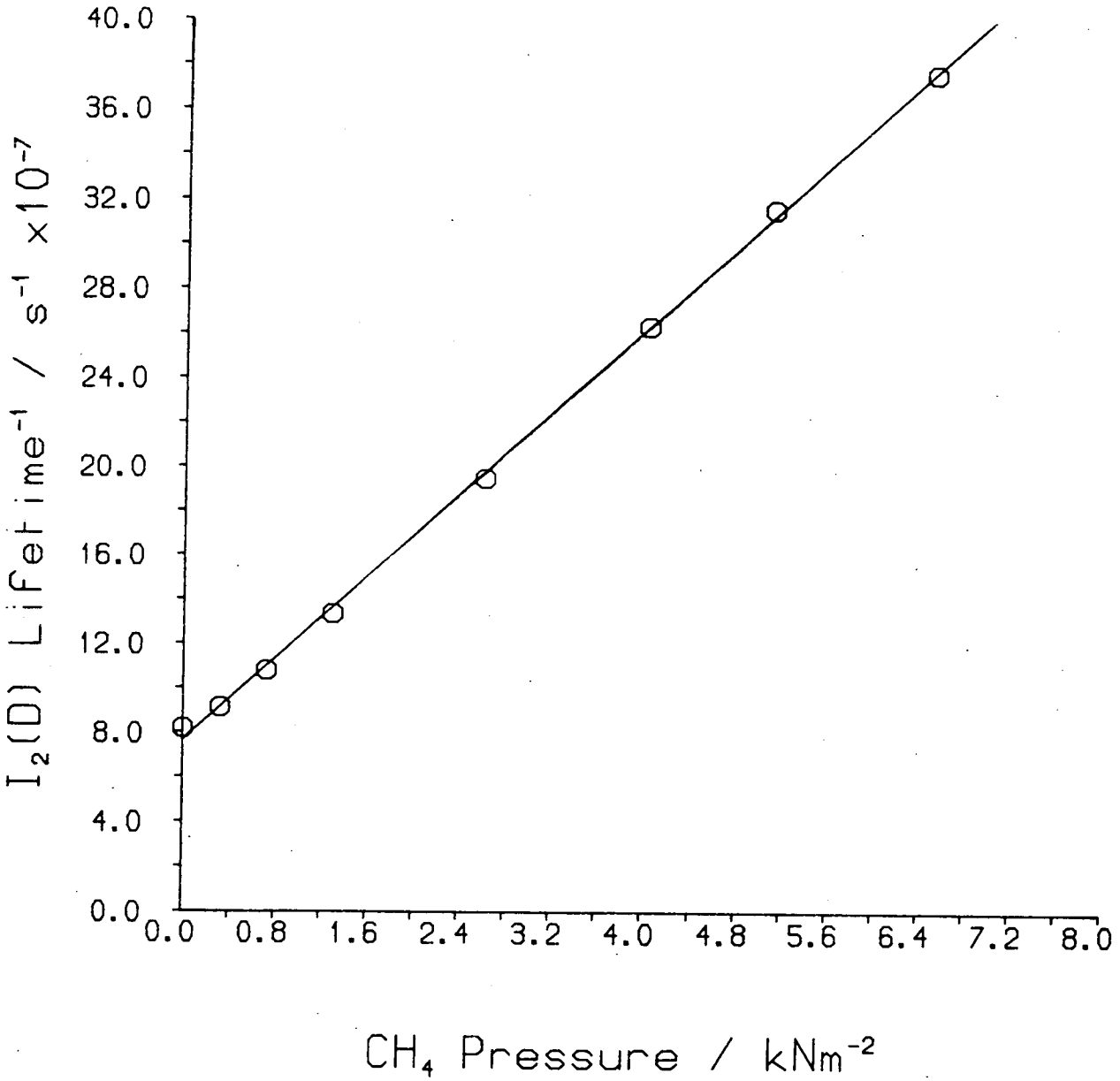

Figure 5.8 : Plot of the reciprocal of the fluorescence lifetime of $I_2^*(27Nm^{-2})$, following 192nm excitation, against added pressure of CH_4. The identity of I_2^* is discussed in the text and states other than DO_u^+ may be involved.

value of $k_{REM} = (1.9 \pm 0.2) \times 10^{-10} cm^3 molec^{-1} s^{-1}$ was obtained.

(4) XeI* formation : Evidence for the formation of XeI(B) from the reaction of $I_2(DO_u^+)$ plus Xe was presented in section 4.3, based on excitation fluorescence spectra, with the energetic threshold of formation at 190 ± 1nm. Lifetime decays were measured for I_2^* excited at 184nm, in the presence of $7.1 kNm^{-1}$ of Xe, using various filters. Figure 5.9 shows two such decay plots, recorded under identical conditions excepting the use of LF40 filter in one case (top trace) and a 254nm interference filter in the other (bottom trace). The top trace gives an extremely poor fit to a single exponential decay and shows a marked risetime of ~ 2ns. Thus the fluorescence being monitored here is largely from a state that has been collisionally populated, most likely the D'^2_g state of I_2 which has an emission system at 505nm[15]. The lifetime calculated from this decay plot is 5.6ns which, even allowing for error due to the poor fit, is short compared to the pure radiative lifetime of 7.25ns for $I_2(D'^2_g)$. It therefore seems likely that $I_2(D'^2_g)$ is quenched by Xe with moderate efficiency.

In sharp contrast, the plot recorded using the 254nm interference filter gives a better fit, has a minimal risetime, and yields a fluorescence decay lifetime of 8.57ns (note the different time scales for the two traces in Figure 5.9). A different species, which is formed extremely rapidly, is being monitored here. In view of the excitation

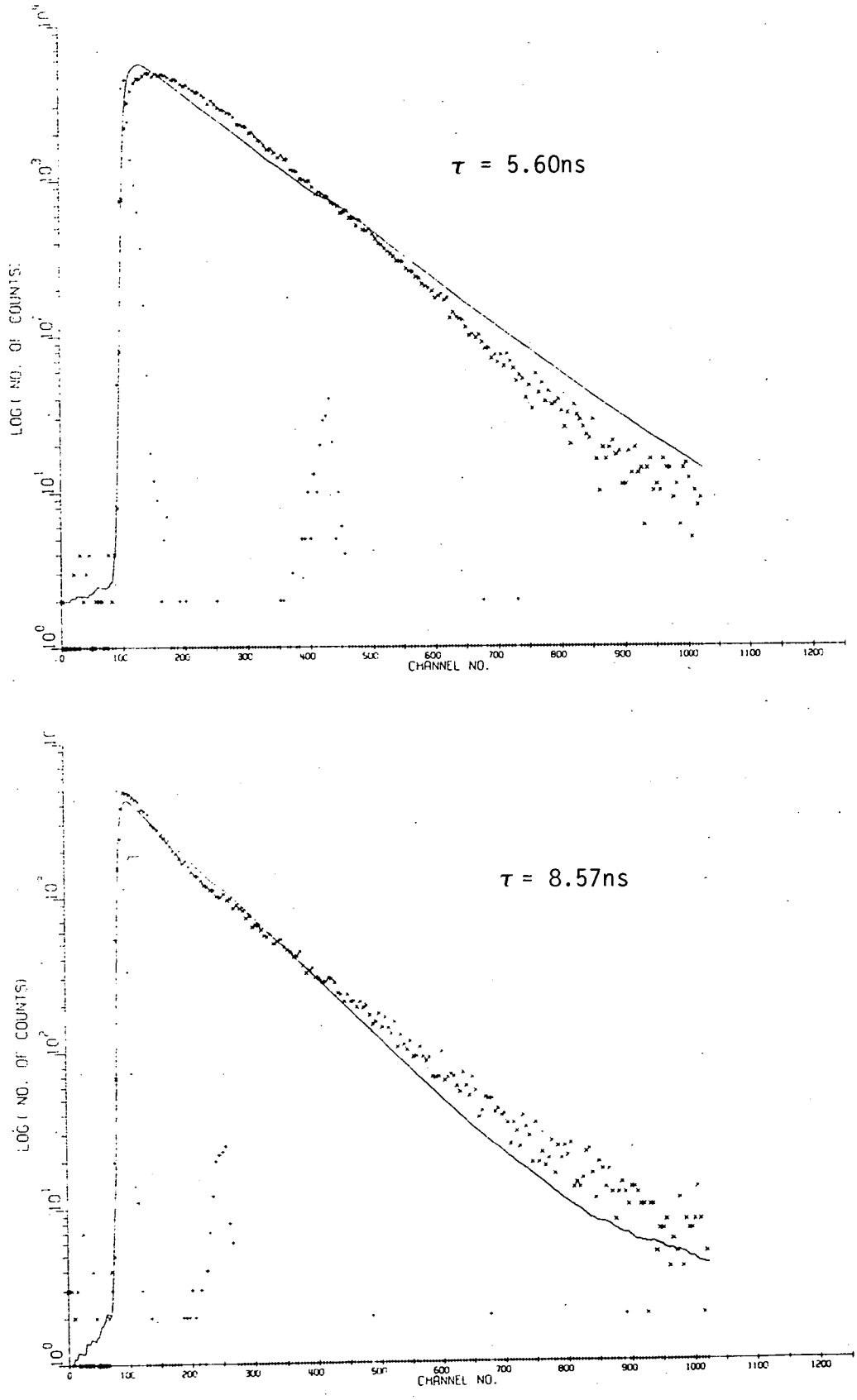

Figure 5.9 : Fluorescence decay from a sample of $I_2(27Nm^{-2})$ + $Xe(7.1kNm^{-2})$, following 184nm excitation, observed through different filters. Top trace - LF40 filter ($\lambda \geq 400nm$), 0.0402ns/channel. Bottom trace - 254nm interference filter, 0.0792ns/channel.

spectra (see Figure 4.3, section 4.3) this is most likely to be XeI(B), emitting at 253nm. (NB it cannot be the initially populated $I_2(DO_u+)$ state that is being monitored as other experiments showed that the lifetime of this state is reduced to less than 8.5ns by the addition of Xe at pressures $\geq 3kNm^{-2}$). Comparison with XeCl(B) lends further support to this assignment ; the reaction of the analogous $^1\Sigma_u+$ ion-pair state of Cl_2 with Xe to form XeCl(B) has been found to be extremely rapid ($k_{FORMATION}=(3.0\pm0.5)x10^{-10}cm^3molec^{-1}s^{-1}$)[144], and the lifetime of XeCl(B), $\tau_{RAD}=11.1\pm0.2ns$[145], is of the same order as the decay lifetime derived from the bottom trace.

DISCUSSION

The measured radiative lifetimes for $IBr(DO^+)$, IBr(D'2) and $I_2(D'2_g)$ are clear cut, with good agreement between the latter and the previously reported literature value of $6.7\pm0.5ns$[31]. However, the situation is more complicated in the measurement of lifetimes for $I_2(DO_u+)$ excited in the absence of buffer gas. With the exception of decays recorded at low temperatures, and hence low I_2 vapour pressures, the data cannot be satisfactorily fitted to a single exponential decay. Two possible explanations exist : (1) more than one state is populated in the initial excitation process, or (2) the initially populated DO_u+ state is transferred collisionally to one or more other states which subsequently fluoresce.

The emission from excited iodine in the region 430 - 470nm (see Figure 1.6), following 193nm excitation, has not been assigned to the DO_u^+ state and probably accounts for the additional decay process(es) observed (a contribution from underlying continuum emission cannot be ruled out). There are five peaks in this region : the peak at ~430nm (on the shoulder of the system at 420nm) is probably the well known $EO_g^+ \rightarrow BO_u^+$ emission, while the other four peaks presumably originate from at least two of the other ion-pair states in the manifold dissociating to $I^+(^3P_2)+I^-(^1S)$. Tellinghuisen and co-workers[15] have assigned I_2^* emission systems in this region, following excitation by an electrical discharge in the presence of Ar, to at least three of these states.

Other than the DO_u^+ state, the only ion-pair state in this region to which transitions are allowed is $1u(^3P_2)$, correlating with $I^+(^3P_2)+I^-(^1S)$. This perpendicular transition ($\Delta\Omega = +1$) is expected to be weaker than $DO_u^+ \leftarrow XO_g^+$, and therefore should only make a minor contribution to the absorption process. Mulliken[13] has noted the distinct possibility of a small contribution from the $1u(^3P_2) \leftarrow XO_g^+$ transition to the absorption spectrum in the region of the $D \leftarrow X$ system, but it has not been positively identified. Viswanathan and Tellinghuisen[52] have tentatively ascribed the γ state of King et al[49] to the $1u(^3P_2)$ state. However the γ state was produced in two-photon excitation : a two-photon transition from the ground state to the $1u(^3P_2)$ state is parity forbidden making

this assignment dubious. The $lu(^3P_2)$ state is thus an unknown quantity, and it is highly improbable that a single electronic state could give rise to all five extraneous emission peaks in Figure 1.6.

Therefore the second possibility, that of collisional transfer to other ion-pair states followed by emission therefrom, is the most plausible. At first glance this might seem unlikely, given the low I_2 vapour pressures and the short lifetime of $I_2(DO_u+)$. However, the cross section for the process:

$$I_2(DO_u+) + I_2 \longrightarrow I_2^* + I_2 \qquad -(5.1)$$

is expected to be extremely large (cf rate constants in Table 5.1). The emission at $430 \leq \lambda \leq 470$nm is only a small fraction of that from the DO_u+ state (the instrument response in Figure 1.6 falls off drastically at shorter wavelengths), so what is witnessed is only the initial phase of a cascade through the vibrational levels of the ion-pair states, which would ultimately populate the (lowest) D'2g state. This also explains the fact that the I_2^* fluorescence decay plots recorded at low temperatures give satisfactory fits to a single exponential decay, ie at very low vapour pressures the interstate transfer process is negligible. Extra, diffuse I_2^* emission bands at long wavelenghts, which are absent at low temperatures, have previously been observed upon raising the temperature of the

sample[13].

The efficiency of the cascade process can be understood in terms of the very high density of rovibrational levels per cm^{-1} : those of the DO_u+ state are embedded in a densely packed manifold of levels belonging to the other electronic states in the ion-pair cluster. There is no discernible risetime on the I_2* decay plots because emission from these other states only constitutes a small fraction of the total emission intensity. (In their determination of the $I_2(DO_u+)$ lifetime, Callear and co-workers[142] used a high frequency detection technique which samples narrow spectral regions, so they only observed a single exponential decay of the fluorescence intensity).

In contrast to $I_2(DO_u+)$, $IBr(D0^+)$ does not appear to undergo a cascade process of this type through self-collisions or collisions with Br_2, even when much higher reagent pressures are employed. This could be partly explained by the lower density of vibrational levels in the lowest IBr ion-pair manifold, due to the fact that there are only half as many states and the vibrational frequencies are slightly higher. However it seems likely that collisional deactivation (ie quenching out of the ion-pair manifold) assumes a greater importance in the case of IBr, relative to interstate transfer. This is borne out by the invariance of the IBr* fluorescence spectral profile (ie Figure 3.13) with changing IBr/Br_2 pressure.

It seems reasonable that the removal rate constants of I_2^* and IBr* by CH_4 should be of the same order of magnitude. However, for I_2^* k_{REM} is a factor of 4 less than the previously reported value[18] of 7.9×10^{-10} $cm^3 molec^{-1} s^{-1}$. This discrepancy is due to the fact that a large spectral region is being monitored in this work, whereas the previous value was derived from Stern-Volmer analysis of spectrally resolved I_2^* fluorescence over a range of CH_4 pressures. With the latter method, contributions from other fluorescing states are excluded as areas are measured under a single, isolated peak originating from the DO_u^+ state. From Figure 2 of reference 18 is it obvious that, in addition to reacting, CH_4 promotes significant interstate transfer from $I_2(DO_u^+)$ to other ion-pair states which subsequently fluoresce (or react). Thus the temporally resolved I_2^* fluorescence decays (which monitor undispersed fluorescence) will contain contributions from ion-pair states which are collisionally populated and yield lifetime values longer than those of the DO_u^+ state itself. This in turn leads to a value of k_{REM} which is too small, and implies an approximate value of 0.75 for the quantum yield for interstate transfer from $I_2(DO_u^+)$. It will be seen in the next section that these considerations also apply to the removal rate constant for $IBr(DO^+)$ with CH_4.

The results for I_2^* + Xe support the assertion that XeI(B) is formed in the reaction of $I_2(DO_u^+)$ with Xe. Assuming that quenching of XeI(B) by Xe is slow, a radiative lifetime of

- 8.5ns is obtained for XeI(B). This assumption can be justified on the basis of the following comparisons between the halogen ion-pair states and the bound states of XeI.

Table 5.3 compares the spectroscopic constants of the D/D' states of I_2/IBr and the C/B states of XeI. These constants are very similar for all six species. The XeI* exciplexes resemble the halogen ion-pair states in several ways:

(1) they give ions ($Xe^+ + I^-$) is the dissociation limit,
(2) they emit to repulsive lower states giving rise to oscillatory continuum fluorescene (see Figure 2 of reference 139),
(3) interstate transfer from C $\rightarrow$ B is efficient with a range of collision partners,[139]
(4) they generally have extremely large removal cross sections (k_{REM} of the order of $10^{-10} - 10^{-9}$ $cm^3 molec^{-1} s^{-1}$).

It can therefore be concluded that the C and B states of XeI exhibit behaviour which parallels that of the D and D' states of the halogens. As the D' states of I_2 and IBr are not efficiently removed by inert gases, it seems reasonable to assume that the same applies to XeI(B).

Additionally, in an analogous system, IBr excited at 193nm in the presence of 7.09kNm^{-1} of Xe gave rise to an intense XeBr B $\rightarrow$ X emission.[39] Therefore quenching of XeBr(B) by Xe does

TABLE 5.3 : Comparison of the spectroscopic constants of the D/D' states of I_2/IBr with those of the C/B states of XeI

	I_2			IBr			XeI		
	DO_u^+ [a]	$D'2_g$ [b]	(Δ)	DO^+ [c]	$D'2$ [d]	(Δ)	C [e]	B [e]	(Δ)
T_e/cm^{-1}	41011	40388	(623)	39487	~38850	(~637)	40595	39900	(695)
D_e/cm^{-1}	31150	31773		32502	~33139		30797	31188	
ω_e/cm^{-1}	98.8	104.0		119.5			105.5	106.5	
$r_e/\mathring{A}$	3.56	3.61		3.42			3.54	3.58	

a Reference 132
b Reference 41
c Reference 54
d See discussion in section 3.4
e Reference 139

not appear to be very efficient. These considerations vindicate the assumption that the removal of XeI(B) by Xe is slow.

5.3 IBr* QUENCHING STUDIES ON THE SPECTROFLUORIMETER

Experiments were carried out on the Perkin-Elmer 650-40 Spectrofluorimeter to elucidate the kinetics of physical and chemical processes involving the DO^+ and D'2 states of IBr with a range of foreign gases. (For experimental details see section 2.4) Previous studies of the kinetics of IBr* - rare gas systems are here extended to systems with reactive and inert molecules. These molecules can be divided into three classes according to the effect which they have upon the IBr* fluorescence spectrum.

Class 1 gases, while altering the overall intensity, have no effect upon the fluorescence spectral profile. Br_2 and IBr itself fall into this category. Class 2 gases display similar behavious to the lighter rare gases in collisions with IBr*, ie they bring about $D \longrightarrow D'$ interstate transfer while chemical reaction is insignificant. Included in this category are SF_6, CF_4 and N_2. Class 3 gases are more complicated both reacting with IBr*, and effecting collisional transfer between the ion-pair states.

The reactive gases studied were CH_4, CH_3Cl, C_2H_6, CF_3Cl and O_2. All three classes of molecules bring about some physical quenching to the lower valence states, with the possible exception of SF_6. For Class 1 molecules this appears to be the principal deactivation pathway.

The features of the fluorescence spectrum of IBr* excited at 200nm (see Figures 3.13) have already been discussed in section 3.4.

RESULTS

(1) Class 1 molecules : IBr and Br_2 have been dealt with in the previous section.

(2) Class 2 molecules : The effect of intermediate added pressures of CF_4 are demonstrated in Figure 5.10. The DO^+ emission intensity can be seen to diminish with increasing CF_4 pressure (witness the main peak in the long-wavelength oscillatory continuum system at 447nm) while peaks at 342, 385, 410 and 505nm assume greater intensity. The intensity of the small peak at 490nm remains practically invariant over the pressure range presented. At high CF_4 pressures, a fluorescence spectrum identical to that obtained in the presence of 14.26 kNm^{-2} of SF_6 is obtained (see Figure 3.14), with the IBr(D'2 $\longrightarrow$ A'2) emission at 385nm dominant. The height of this peak increases, with concurrent narrowing, up to a CF_4 pressure of $\sim$50kNm^{-2}, and remains virtually

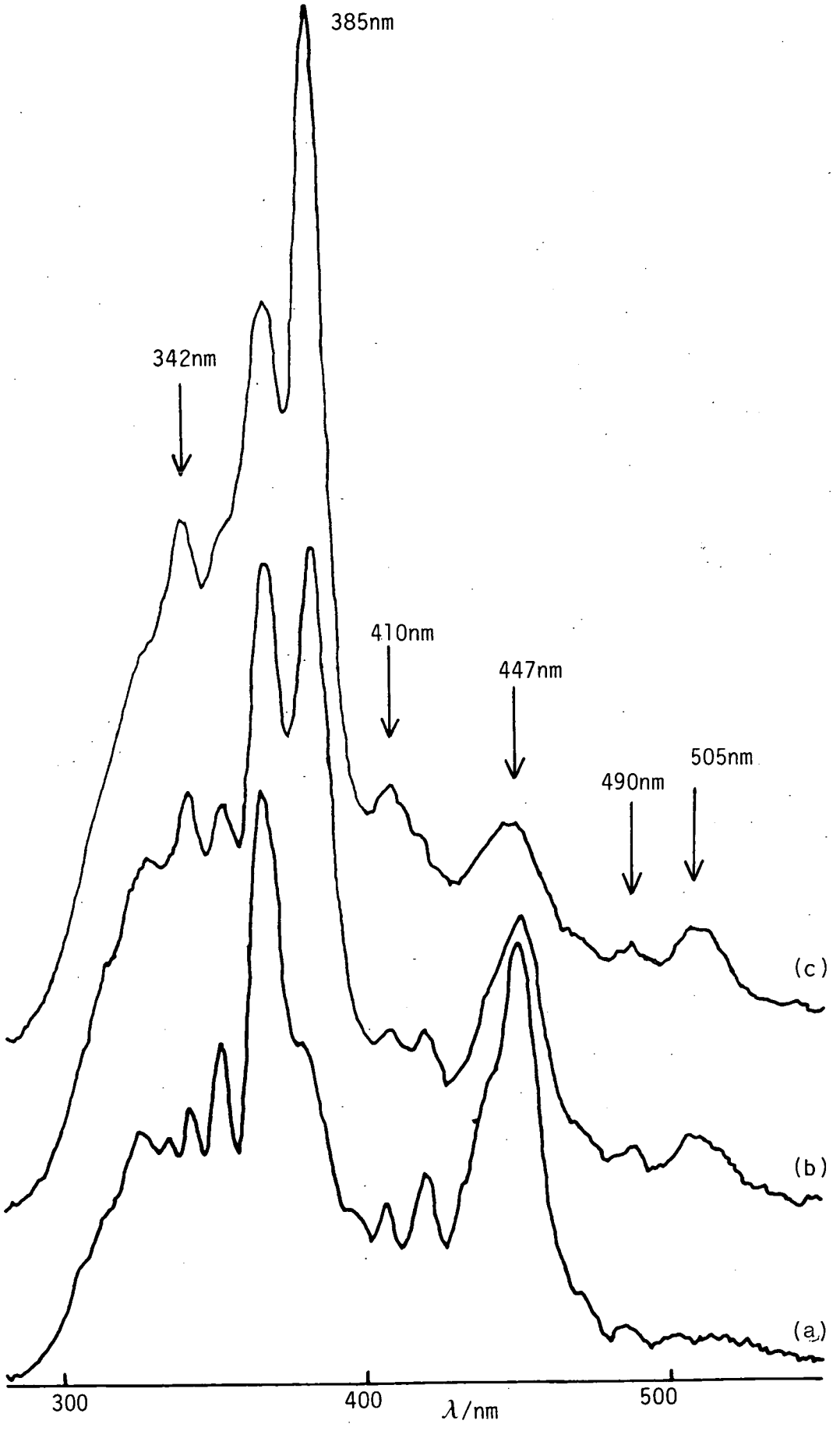

Figure 5.10 : The effect of added CF_4 upon the fluorescence spectrum of IBr*, excited at 200nm. $P_{IBr}=P_{Br_2}=213Nm^{-2}$ plus (a) $P_{CF_4}=0$, (b) $P_{CF_4}=733Nm^{-2}$, (c) $P_{CF_4}=2.08kNm^{-2}$.

constant at higher pressures. The features at 342, 385, 410 and 490nm have been discussed in section 3.4, leaving only the broad emission at 505nm to be accounted for. In fact this is an I_2^* emission peak which has been assigned to a bound-free, $D'2_g \rightarrow 2_u(^3\Delta)$, transition[146].

Using fluorescence intensities measured at 447nm, a Stern-Volmer plot of $\ln(I_o/I)$ vs. CF_4 pressure was constructed and is shown in Figure 5.11. The slope of this plot divided by the lifetime of $IBr(DO^+)$ under these conditions gives the total removal rate constant (all channels) for $IBr(DO^+)$ with CF_4, $k_{REM} = 4.3\pm0.2\times10^{-10}$ $cm^3molec^{-1}s^{-1}$. This rate constant and others are gathered in Table 5.4.

The effects of added SF_6 and N_2 upon the IBr* fluorescence were similar, except for differences in the rate of disappearance of the 447nm peak. Stern-Volmer plots of the DO^+ emission intensities at 447nm are shown for these two quenching gases in Figure 5.12. The slopes give total removal rate constants of $(8.2\pm0.7)\times10^{-10}$ and $(5.0\pm1.0)\times10^{-10}$ $cm^3molec^{-1}s^{-1}$ for SF_6 and N_2 respectively.

(3) Class 3 molecules : The effects of small added pressures of CH_4 are demonstrated in Figure 5.13. The DO^+ emission intensity is observed to fall off very rapidly with increasing CH_4 pressure, and this is

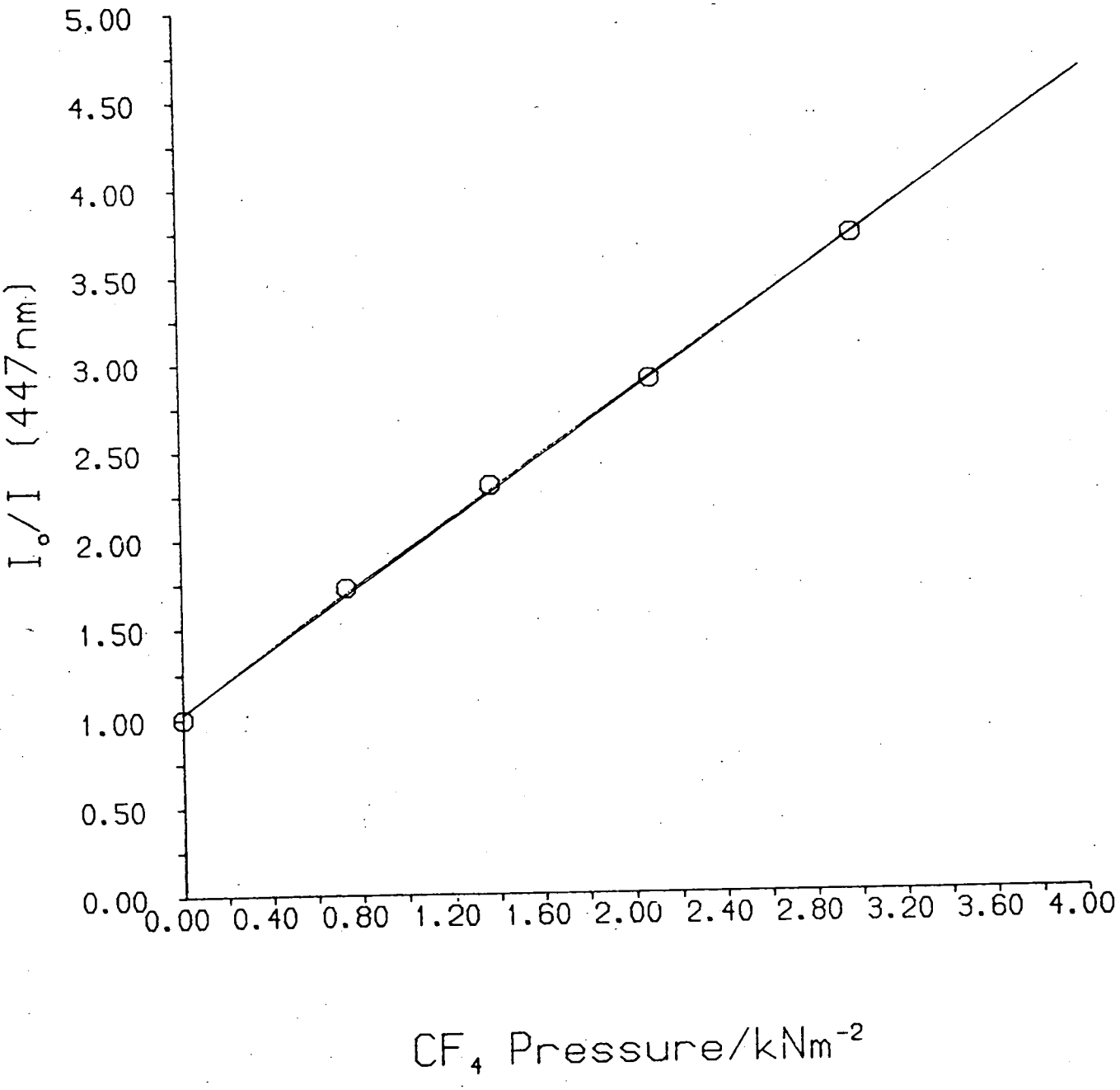

Figure 5.11 : Stern-Volmer plot for the removal of $IBr(DO^+)$ (intensities measured under the 447nm peak) by CF_4.

TABLE 5.4 : Removal rate constants, k_{REM}, for $IBr(DO^+)$ and IBr(D'2) with various foreign gases

Foreign gas	$k_{REM}IBr(D)/cm^3molec^{-1}s^{-1}x10^{10}$	$k_{REM}IBr(D')/cm^3molec^{-1}s^{-1}x10^{10}$
CF_4	4.3 ± 0.2	
SF_6	8.2 ± 0.7	
N_2	5.0 ± 1.0	
CH_4	9.4 ± 1.0	7.0 ± 0.8
CH_3Cl	9.6 ± 1.4	13.9 ± 1.7
C_2H_6	11.0 ± 1.2	12.3 ± 1.1
CF_3Cl	8.1 ± 0.8	2.6 ± 0.5
O_2	2.1 ± 0.3	2.9 ± 0.3

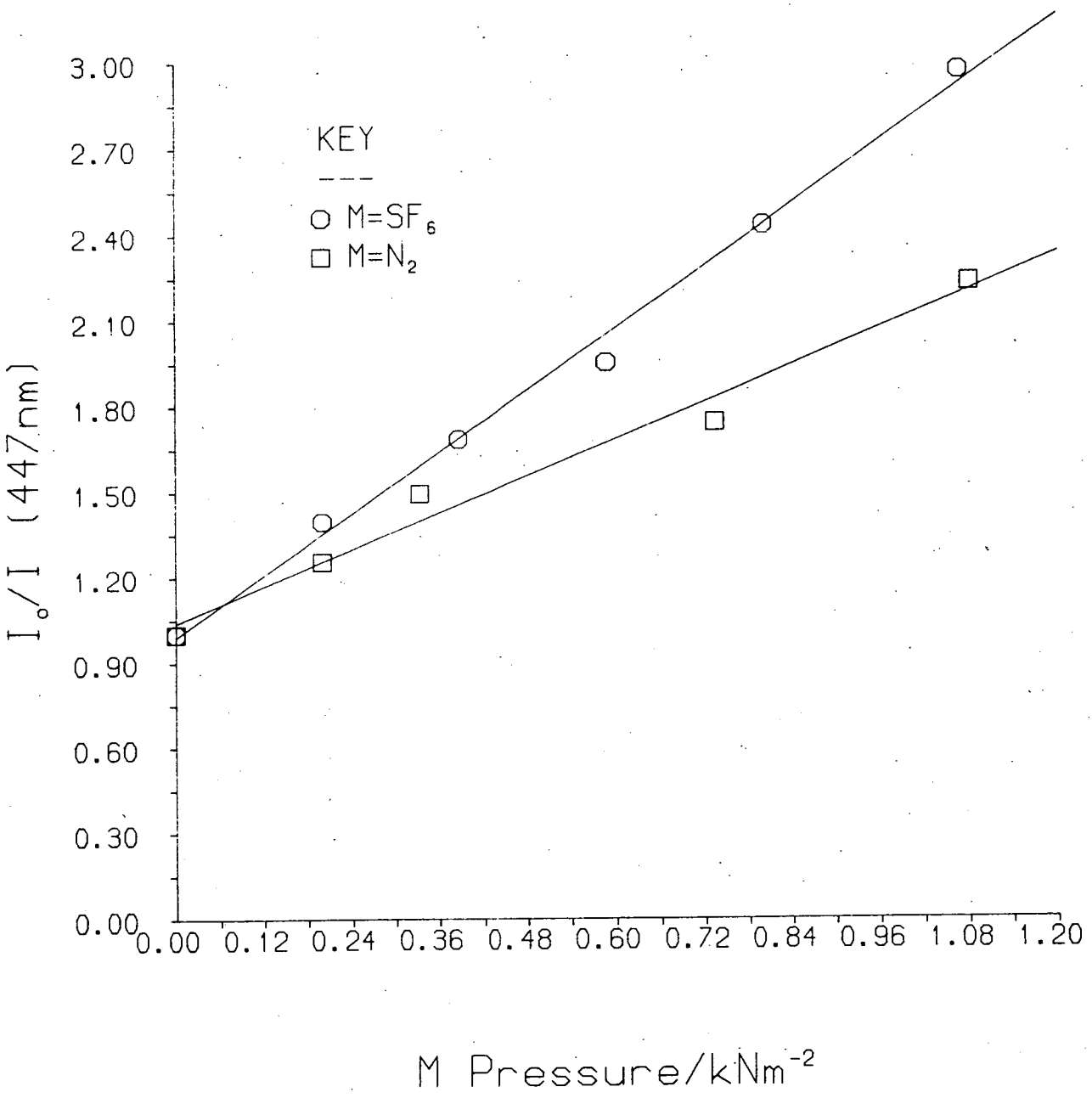

Figure 5.12 : Stern-Volmer plot for the removal of $IBrDO^+$ (intensities measured under the 447nm peak) by non-reactive gases SF_6 and N_2.

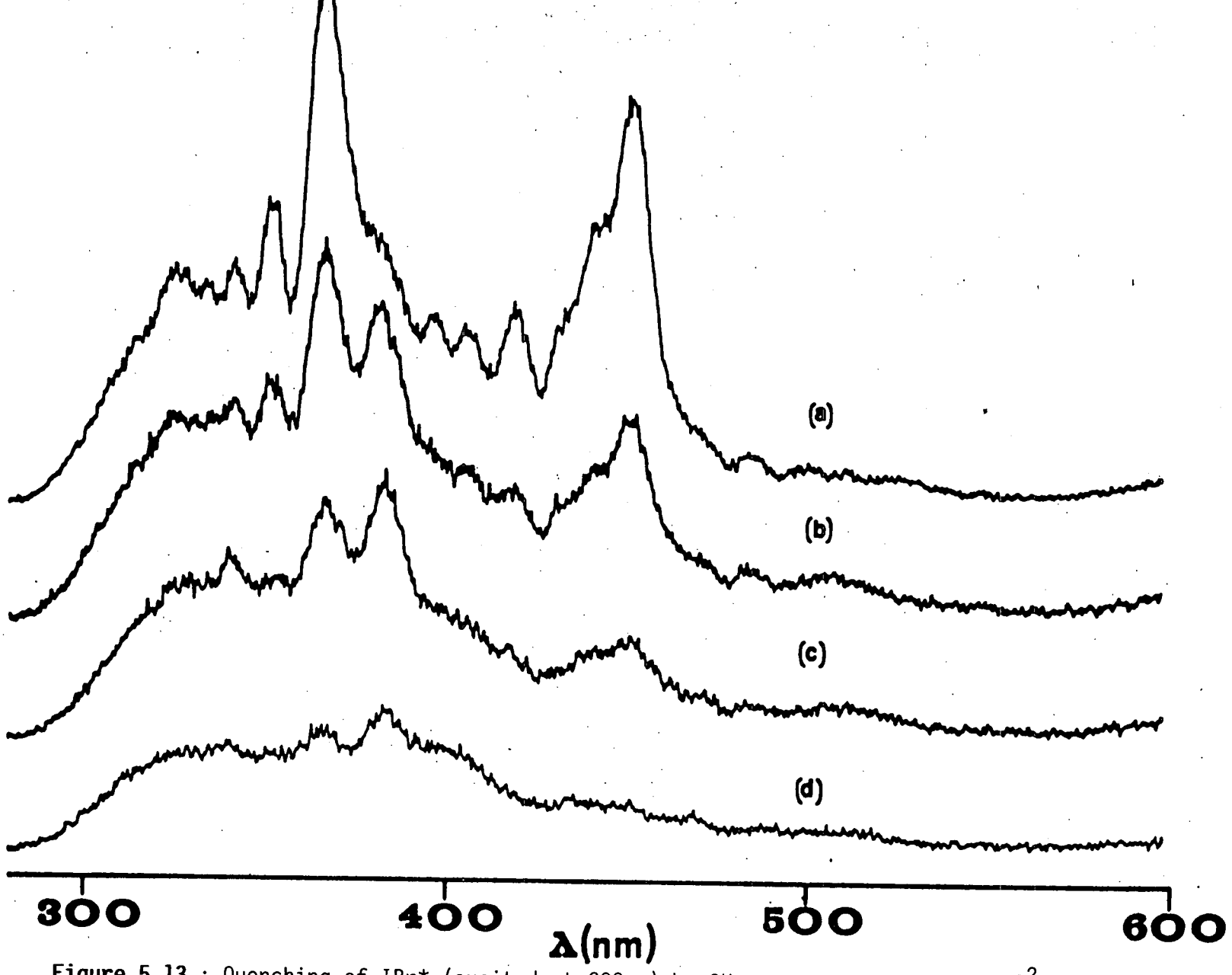

Figure 5.13 : Quenching of IBr* (excited at 200nm) by CH_4. $P_{IBr} = P_{Br} = 120Nm^{-2}$ plus (a) $P_{CH_4} = 0$, (b) $P_{CH_4} = 280Nm^{-2}$, (c) $P_{CH_4} = 1.3kNm^{-2}$, (d) $P_{CH_4} = 6.7kNm^{-2}$.

reflected in the large removal rate constant, k_{REM} = $(9.4 \pm 1.0) \times 10^{-10}$ $cm^3 molec^{-1} s^{-1}$, obtained from a Stern-Volmer analysis of the intensity under the 447nm peak (plotted in Figure 5.14). The D'2 $\rightarrow$ A'2 emission at 385nm increases in intensity up to a CH_4 pressure of $1.3 kNm^{-2}$, then decreases at higher CH_4 pressure. At a CH_4 pressure of $6.7 kNm^{-2}$, where emissions from the D and D' states of IBr are virtually eliminated, a moderately intense continuum emission remains. This continuum emission is prevalent between 300 and 400nm, and may be due to scattered white light.

The other group 3 molecules exhibited similar behaviour to CH_4. The overall intensity removal followed the same pattern except for a variation in the relative magnitude of the 385nm emission peak. This variation was small in the case of CH_3Cl, C_2H_6 and O_2 while an increase in the relative intensity at 385nm was observed with CF_3Cl (see Figure 5.15). Stern-Volmer analyses of spectrofluorimeter traces were performed for the removal of IBr($D0^+$) by CH_3Cl, C_2H_6, CF_3Cl and O_2. These are shown graphically in Figures 5.16 - 5.19, and the removal rate constants derived from them are presented in Table 5.4.

(4) IBr(D'2) removal by class 3 molecules : In order to study the removal of IBr(D'2) by class 3 molecules, a series of experiments was carried out in the manner described above but with the addition of large excesses

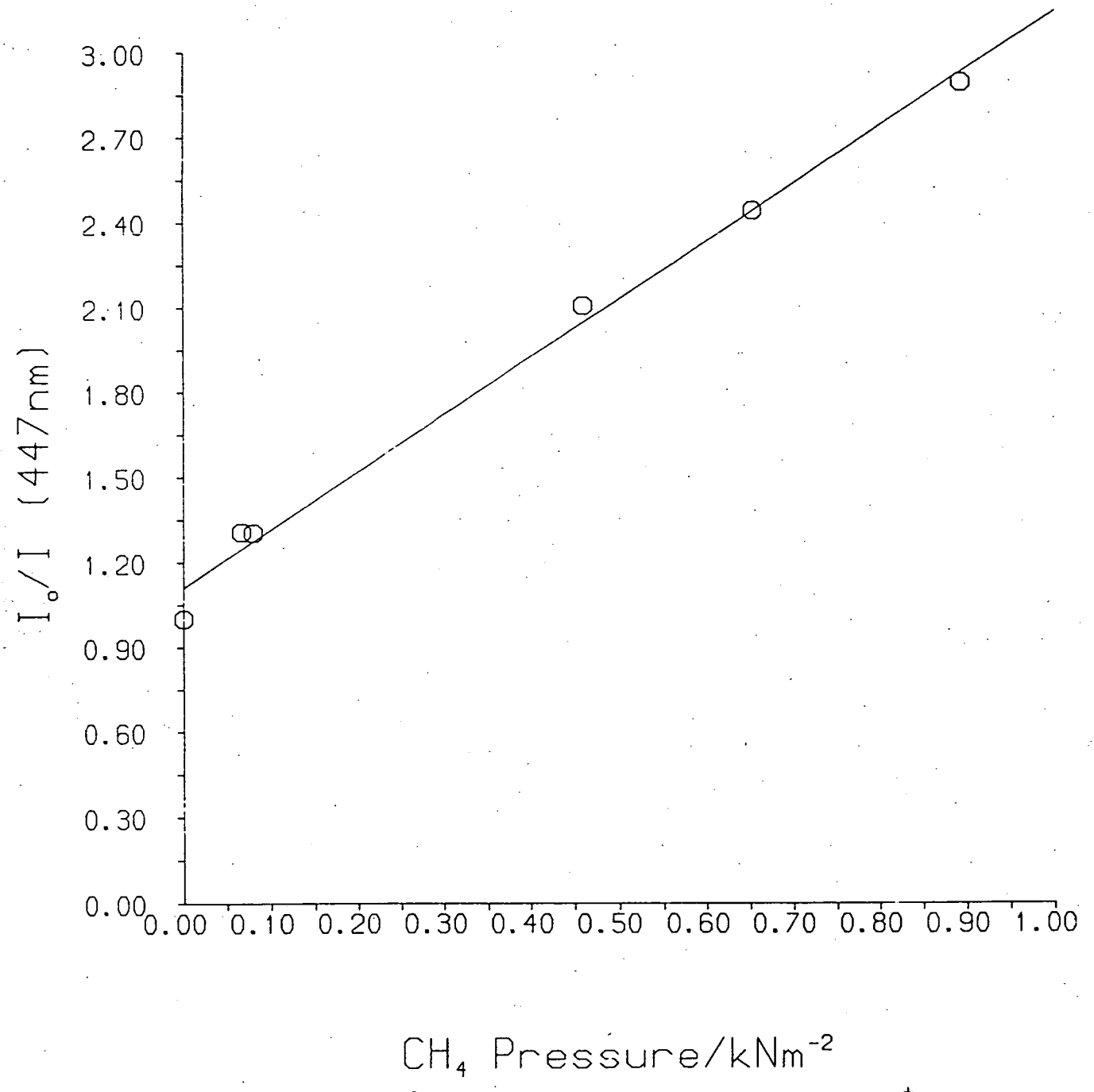

Figure 5.14 : Stern-Volmer plot for the removal of $IBr(DO^+)$ by CH_4.

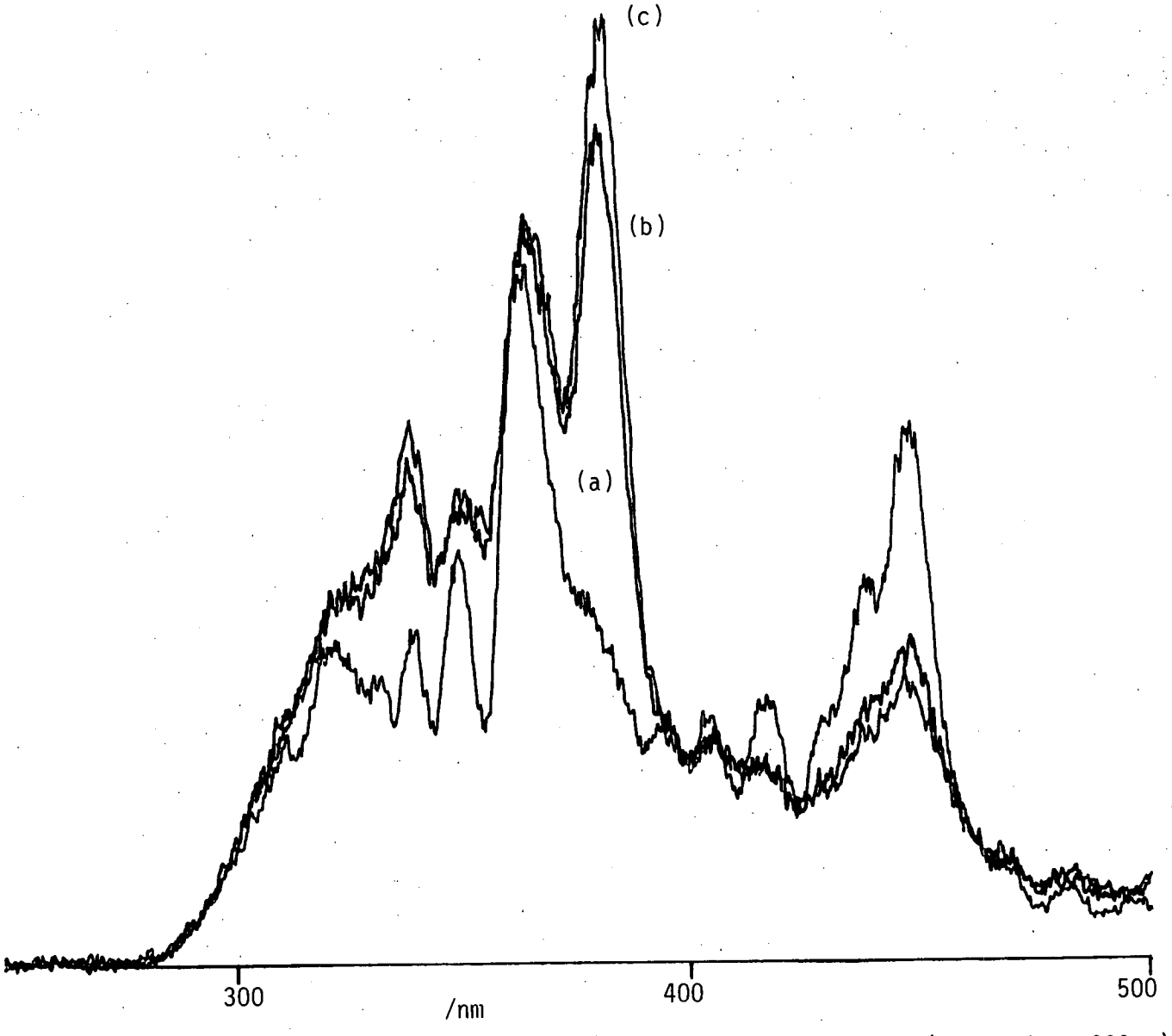

Figure 5.15 : Effect of added CF_3Cl on the fluorescence spectrum of IBr* (excited at 200nm).

$P_{IBr} = P_{Br_2} = 213\ Nm^{-2}$ plus (a) $P_{CF_3Cl} = 0$, (b) $P_{CF_3Cl} = 933Nm^{-2}$, (c) $P_{CF_3Cl} = 1.48kNm^{-2}$.

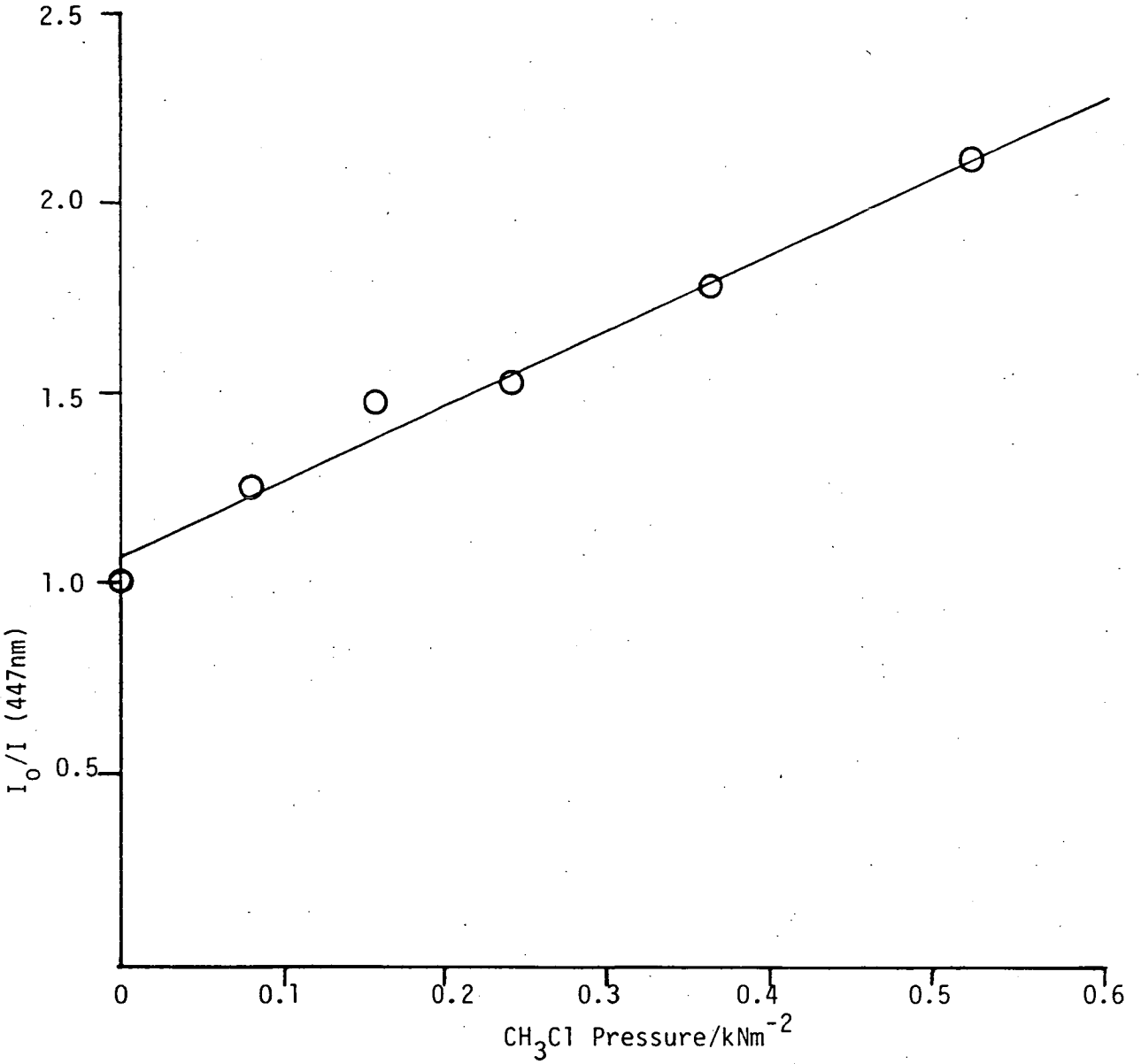

Figure 5.16 : Stern-Volmer plot for the removal of $IBr(DO^+)$ by CH_3Cl.

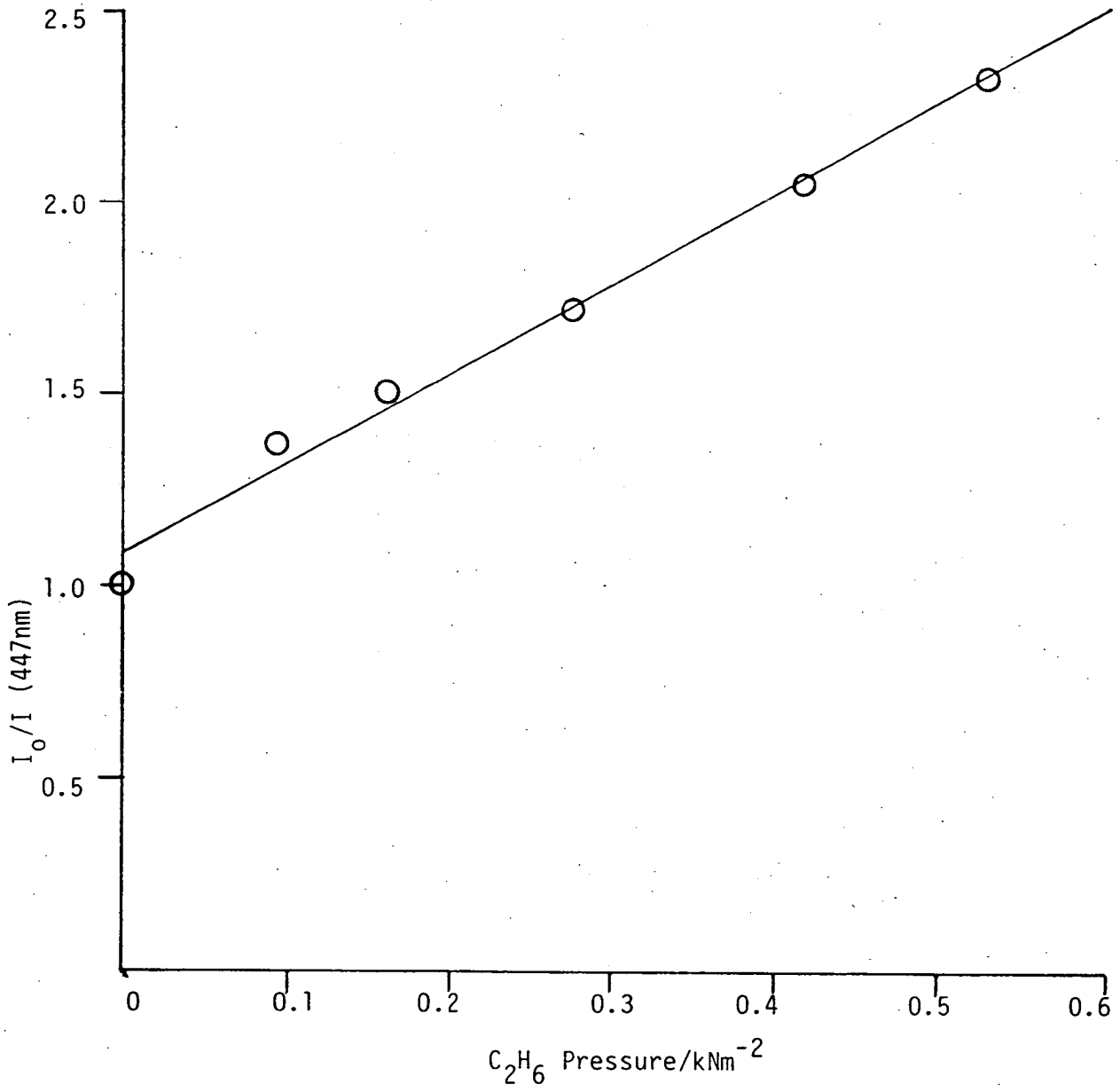

Figure 5.17 : Stern-Volmer plot for the removal of $IBr(D0^+)$ by C_2H_6.

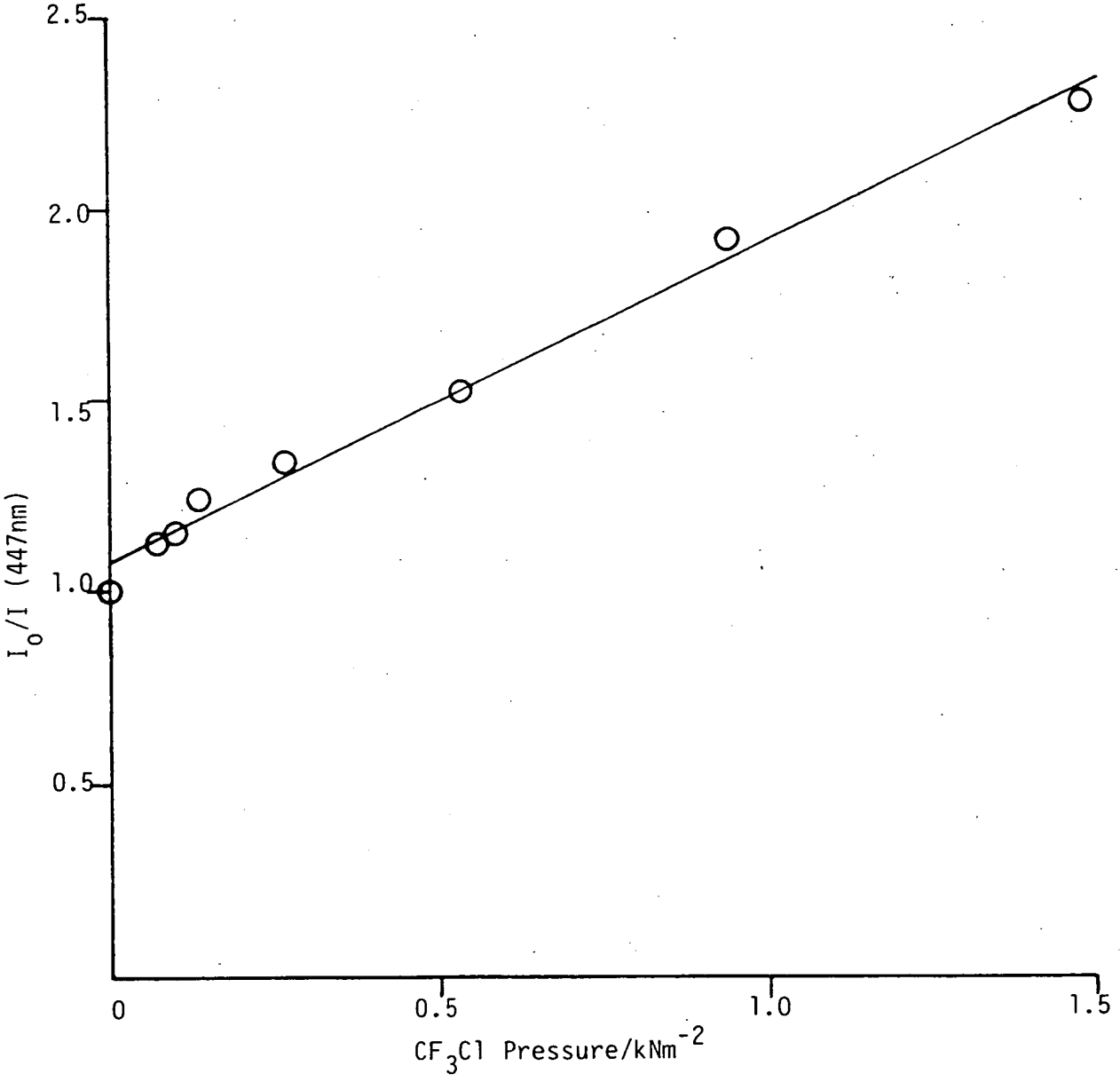

Figure 5.18 : Stern-Volmer plot for the removal of $IBr(D0^+)$ by CF_3Cl

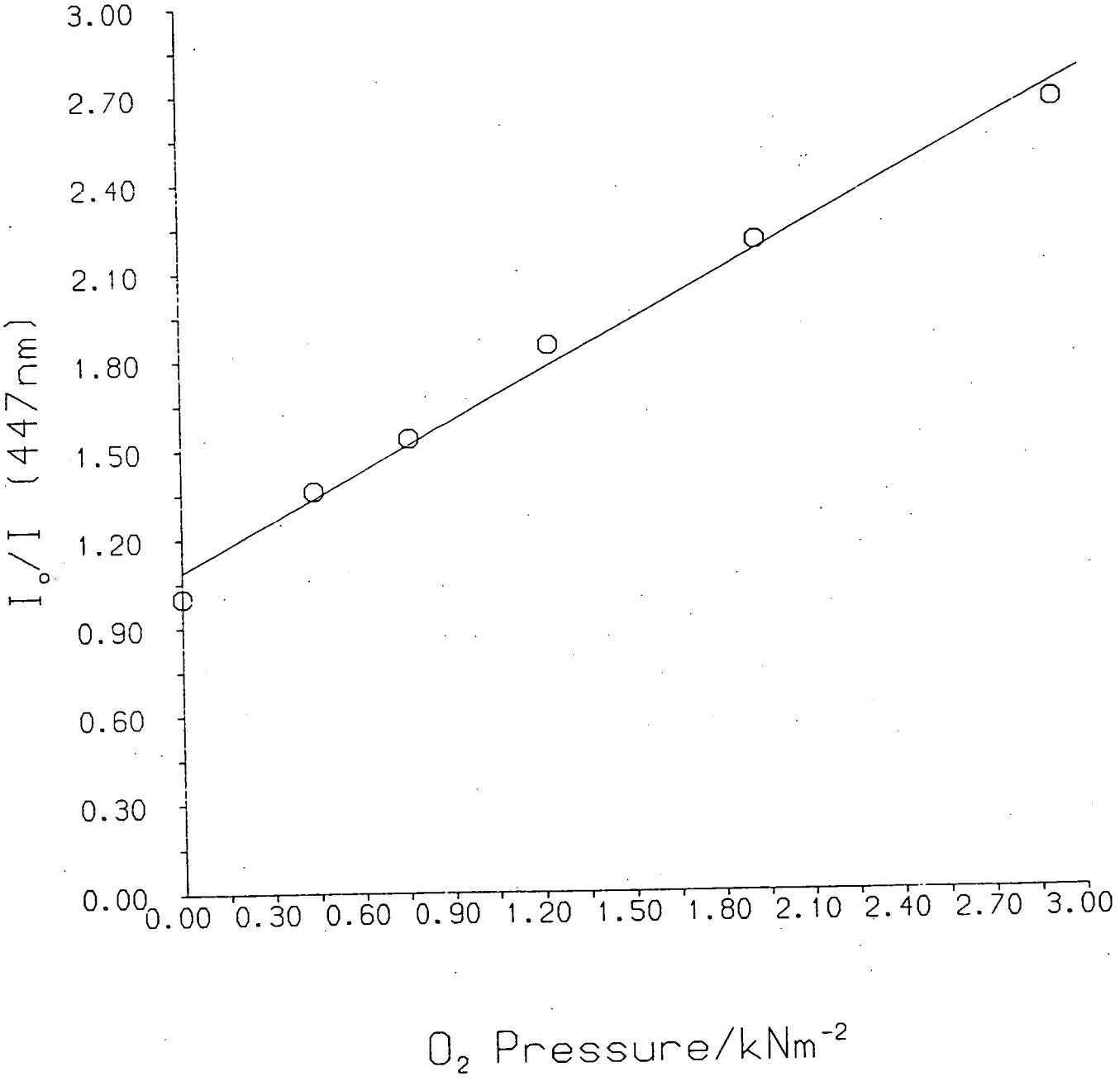

Figure 5.19 : Stern-Volmer plot for the removal of $IBr(D0^+)$ by O_2.

of SF_6 (a non-reactive, class 2 molecule) to the sample cell in addition to various pressures of class 3 molecules. Rapid IBr($D0^+ \longrightarrow D'2$) interstate transfer is promoted by SF_6 (see section 3.4 and Figure 3.14) and the addition of a sufficiently high pressure ensures that virtually all IBr* molecules are transferred to the D'2 state prior to collision with a class 3 molecule.

Figure 5.20 shows the effect of the addition of small pressures of CH_4 on the fluorescence spectrum of IBr(D'2) excited at 200nm in the presence of 12.7kNm^{-2} of SF_6. The intensities of all the peaks fall off steadily with increasing CH_4 pressure. The IBr($D'2 \longrightarrow A'2$) peak intensity at 385nm was utilised in a Stern-Volmer analysis (see Figure 5.21) which yielded a removal rate constant for IBr(D'2) by CH_4, $k_{REM}=(7.0\pm0.8)\times10^{-10}$ cm^{3}molec^{-1}s^{-1}. Figures 5.22-5.25 show the Stern-Volmer plots for the removal of IBr(D'2) by CH_3Cl, C_2H_6, CF_3Cl and O_2. The removal rate constants thus obtained are included in Table 5.4.

DISCUSSION

The preceding results can be rationalised in terms of the following scheme:

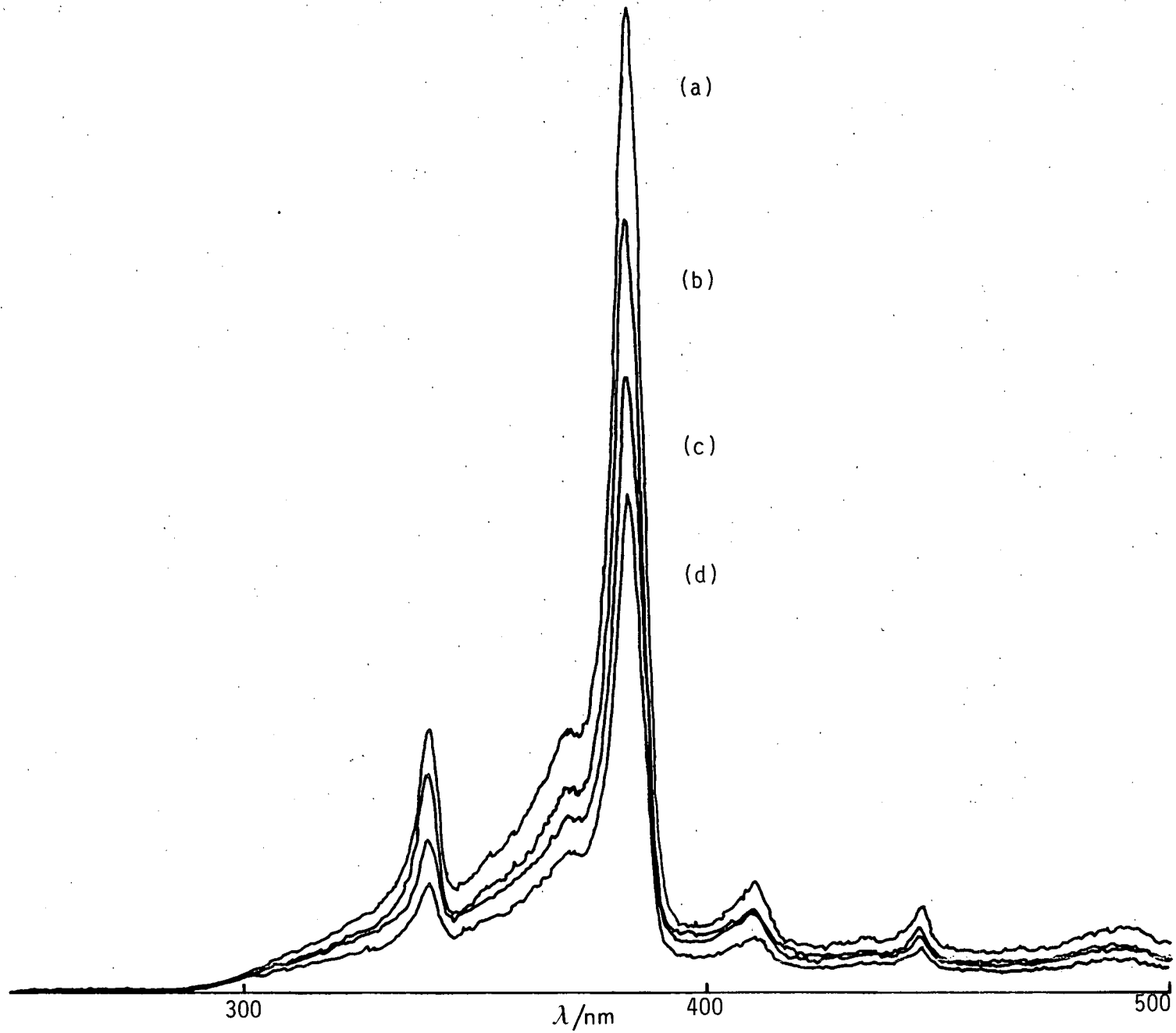

Figure 5.20 : Quenching of IBr(D'2) by CH_4 . $P_{IBr} = P_{Br_2} = 213Nm^{-2}$, $P_{SF_6} = 12.7kNm^{-2}$ plus (a) $P_{CH_4} = 0$, (b) $P_{CH_4} = 133Nm^{-2}$, (c) $P_{CH_4} = 260Nm^{-2}$, (d) $P_{CH_4} = 400Nm^{-2}$.

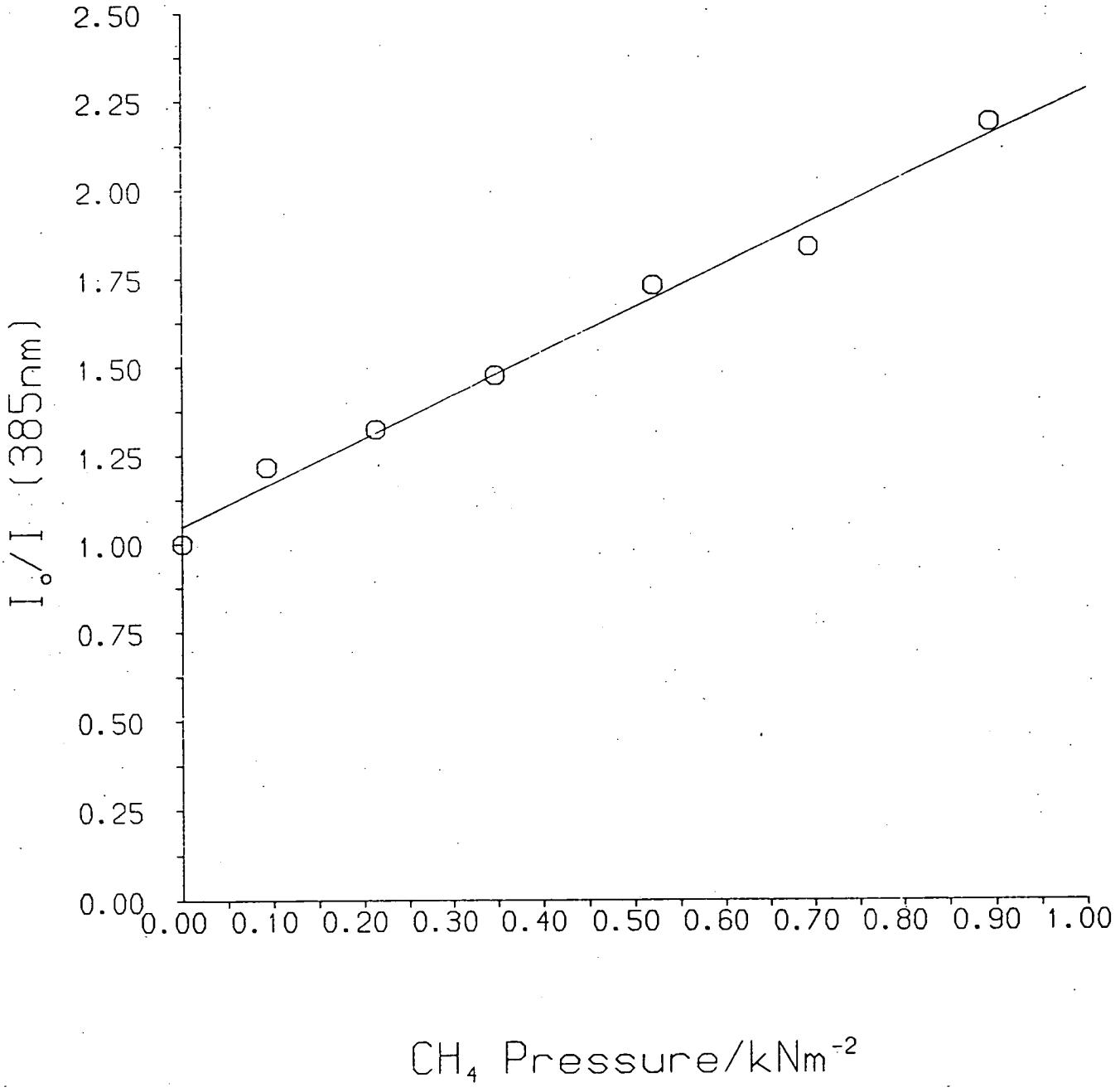

Figure 5.21 : Stern-Volmer plot for the removal of IBr(D'2) by CH_4.
(Intensities measured under the 385nm peak).

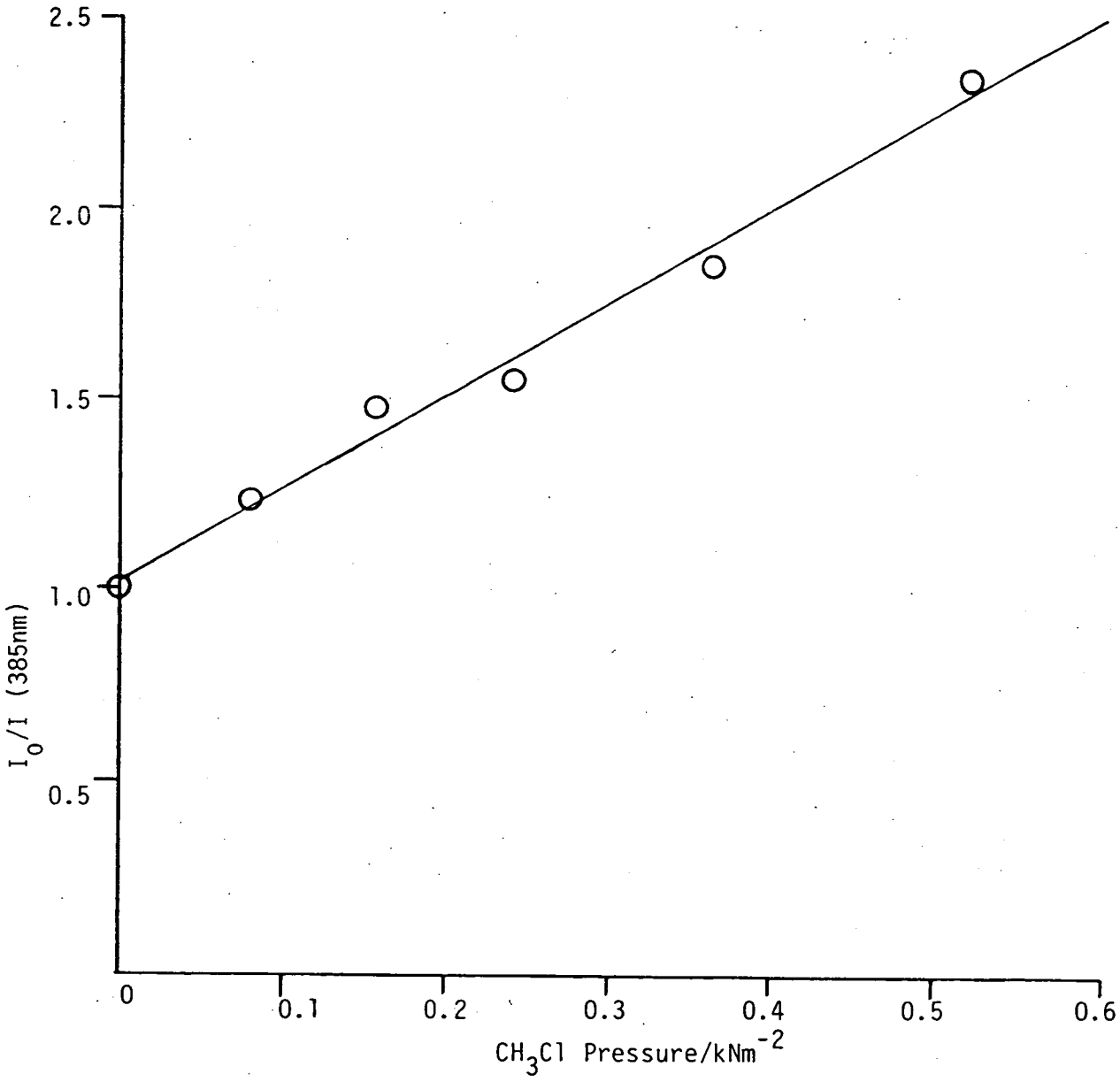

Figure 5.22 : Stern-Volmer plot for the removal of IBr(D'2) by CH_3Cl

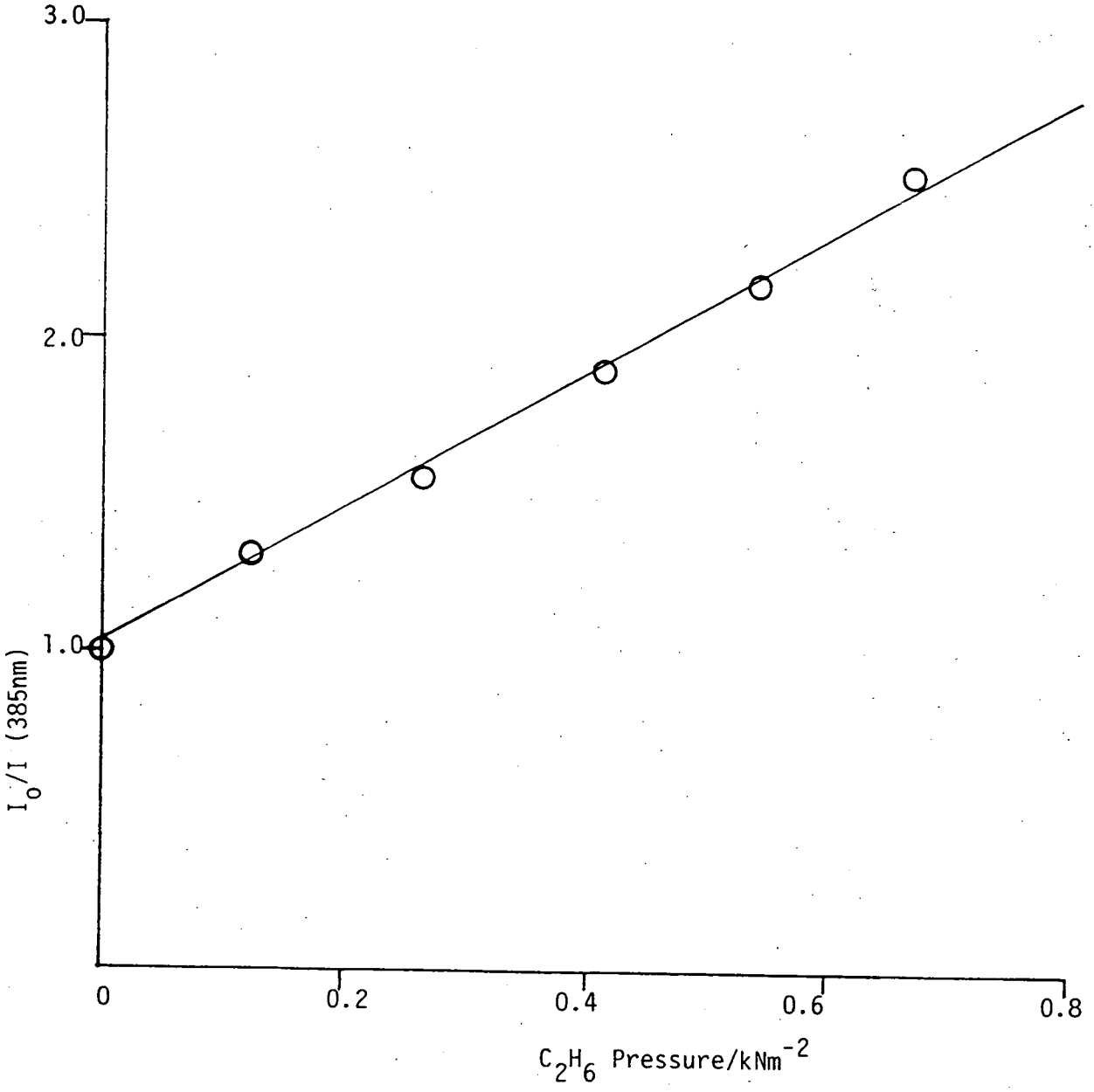

Figure 5.23 : Stern-Volmer plot for the removal of IBr(D'2) by C_2H_6

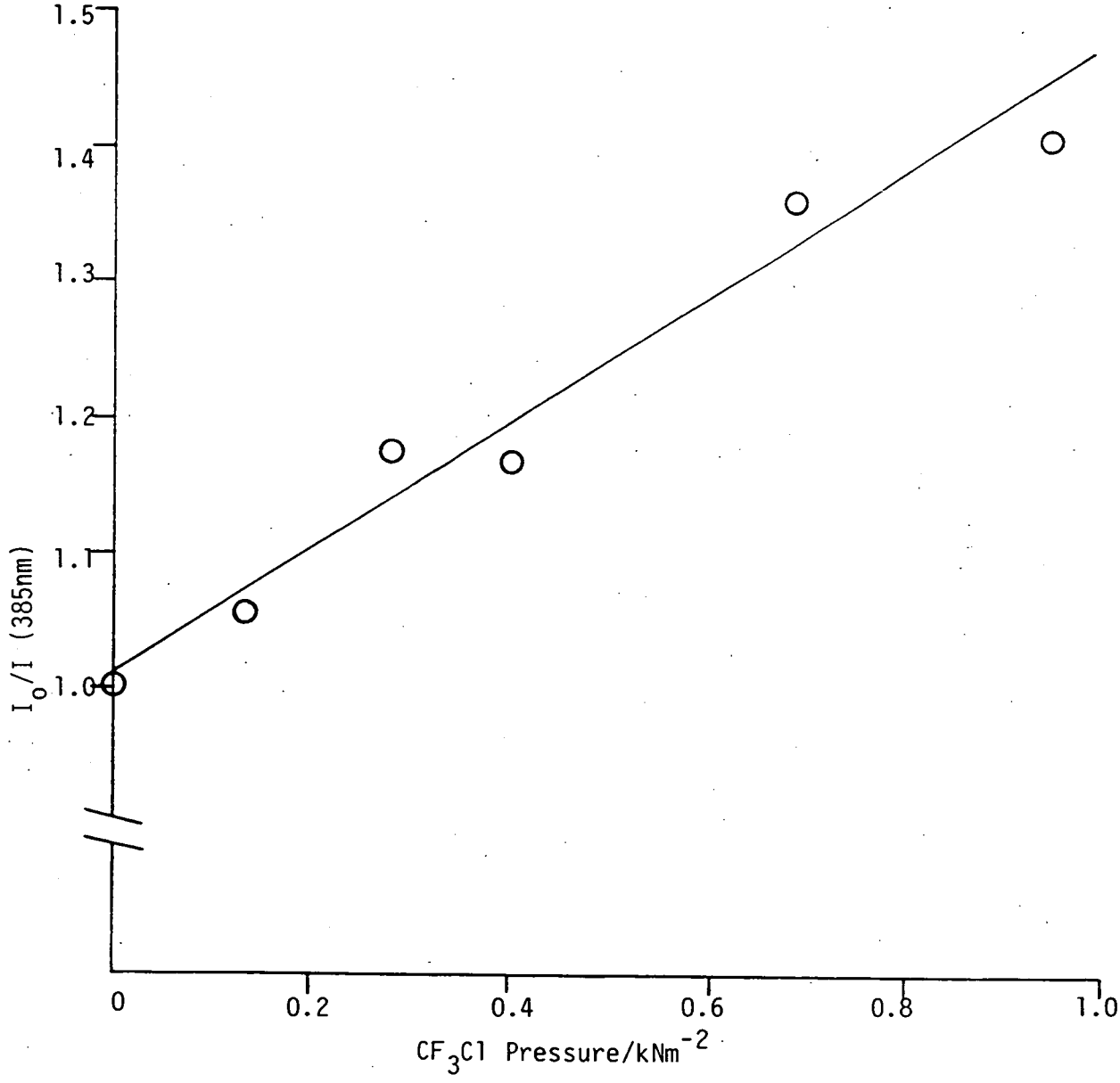

Figure 5.24 : Stern-Volmer plot for the removal of IBr(D'2) by CF_3Cl.

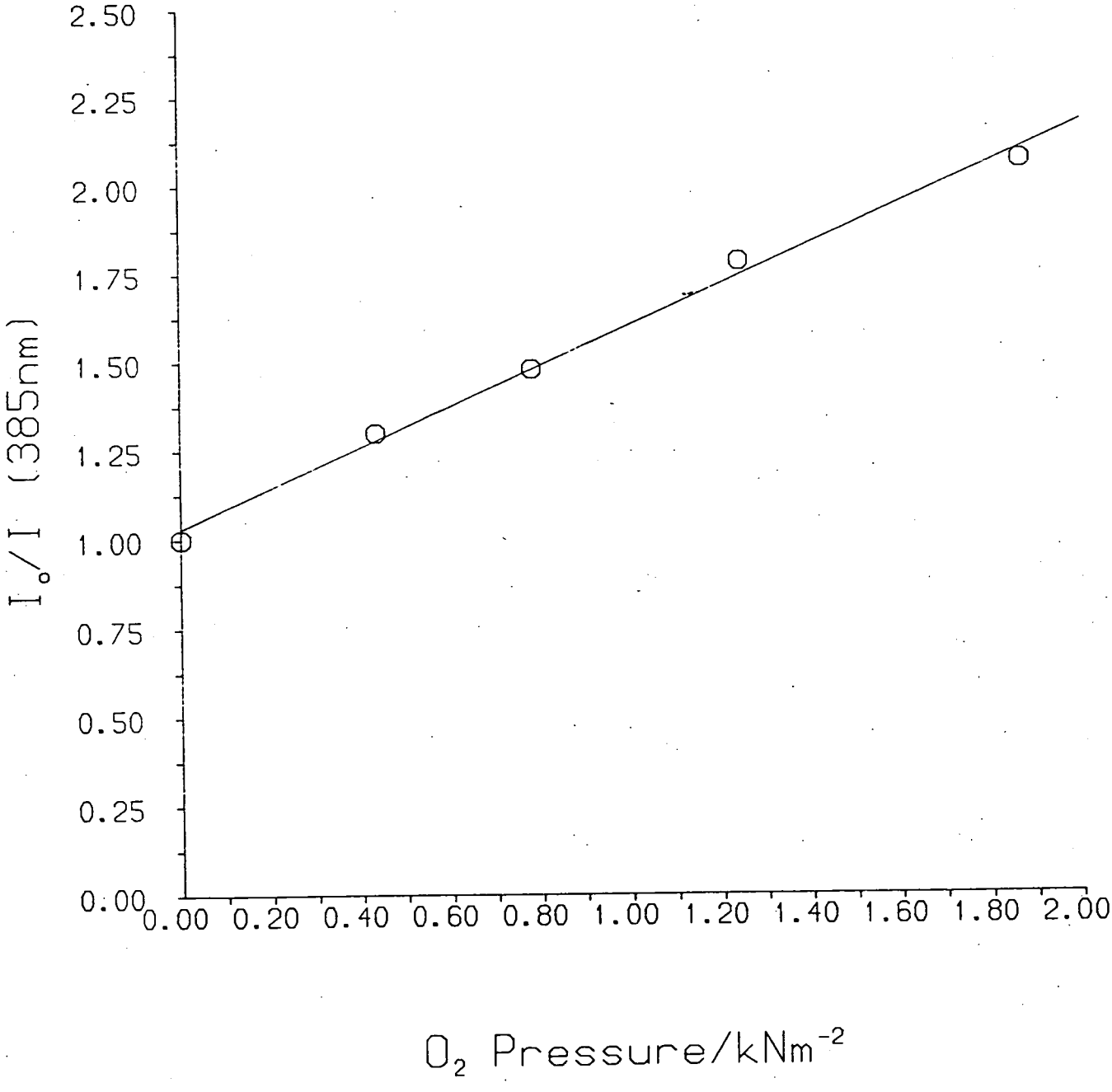

Figure 5.25 : Stern-Volmer plot for the removal of IBr(D'2) by O_2.

$$IBr(XO^+) + h\nu \xrightarrow{I_a} IBr(DO^+)$$

$$IBr(DO^+) \xrightarrow{k_D} \text{SPONTANEOUS DECAY}$$

$$IBr(DO^+) + M(R) \xrightarrow{k_M} IBr(D'2) + M(R)$$

$$IBr(DO^+) + R \xrightarrow{k_1} \text{PRODUCTS}$$

$$IBr(D'2) + R \xrightarrow{k_2} \text{PRODUCTS}$$

$$IBr(D'2) \xrightarrow{k_F} IBr(A'2) + h\nu$$

where M is a class 2 molecule and R is a class 3 molecule.

(1) Removal mechanism for IBr* (DO^+) : The large removal rate constants are not entirely unexpected. A previous study produced comparable values for the removal of $I_2(DO_u+)$ by a range of molecules[18]. The fact that the removal rate constants are extremely large and virtually independent of the polarity of the collision partner suggests that a curve-crossing mechanism plays a major part in these processes. Although IBr* has a relatively diffuse electron cloud, it would be impossible to account for the rate constants in Table 5.4 on the basis of a mechanism where the dispersion forces are responsible for the attraction between the collision partners. When long-range permanent dipole-dipole interactions are

involved the 'Golden Rule' quenching mechanism can give rise to rate constants which are greater than gas kinetic. However, with the exception of CH_3Cl and CF_3Cl all of the quenching molecules in the present study are apolar.

Figure 5.26 illustrates the curve-crossing mechanism which is proposed to account for the kinetic data collected in this chapter. The entrance and exit channels for the quenching processes are coupled by a steep ionic potential which dissociates to $IBr^- + Q(R)^+$ in the diabatic dissociation limit. In the quenching of $IBr(D0^+)$ the initial entrance channel corresponds to $IBr(D0^+,v' = 107) + Q(R)$: 200nm excitation populates v' = 107 (see section 3.2). In addition there may be subsequent re-entry from other vibrational levels following inelastic collisions : although only one potential curve is shown to represent each of the neutral channels and the ionic state, in reality each would comprise a nested series of curves representing the various vibrational levels. Crossings will occur at the intersections of the ionic state with the various channels with probability P_x, so the initial crossing onto the ionic curve will occur with probability P_{1a}. Once an ionic intermediate (ion-pair) has been formed, it can exit the ionic state via various routes, with the following possible outcomes : (a) elastic recoil (exit channel = entrance channel) (b) inelastic recoil with

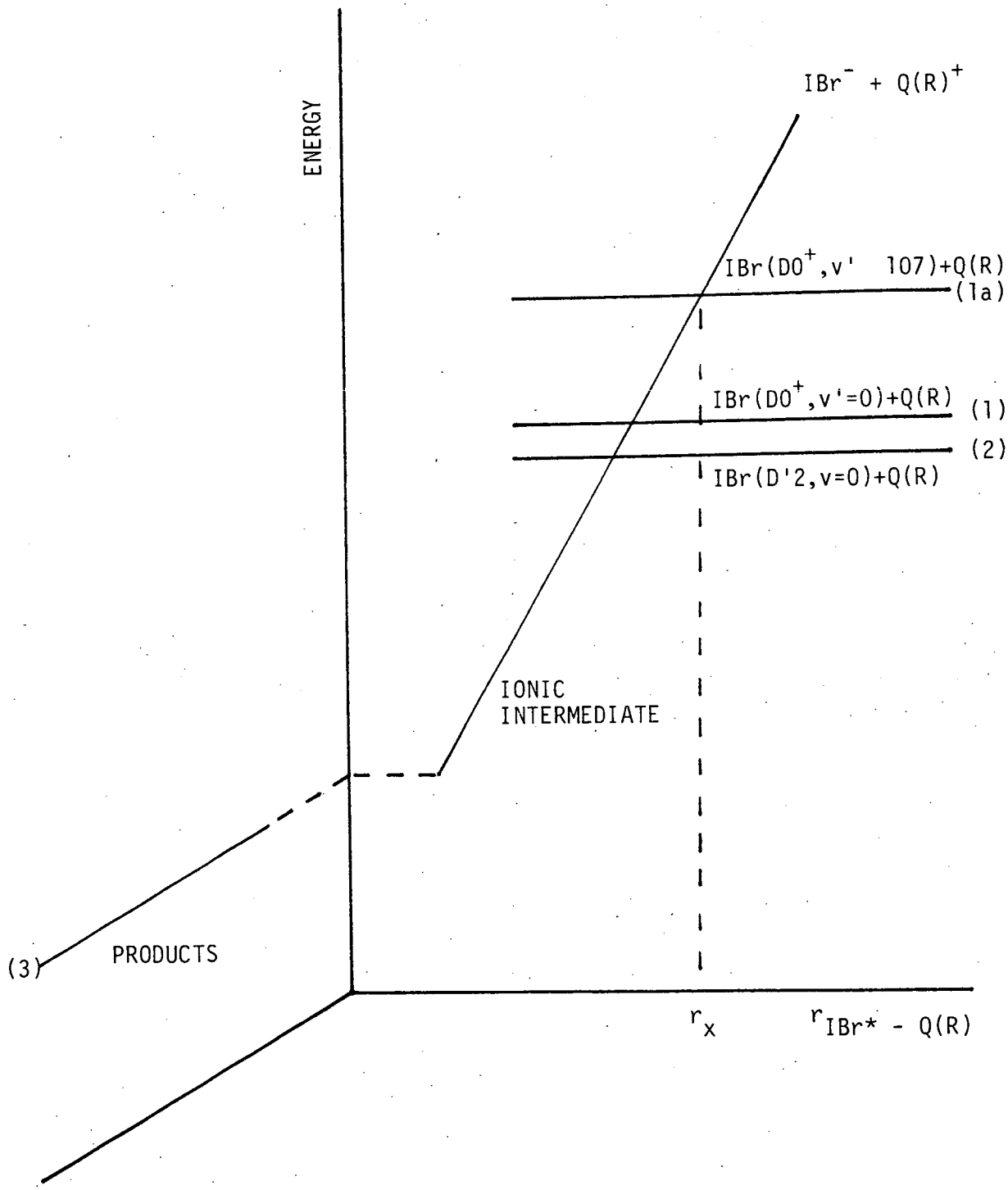

Figure 5.26 : Schematic of the curve-crossing mechanism operative in the removal of IBr ion-pair states by various foreign gases (not to scale). The ionic intermediate is formed by partial donation of an electron from Q(R) into the vacancy in an inner orbital of IBr*.

the production of $IBr(DO^+, v' < 107) + Q(R)^{\ddagger}$, (c) interstate transfer with the production of $IBr(D'2,v) + Q(R)^{\ddagger}$, or (d) chemical reaction with the formation of some other products. The extent of vibrational relaxation within the D-state (ie route (b)) is indeterminate in these experiments since the spectral profile of the oscillatory continuum fluorescence is virtually unaltered (at the resolution of these experiments) for small changes in the upper vibrational level, v', from which the transition occurs. The fourth possibility only exists for reactive gases, R.

The situation is simplified in the case of IBr(D'2) removal as studied here, since a large excess of buffer gas ensures thermalisation of the vibrational levels prior to collision. The entrance channel corresponds to IBr(D'2, low v) + Q(R) and crossing to the ionic curve occurs with probability P_2. Only elastic collisions are possible with inert gases, which have no product channel available. However, elastic and reactive processes are possible with some gases.

Large quenching cross-sections are possible with this model as the ionic curve will extend to very large separations (attractive potential, $V \propto 1/r$), and there will be a high density of neutral exit channels available

to the ionic intermediate as a result of the high density of rovibrational levels.

In view of this mechanistic proposal the results for the removal of $IBr(D0^+)$ and IBr(D'2) are similar to each other : they correspond to different entrance channels but the exit channels in the case of IBr(D'2) are a subset of those available in quenching from $IBr(D0^+)$. In both cases the branching between the available exit channels will be determined by the various P_x. A similar situation will exist for each of the collision partners (Q,R) except for displacements in the position of the ionic curve due to the different ionization potentials of these species.

In the quenching of $IBr(D0^+)$ by class 2 molecules exit channels (1) and (2) dominate with little (if any) chemical reaction. This is not surprising in the case of N_2 as excitation at 200nm corresponds to an energy of 598 $kJmol^{-1}$ which is insufficient to break the extremely strong triple bond ($N \equiv N$ bond energy = 946$kJmol^{-1}$). Although there is sufficient energy to break an S-F bond (bond energy = 326 $kJmol^{-1}$), SF_6 is known to be extremely inert. This is attributed[147] to a combination of factors : (1) the S-F bond is strong, (2) the S-atom is coordinately saturated, (3) the S-atom is sterically

hindered, and (4) the molecule is apolar. Similar considerations apply to CF_4 which, like SF_6, is extremely inert (C-F bond energy = 485 $kJmol^{-1}$). The relative magnitudes of the rate constants for the removal of $IBr(DO^+)$ by these gases is thus determined by the density of entrance and exit channels and the magnitudes of the crossing probabilities for these channels.

In the quenching of $IBr(DO^+)$ by class 3 molecules, all 3 exit channels are available. The removal rates for CH_4, CH_3Cl, C_2H_6 and CF_3Cl are very similar, which implies that the crossing points (r_x) and probabilities (P_{1a}) have similar magnitudes. However, removal by O_2 is appreciably slower implying smaller magnitudes in this case. Previous studies[18,34] indicate dthat a similar situation exists for the removal of $I_2(DO_u+)$ by class 3 molecules, ie removal by O_2 is also appreciably slower (see Table 5.5).

Qualitative observations can be made on the relative contributions of exit channels (2) and (3) for the various reactive gases, on the basis of spectra such as those shown in Figures 5.13 and 5.15.

TABLE 5.5 : Removal rate constants, k_{REM}, for $I_2(DO_u+)$ with various foreign gases.

Foreign gas	$k_{REM}/cm^3molec^{-1}s^{-1} \times 10^{10}$	Reference
CH_4	7.9 ± 0.2	18
CH_3Cl	21.0 ± 1.0	18
CF_3Cl	7.1 ± 0.4	18
O_2	0.96	43

The intensity of the peak at 385nm reflects the extent of the contribution from exit channel (2), but the picture is complicated by subsequent reaction of IBr(D'2) with these gases. For CH_4, CH_3Cl, C_2H_6 and O_2 exit channel (3) appears to dominate over exit channel (2), while for CF_3Cl exit channel (2) assumes a greater importance (see Figure 5.15). In fact CF_3Cl would be better classified as being intermediate between classes (2) and (3). In a study of the reactions of $I_2(DO_u+)$ with methane and various halomethanes, Willard and Glasgow[17] found a marked decrease in the quantum yield for reaction (exit channel (3)) upon increasing the number of F atoms, n, in the serious CF_nH_{4-n}, and an increase upon including a Cl atom (see Table 5.6). Therefore an intermediate classification for CF_3Cl fits in with previously observed behaviour in the removal of the analogous DO_u+ state of I_2.

Collisions between thermalised IBr(D'2) and class 3 molecules (entrance channel 2) can result in either elastic recoil (exit channel 2) or reaction (exit channel 3). Again the variations in the removal rates can be explained by the following factors : (1) differences in the curve-crossing positions and probabilities, and (2) differences in the relative contributions of the two exit channels. Since the intermediate ionic curve (or nest of curves) is common to the removal of $IBr(DO^+)$ and IBr(D'2) for a particular collision partner, it seems most plausible that the relatively small

TABLE 5.6 : Quantum yields for the reactive removal of $I_2(DO_u+)$ by methane and various halomethanes (100 torr). From reference 17.

Molecule	Φ_R
CF_4	0.002
CF_3H	0.07
CFH_3	0.20
CH_4	0.30
CH_3Cl	0.40

removal rate constant for IBr(D'2) with O_2 is a result of a small crossing probability, P_2, to form the intermediate ionic species. Taking the ionization potentials of the class 3 molecules in the present study into account, the intersection of the neutral and ionic curves should occur at a relatively large separation for $R=O_2$ - see Table 5.7. The relatively small removal rate found for IBr(D'2) with CF_3Cl is a result of the predominance of exit channel (2) over exit channel (3), as previously discussed for $IBr(DO^+)$.

The extremely large removal rate constant for IBr(D'2) with CH_3Cl and C_2H_6, in relation to CH_4, will be due primarily to the lower ionization potentials of these molecules which will result in larger values of r_x. In addition to this it is likely that IBr(D'2) has a greater reactivity towards C-Cl and C-C bonds, both of which are weaker than C-H bonds. This would correspond to a higher probability for crossing onto the reactive exit channel (P_3) with these molecules.

(2) Discrepancy between the removal rates for $IBr(DO^+)$ with CH_4 as measured on SRS port HA12 (time resolved) and on the spectrofluorimeter : the temporally resolved studies reported in section 5.2 yielded a value of 1.9×10^{-10} $cm^3molec^{-1}s^{-1}$ for the removal of $IBr(DO^+)$ by CH_4. This is a factor of 5 less than the value derived from Stern-Volmer analysis of spectrofluorimeter traces. As discussed for $I_2(DO_u+)$ in section 5.2, this discrepancy is due to the fact that a large spectral region was monitored in the time

TABLE 5.7: Ionization potentials for the class 3 molecules discussed in this chapter. (Taken from "Ionization Potentials, Appearance Potentials, and Heats of Formation of Gaseous Positive Ions", US Department of Commerce, National Bureau of Standards, NSRDS-NBS 26 (1969).

MOLECULE	IONIZATION POTENTIAL (eV)
CH_4	13.21
C_2H_6	11.93
CH_3Cl	11.60
CF_3Cl	12.90
O_2	12.20

resolved work on port HA12 and so contributions from the underlying continuum emission and possibly from other ion-pair states cannot be precluded. In the Stern-Volmer analysis of the spectrofluorimeter traces data were derived from a single $IBr(DO^+)$ emission peak, and thus result in an accurate removal rate constant.

5.4 CONCLUSION

The values obtained for pure radiative lifetimes of halogen ion-pair states are summarised in Table 5.8. The value obtained for $I_2(D'^2_g)$ agrees well with a previously reported value of 6.7ns[31]. It was not possible to determine the radiative lifetime of $I_2(DO_u+)$ as it was found that more than one electronic state of I_2 was responsible for the signal detected following excitation. It is postulated that the additional state(s) is populated as a result of collisional transfer from $I_2(DO_u+)$ rather than by direct excitation.

The lowest bound state of XeI*, the B-state, which resembles the D'-states of IBr and I_2 in its physical behaviour, has a radiative lifetime of 8.57ns.

The principal deactivation pathway in the removal of

The following conclusions can be drawn for the reactive gases studied : (1) IBr(D'2) is removed more rapidly by CH_3Cl and C_2H_6, in comparison to CH_4, as a result of the lower ionization potentials of these molecules which result in larger values for r_x (see Figure 5.26). In the removal of $IBr(DO^+)$, where the picture is complicated by additional exit channels, only C_2H_6 shows a marked increase relative to CH_4. (2) As expected on the basis of it's ionization potential, CF_3Cl removes $IBr(DO^+)$ at a rate comparable to CH_4. However it is less reactive than CH_4 in that interstate transfer (ie $DO^+ \longrightarrow D'2$, exit channel 2) plays a more dominant role in the removal process. The assertion is supported by the relatively small removal rate found for IBr(D'2) with CF_3Cl : as the intermediate ionic curve is common to both removal processes it can be concluded that crossing onto the reactive exit channel is not very efficient (ie P_3 is low). (3) O_2, which has an ionization potential ca. 1eV lower than CH_4, provides an intriguing exception to the behaviour observed for the other class 3 molecules. The results indicate that removal of IBr(D/D') by O_2 is relatively inefficient due to inefficiency in crossing onto the ionic intermediate curve (ie P_{1a} and P_2 are low).

While the curve-crossing model provides a good basis for explaining these results, the true picture is more complicated. This is to be expected since the model, which was developed to rationalise a range of atomic collisional

processes, takes no account of the internal degrees of freedom of the colliding molecules.

CHAPTER 6 - STUDIES OF CH($A^2\Delta$) FORMATION IN PHOTOFRAGMENTATION PROCESSES

6.1 INTRODUCTION

In this chapter photofragmentation processes leading to the production of the first excited state of the methylidyne radical, $CH(A^2\Delta)$, will be examined. Several small organic molecules which give rise to $CH(A^2\Delta \longrightarrow X^2\Pi)$ emission following multiphoton absorption at 193nm (ArF laser) will be dealt with.

There are three categories of excitation mechanisms which could be involved in the dissociation processes : (1) sequential excitation of the parent molecule via real intermediate state(s), (2) simultaneous excitation of the parent molecule via virtual state(s), and (3) stepwise dissociative excitation via intermediate fragment(s). These are described more fully in section 1.8. The objectives of the investigations were two-fold : firstly, to address the crucial question as to which of the excitation mechanisms dominates, and secondly, to give guidance in the selection of a suitable precursor for the study of collisional processes involving $CH(A^2\Delta)$ (see next chapter).

Various other excited species were observed in emission, but will not be dealt with here.

6.2 RESULTS

With the exception of CH_2I_2, all of the investigations were carried out at Edinburgh using the experimental set-up described in section 2.6. CH_2I_2 was investigated at the laser facility of the Rutherford Appleton Laboratory using the experimental set-up described in section 2.7.

(a) CH_3Br

Absorption by CH_3Br in the UV sets in at 285nm and results primarily in dissociation to CH_3+Br. At 193nm the molar extinction coefficient is $\simeq$ 100 l/mole cm[148]. Figure 6.1a shows the CH($A^2\Delta \longrightarrow X^2\Pi$) fluorescence that results from 193nm laser photolysis of CH_3Br, at a resolution of 0.13nm. The CH_3Br pressure employed was 14.7Nm^{-2}. The effective rotational 'temperature' of CH($A^2\Delta$)thus produced was determined from the relative intensities of the R-branch rotational lines (v'=0) using a method previously detailed in the literature[149,150]. The graphical determination (see Figure 6.2) yielded the value T_{rot} = 2900$\pm$150K. This value and several others are collected in Table 6.1. The extent of vibrational excitation is not so easily quantified due to the high degree of overlap, particularly at the Q(0,0) band-head, of the various transitions from the three bound upper vibrational levels. However a simulated spectrum (Figure 6.1b) with T_{rot} = 3000K and the vibrational populations in

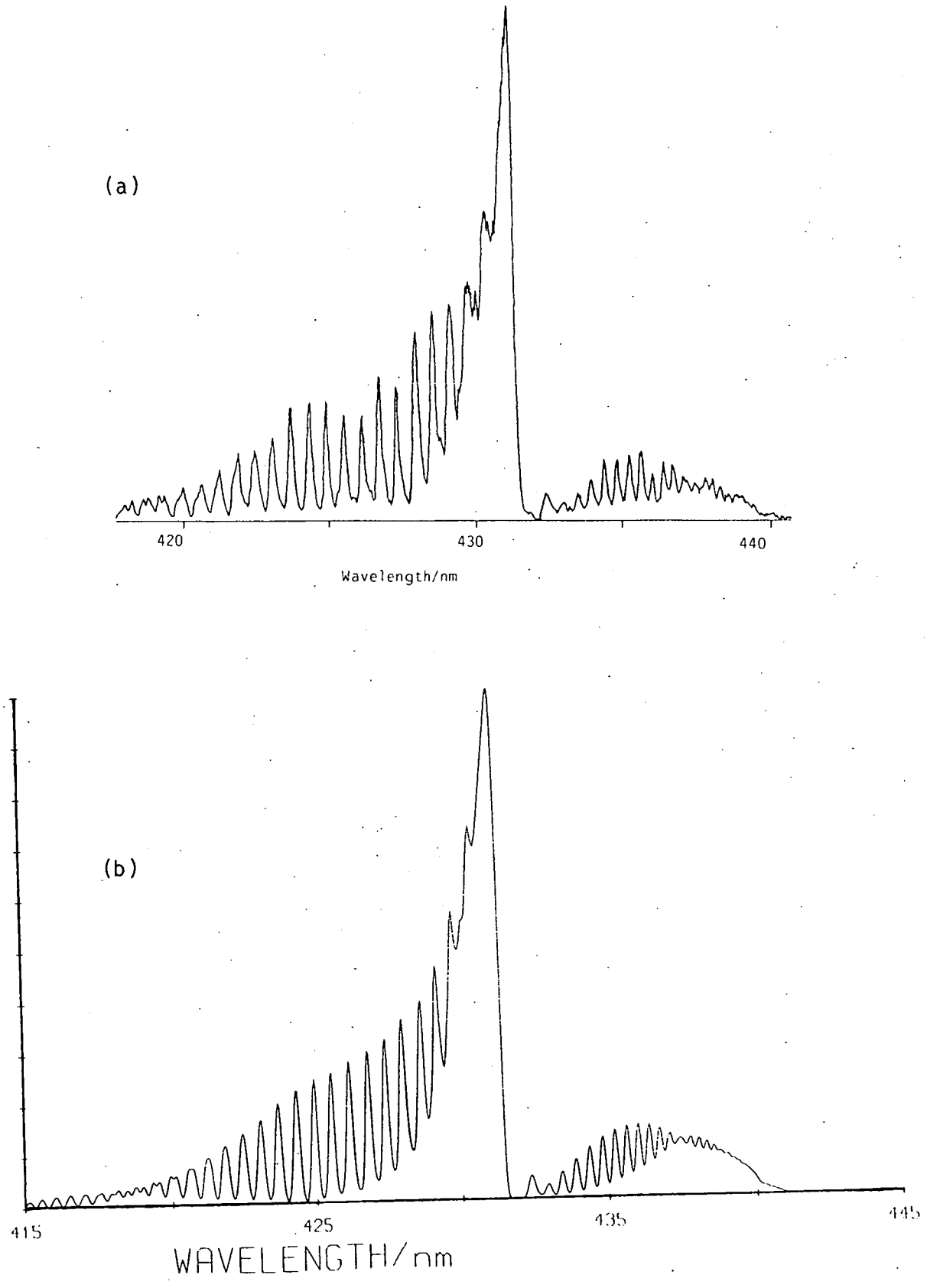

Figure 6.1 : (a) $CH(A^2\Delta \rightarrow X^2\Pi)$ photofragment fluorescence following ArF laser photolysis of CH_3Br ($p = 13.3Nm^{-2}$); (b) computer simulation of spectrum (a).

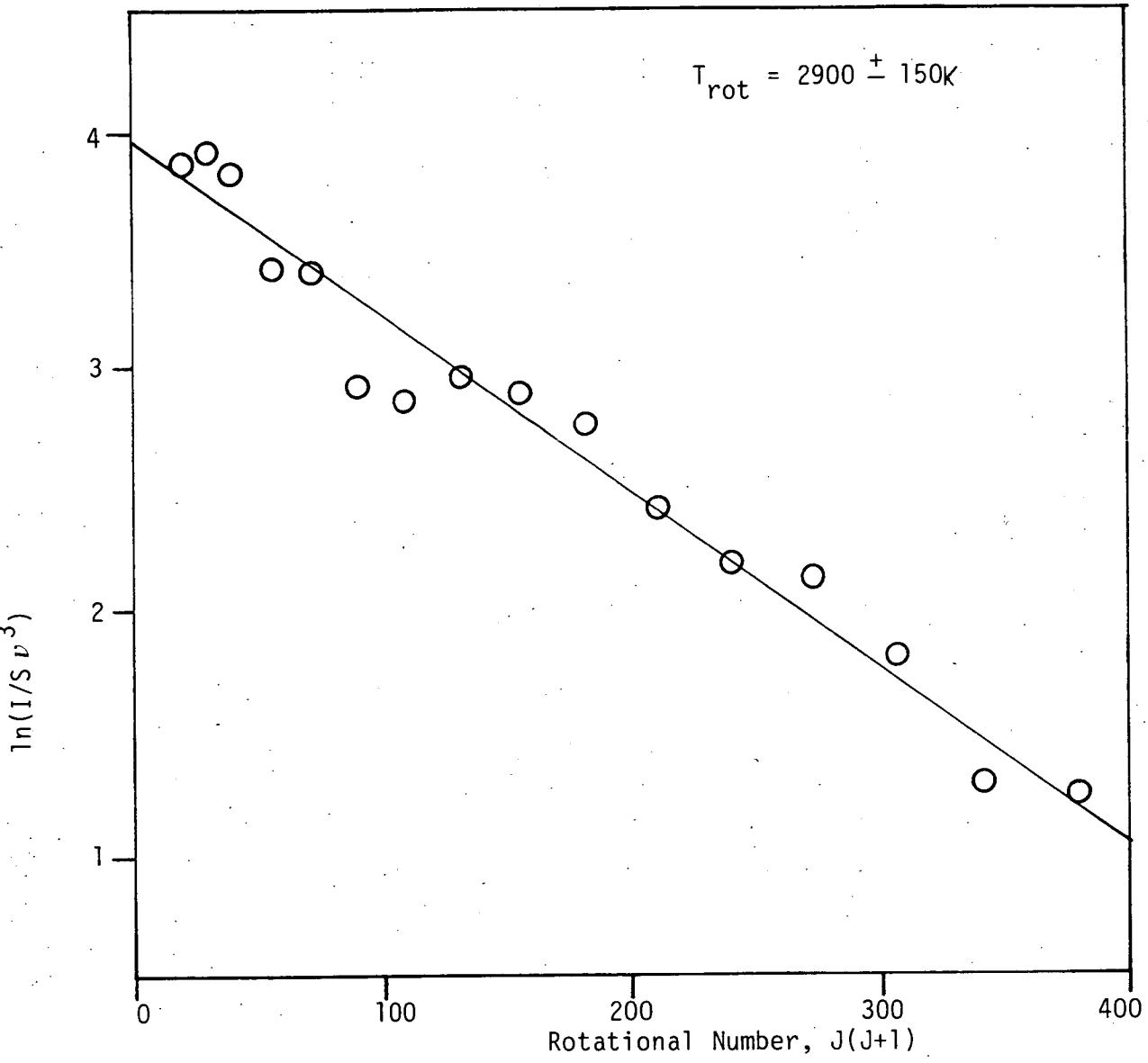

Figure 6.2 : Relative rotational populations of $CH(A^2\Delta, v'=0)$, produced in the 193nm laser photolysis of CH_3Br, as a function of rotational quantum number, J (J + 1). The error quoted for T_{rot} is 2σ. (Relative population, $P_J = \ln(I/S\nu^3)$ where I = measured intensity, S = linestrength and ν is the transition frequency.)

TABLE 6.1 : Rotational temperatures of $CH(A^2\Delta)$ radicals produced in 193nm laser photolysis of various precursors.

PRECURSOR	$T_{rot}(A^2\Delta)/K$
CH_3Br	2900 ± 150
$CHBr_3$	2600 ± 100
CH_3OH	2250 ± 300
$(CH_3)_2CO$	2250 ± 200
CH_2I_2	~ 3000
CH_3NH_2	2200 ± 250 [a]
C_2H_3CHO	4700 ± 200 [b]

a Calculated from Figure 1 of reference 94

b reference 91

v=0, 1 and 2 corresponding to a Boltzmann temperature of 2000K, gives a good fit to the experimentally observed spectrum. The computer program used for the simulation was based on one described by Baas and Beenakker[151], and an annotated copy is presented in Appendix 1.

Figure 6.3 illustrates the effect of increased vibrational excitation on the $CH(A^2\Delta \longrightarrow X^2\Pi)$ emission spectrum, with a fixed amount of rotational excitation (T_{rot} = 3000K). These simulations were used to estimate the vibrational temperatures in other spectra through comparison of the intensities at the Q(0,0) and Q(2,2) band-heads.

(b) $CHBr_3$

Bromoform absorbs strongly from 285nm to shorter wavelengths, with excitation at 193nm corresponding to absorption in the highest of the four bands predicted by symmetry considerations[152]. In the flash photolysis of $CHBr_3$ at $\lambda \geq 165$nm, $CH(X^2\Pi)$ is believed to be generated by a successive photodetachment process:[82]

$$CHBr_3 + h\nu\ (\lambda \geq 165nm) \longrightarrow \longrightarrow \longrightarrow CH(X^2\Pi) + 3Br \qquad -(6.1)$$

Figure 6.4 shows part of the $CH(A^2\Delta \longrightarrow X^2\Pi)$ photofragment fluorescence which follows 193nm laser photolysis of $CHBr_3$. The R-branch rotational lines of the v=0 level are identified. A $CH(A^2\Delta)$ rotational temperature of 2600 ± 100K was determined graphically from the relative intensities of

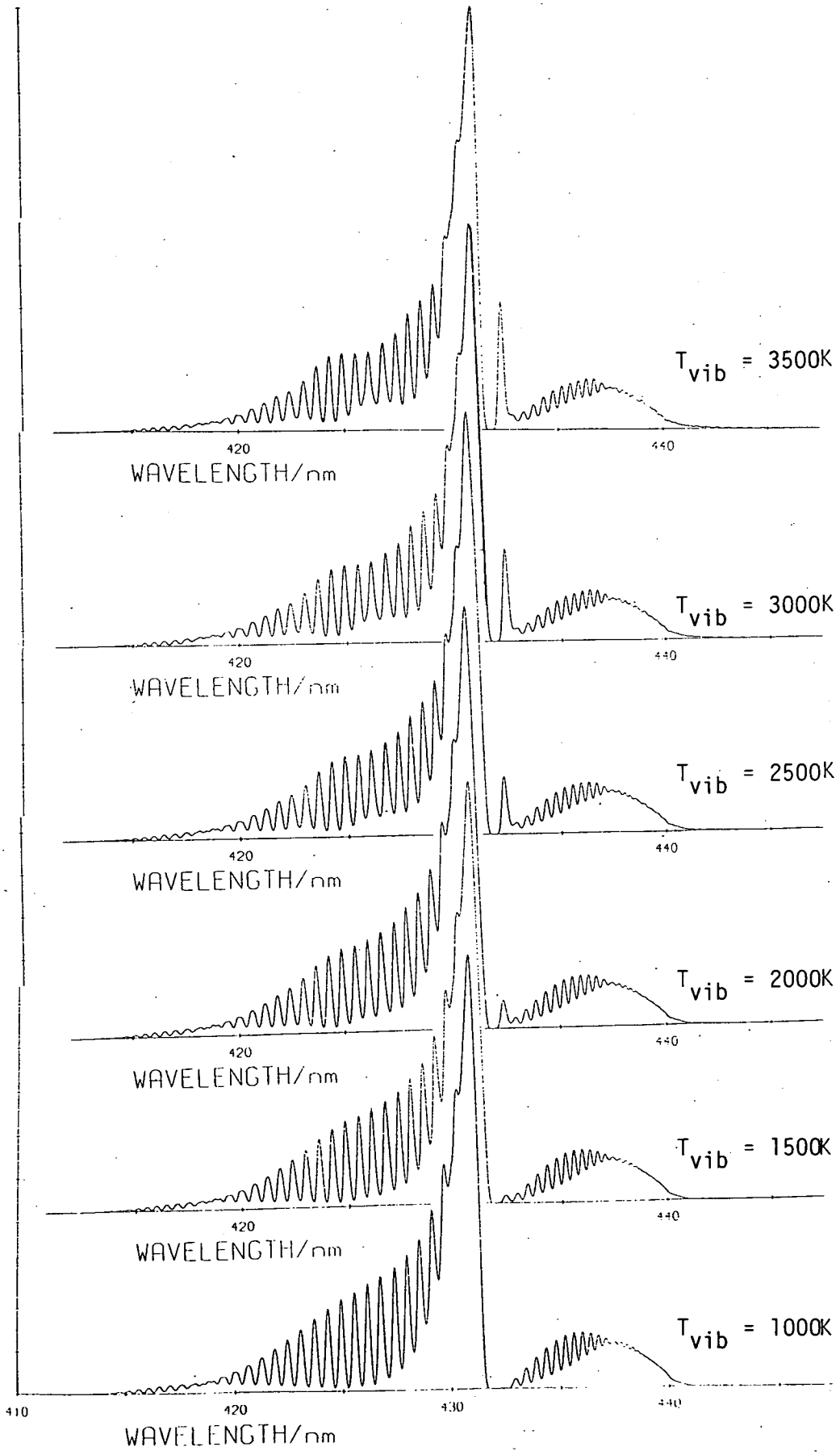

Figure 6.3 : Simulated CH($A^2\Delta \rightarrow X^2\Pi$) emission spectra illustrating the manifestation of increased vibrational excitation (T_{rot}=3000K).

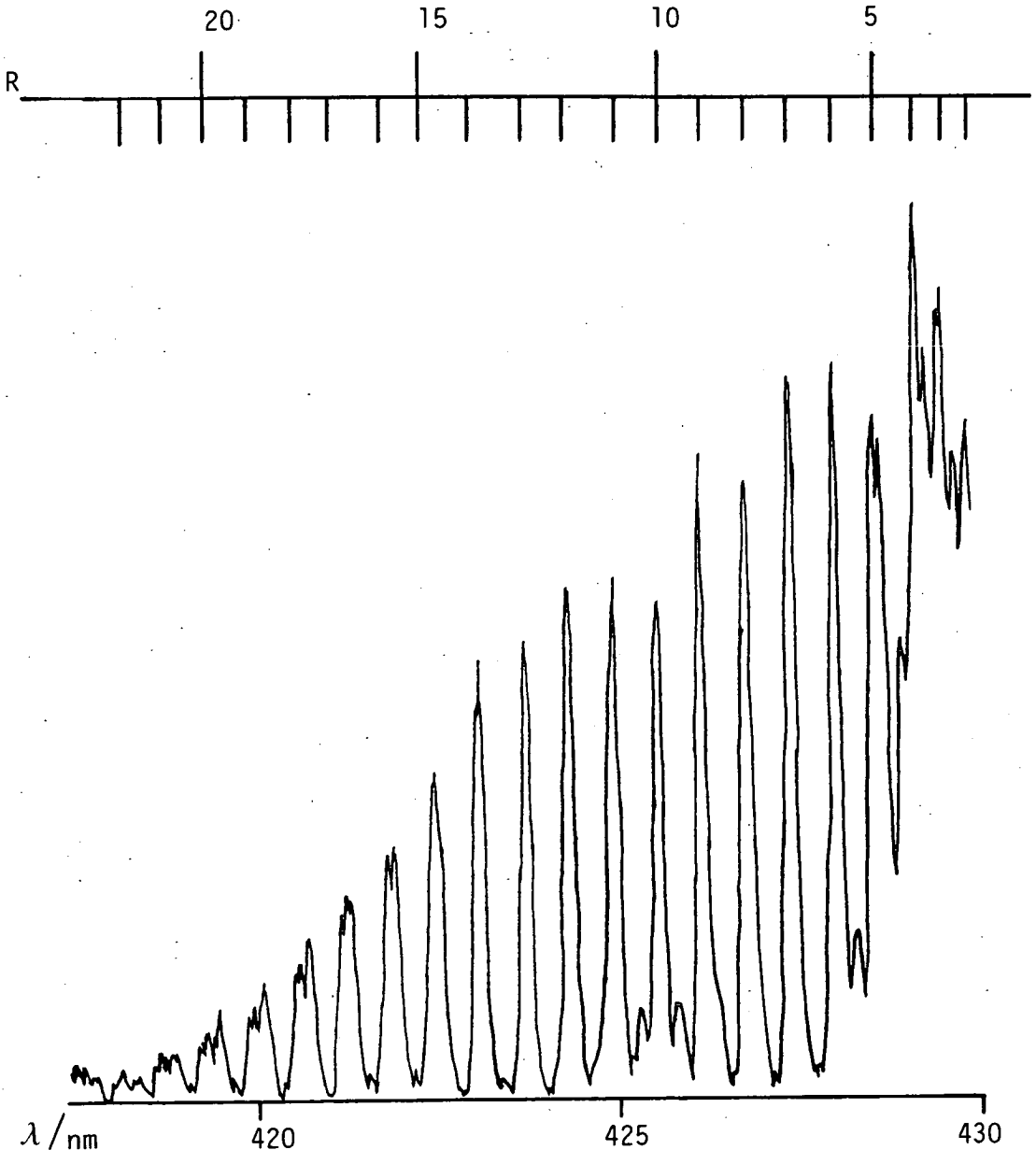

Figure 6.4 : R-branch of CH($A^2\Delta \rightarrow X^2\Pi$) photofragment fluorescence following ArF laser excitation of $CHBr_3$(p = 13.3Nm^{-2}, resolution = 0.13nm). The v=0 rotational levels are identified.

the lines : see Figure 6.5a.

c) C_2H_2

Acetylene is the simplest molecule from which CH radicals can be produced. The absorption spectrum is highly structured between 237nm (the onset of the $\tilde{A}^1A_u \longleftarrow \tilde{X}^1\Sigma_g^+$ transition)[153,154] and the ionization limit near 110nm.[155,156] In the 237-150nm region it consists of many weak, diffuse bands corresponding to the forbidden $\tilde{A}^1A_u \longleftarrow \tilde{X}^1\Sigma_g^+$ and $\tilde{B}^1B_u \longleftarrow \tilde{X}^1\Sigma_g^+$ transitions, with the $\tilde{B}^1B_u \longleftarrow \tilde{X}^1\Sigma_g^+$ origin occuring near 185nm.[157] Absorption of a single 193nm photon corresponds to excitation of a very high vibrational level of the $\tilde{A}^1A_u$ state and the resultant fluorescence is weak.[93]

The weak $CH(A^2\Delta \longrightarrow X^2\Pi)$ fluorescence which results from 193nm laser photolysis of C_2H_2 is shown in Figure 6.6. The $CH(A^2\Delta)$ emission is confined to the region 427-433nm, with the 'structure' to shorter wavelengths illustrating the noise level. Thus it can be concluded that $CH(A^2\Delta)$ is produced with very little internal excitation. It is noteworthy that, unlike the other precursors studied, C_2H_2 did not give rise to $CH(B^2\Sigma^- \longrightarrow X^2\Pi)$ or $CH(C^2\Sigma^+ \longrightarrow X^2\Pi)$ emissions. The anomalously high 'P-branch' intensity in Figure 6.6 at λ = 433-440nm is in fact assignable to the $\Delta v = -2$ progression of the $C_2(d^3\Pi_g \longrightarrow a^3\Pi_u)$ Swan bands[158].

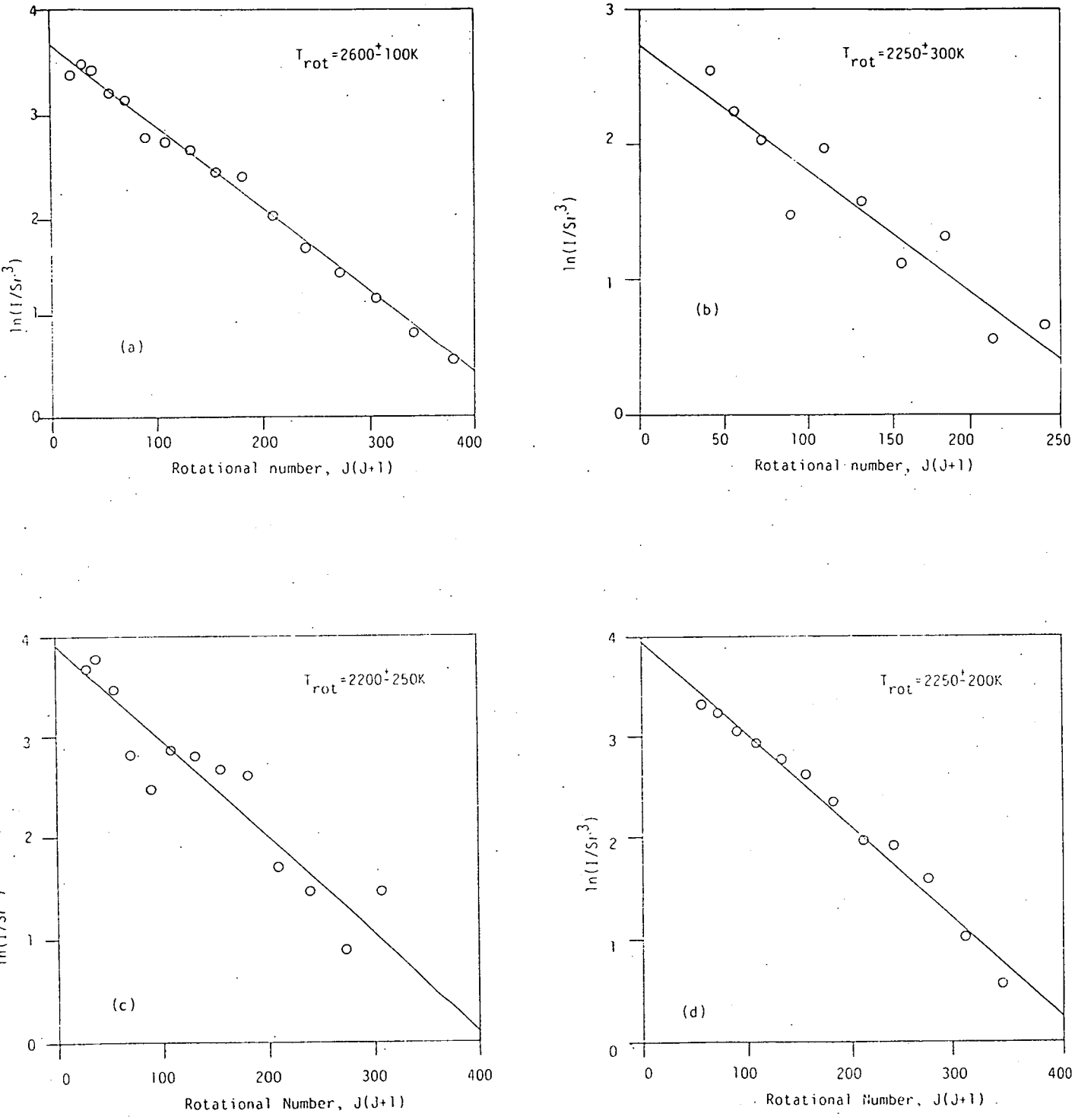

Figure 6.5 : Relative rotational populations of $CH(A^2\Delta$, v'=0), produced in the 193nm laser photolysis of (a) $CHBr_3$, (b) CH_3OH, (c) $(CH_3)_2CO$, and (d) CH_3NH_2, as a function of rotational quantum number, J(J+I).

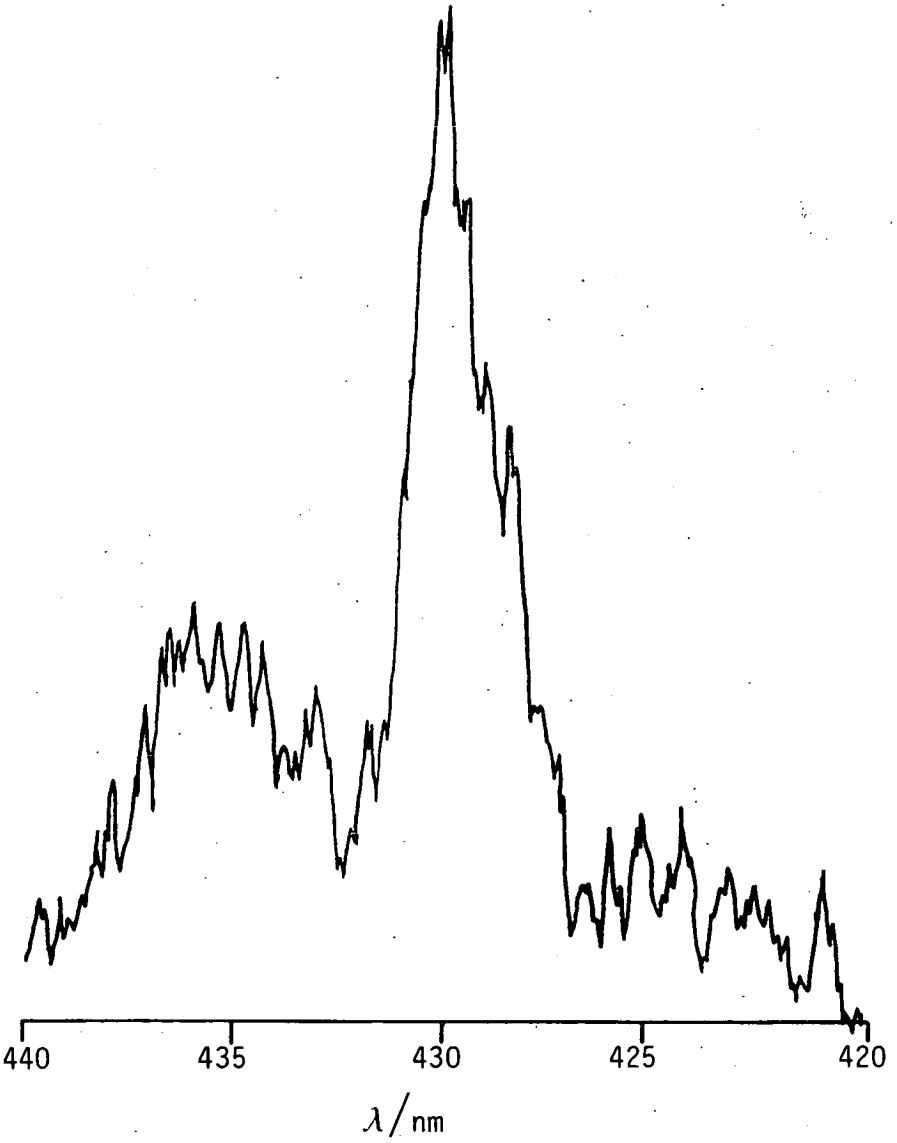

Figure 6.6 : $CH(A^2\Delta \rightarrow X^2\Pi)$ photofragment fluorescence following ArF laser photolysis of C_2H_2 ($p = 26.7 Nm^{-2}$). The intensity in the region 440-433nm is attributed to the $C_2(d^3\Pi_g \rightarrow a^3\Pi_u, \Delta v = -2)$ emission band.

(d) CH_3OH

Methanol shows only continuous absorption in the UV/vacuum UV region. It absorbs weakly at 193nm ($\epsilon \approx 125$)[159]. Figure 6.7 shows the $CH(A^2\Delta \longrightarrow X^2\Pi)$ fluorescence that results from 193nm laser photolysis of CH_3OH. The $CH(A^2\Delta)$ rotational temperature was determined to be 2250±300K (see Figure 6.5b), while an estimate of 1500-2000K can be made for the vibrational temperature.

(e) $(CH_3)_2CO$

Acetone has a moderately strong absorption in the near UV extending from 330-220nm which corresponds to the $A \longleftarrow X$ electronic transition. To shorter wavelengths there are three or four strong band groups. The ArF laser transition coincides with the first of these, the $B \longleftarrow X$ transition, which comprises sharp bands and extends from 194.5-179nm ($\log \epsilon \approx 3.5$ at 193nm).[160] Figure 6.8 shows the $CH(A^2\Delta \longrightarrow X^2\Pi)$ fluorescence that results from 193nm laser photofragmentation of $(CH_3)_2CO$. The intensity distribution of the rotational lines corresponds to a rotational temperature of 2250±200K (see Figure 6.5c), while an estimate of ~1500K can be made for the vibrational temperature.

(f) CH_2I_2

Methylene iodide absorbs strongly from ~350nm to shorter wavelengths,[152] and has four absorption bands extending through the UV. 193nm excitation coincides with the highest of these bands, and absorption is very strong ($\epsilon \approx 12000$

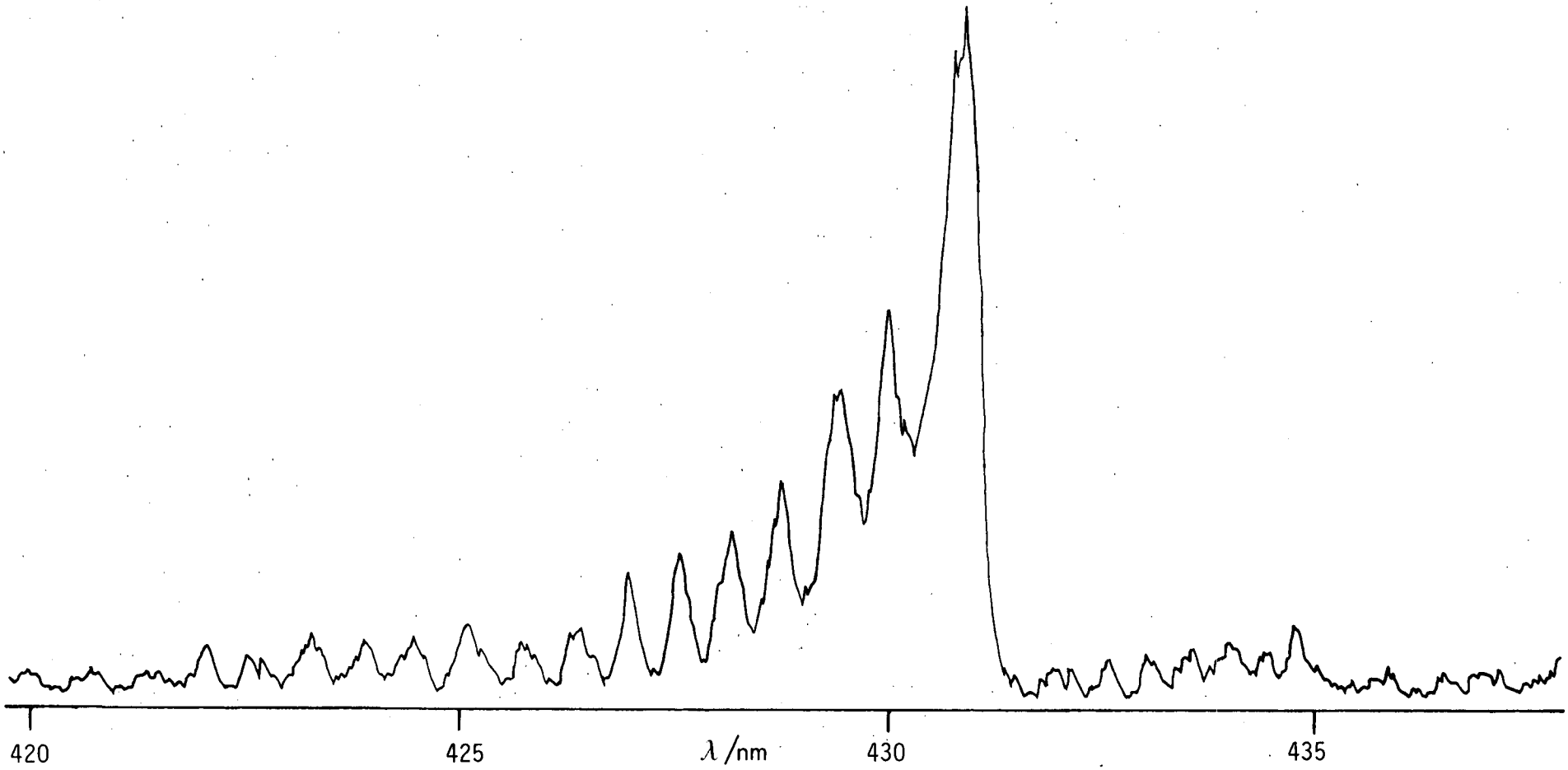

Figure 6.7 : $CH(A^2\Delta \rightarrow X^2\Pi)$ photofragment fluorescence following ArF laser excitation of CH_3OH ($p=13.3Nm^{-2}$).

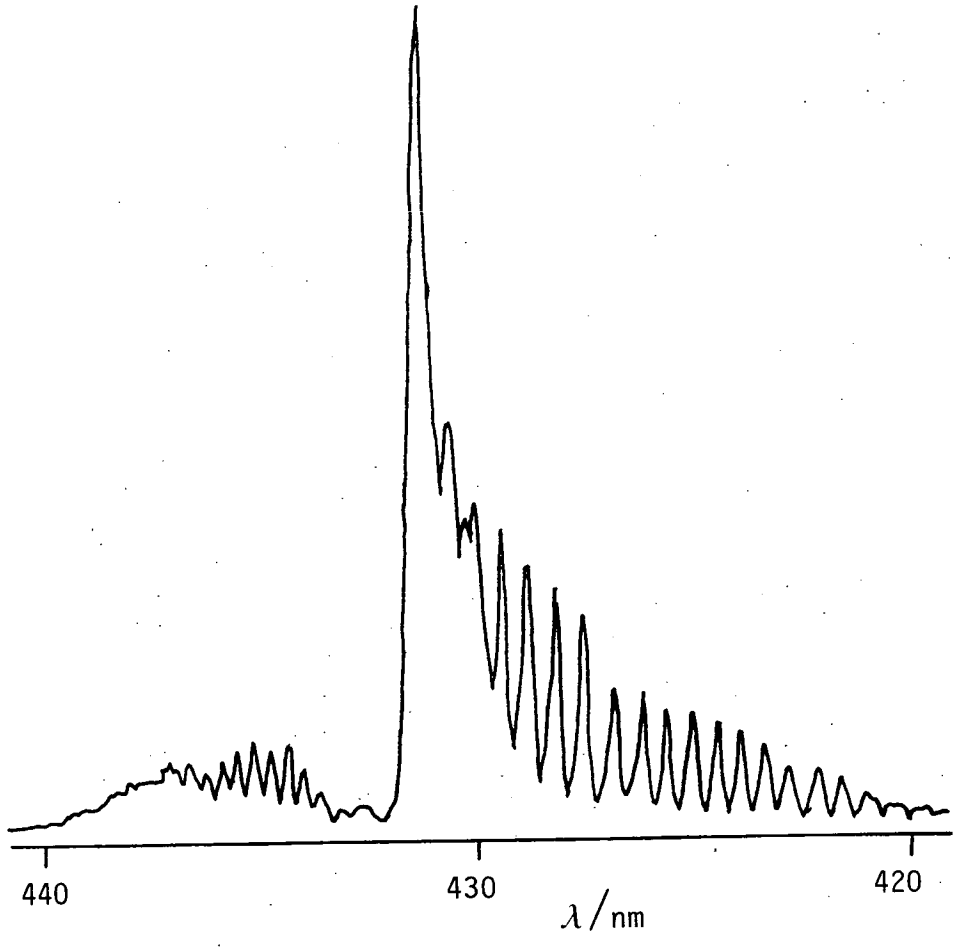

Figure 6.8 : $CH(A^2\Delta \rightarrow X^2\Pi)$ photofragment fluorescence following ArF laser excitation of $(CH_3)_2CO$ (p = 16Nm^{-2}, resolution = 0.2nm)

$l\ mol^{-1}cm^{-1}$).[161] Figure 6.9 shows the $CH(A^2\Delta \longrightarrow X^2\Pi)$ photofragment fluorescence which follows 193nm laser excitation of CH_2I_2. The spectrum was recorded in a single laser shot on an OMA (see section 2.7). It was necessary to record the spectrum in this way as I_2 is a product in the UV photolysis of CH_2I_2 at this wavelength, and itself gives rise to strong fluorescence when excited at 193nm (see Figure 1.6).

Although the resolution is insufficient for a graphical determination of the $CH(A^2\Delta)$ rotational temperature, the profile of the R-branch indicates that $T_{rot} \approx 3000K$. The relative intensity of the Q(2,2) band-head indicates a vibrational temperature of about 2000K.

(g) CH_3NH_2

Nishi and co-workers[94] have published a rotationally resolved $CH(A^2\Delta \longrightarrow X^2\Pi)$ emission spectrum, produced in the 193nm laser photolysis of CH_3NH_2. From this a $CH(A^2\Delta)$ rotational temperature of $2200 \pm 250K$ was ascertained : see Figure 6.5d.

(h) Other Precursors

All of the precursors discussed so far absorb to some degree at 193nm. Two molecules which are completely transparent at 193nm, but which are potential sources of CH radicals, were photolysed with an ArF laser. Of these, acetaldehyde gave an extremely weak fluorescence signal at 431nm, while acetonitrile did not yield CH(A). Therefore it appears that

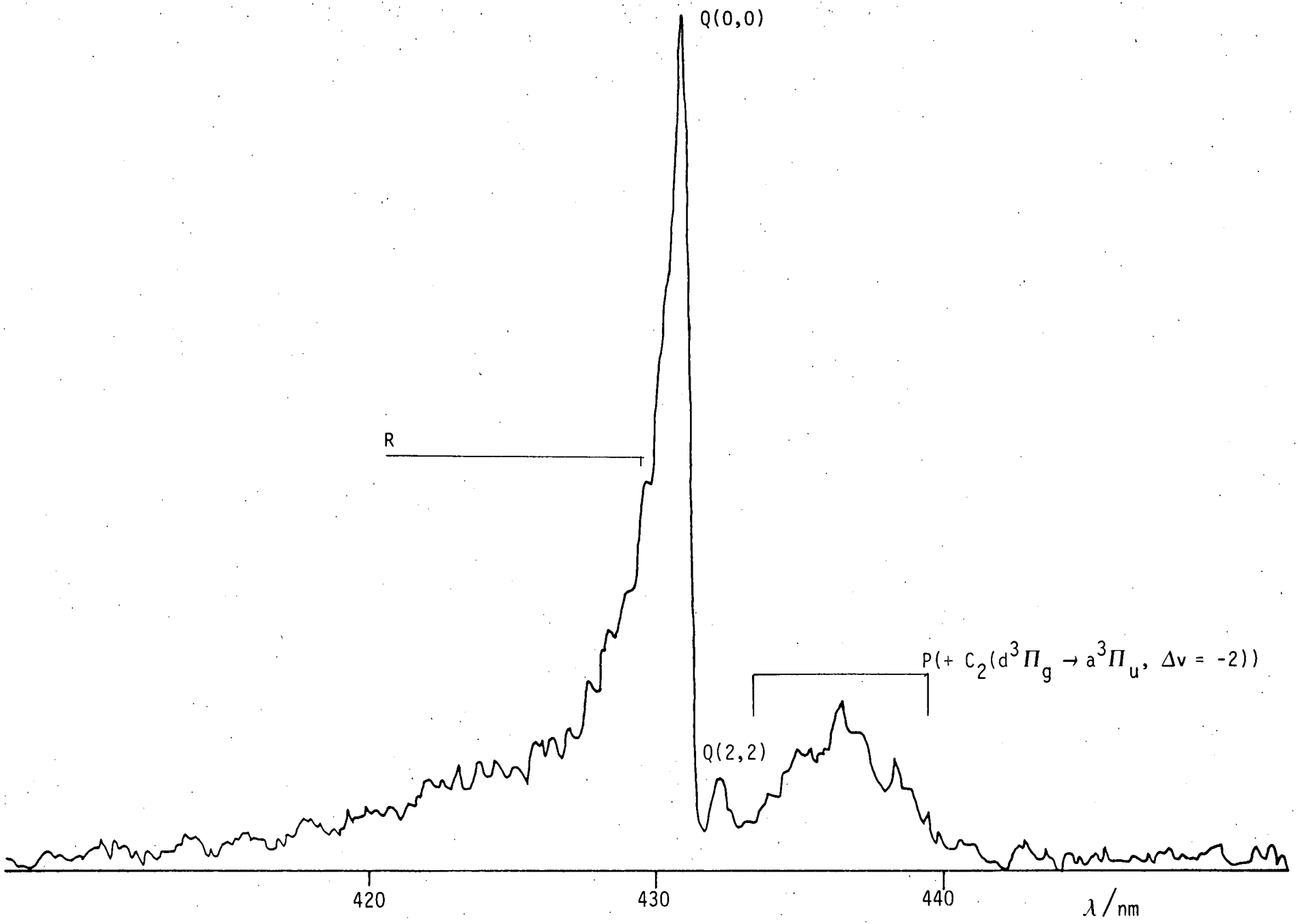

Figure 6.9 : $CH(A^2\Delta \rightarrow X^2\Pi)$ photofragment fluorescence following ArF laser excitation of CH_2I_2 ($p=13.3 Nm^{-2}$). Resolution ~ 0.35nm

purely simultaneous absorption processes are insignificant at the laser energies employed in these experiments.

6.3 DISCUSSION

The two most striking aspects of the $CH(A^2\Delta)$ internal energy distributions in these studies are : (1) with the possible exception of C_2H_2 the rotational level populations always correspond to Boltzmann distributions (in the temperature range 2000-3000K), and (2) invariably there is more energy partitioned into the rotational degrees of freedom than into the vibrational degree of freedom. C_2H_2, which gives rise to $CH(A^2\Delta)$ with very little internal excitation, will be dealt with later.

The fact that the rotational distributions appear Boltzmann, and may be assigned 'temperatures', implies statistical behavior of the internal energy of the precursor species. (Note that if $CH(A^2\Delta)$ production involves secordary photolysis of primary photofragments the precursor and parent molecule will be different species). Such distributions can be computed using formalisms such as Phase-space theory (PST)[162-167] or statistical adiabatic-channel theory (SACT)[168,169]. Both of these models assume statistical behaviour of internal energy in the precursor while they contain different assumptions

concerning the dynamical constraints associated with the fragmentation. In PST angular-momentum coupling together with the form of the radial potential describing the separating fragments are included. Due to lack of constraints on the range of the angular potential between separating fragments PST tends to predict similar values of T_{rot} and T_{vib}, sometimes in contrast to experimental observations (as is the case here). However SACT does contain a parameter which describes the range of the angular potential, and Beresford and co-workers[170] have used it successfully to reproduce their experimentally observed 'temperatures' ($T_{rot} \neq T_{vib}$) for $CN(X^2\Sigma^+)$ produced in the IR multiple-photon dissociation of CF_3CN. Therefore it is possible, using theories such as SACT, to account for internal energy distributions in photofragments such as have been observed in these experiments.

The similarity of the values of T_{rot} for a range of molecules, together with the consistent finding of $T_{rot} > T_{vib}$, suggests that a common route may be operative in the production of $CH(A^2\Delta)$ and that to some extent the internal energy distribution is independent of the parent molecule. A number of mechanistic proposals have been put forward for the production of CH* in the 193nm laser photolysis of molecules of the type CH_3X (X=halogen, OH, NH_2, etc.).

Fotakis and co-workers[88] favour a simultaneous two-photon

absorption into a doubly excited CH_3*X* state (see equation 1.9) which subsequently fragments to yield CH* and other products. The CH($A^2\Delta \longrightarrow X^2\Pi$) fluorescence intensity was found to depend quadratically upon the laser energy. Jackson and co-workers have also suggested a two-photon mechanism but with the precursor produced via sequential absorption[171], while another group[94] opt for a doubly excited precursor to CH* without specifying the absorption mechancism.

Although CH_3 is transparent to 193nm radiation,[172] Baronavski and co-workers[89] suggest that secondary photolysis of an intermediate methyl radical is the route to CH*, viz:

$$CH_3X + h\nu\ (\lambda = 193nm) \longrightarrow CH_3 + X \qquad -(6.2a)$$

$$CH_3 + h\nu\ (\lambda = 193nm) \longrightarrow CH^* + H_2 \qquad -(6.2b)$$

Nagata and co-workers[92] have managed to resolve the Λ-doublet components of the higher rotational levels of the R-branch in the CH($A^2\Delta \longrightarrow X^2\Pi$) emission spectrum following 193nm laser excitation of three methyl-containing molecules. On the basis of the unequal Λ-doublet intensities and the cubic power dependence of the emission intensity they have proposed that CH($A^2\Delta$) is produced through multiple processes where either CH_3, or CH_2, or both, are the precursors, viz:

$$CH_3X + h\nu \longrightarrow CH_3 + X \qquad -(6.3a)$$

$$CH_3 + 2h\nu \longrightarrow CH(A^2\Delta) + 2H \text{ (or } H_2) \qquad -(6.3b)$$

$$CH_3 + h\nu \longrightarrow CH_2 + H \qquad -(6.3c)$$

$$CH_2 + h\nu \longrightarrow CH(A^2\Delta) + H \qquad -(6.3d)$$

This last mechanism is most likely to be prevalent as it best explains the similarities in the internal energy disposals in $CH(A^2\Delta)$ produced from a range of methyl containing molecules, ie once the C-X bond has been broken the processes are identical except for the extent of internal excitation of the precursor fragment. The following arguments give additional support to this proposal.

Firstly, the differences in the $CH(A^2\Delta)$ rotational temperatures can be explained primarily by differences in the C-X bond strengths : if the C-X bond is weak (eg C-I, C-Br) there is a greater excess of energy available for disposal in the various degrees of freedom of the departing fragments. This excess energy will subsequently be transmitted to the secondary photofragments.

Secondly, it has been demonstrated in the photodissociation of CH_3I at 248 and 266nm :[173,174]

$$CH_3I + h\nu\ (\lambda = 248 \text{ or } 266nm) \longrightarrow CH_3^{\ddagger} + I \qquad -(6.4)$$

that internal excitation of the recoiling CH_3 group is exclusive to the $\nu 2$ out-of-plane ('umbrella') bending mode. As repulsive excited states are accessed in the 193nm excitation of the other molecules studied here, it seems likely that they will also produce $CH_3^{\ddagger}$ as a primary photofragment. $CH(A^2\Delta)$ could then be produced by some combination of processes 6.3b-d. Changes in the H-C-H bond angle upon going from parent molecule to CH_3 and/or CH_2 precursor fragments, coupled with excitation of bending modes such as the ν_2 'umbrella' mode of CH_3 or the ν_2 'scissors' mode of CH_2, will provide the torque necessary to excite rotation of $CH(A^2\Delta)$ as the fragments dissociate on a repulsive surface. Additionally, any change(s) in the equilibrium C-H bond length en route will favour vibrational excitation of $CH(A^2\Delta)$.

Thirdly, the phenomenon of unequal Λ-doublet populations, reported by Nagata and co-workers in the production of $CH(A^2\Delta)$ from CH_3X type molecules,[92] has also been observed in the production of $NH(c^1\Pi)$ following the VUV photodissociation of NH_3.[175] This is strong supporting evidence for the involvement of $CH_3^{\ddagger}$ in these photodissociation processes.

Fourthly, the parent species with the strongest (continuous) absorptions at 193nm gave rise to the greatest

$CH(A^2\Delta \longrightarrow X^2\Pi)$ emission intensities. Thus it is unlikely that simultaneous multiphoton absorption by the parent species plays a significant role in the production of $CH(A^2\Delta)$. The quadratic power dependence reported for the $CD(A^2\Delta \longrightarrow X^2\Pi)$ fluorescence intensity following 193nm laser photolysis of CD_3I[88] is probably the result of saturation of the primary absorption:

$$CD_3I + h\nu \ (\lambda = 193nm) \longrightarrow CD_3^{\ddagger} + I \qquad -(6.5)$$

in a 3-photon process (it is unlikely that a simultaneous mechanism is dominant as CD_3I absorbs strongly at 193nm).

Finally, this mechanistic proposal can be extended to cover $CH(A^2\Delta)$ production from all saturated parent species (ie of the type CH_2X_2 and CHX_3), which absorb to repulsive electronic states at 193nm, by invoking intermediate precursor fragments of the type CH_nX_{3-n} (pseudo-methyl) and CH_nX_{2-n} (pseudo-methylenic). The results for CH_2I_2 and $CHBr_3$ indicate that this is the case, and it has previously been suggested that this type of mechanism is operative in the flash photolysis of $CHBr_3$ [82] (see equation 6.1).

Results for unsaturated parent species are limited to C_2H_3CHO[91] and C_2H_2, neither of which fit the pattern observed for their saturated counterparts. McDonald and co-workers[93] have examined the production of $CH(A^2\Delta)$ from C_2H_2 in detail and concluded that a sequential 2-photon

mechanism, with a high vibrational level of the $\tilde{A}^1A_u$ state functioning as the resonant intermediate state, is most likely.

6.4 CONCLUSION

The dominant mechanism involved in the production of $CH(A^2\Delta)$ from parent species of the type CH_nX_{4-n} (n=1,2,3) is a 3-photon mechanism involving the secondary photolysis of CH_3 (CH_nX_{3-n}) and/or CH_2 (CH_nX_{2-n}) primary photofragments.

Parent species which absorb strongly at 193nm, such as $(CH_3)_2CO$ and CH_2I_2, are most suitable for kinetic studies on $CH(A^2\Delta)$ as they give rise to the greatest $CH(A^2\Delta \longrightarrow X^2\Pi)$ fluorescence intensities.

CHAPTER 7 - COLLISIONAL PROCESSES INVOLVING $CH(A^2\Delta)$

7.1 INTRODUCTION

This chapter is devoted to collisional processes involving $CH(A^2\Delta)$, subsequent to its production in the multiphoton dissociation of $(CH_3)_2CO$ and CH_2I_2. These processes fall into two categories ; inelastic and reactive.

Firstly, the rotational relaxation of $CH(A^2\Delta)$ by a range of molecules was studied. The experiments were carried out at the Rutherford Appleton Laboratory (RAL). Spectrally resolved $CH(A^2\Delta \rightarrow X^2\Pi)$ emission was recorded on an OMA, as detailed in section 2.7, following the 193nm laser photolysis of CH_2I_2 or $(CH_3)_2CO$ in the presence of increasing partial pressures of foreign gases. Changes in the rotational temperature of $CH(A^2\Delta)$ could be deduced from changes in the emission band contour. In this way, approximate collision numbers for the rotational deactivation of $CH(A^2\Delta)$ by He, Ar, SF_6 and H_2 were determined. The considerable convenience of being able to record entire fluorescence spectra from a single laser shot allowed a wide range of conditions to be explored efficiently and this compensated for the partial loss of resolution.

Following this, the removal of $CH(A^2\Delta)$ by a range of molecules was studied. These experiments were also carried out at RAL, and the experimental details are given in section 2.8.

7.2 ROTATIONAL RELAXATION OF $CH(A^2\Delta)$

RESULTS

Semi-quantitative investigations of the rotational relaxation of $CH(A^2\Delta)$ were made by adding increasing partial pressures of He, Ar, SF_6 and H_2 to the mixtures with CH_2I_2 undergoing photolysis. With the exception of H_2, none of these gases are efficient with regard to electronic quenching of $CH(A^2\Delta)$, with He being totally ineffective (see section 7.3). Increasing the CH_2I_2 pressure caused a decrease in the overall emission intensity without effecting any change in the band contour.

Figure 7.1 illustrates the effect of an added excess of He upon the $CH(A^2\Delta \rightarrow X^2\Pi)$ emission band contour. The nascent rotational distribution (dashed curve) corresponds to a rotational temperature of ca. 3000K while the distribution in the presence of $99kNm^{-2}$ of He (solid curve) corresponds to a rotational temperature of ca. 300K (ie thermalised). A gradual decrease in the rotational temperature was noted at intermediate He pressures, ie as the average number of collisions suffered by the $CH(A^2\Delta)$ radical during its effective lifetime increased (the effective lifetime takes account of removal by CH_2I_2, the rate constant for which was determined - see section 7.3). The rotational relaxation is manifest as a decrease in intensity in the high rotational levels of the P- and R-branches coupled with a red shift and sharpening of the Q-branch. As the distribution approaches

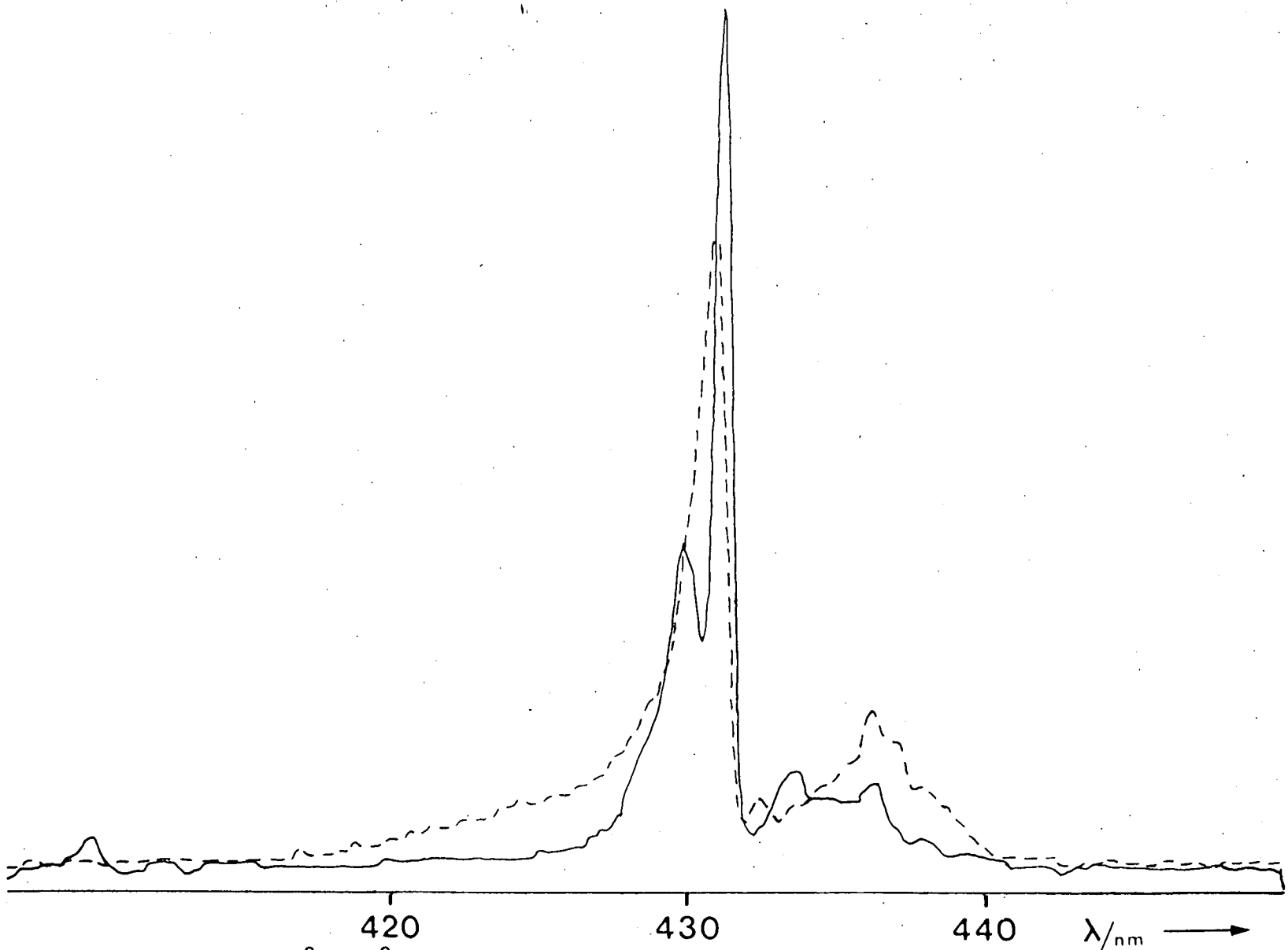

Figure 7.1 : $CH(A^2\Delta \rightarrow X^2\Pi)$ photofragment fluorescence following ArF laser excitation of CH_2I_2 ($p = 46.7 Nm^{-2}$), resolution ≈0.35nm. Dashed curve : no added gas. Solid curve : with $99 kNm^{-2}$ of added He.

room temperature the extent of overlap between the Q- and R-branches decreases, and eventually a gap appears between the branches at $\lambda \approx 430.5$nm. The R-branch in the solid curve of Figure 7.1 peaks at J=2, which is predicted for a rotational temperature of 300K.

No evidence was seen for a bimodal rotational distribution at intermediate pressures, however this may be due to the limited resolution available with the equipment. The total area under the curve remained constant within experimental error, reflecting the inefficient electronic quenching.

The results indicate that $99 kNm^{-2}$ of He is necessary to transform the rotationally hot spectrum ($T_{ROT} \approx 3000K$, $J_{MAX} \approx 8$) to the 'room temperature' spectrum ($T_{ROT} \approx 300K, J_{MAX}=2$) under the conditions employed. The average number of collisions suffered by a $CH(A^2\Delta)$ radical at this pressure (during its effective radiative lifetime) was calculated to be approximately 47 [176]. If this is considered as an average change in J after 47 collisions, bearing in mind that higher J states will relax less efficiently than lower ones due to the larger energy spacings involved, it can be deduced that ca. 8 collisions (since J_{MAX} changes from 8 to 2) are required for the loss of one rotational quantum from $CH(A^2\Delta, v'=0, J' \approx 8)$. The relative rotational relaxation efficiences of He and the other gases studied are given in Table 7.1 in terms of collision numbers, Z_R.

TABLE 7.1 : Collison numbers for the rotational relaxation of $CH(A^2\Delta, v'=0, J' \approx 8)$ by various foreign gases.

COLLISON PARTNER	Z_R
He	8
Ar	4
SF_6	5
H_2	3.5

The results obtained for rotational deactivation of $CH(A^2\Delta)$ by Ar and SF_6 were similar to those obtained with He. In both cases, however, lower pressures were necessary to promote a thermal distribution and some reduction in the overall emission intensity was observed at higher pressures indicating that electronic quenching, although inefficient, is operative with these collision partners. Figure 7.2 illustrates this for SF_6 as the added gas. Collision numbers, Z_R, for the rotational relaxation of $CH(A^2\Delta)$ by these gases can be found in Table 7.1.

Figure 7.3 shows the effect of increasing partial pressures of H_2 upon the $CH(A^2\Delta \rightarrow X^2\Pi)$ emission. It is clear that the removal of $CH(A^2\Delta)$ either by reaction or electronic quenching competes efficiently with rotational relaxation as the intensity of emission is greatly reduced before a significant change in the rotational distribution is observed. A value of Z_R=3.5 was obtained for the rotational relaxation of $CH(A^2\Delta)$ by H_2.

DISCUSSION

These data provide an interesting view of the rotational cascading that occurs as the initially hot rotational distribution relaxes towards the much cooler distribution associated with the translational degrees of freedom of the bulk sample. It should be borne in mind, however, that the results only reflect the net dissipation of rotational energy, and there will be contributions from collisions which

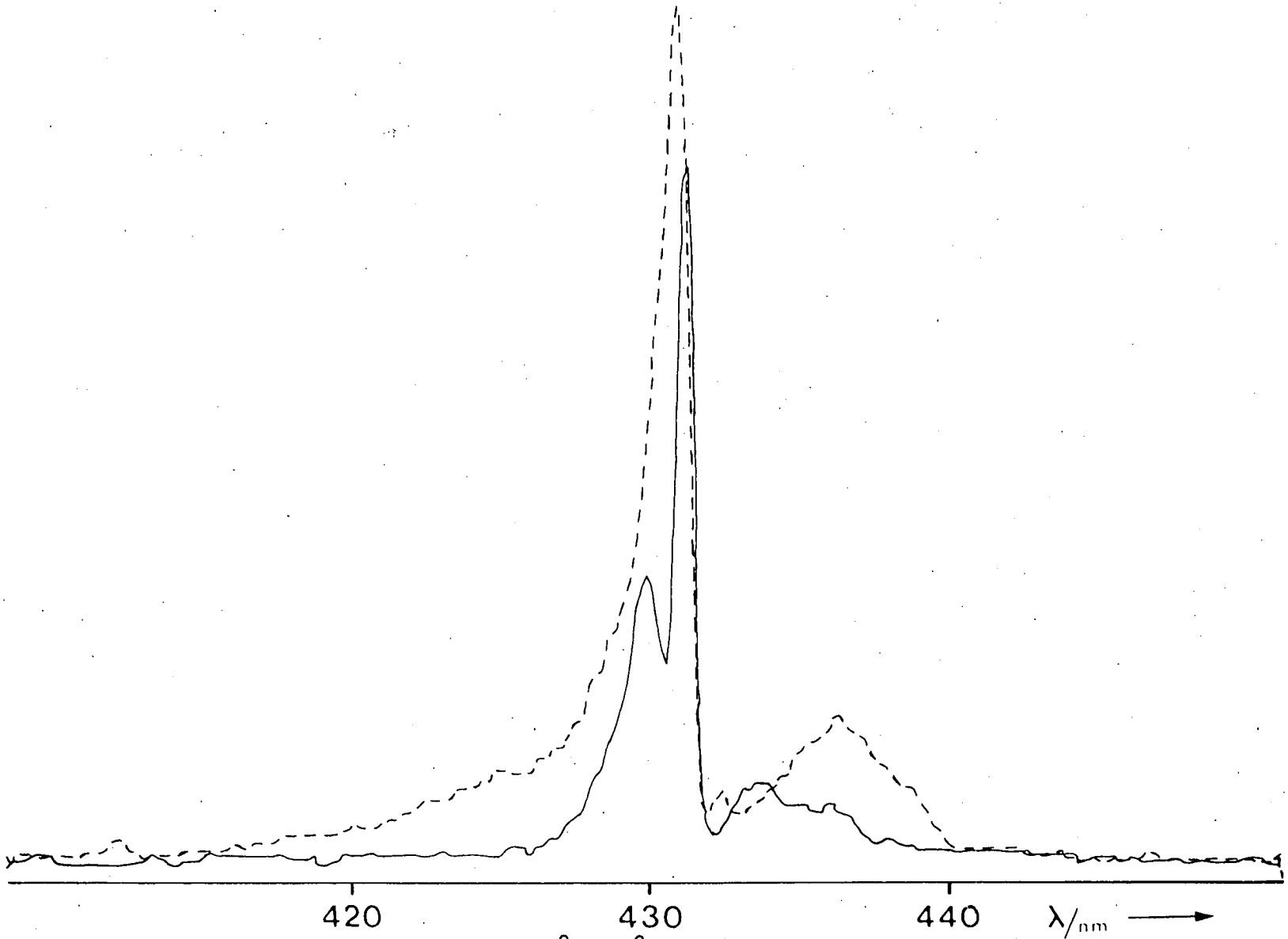

Figure 7.2 : Effect of added SF_6 on $CH(A^2\Delta \rightarrow X^2\Pi)$ photofragment fluorescence following ArF laser excitation of CH_2I_2 ($p = 13.3 Nm^{-2}$). Dashed curve : no added SF_6. Full curve : with $13.3 kNm^{-2}$ of SF_6 added.

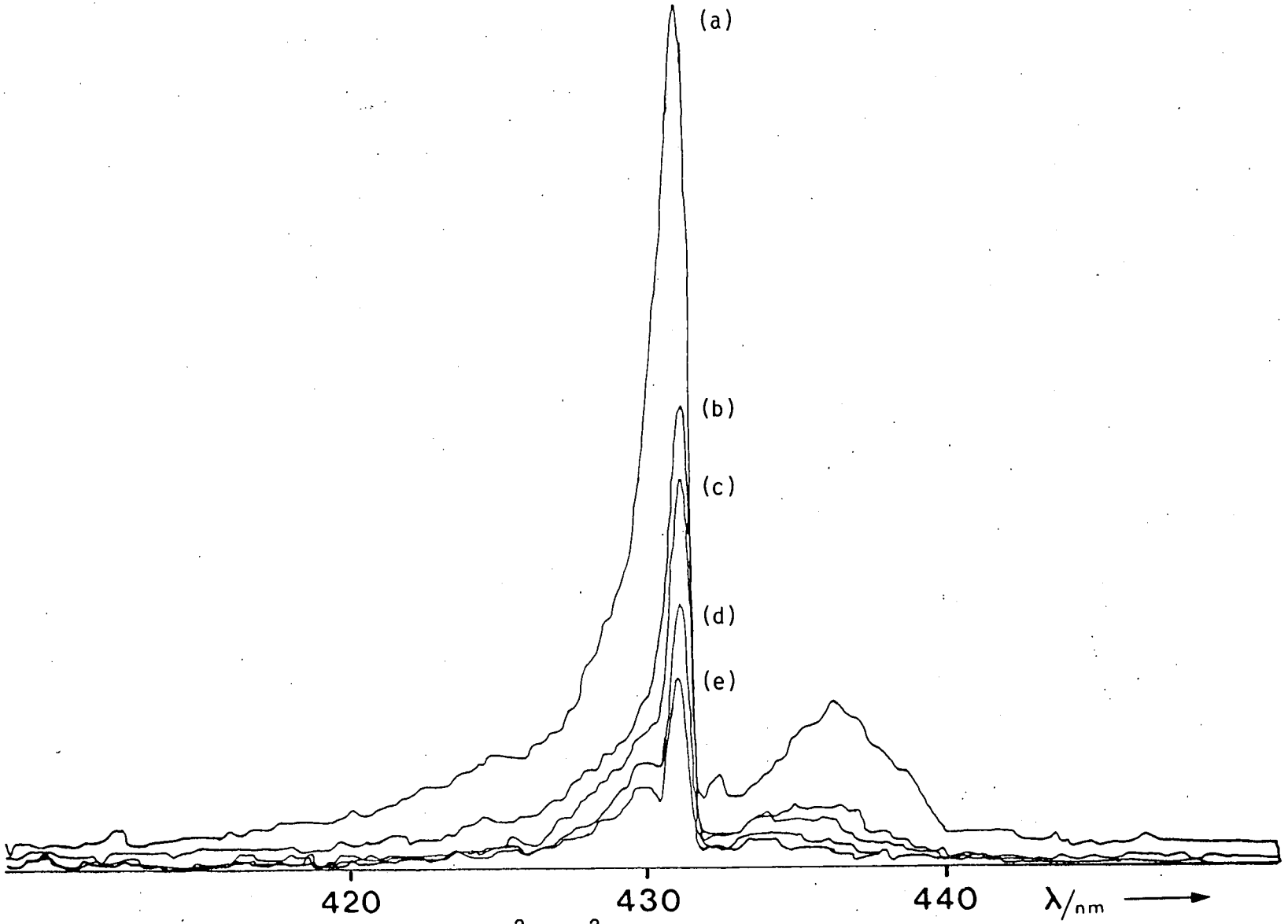

Figure 7.3 : Effect of added H_2 on $CH(A^2\Delta \rightarrow X^2\Pi)$ photofragment fluorescence following ArF laser excitation of CH_2I_2 ($p = 13.3 Nm^{-2}$). H_2 pressure : (a) 0, (b) $550 Nm^{-2}$, (c) $2.02 kNm^{-2}$, (d) $4.81\ kNm^{-2}$, (e) $8.25 kNm^{-2}$.

increase J. It is also likely that collisions giving rise to jumps of $|\Delta J| > 1$ will contribute, especially in collisions at low impact parameters. (Although multiple quantum transitititions occur most readily in heavier diatomics[9,177-179], transitions of $|\Delta J| \leq 3$ have been observed in collisions of $BH(A^1\Pi, v'=0)$ with He, Ar and H_2.[180])

Two reports on the rotational relaxation of $CH(A^2\Delta)$ by ranges of molecules, including He and Ar, have previously been published.[181,182] Brennen and Carrington[181] interpreted their spectra as the superposition of two Boltzmann distributions with the fraction of molecules in the low-temperature rotational distribution giving a measure of the extent of relaxation. However, their results have since been shown to be erroneous due to their misinterpretation of the $A^2\Delta \longrightarrow X^2\Pi$ emission spectrum[149], the apparent low temperature distribution being due to strong contamination of the R-branch by the Q-branch at wavelengths near 430nm.

Clerc and Schmidt[182], studying the rotational relaxation of $CH(A^2\Delta)$ produced in the pulsed radiolysis of C_2H_2 and CH_4, also mistakenly interpreted the 'hot' rotational distribution ($T_{ROT} \geq 4600K$) observed when C_2H_2 was used as the precursor as the superposition of two Boltzmann distributions. However, when CH_4 was used as the precursor, $CH(A^2\Delta)$ was produced at a much lower rotational temperature (T_{ROT} = 550K), in which case there is negligible overlap between the Q- and R-

branches. They estimated that 70 binary collisions with He are required, on average, to lower the rotational temperature of $CH(A^2\Delta)$ from 550K (J_{MAX} = 3) to room temperature (J_{MAX} = 2). This is an order of magnitude greater than the collision number obtained in this work.

The results presented herein indicate that Ar, SF_6 and H_2 all bring about rotational relaxation of $CH(A^2\Delta)$ very efficiently, while He is about half as efficient. This is somewhat surprising as high rotational transfer efficiencies are expected for He, relative to Ar and SF_6, on classical mechanical grounds. An improved efficiency is expected for H_2 in comparison to He due to the improved momentum matching, and this could account for the decrease in Z_R. In order to explain the observed behaviour more fully, factors other than the masses of the collision partners must be invoked. The most likely factors to consider are the range and anisotropy of the long-range interaction potentials, and the possibility of rotation-rotation or rotation-vibration energy transfer.

Perhaps the most surprising result is that for Ar. The high efficiency observed suggests that strong torques are experience by $CH(A^2\Delta)$ in the vicinity of Ar atoms and that the interaction potential is strongly anisotropic. This may be connected with the open shell structure of $CH(A^2\Delta)$ and the nature of the interaction between the carbon-end of the

radical and the collison partner. As well as interacting over a longer range than He atoms the larger Ar atoms are much more polarisable, making dipole-induced dipole interactions with the polar $CH(A^2\Delta)$ species possible contributors to the overall relaxation process.

The high efficiency with which SF_6 rotationally relaxes $CH(A^2\Delta)$ is almost certainly due to contributions from rotation-vibration energy transfer processes. This will result from the extremely high density of states of the SF_6 molecule.[183]

Three factors are likely to contribute to the improved efficiency observed for H_2 in comparison with He : (1) the (previously mentioned) improved momentum matching, (2) the strongly anisotropic interaction potential, and (3) the possibility of rotation-rotation energy transfer. From the observation of a cool 300K rotational distribution in the presence of $8kNm^{-2}$ of H_2 is can be concluded that either the high J levels are removed by electronic quenching more rapidly than lower J levels (thus removing the emission from the high rotational component) or that rotational relaxation from high J into low J levels occurs at a rate which is at least comparable to the rate for total removal of $CH(A^2\Delta)$ with a rotational temperature of 300K. The rate constant for the removal of $CH(A^2\Delta)$ has been determined as $8.8 \times 10^{-12} cm^3 molec^{-1} s^{-1}$ (see section 7.3). Therefore, the second proposal implies an average collison number, $Z_R \leq 20$, for

rotational relaxation by H_2. The value obtained, Z_R = 3.5, is compatible with this, more likely proposal.

Generally, the observed pattern of relaxation can be accounted for by assuming that deactivation occurs predominantly by small changes in J ($|\Delta J|=1$), and that the probability of energy transfer decreases with increasing J according to a law such as Polanyi's Exponential Law[184] which states that the transfer probability is proportional to $\exp(-\Delta E)$, ΔE being the energy defecit. The absence of sharp peaking at intermediate J in the course of relaxation by this mechanism is due to the fact that the rate of transfer into the intermediate levels is slower than the rate of transfer out of them. Consequently, the populations in intermediate J levels cannot accumulate.

7.3 KINETICS OF $CH(A^2\Delta)$ REMOVAL PROCESSES

RESULTS

Figure 7.4 shows a typical $CH(A^2\Delta \longrightarrow X^2\Pi)$ photofragment fluorescence decay. The fluorescence intensity (I_f) is sufficient to allow single-shot observations with a good signal-to-noise ratio. The decay of $CH(A^2\Delta)$, which is formed during the laser pulse, is a smooth exponential and is

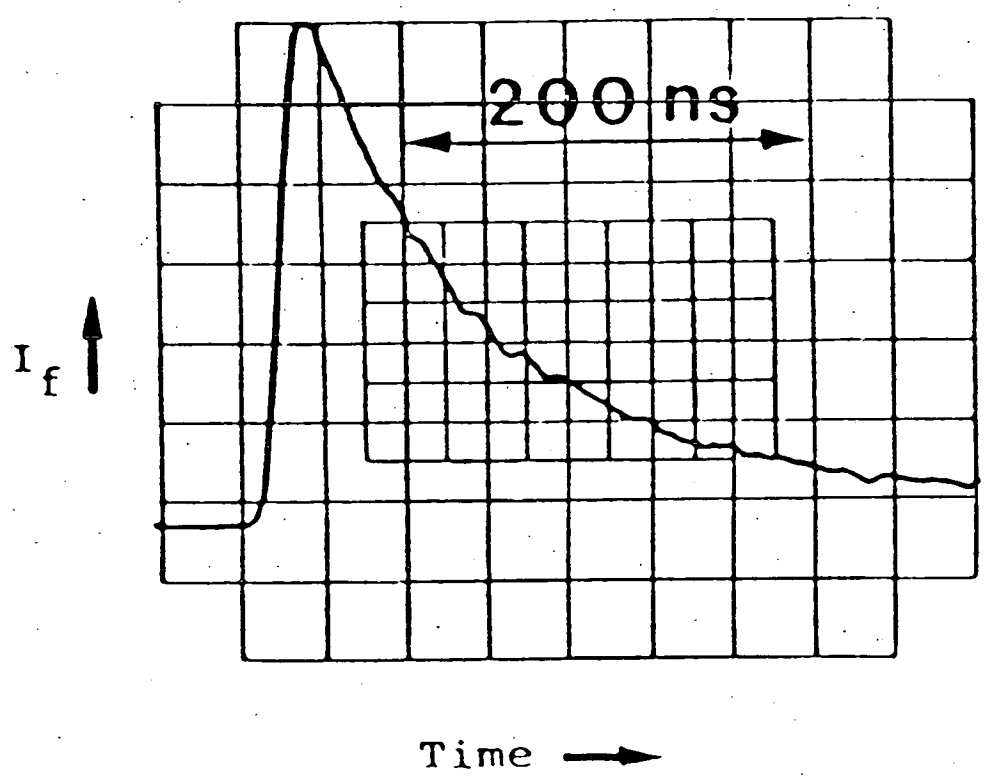

Figure 7.4 : Decay of $CH(A^2\Delta)$, produced by ArF laser excitation of $(CH_3)_2CO$ ($P_{(CH_3)_2CO}$ = 21 Nm^{-2}, P_{H_2} = 62Nm^{-2}.)

dominated by radiative removal in the absence of added quenching gas. The effect of added reactive or quenching gas is to shorten the decay, as illustrated by the first-order plots in Figure 7.5 for increasing pressures of CH_4. The first-order rate constants thus derived are plotted against CH_4 pressure in Figure 7.6, the gradient of which yields a value of $(2.0\pm0.1)\times10^{-11}cm^3molec^{-1}s^{-1}$ for the absolute rate constant for the total removal of $CH(A^2\Delta)$. The rate constants determined in this work, together with rate constants for the removal of ground state CH, are summarised in Table 7.2.

The first-order rate constants used to construct Figure 7.7 were determined in an identical manner to that described above, excepting the use of CH_2I_2 rather than $(CH_3)_2CO$ as the precursor to $CH(A^2\Delta)$. A value of $(1.9\pm0.1)\times10^{-11}cm^3molec^{-1}s^{-1}$ was obtained for the removal rate constant with CH_4. The agreement between the two values is excellent, indicating that the kinetics are independent of the precursor used.

Figure 7.8 illustrates the graphical determination of the rate constant for the removal of $CH(A^2\Delta)$ by CH_2I_2. The effective lifetimes of $CH(A^2\Delta)$ at the CH_2I_2 pressures used in the rotational relaxation studies (previous section) were obtained from the best fit straight line through the data points. The intercept corresponds to a pure radiative lifetime of 435 ± 98ns (2σ error). Given the large uncertainty, this is in reasonable agreement with the most

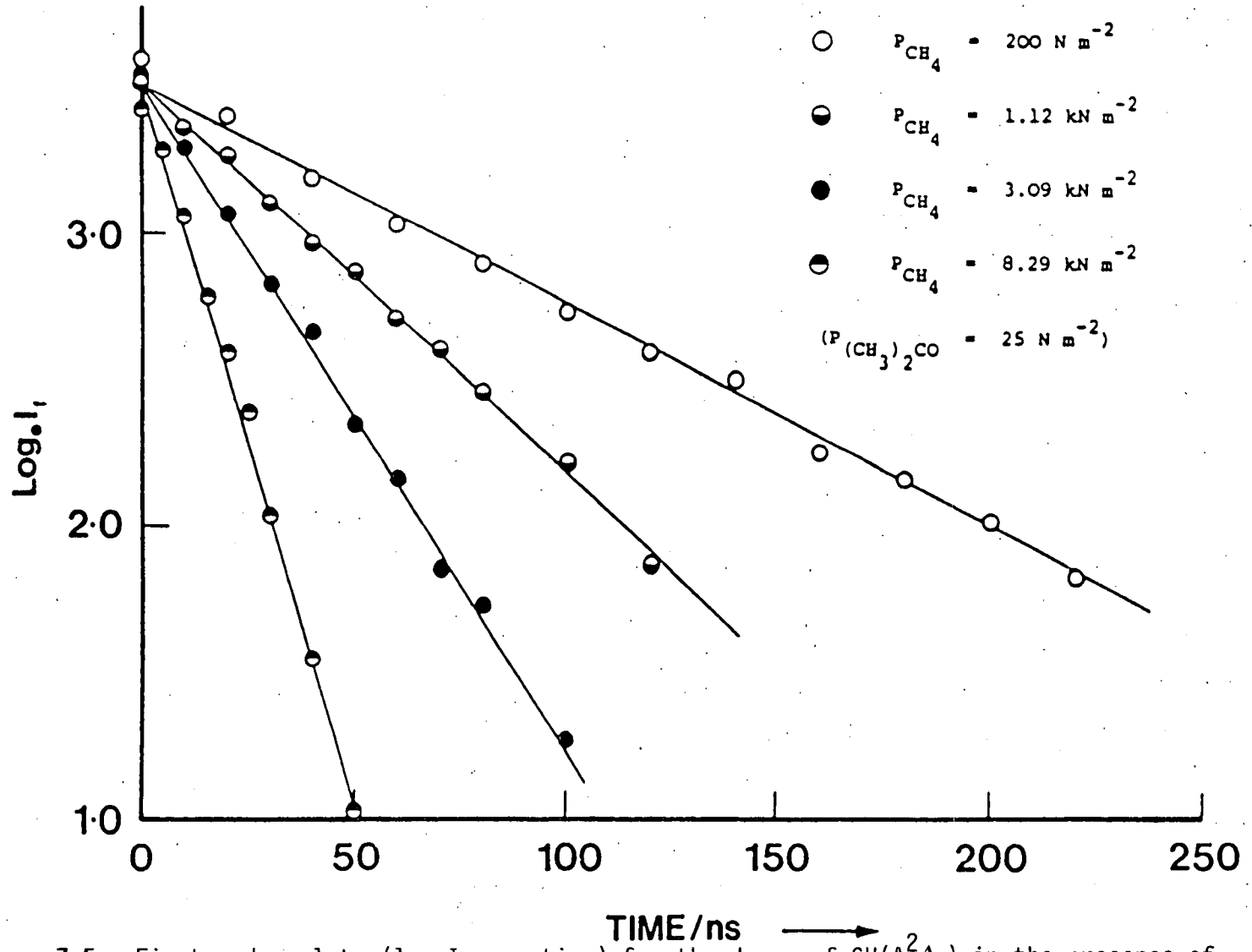

Figure 7.5 : First-order plots ($\log_e I_f$ vs. time) for the decay of $CH(A^2\Delta)$ in the presence of increasing pressures of CH_4.

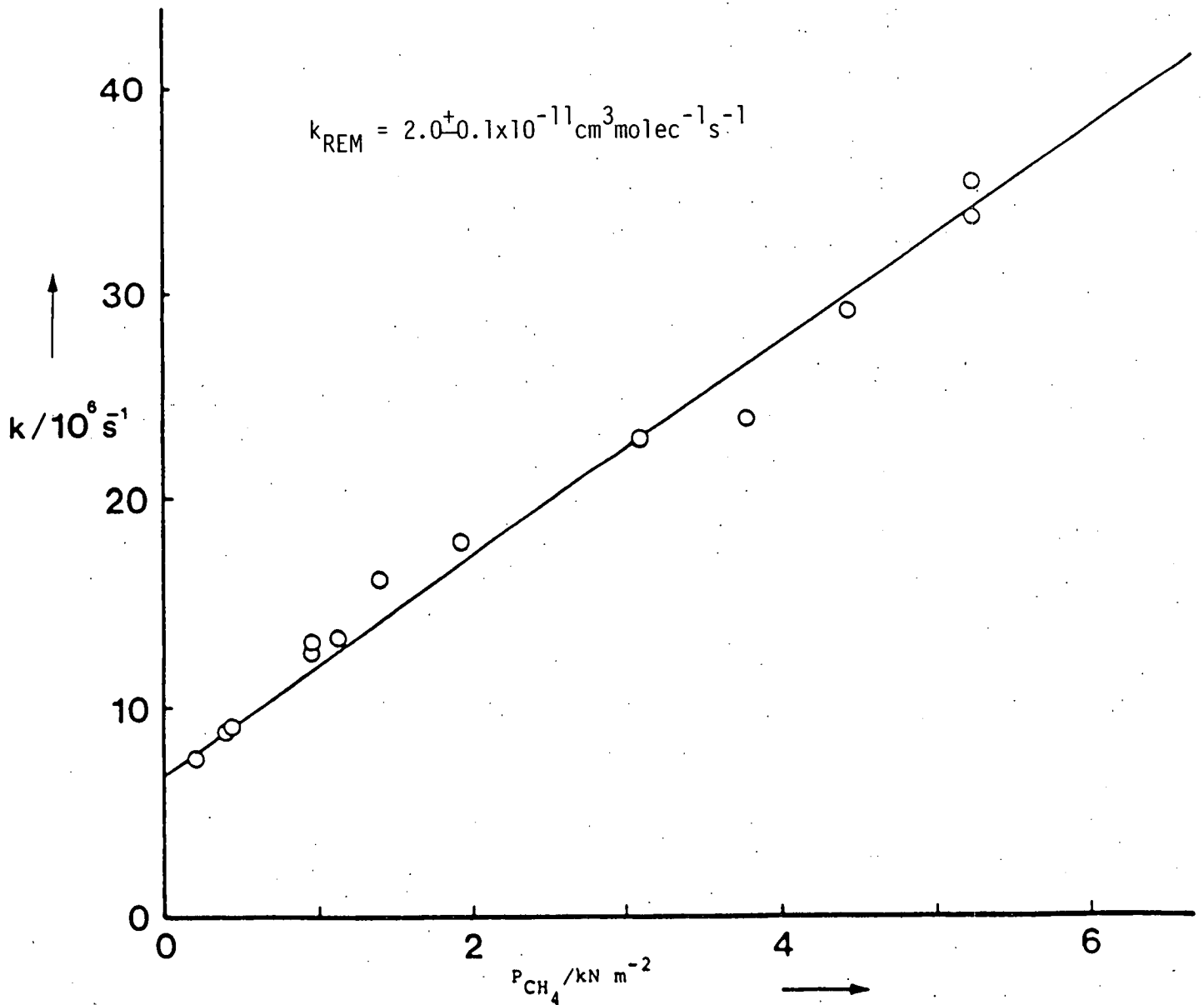

Figure 7.6 : Plot of first-order rate coefficients for quenching of $CH(A^2\Delta)$ against pressure of added CH_4. (Acetone as $CH(A^2\Delta)$ precursor).

TABLE 7.2 : Second-order rate constants for the removal of $CH(A^2\Delta)$ and $CH(X^2\Pi)$ by various reactant/quenching gases.

REACTANT/QUENCHING GAS	$CH(A^2\Delta)$ $k/cm^3molec^{-1}s^{-1}$	$CH(X^2\Pi)$ $k/cm^3molec^{-1}s^{-1}$	SOURCE OF CH(X) DATA
CH_2I_2	$7.9\pm0.6\times10^{-10}$		
CH_4	$1.9\pm0.1\times10^{-11}$ [a] $2.0\pm0.1\times10^{-11}$ [b]	$3.0\pm1.0\times10^{-10}$ $1.0\pm0.3\times10^{-10}$ $1.02\pm0.04\times10^{-10}$	82 62 84
H_2	$8.8\pm1.7\times10^{-12}$ [a] $8.5\pm0.4\times10^{-12}$ [b]	$2.3\pm0.5\times10^{-11}$ $2.63\pm0.5\times10^{-11}$ $1.4\pm0.1\times10^{-11}$	82 62 85
O_2	$1.10\pm0.04\times10^{-11}$ [b]	$5.9\pm0.8\times10^{-11}$ $3.3\pm0.4\times10^{-11}$ $8\pm3\times10^{-11}$	62 79 186
N_2	$4.1\pm0.5\times10^{-13}$ [a]	$7.7\pm2.0\times10^{-13}$ $3.9\pm0.3\times10^{-13}$ $6.3\pm1.3\times10^{-13}$	82 86 83
He	0 [a]		
Ar	$1.6\pm0.7\times10^{-13}$ [a]		
SF_6	$5.9\pm1.1\times10^{-13}$ [a]		

a This work - CH_2I_2 as parent species

b This work - $(CH_3)_2CO$ as parent species

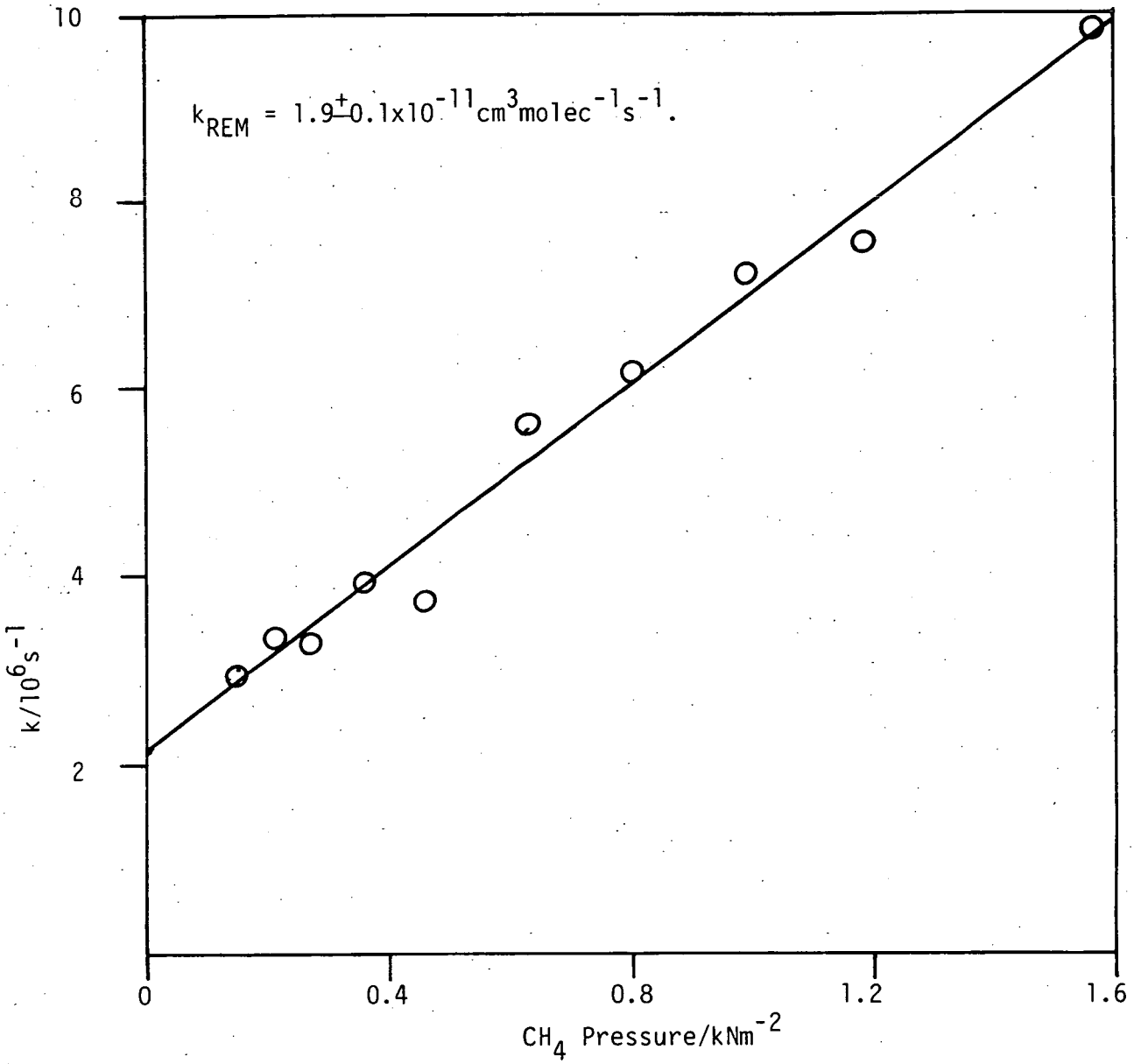

Figure 7.7 : Plot of first-order rate coefficients for quenching of $CH(A^2\Delta)$ against pressure of added CH_4. (CH_2I_2 as $CH(A^2\Delta)$ precursor)

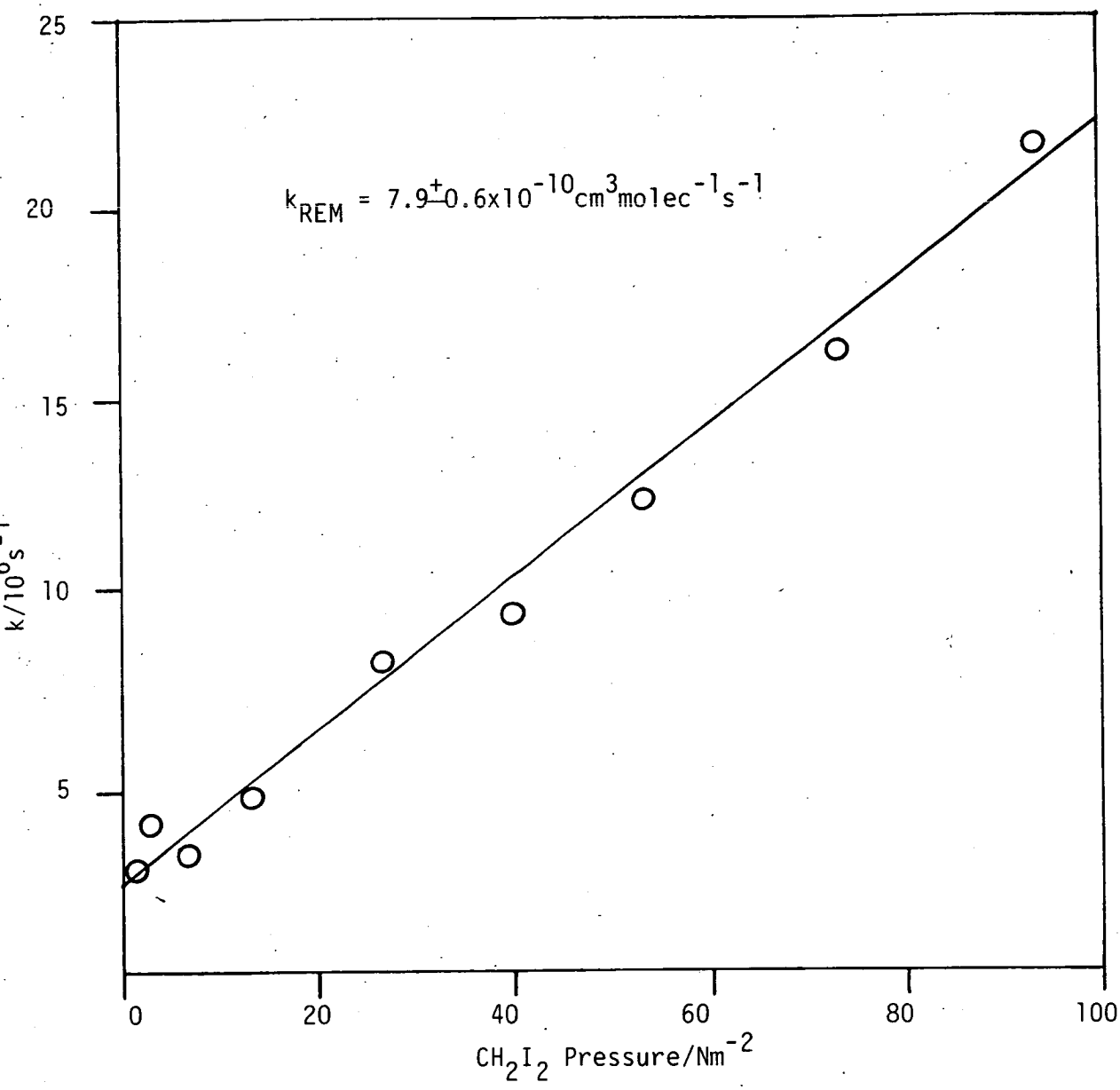

Figure 7.8 : Plot of first-order rate coefficients for quenching of $CH(A^2\Delta)$ against pressure of CH_2I_2

reliable values reported in the literature (for the v'=0 level) of 534 ± 5ns[172] and 537.5 ± 5ns[185].

DISCUSSION

A more detailed study of the temperature and pressure dependencies of the reactions of $CH(A^2\Delta)$ would be necessary in order to establish the nature of the reactive/quenching interaction. However, the data do provide an interesting comparison with $CH(X^2\Pi)$ kinetic data which is relatively abundant in the literature.

The data on $CH(X^2\Pi)$ represent the rates of reaction with the molecules in question. However, the data on $CH(A^2\Delta)$ removal represent contributions from both physical quenching and reactive processes, and thus only give upper limits for the chemical reaction rates. It is apparent from Table 7.2 that the reactions of $CH(A^2\Delta)$ with CH_4, H_2 and O_2 are significantly slower than those of $CH(X^2\Pi)$. As the internal energy content of $CH(A^2\Delta)$ is greater than that of $CH(X^2\Pi)$ by ca. 2.9eV, the explanation for this behaviour must lie in the electronic configurations of the two states : $(1s\sigma)^2(2s\sigma)^2(2p\sigma)^2(2p\pi)$ for the ground state, $(1s\sigma)^2(2s\sigma)^2(2p\sigma)(2p\pi)^2$ for the A-state. This means that the shapes of the potential surfaces are the controlling factors in these reactions. It is well established for atomic reactions that the symmetry of the collision intermediate is of paramount importance in determining the reactivity of individual electronic states, while the total

energy content is of secondary importance.[187] Although there are relatively large numbers of degrees of freedom associated with the collision intermediates in the reactions under study (cf atomic systems), symmetry considerations are still prevalent.

The data for the less/non reactive gases (N_2, He, Ar and SF_6) indicate that $CH(A^2\Delta)$ is relatively stable to physical quenching. The removal rates for both electronic states with N_2 are similar in magnitude and this again must relate to the potential energy surfaces. Nokes and Donovan[188] have noted a broadly parallel kinetic behaviour for $CH(A^2\Delta)$, $CH(X^2\Pi)$ and the equivalent united atom state, $N(^2D)$, with the order of reactivity $CH(X^2\Pi) > CH(A^2\Delta) > N(^2D)$.

The mechanistic possibilities which could be considered for these reactions include insertion into bonds, addition across unsaturated bonds, and direct abstraction. The mechanism proposed by Berman and Lin[84] for the reaction of $CH(X^2\Pi)$ with saturated hydrocarbons and H_2 involves the formation of a chemically activated, radical intermediate by insertion through a loose transition state. In the case of hydrocarbons this is followed by fragmentation of the adduct to form more stable reaction products. Wagal and co-workers[83] have proposed that the removal of $CH(X^2\Pi)$ by N_2 is due to collisional stabilization of an intermediate HCN_2 complex, most likely of C_{2v} symmetry. This corresponds to

addition across the unsaturated N N bond. If these proposals are correct the implication is that symmetry considerations favour CH($X^2\Pi$) over CH($A^2\Delta$) for insertion into σ bonds, while there is little discrimination between the two states for addition across the N≡N bond.

7.4 CONCLUSION

Rotationally hot CH($A^2\Delta$) radicals are relaxed more efficiently by H_2, Ar and SF_6 than by He. Therefore classical collision theory (ie momentum matching) is not applicable to these inelastic processes. The observed pattern of relaxation can be interpreted by assuming that deactivation occurs by small changes in J, and that the probability of energy transfer decreases with increasing J.

In general, CH($A^2\Delta$) is not efficiently removed by reactive or non-reactive (quenching) gases. With the exception of CH_2I_2, for each reactive gas studied the rate constant for removal of CH($A^2\Delta$) is less than that for the ground electronic state, CH($X^2\Pi$). This indicates that the reactivities of the species are determined principally by the symmetry of the collision intermediate, rather than the internal energy content.

The resilient nature of CH($A^2\Delta$), to both chemical and physical quenching processes, provides at least a partial

explanation for the wide ranging observations of fluorescence from this state under what would generally be regarded as chemically hostile conditions.

APPENDIX 1 : ANNOTATED COPY OF COMPUTER PROGRAM

USED TO SIMULATE CH($A^2\Delta \rightarrow X^2\Pi$) SPECTRA.

```
C      SIMULATION OF CH(A-X) EMISSION SPECTRUM
C      ***************************************
C
C    This program computes the spectrum of the CH(A-X) electronic transition.
C    The first section calculates the Rotational Term Values (RTV) in the ground
C    (X:ST=1) and 1st excited (A:ST=2) electronic states.
      IMPLICIT DOUBLE PRECISION(A-H,O-Z)
      INTEGER K,V,ST,SI,F,BR,A,B,KO,K1,K2,RB,ZEROS,POINTS,PT
      INTEGER TEMPBR,TEMPK,TEMPV
      DOUBLE PRECISION VO,L,G,LA,BV,DV,Y,RTV,WL,U,C,S,P,T,I,CF,H,SOL,KB
      DOUBLE PRECISION E,IMAX,WLMIN
      CHARACTER*20 OUTPUT
      DIMENSION L(2),G(2),LA(2),BV(0:2,2),DV(0:2,2),Y(0:2,2)
      DIMENSION U(2,35,0:2,2),C(2,35,0:2,2)
      COMMON/BLOCK1/WL(20,35,0:2),RTV(4,35,0:2,2)
      COMMON/BLOCK2/CF,VO(0:2)
      COMMON/BLOCK3/S(10,35,0:2),I(20,35,0:2),P(0:2),T(0:2),E,IMAX
C    In the following calculations the Quantum Numbers / Constants /
C    / Variables used are :
C     K = Total angular momentum apart from spin.
C     V = Vibrational quantum number.
C     L = Component of electronic angular momentum along internuclear axis.
C     Y = Measure of strength of the spin-orbital coupling.
C     BV/DV = Rotational constants dependent on V.
C     G = Measure of strength of spin splitting.
C     LA = Measure of strength of Lambda-type doubling.
C     ST = Electronic state.
C     SI = Sign (+/-) : upper and lower levels from spin-orbital coupling.
C     F = Label of rotational sublevel (see later).
C     P = (Relative) Population of vibrational level.
C     T = Rotational temperature.
C     H = Planck's constant.
C     SOL = Speed of Light (cm/s).
C     KB = Boltzmann constant.
      DATA L(1)/1.0/L(2)/2.0/G(1)/-0.016/G(2)/0.021/LA(1)/0.036/LA(2)/0/
      DATA BV(0,1)/14.19/BV(1,1)/13.655/BV(2,1)/13.122/
      DATA BV(0,2)/14.577/BV(1,2)/13.907/BV(2,2)/13.182/
      DATA DV(0,1)/1.432D-3/DV(1,1)/1.39D-3/DV(2,1)/1.39D-3/
      DATA DV(0,2)/1.564D-3/DV(1,2)/1.58D-3/DV(2,2)/1.65D-3/
      DATA Y(0,1)/2.0/Y(1,1)/2.0/Y(2,1)/2.0/
      DATA H/6.62618D-34/SOL/2.997925D10/KB/1.38066D-23/
      VO(0)=23217.56
      VO(1)=23388.3
      VO(2)=23159.6
      CF=0.9997004
      CALL FFRMPT ('Relative Populations V= 0:1,2 ?',32)
      READ(5,*)P(V),V=0,2)
      CALL FFRMPT ('Rot. Temperatures V= 0:1,2 ?',29)
      READ(5,*)T(V),V=0,2)
      CALL FFRMPT ('Output Filename : ',18)
      READ(5,5) OUTPUT
C    Calculation of the Y' values.
      DO 20 V=0,2
        Y(V,2)=0.96/BV(V,2)
   20 CONTINUE
C    The Rotational Term Values array is dimensioned thus : RTV(F,K,V,ST)
C     K = Rotational Quantum Number
C     V = Vibrational Quantum Number
C     ST = Electronic State
C     F = 1 .. The F1c sublevel
C     F = 2 .. The F1d sublevel
C     F = 3 .. The F2c sublevel
C     F = 4 .. The F2d sublevel
      DO 80 ST=1,2
        DO 60 V=0,2
          DO 40 K=1,35
          W=BV(V,ST)*(K*(K+1)-L(ST)**2)-DV(V,ST)*(K+0.5)**4
          X1=1.0+Y(V,ST)*(Y(V,ST)-4.0)*L(ST)**2/(4.0*(K+1)**2)
          X2=1.0+Y(V,ST)*(Y(V,ST)-4.0)*L(ST)**2/(4.0*K**2)
          Y1=G(ST)*K/2.0
          Y2=G(ST)*(K+1.0)/2.0
          Z=0.5*LA(ST)*K*(K+1.0)
          IF(X1.LT.1.0D-9)THEN
            RTV(1,K,V,ST)=0.0
            RTV(2,K,V,ST)=0.0
            GOTO 30
            END IF
          XX=SQRT(X1)
          X1=BV(V,ST)*(K+1.0)*(1.0-XX)
          YY=W+X1+Y1
          RTV(1,K,V,ST)=YY+Z
```

```
            RTV(2,K,V,ST)=YY-Z
   30       IF(X2.LT.1.0D-9)THEN
              RTV(3,K,V,ST)=0.0
              RTV(4,K,V,ST)=0.0
              GOTO 40
              END IF
            XX=SQRT(X2)
            X2=BV(V,ST)*K*(1.0-XX)
            YY=W-X2-Y2
            RTV(3,K,V,ST)=YY+Z
            RTV(4,K,V,ST)=YY-Z
   40       CONTINUE
   60     CONTINUE
   80   CONTINUE
C     The next section calculates the wavelengths of the individual transitions.
C     The wavelength array is dimensioned thus : WL(BR,K,V)
C     BR = Rotational Branch.
C      BR = 1   : P1cd Branch
C      BR = 2   : P1dc Branch
C      BR = 3   : P2cd Branch
C      BR = 4   : P2dc Branch
C      BR = 5   : Q1c  Branch
C      BR = 6   : Q1d  Branch
C      BR = 7   : Q2c  Branch
C      BR = 8   : Q2d  Branch
C      BR = 9   : R1cd Branch
C      BR = 10  : R1dc Branch
C      BR = 11  : R2cd Branch
C      BR = 12  : R2dc Branch
C      BR = 13  : PQ1c2d Branch
C      BR = 14  : PQ1d2c Branch
C      BR = 15  : QP2c1c Branch
C      BR = 16  : QP2d1d Branch
C      BR = 17  : QR1c2c Branch
C      BR = 18  : QR1d2d Branch
C      BR = 19  : RQ2c1d Branch
C      BR = 20  : RQ2d1c Branch
C     Wavelengths are converted from vacuum to air using the conversion factor(CF).
C      Subroutines WAVLN1-3 calcalate the wavelengths of transitions in
C      particular branches.
C     BR = 1 : The P1cd-branch.
       BR=1
       A=1
       B=2
       CALL WAVLN1(BR,A,B)
C     BR = 2 : The P1dc-branch.
       BR=2
       A=2
       B=1
       CALL WAVLN1(BR,A,B)
C     BR = 3 : The P2cd-branch.
       BR=3
       A=3
       B=4
       CALL WAVLN1(BR,A,B)
C     BR = 4 : The P2dc-branch.
       BR=4
       A=4
       B=3
       CALL WAVLN1(BR,A,B)
C     BR = 5 : The Q1c-branch.
       BR=5
       A=1
       B=1
       CALL WAVLN2(BR,A,B)
C     BR = 6 : The Q1d-branch.
       BR=6
       A=2
       B=2
       CALL WAVLN2(BR,A,B)
C     BR = 7 : The Q2c-branch
       BR=7
       A=3
       B=3
       CALL WAVLN2(BR,A,B)
C     BR = 8 : The Q2d-branch.
       BR=8
       A=4
       B=4
```

```
161             CALL WAVLN2(BR,A,B)
162       C     BR = 9 : The R1cd-branch.
163             BR=9
164             A=1
165             B=2
166             CALL WAVLN3(BR,A,B)
167       C     BR = 10 : The R1dc-branch.
168             BR=10
169             A=2
170             B=1
171             CALL WAVLN3(BR,A,B)
172       C     BR = 11 : The R2cd-branch.
173             BR=11
174             A=3
175             B=4
176             CALL WAVLN3(BR,A,B)
177       C     BR = 12 : The R2dc-branch.
178             BR=12
179             A=4
180             B=3
181             CALL WAVLN3(BR,A,B)
182       C     BR = 13 : The PQ1c2d-branch.
183             BR=13
184             A=1
185             B=4
186             CALL WAVLN1(BR,A,B)
187       C     BR = 14 : The PQ1d2c-branch.
188             BR=14
189             A=2
190             B=3
191             CALL WAVLN1(BR,A,B)
192       C     BR = 15 : The QP2c1c-branch.
193             BR=15
194             A=3
195             B=1
196             CALL WAVLN2(BR,A,B)
197       C     BR = 16 : The QP2d1d-branch.
198             BR=16
199             A=4
200             B=2
201             CALL WAVLN2(BR,A,B)
202       C     BR = 17 : The QR1c2c-branch.
203             BR=17
204             A=1
205             B=3
206             CALL WAVLN2(BR,A,B)
207       C     BR = 18 : The QR1d2d-branch.
208             BR=18
209             A=2
210             B=4
211             CALL WAVLN2(BR,A,B)
212       C     BR = 19 : The RQ2c1d-branch.
213             BR=19
214             A=3
215             B=2
216             CALL WAVLN3(BR,A,B)
217       C     BR = 20 : The RQ2d1c-branch.
218             BR=20
219             A=4
220             B=1
221             CALL WAVLN3(BR,A,B)
222       C     The next section of program the linestrengths for all the rovibronic
223       C     transitions.
224       C     Initially the 'U-Factors' and 'C-Factors' are calculated.
225       C      +/- = + : SI(sign) = 1
226       C      +/- = - : SI = 2
227       C      SI=1 c/w ST=1 corresponds to U"+ & C"+
228       C      SI=1 c/w ST=2 corresponds to U'+ & C'+
229       C      SI=2 c/w ST=1 corresponds to U"- & C"-
230       C      SI=2 c/w ST=2 corresponds to U'- & C'-
231             DO 100 ST=1,2
232               DO 120 V=0,2
233                 DO 140 K=1,35
234                   Z=(Y(V,ST)*(Y(V,ST)-4.0)*L(ST)**2+4.0*K**2)
235                   IF(Z.LT.ID-6)THEN
236                     DO 180 SI=1,2
237                       U(SI,K,V,ST)=0.0
238                       C(SI,K,V,ST)=0.0
239       180           CONTINUE
```

```
240                   GOTO 140
241                 END IF
242                 YY=SQRT(Z)
243                 X=L(ST)*(Y(V,ST)-2.0)
244                 W=4.0*(K**2-L(ST)**2)
245                 U(1,K,V,ST)=YY+X
246                 U(2,K,V,ST)=YY-X
247                 DO 160 SI=1,2
248                   C(SI,K,V,ST)=0.5*(U(SI,K,V,ST)**2+W)
249       160       CONTINUE
250       140     CONTINUE
251       120   CONTINUE
252       100 CONTINUE
253     C     The following section of program calculates the linestrengths for the
254     C     rovibronic transitions in the following branches :
255     C       BR = 1   : P1
256     C       BR = 2   : P2
257     C       BR = 3   : Q1
258     C       BR = 4   : Q2
259     C       BR = 5   : R1
260     C       BR = 6   : R2
261     C       BR = 7   : PQ12
262     C       BR = 8   : QP21
263     C       BR = 9   : QR12
264     C       BR = 10  : RQ21
265     C     The P1-Branch : BR = 1
266           BR=1
267           SI=2
268           DO 200 V=0,2
269             DO 220 K=1,34
270               K1=K+1
271               YY=8.0*(K+0.5)*C(SI,K,V,2)*C(SI,K1,V,1)
272               IF(ABS(YY).LT.1D-6)THEN
273                 S(BR,K,V)=0.0
274                 GOTO 220
275               END IF
276               X=(K-L(1)-1.0)*(K-L(1))
277               ZZ=4.0*K*(K+2.0)
278               Z=(U(SI,K,V,2)*U(SI,K1,V,1)+ZZ)**2
279               S(BR,K,V)=(X*Z)/YY
280       220   CONTINUE
281       200 CONTINUE
282           DO 205 V=0,2
283             S(BR,35,V)=16.2525
284       205 CONTINUE
285     C     The P2-Branch : BR = 2
286           BR=2
287           SI=1
288           DO 225 V=0,2
289             DO 230 K=1,2
290               S(BR,K,V)=0.0
291       230   CONTINUE
292     C     The following calculations give a value of zero for S(P2,K=3,V=0-2).
293     C     However these 3 lines are observed in the spectrum , so a linestrength
294     C     value of 0.236 is assigned to them :
295       225 CONTINUE
296           DO 235 V=0,2
297             S(BR,3,V)=0.236
298       235 CONTINUE
299           DO 240 V=0,2
300             DO 260 K=4,35
301               K0=K-1
302               YY=8.0*(K-0.5)*C(SI,K0,V,2)*C(SI,K,V,1)
303               IF(ABS(YY).LT.1D-6)GOTO 260
304               X=(K-L(1)-2.0)*(K-L(1)-1.0)
305               ZZ=4.0*(K-1.0)*(K+1.0)
306               Z=(U(SI,K0,V,2)*U(SI,K,V,1)+ZZ)**2
307               S(BR,K,V)=(X*Z)/YY
308       260   CONTINUE
309       240 CONTINUE
310     C     The Q1-Branch : BR = 3
311           BR=3
312           SI=2
313           DO 270 V=0,2
314             S(BR,1,V)=0.0
315       270 CONTINUE
316     C     Values of 1.766 assigned to S(Q1,K=2,V=0-2) - (see P2 above)
317           DO 275 V=0,2
318             S(BR,2,V)=1.766
319       275 CONTINUE
```

```
320           DO 280 V=0,2
321             DO 300 K=2,34
322               K1=K+1
323               YY=4.0*(K+0.5)*(K+1.5)*C(SI,K1,V,2)*C(SI,K1,V,1)
324               IF(ABS(YY).LT.1D-6)GOTO 300
325               X=(K-L(1))*(K+1.0)*(K+L(1)+2.0)
326               ZZ=4.0*K*(K+2.0)
327               Z=(U(SI,K1,V,2)*U(SI,K1,V,1)+ZZ)**2
328               S(BR,K,V)=(X*Z)/YY
329       300   CONTINUE
330       280 CONTINUE
331           DO 290 V=0,2
332             S(BR,35,V)=35.91
333       290 CONTINUE
334     C     The G2-Branch : BR = 4
335           BR=4
336           SI=1
337           DO 320 V=0,2
338             S(BR,1,V)=0.0
339       320 CONTINUE
340     C     Values of 1.07 assigned to S(Q2,K=2,V=0-2) - (see P2 above).
341           DO 330 V=0,2
342             S(BR,2,V)=1.07
343       330 CONTINUE
344           DO 340 V=0,2
345             DO 360 K=3,35
346               YY=4.0*(K-0.5)*(K+0.5)*C(SI,K,V,2)*C(SI,K,V,1)
347               IF(ABS(YY).LT.1D-6)GOTO 360
348               X=(K-L(1)-1.0)*K*(K+L(1)+1.0)
349               ZZ=4.0*(K-1.0)*(K+1.0)
350               Z=(U(SI,K,V,2)*U(SI,K,V,1)+ZZ)**2
351               S(BR,K,V)=(X*Z)/YY
352       360     CONTINUE
353       340 CONTINUE
354     C     The R1-Branch : BR = 5
355           BR=5
356           SI=2
357           DO 380 V=0,2
358             DO 400 K=1,33
359               K1=K+1
360               K2=K+2
361               YY=8.0*(K+1.5)*C(SI,K2,V,2)*C(SI,K1,V,1)
362               IF(ABS(YY).LT.1D-6)GOTO 400
363               X=(K+L(1)+2.0)*(K+L(1)+3.0)
364               ZZ=4.0*K*(K+2.0)
365               Z=(U(SI,K2,V,2)*U(SI,K1,V,1)+ZZ)**2
366               S(BR,K,V)=(X*Z)/YY
367       400     CONTINUE
368       380 CONTINUE
369           DO 390 V=0,2
370             S(BR,34,V)=19.278
371             S(BR,35,V)=19.778
372       390 CONTINUE
373     C     The R2-Branch : BR = 6
374           BR=6
375           SI=1
376     C     Values of 1.905 assigned to S(R2,K=1,V=0-2) - (see P2 above)
377           DO 410 V=0,2
378             S(BR,1,V)=1.905
379       410 CONTINUE
380           DO 420 V=0,2
381             DO 440 K=2,34
382               K1=K+1
383               YY=8.0*(K+0.5)*C(SI,K1,V,2)*C(SI,K,V,1)
384               IF(ABS(YY).LT.1D-6)GOTO 440
385               X=(K+L(1)+1.0)*(K+L(1)+2.0)
386               ZZ=4.0*(K-1.0)*(K+1.0)
387               Z=(U(SI,K1,V,2)*U(SI,K,V,1)+ZZ)**2
388               S(BR,K,V)=(X*Z)/YY
389       440     CONTINUE
390       420 CONTINUE
391           DO 430 V=0,2
392             S(BR,35,V)=19.2502
393       430 CONTINUE
394     C     The PQ12-Branch : BR = 7
395           BR=7
396           DO 460 V=0,2
397             DO 480 K=1,2
398               S(BR,K,V)=0.0
399       480     CONTINUE
```

```
      460 CONTINUE
          DO 500 V=0,2
            DO 520 K=3,35
              YY=4.0*(K-0.5)*(K+0.5)*C(2,K,V,2)*C(1,K,V,1)
              IF(ABS(YY).LT.1D-6)GOTO 520
              X=(K-L(1)-1.0)*K*(K+L(1)+1.0)
              ZZ=4.0*(K-1.0)*(K+1.0)
              Z=(U(2,K,V,2)*U(1,K,V,1)-ZZ)**2
              S(BR,K,V)=(X*Z)/YY
      520   CONTINUE
      500 CONTINUE
C     The QP21-Branch : BR = 8
          BR=8
          DO 540 V=0,2
            DO 560 K=1,2
              S(BR,K,V)=0.0
      560   CONTINUE
      540 CONTINUE
          DO 580 V=0,2
            DO 600 K=3,34
              K1=K+1
              YY=8.0*(K+0.5)*C(1,K,V,2)*C(2,K1,V,1)
              IF(ABS(YY).LT.1D-6)GOTO 600
              X=(K-L(1)-1.0)*(K-L(1))
              ZZ=4.0*K*(K+2.0)
              Z=(U(1,K,V,2)*U(2,K1,V,1)-ZZ)**2
              S(BR,K,V)=(X*Z)/YY
      600   CONTINUE
      580 CONTINUE
          DO 590 V=0,2
            S(BR,35,V)=0.029
      590 CONTINUE
C     The QR12-Branch : BR = 9
          BR=9
          DO 620 V=0,2
            S(BR,1,V)=0.0
      620 CONTINUE
          DO 640 V=0,2
            DO 660 K=2,34
              K1=K+1
              YY=8.0*(K+0.5)*C(2,K1,V,2)*C(1,K,V,1)
              IF(ABS(YY).LT.1D-6)GOTO 660
              X=(K+L(1)+1.0)*(K-L(1)+2.0)
              ZZ=4.0*(K-1.0)*(K+1.0)
              Z=(U(2,K1,V,2)*U(1,K,V,1)-ZZ)**2
              S(BR,K,V)=(X*Z)/YY
      660   CONTINUE
      640 CONTINUE
          DO 680 V=0,2
            S(BR,35,V)=0.0314
      680 CONTINUE
C     The RQ21-Branch : BR = 10
          BR=10
          DO 680 V=0,2
            S(BR,1,V)=0.672
      680 CONTINUE
          DO 700 V=0,2
            DO 720 K=2,34
              K1=K+1
              YY=4.0*(K+0.5)*(K+1.5)*C(1,K1,V,2)*C(2,K1,V,1)
              IF(ABS(YY).LT.1D-6)GOTO 720
              X=(K-L(1))*(K+1.0)*(K+L(1)+2.0)
              ZZ=4.0*K*(K+2.0)
              Z=(U(1,K1,V,2)*U(2,K1,V,1)-ZZ)**2
              S(BR,K,V)=(X*Z)/YY
      720   CONTINUE
      700 CONTINUE
          DO 710 V=0,2
            S(BR,35,V)=0.02695
      710 CONTINUE
C     The next section of program calculates the intensity of each individual
C     rovibronic transition
C     Three subroutines - INTEN1-3 - are used.
          E=-(H*SOL)/KB
          IMAX=0.0
C     The P1cd-Branch : BR = 1
          BR=1
          RB=1
          F=1
          CALL INTEN1(BR,RB,F)
C     The P1dc-Branch : BR = 2
          BR=2
```

```
482             RB=1
483             F=2
484             CALL INTEN1(BR,RB,F)
485       C     The P2cd-Branch : BR = 3
486             BR=3
487             RB=2
488             F=3
489             CALL INTEN1(BR,RB,F)
490       C     The P2dc-Branch : BR = 4
491             BR=4
492             RB=2
493             F=4
494             CALL INTEN1(BR,RB,F)
495       C     The G1c-Branch : BR = 5
496             BR=5
497             RB=3
498             F=1
499             CALL INTEN2(BR,RB,F)
500       C     The G1d-Branch : BR = 6
501             BR=6
502             RB=3
503             F=2
504             CALL INTEN2(BR,RB,F)
505       C     The G2c-Branch : BR = 7
506             BR=7
507             RB=4
508             F=1
509             CALL INTEN2(BR,RB,F)
510       C     The G2d-Branch : BR = 8
511             BR=8
512             RB=4
513             F=4
514             CALL INTEN2(BR,RB,F)
515       C     The R1cd-Branch : BR = 9
516             BR=9
517             RB=5
518             F=1
519             CALL INTEN3(BR,RB,F)
520       C     The R1dc-Branch : BR = 10
521             BR=10
522             RB=5
523             F=2
524             CALL INTEN3(BR,RB,F)
525       C     The R2cd-Branch : BR = 11
526             BR=11
527             RB=6
528             F=3
529             CALL INTEN3(BR,RB,F)
530       C     The R2dc-Branch : BR = 12
531             BR=12
532             RB=6
533             F=4
534             CALL INTEN3(BR,RB,F)
535       C     The PG1c2d-Branch : BR = 13
536             BR=13
537             RB=7
538             F=1
539             CALL INTEN1(BR,RB,F)
540       C     The PG1d2c-Branch : BR = 14
541             BR=14
542             RB=7
543             F=2
544             CALL INTEN1(BR,RB,F)
545       C     The GP2c1c-Branch : BR = 15
546             BR=15
547             RB=8
548             F=3
549             CALL INTEN2(BR,RB,F)
550       C     The GP2c1d-Branch : BR = 16
551             BR=16
552             RB=8
553             F=4
554             CALL INTEN2(BR,RB,F)
555       C     The GR1c2c-Branch : BR = 17
556             BR=17
557             RB=9
558             F=1
559             CALL INTEN2(BR,RB,F)
560       C     The GR1c2d-Branch : BR = 18
561             BR=18
562             RB=9
563             F=2
```

```
564           CALL INTEN2(BR,RB,F)
565     C     The RG2c1d-Branch : BR = 19
566           BR=19
567           RB=10
568           F=3
569           CALL INTEN3(BR,RB,F)
570     C     The RG2a1c-Branch : BR = 20
571           BR=20
572           RB=10
573           F=4
574           CALL INTEN3(BR,RB,F)
575     C     The next section takes account of "dummy" points (zero intensity) then
576     C     arranges the real points in order of increasing wavelength.
577           ZEROS=0
578           DO 1000 BR=1,20
579             DO 1010 V=0,2
580               DO 1020 K=1,35
581                 IF(WL(BR,K,V).LT.400.0)THEN
582                   ZEROS=ZEROS+1
583                   WL(BR,K,V)=1000.0
584                 END IF
585      1020       CONTINUE
586      1010     CONTINUE
587      1000   CONTINUE
588           POINTS=2100-ZEROS
589           OPEN(1,FILE=OUTPUT,FILETYPE='CHARACTER')
590           WRITE(1,10) POINTS
591           DO 1050 PT=1,POINTS
592             WLMIN=900
593             DO 1060 BR=1,20
594               DO 1070 V=0,2
595                 DO 1080 K=1,35
596                   IF(WL(BR,K,V).LT.WLMIN)THEN
597                     TEMPBR=BR
598                     TEMPK=K
599                     TEMPV=V
600                     WLMIN=WL(BR,K,V)
601                   END IF
602      1080         CONTINUE
603      1070       CONTINUE
604      1060     CONTINUE
605           WRITE(1,15) WL(TEMPBR,TEMPK,TEMPV),I(TEMPBR,TEMPK,TEMPV)/IMAX
606           WL(TEMPBR,TEMPK,TEMPV)=WL(TEMPBR,TEMPK,TEMPV)+1000.0
607      1050 CONTINUE
608         5 FORMAT(A20)
609        10 FORMAT(1X,I5)
610        15 FORMAT(1X,F9.4,4X,F9.6)
611           STOP
612           END



613           SUBROUTINE WAVLN1(BR,A,B)
614           DOUBLE PRECISION WL,RTV,CF,VO
615           INTEGER BR,A,B,K,KO,V
616           COMMON/BLOCK1/WL(20,35,0:2),RTV(4,35,0:2,2)
617           COMMON/BLOCK2/CF,VO(0:2)
618           DO 8005 V=0,2
619             DO 8010 K=1,2
620               WL(BR,K,V)=0.0
621      8010     CONTINUE
622      8005   CONTINUE
623           DO 8000 V=0,2
624             DO 8020 K=3,35
625               KO=K-1
626               WL(BR,K,V)=CF*10**7/(VO(V)+RTV(A,KO,V,2)-RTV(B,K,V,1))
627      8020     CONTINUE
628      8000   CONTINUE
629           RETURN
630           END



631           SUBROUTINE WAVLN2(BR,A,B)
632           DOUBLE PRECISION WL,RTV,CF,VO
633           INTEGER BR,A,B,K,V
634           COMMON/BLOCK1/WL(20,35,0:2),RTV(4,35,0:2,2)
635           COMMON/BLOCK2/CF,VO(0:2)
636           DO 8110 V=0,2
637             WL(BR,1,V)=0.0
```

```
      8110 CONTINUE
           DO 8100 V=0,2
             DO 8120 K=2,35
               IF(ABS(RTV(A,K,V,2)).LT.1D-6.OR.ABS(RTV(B,K,V,1)).LT.1D-6)THEN
                 WL(BR,K,V)=0.0
                 GOTO 8120
               END IF
               WL(BR,K,V)=CF*10**7/(V0(V)+RTV(A,K,V,2)-RTV(B,K,V,1))
      8120   CONTINUE
      8100 CONTINUE
           RETURN
           END


           SUBROUTINE WAVLN3(BR,A,B)
           DOUBLE PRECISION WL,RTV,CF,V0
           INTEGER BR,A,B,K,K1,V
           COMMON/BLOCK1/WL(20,35,0:2),RTV(4,35,0:2,2)
           COMMON/BLOCK2/CF,V0(0:2)
           DO 8210 V=0,2
             WL(BR,35,V)=0.0
      8210 CONTINUE
           DO 8200 V=0,2
             DO 8220 K=1,34
               K1=K+1
               WL(BR,K,V)=CF*10**7/(V0(V)+RTV(A,K1,V,2)-RTV(B,K,V,1))
      8220   CONTINUE
      8200 CONTINUE
           RETURN
           END


           SUBROUTINE INTEN1(BR,RB,F)
           DOUBLE PRECISION WL,RTV,S,I,P,T,E,IMAX,X,V3
           INTEGER V,K,K0,BR,RB,F
           COMMON/BLOCK1/WL(20,35,0:2),RTV(4,35,0:2,2)
           COMMON/BLOCK2/S(10,35,0:2),I(20,35,0:2),P(0:2),T(0:2),E,IMAX
           DO 8500 V=0,2
             DO 8520 K=1,2
               I(BR,K,V)=0.0
      8520   CONTINUE
      8500 CONTINUE
           DO 8540 V=0,2
             DO 8560 K=3,35
               K0=K-1
               X=E*RTV(F,K0,V,2)/T(V)
               V3=(10**7/WL(BR,K,V))**3
               I(BR,K,V)=V3*S(RB,K,V)*DEXP(X)*P(V)
               IF(I(BR,K,V).GT.IMAX)IMAX=I(BR,K,V)
      8560   CONTINUE
      8540 CONTINUE
           RETURN
           END


           SUBROUTINE INTEN2(BR,RB,F)
           DOUBLE PRECISION WL,RTV,S,I,P,T,E,IMAX,X,V3
           INTEGER V,K,BR,RB,F
           COMMON/BLOCK1/WL(20,35,0:2),RTV(4,35,0:2,2)
           COMMON/BLOCK2/S(10,35,0:2),I(20,35,0:2),P(0:2),T(0:2),E,IMAX
           DO 8600 V=0,2
             I(BR,1,V)=0.0
      8600 CONTINUE
           DO 8620 V=0,2
             DO 8640 K=2,35
               X=E*RTV(F,K,V,2)/T(V)
               V3=(10**7/WL(BR,K,V))**3
               I(BR,K,V)=V3*S(RB,K,V)*DEXP(X)*P(V)
               IF(I(BR,K,V).GT.IMAX)IMAX=I(BR,K,V)
      8640   CONTINUE
      8620 CONTINUE
           RETURN
           END
```

```
      SUBROUTINE INTEN3(BR,RB,F)
      DOUBLE PRECISION WL,RTV,S,I,P,T,E,IMAX,X,V3
      INTEGER V,K,K1,BR,RB,F
      COMMON/BLOCK1/WL(20,35,0:2),RTV(4,35,0:2,2)
      COMMON/BLOCK3/S(10,35,0:2),I(20,35,0:2),P(0:2),T(0:2),E,IMAX
      DO 8700 V=0,2
        I(BR,35,V)=0.0
 8700 CONTINUE
      DO 8720 V=0,2
        DO 8740 K=1,34
          K1=K+1
          X=E*RTV(F,K1,V,2)/T(V)
          V3=(10**7/WL(BR,K,V))**3
          I(BR,K,V)=V3*S(RB,K,V)*DEXP(X)*P(V)
          IF(I(BR,K,V).GT.IMAX)IMAX=I(BR,K,V)
 8740   CONTINUE
 8720 CONTINUE
      RETURN
      END
```

APPENDIX 2

LECTURE COURSES ATTENDED

In accordance with the regulations of the University of Edinburgh (Department of Chemistry) the following lecture courses were attended.

1. Fortran 77 Computing

2. Microcomputers

3. Quantum Optics - Lasers

4. Lasers in Chemistry

5. History of the Department of Chemistry

6. The Chemistry of Photographic Processes

7. Case Studies in Molecular Reaction Dynamics

Additionally, many of the regular departmental seminars and all research group meetings were attended.

BIBLIOGRAPHY

1. J A Coxon, Chem. Soc. Specialist Periodical Reports - Mol. Spectrosc., **1**, 177 (1973) and references therein.
2. M A A Clyne and M C Heaven, J. Chem. Soc. Farady Trans. II, **76**, 49 (1980)
3. E M Weinstock and A Preston, J. Mol. Spectrosc., **70**, 188 (1978)
4. H D Hartmann, H Knockel and E Tiemann, Chem. Phys. Lett., **113**, 364 (1985)
5. M S Child and R B Bernstein, J. Chem. Phys., **59**, 5916 (1973)
6. M D Danyluk and G W King, Chem. Phys. Lett., **43**, 1 (1976)
7. R B Kurzel, J I Steinfeld, D A Hatzenbuhler and G E Leroi, J. Chem. Phys., **55**, 4822 (1971) and references therein.
8. R B Kurzel and J I Steinfeld, J. Chem. Phys., **53**, 3293 (1970).
9. J I Steinfeld and W Klemperer, J. Chem. Phys., **42**, 3475 (1965).
10. J Derouard and N Sadeghi, J. Chem. Phys., **81**, 3002 (1984).
11. J C McLennan, Proc. Roy. Soc., **A88**, 289 (1913).
12. J C McLennan, Proc. Roy. Soc., **A91**, 23 (1914).
13. R S Mulliken, J. Chem. Phys., **55**, 288 (1971).
14. F Duschinsky and P Pringsheim, Physica, **2**, 923 (1935).
15. A L Guy, K S Viswanathan, A Sur and J Tellinghuisen, Chem. Phys. Lett., **73**, 582 (1980).
16. J Tellinghuisen, J. Mol. Spectrosc., **94**, 231 (1982).
17. L C Glasgow and J E Willard, J. Phys. Chem., **77**, 1585 (1973).
18. R J Donovan, B V O'Grady, L Lain and C Fotakis, J. Chem. Phys., **78**, 3727 (1983).

19. Z Yun-wu, W Fuss and K L Kompa, J. Photochem., **23**, 311 (1983).

20. R S Bradford Jr., E R Ault, and B L Bhaumik, Appl. Phys. Lett., **27**, 546 (1975).

21. J J Ewing and C A Brau, Appl. Phys. Lett., **27**, 557 (1975).

22. A K Hays, J M Hoffman and G C Tisone, Chem. Phys. Lett., **39**, 353 (1976).

23. J R Murray, J C Swingle and C E Turner Jr., Appl. Phys. Lett., **28**, 530 (1976).

24. J J Ewing, J H Jacov, J A Mangana and H A Brown, Appl. Phys. Lett., **28**, 656 (1976).

25. M Diegelmann, H P Grieneisen, K Hohla, X-j Hu, J Krasinski and K L Kompa, Appl. Phys., **23**, 283 (1980).

26. M Diegelmann, K Hohla, F Rebentrotst and K L Kompa, J. Chem. Phys., **76**, 1233 (1982).

27. M J Shaw, C B Edwards, F O'Neill, C Fotakis and R J Donovan, Appl. Phys. Lett., **37**, 346 (1980).

28. M Martin, C Fotakis, R J Donovan and M J Shaw, Nouvo Cimento, **63B**, 300 (1981).

29. J Tellinghuisen, Chem. Phys. Lett., **49**, 485 (1977).

30. M V McCusker, R M Hill, D L Heustis, D C Lorents, R A Gutcheck and H H Nakano, Appl. Phys. Lett., **27**, 263 (1975).

31. M C Sauer Jr., W A Mulac, R Cooper and F Grieser, J. Chem. Phys., **64**, 4587 (1976).

32. A B Callear and M P Metcalfe, Chem. Phys. Lett., **43**, 197 (1976).

33. M F Golde and B A Thrush, Chem. Phys. Lett., **29**, 486 (1974).

34. J E Velazco and D W Setser, J. Chem. Phys., **62**, 1990 (1975).

35. S K Searles and G A Hart, Appl. Phys. Lett., **27**, 243 (1975).

36. J J Ewing and C A Brau, Appl. Phys. Lett., **27**, 350 (1975).

37. C A Brau and J J Ewing, Appl. Phys. Lett., **27**, 435 (1975).

38. E R Ault, R S Bradford Jr. and M L Bhaumik, Appl. Phys. Lett., **27**, 413 (1975); **28**, 23 (1975).

39. J P T Wilkinson, M MacDonald and R J Donovan, Chem. Phys. Lett., **101**, 284 (1983).

40. S D Peyerimhoff and R J Buenker, Chem. Phys., **57**, 279 (1981).

41. J Tellinghuisen, J. Chem. Phys., **78**, 2374 (1983).

42. J P Perrot, M Brayer, J Chevaleyre and B Femelat, J. Mol. Spectrosc., **98**, 161 (1983).

43. A B Callear and M P Metcalfe, Chem. Phys., **20**, 233 (1977).

44. B V O'Grady, L Lain, R J Donovan and M C Gower, Chem. Phys. Lett., **91**, 491 (1982).

45. H Hemmati and G J Collins, Chem. Phys. Lett., **75**, 488 (1980).

46. M MacDonald, J P T Wilkinson, C Fotakis, M Martin and R J Donovan, Chem. Phys. Lett., **99**, 250 (1983).

47. J C D Brand and A R Hoy, J. Mol. Spectrosc., **97**, 379 (1983).

48. A D Williamson, Chem. Phys. Lett., **60**, 451 (1978).

49. G W King, I M Littlewood and J R Robins, Chem. Phys., **56**, 145 (1981).

50. J Chevaleyre, J P Perrot, J M Chastan, S Valignat and M Broyer, Chem. Phys., **67**, 59 (1982).

51. T I Ishiwata, H Ohtoshi, M Sakaki and I Tanaka, J. Chem. Phys., **80**, 1411 (1984).

52. K S Viswanathan and J Tellinghuisen, J. Mol. Spectrosc., **101**, 285 (1983).

53. G W King, I M Littlewood and J R Robins, Chem. Phys., **62**, 359 (1981).

54. J C D Brand, V D Deshpande, A R Hoy, S M Jaywant and E J Woods, J. Mol. Spectrosc., **99**, 339 (1983).

55. G Das and A C Wahl, J. Chem. Phys., **69**, 53 (1978).

56. J C D Brand, A R Hoy, A K Kalkar and A B Yamashita, J. Mol. Spectrosc., **95**, 350 (1982).

57. J Tellinghuisen, Chem. Phys. Lett., **29**, 359 (1974).

58. A G Gaydon and H G Wolfhard, "Flames - their structure, radiation and temperature", (Chapman and Hall, London, 1979).

59. S L N G Krishnamachari and H P Broida, J. Chem. Phys., **34**, 1709 (1961).

60. R Bleekrode and W C Nieuwpoort, J. Chem. Phys., **43**, 3680 (1965).

61. R Harvey and P F Jessen, Phys. Sci., **241**, 102 (1973).

62. J E Bulter, J W Fleming, L P Goss and M C Lin, Chem. Phys., **56**, 355 (1981).

63. C A Arrington, W Brennen, G P Glass, J V Michael and H Niki, J. Chem. Phys., **43**, 1489 (1965).

64. I Tokue and M Ikarashi, Bull. Chem. Soc. Jpn., **54**, 2802 (1981).

65. M Noguchi, Y Tanaka, T Tanaka and Y Takeuchi, Nenryo Oyobi Nensho, **45**, 1100 (1978).

66. I Kusunoki and C Ottinger, J. Chem. Phys., **70**, 710 (1979).

67. I Kusunoki, C Ottinger and S Kimmerman, J. Chem. Phys., **71**, 894 (1979).

68. R Marx, M Gerard, T R Govers and G Mauclaire, Adv. Mass Spectrom., **7A**, 307 (1978).

69. K Suzuki and K Kuchitsu, Bull. Chem. Soc. Jpn., **50**, 1905 (1977).

70. G Herzberg, "Molecular spectra and molecular structure. I. Spectra of diatomic molecules", (Van Nostrand, New York, 1950).

71. V V Smith, C Sneder and C A Pilachowski, Publ. Astron. Soc. Pac., **92**, 809 (1981).

72. G F Gahm and K P Lindroos, Phys. Scr., **20**, 563 (1979).

73. B F Peery Jr., Publ. Astron. Soc. Jpn., **31**, 461 (1979).

74. S Green, Ann. Rev. Phys. Chem., **32**, 103 (1981).

75. K R Lang and R F Wilson, Astrophys. J., **224**, 125 (1978).

76. R Genzel, D Downes, T Pauls, T L Wilson and J Bieging, Astron. Astrophys., **73**, 253 (1979).

77. G Sandell, L E B Johansson, Nguyen-Q-Rieu and K Mattila, Astron. Astrophys., **97**, 317 (1981).

78. A Dalgarno, At. Processes Appl., 109 (1976), Ed P G Burke and B L Moiseiwitsch - references therein.

79. I Messing, C H Sadowski and S V Filseth, Chem. Phys. Lett., **66**, 95 (1979).

80. T A Cool and P J H Tjossem, Chem. Phys. Lett., **111**, 82 (1984).

81. C Vinckier, J. Phys. Chem., **83**, 1234 (1979).

82. J E Butler, L P Goss, M C Lin and J W Hudgens, Chem. Phys. Lett., **63**, 104 (1979).

83. S S Wagal, T Carrington, S V Filseth and C M Sadowski, Chem. Phys. **69**, 61 (1982).

84. M R Berman and M C Lin, Chem. Phys., **82**, 435 (1983).

85. M R Berman and M C Lin, J. Chem. Phys., **81**, 5743 (1984).

86. M R Berman and M C Lin, J. Phys. Chem., **87**, 3933 (1983).

87. J A Duncanson Jr. and W A Guillory, J. Chem. Phys., **78**, 4958 (1983).

88. C Fotakis, M Martin, K P Lawley and R J Donovan, Chem. Phys. Lett., **67**, 1 (1979).

89. A P Baronavski and J R McDonald, Chem. Phys. Lett., **56**, 369 (1978).

90. C Fotakis, M Martin and R J Donovan, J. Chem. Soc. Faraday Trans. II, **78**, 1363 (1982).

91. H Shinohara and N Nishi, J. Chem. Phys., **77**, 234 (1982).

92. T Nagata, M Suzuki, K Suzuki, T Kondow and K Kuchitsu, Chem. Phys., **88**, 163 (1984).

93. J R McDonald, A P Baronavski and V M Donnelly, Chem. Phys., **33**, 161 (1978).

94. N Nishi, H Shinohara and I Hanazaki, Chem. Phys. Lett., **73**, 473 (1980).

95. B B Craig, W L Faust, L S Goldberg and R G Weiss, J. Chem. Phys., **76**, 5014 (1982).

96. H K Haak and F Stuhl, J. Phys. Chem., **88**, 3627 (1984).

97. G Cairo, Z. Phys., **10**, 185 (1922).

98. G Cairo and J Franck, Z. Phys., **11**, 161 (1922).

99. R Mannkopft, Z. Phys., **36**, 22 (1926).

100. J G Winans, Z. Phys., **40**, 63 (1930).

101. L Krause, Adv. Chem. Phys., **28**, 267 (1975)

102. J T Yardley, "Introduction to Molecular Energy Transfer" (Academic Press, 1980, New York) page 221, equations 8.3-1 - 8.3-6

103. E H Fink, D Wallach and C B Moore, J. Chem. Phys., **56**, 3608 (1972)

104. H Reisler and C Wittig, J. Chem. Phys., **69**, 3729 (1978)

105. A T Pritt and R D Coombe, J. Chem. Phys., **65**, 2096 (1976)

106. J J Ewing, Chem. Phys. Lett., **29**, 50 (1974)

107. D L King and D W Setser, Ann. Rev. Phys. Chem., **27**, 407 (1976).

108. E R Fisher and G K Smith, Appl. Opt., **10**, 1803 (1971).

109. R Grice and D R Herschbach, Mol. Phys., **27**, 159 (1974).

110. D R Herschbach, Adv. Chem. Phys., **10**, 319 (1966).

111. D L Magee, J. Chem. Phys., **8**, 687 (1940).

112. D L Magee, Discuss. Faraday Soc., **12**, 33 (1952).

113. M B Foist and R B Bernstein, J. Chem. Phys., **64**, 2971 (1976).

114. M S Child, Faraday Discuss. Chem. Soc., **53**, 18 (1972).

115. E E Nikitin, Adv. Chem. Phys., **28**, 317 (1975).

116. A E Gislason and J A Sachs, J. Chem. Phys., **62**, 2678 (1975).

117. M S deVries, V I Srdanov, G W Tyndall and R M Martin, Chem. Phys. Lett., **114**, 233 (1985).

118. K J Laidler, J. Chem. Phys., **10**, 34 (1942).

119. J E Velazco, J H Kolts, D W Setser and J A Coxon, Chem. Phys. Lett., **46**, 99 (1977).

120. E Bauer, E R Fisher and F R Gilmore, J. Chem. Phys., **51**, 4173 (1969).

121. A Gedanken, J Jortner, B Raz and A Szoke, J. Chem. Phys., **57**, 3456 (1972)

122. G Karl, P Kruus and J C Polanyi, J. Chem. Phys., **46**, 224 (1967)

123. R D Levine and R B Bernstein, Chem. Phys. Lett., **15**, 1 (1972)

124. J C Tully, J. Chem. Phys., **61**, 61 (1974)

125. R F Heidner, D Husain and J R Weisenfeld, J. Chem. Soc. Faraday Trans. II, **69**, 927 (1973)

126. T G Slanger and G Black, J. Chem. Phys., **60**, 468 (1974)

127. K P Huber and G Herzberg, "Molecular Structure and Molecular Spectra, Vol. 4, Constants of Diatomic Molecules " (Van Nostrand, Princeton, 1979).

128. W H Evans, T R Munson and D D Wagmann, J. Res. Natl. Bur. Std. US, **55**, 147 (1955).

129. R J Donovan and D Husain, Trans. Faraday Soc., **64**, 2325 (1968).

130. K Wieland, J Tellinghuisen and A Nobs, J. Mol. Spectrosc., **41**, 69 (1972).

131. M MacDonald, R J Donovan and M C Gower, Chem. Phys. Lett., **97**, 72 (1983).

132. M MacDonald, Ph. D. Thesis, University of Edinburgh (1984).

133. D Austin, private communication.

134. R S Mulliken, J. Chem. Phys., **55**, 309 (1971).

135. J Tellinghuisen, J. Mol. Spectrosc., **103**, 445 (1984).

136. K P Lawley, M A MacDonald, R J Donovan and A Kvaran, Chem. Phys. Lett., **92**, 322 (1982).

137. J Tellinghuisen, Chem. Phys. Lett., **99**, 373 (1983).

138. J E Velasco, J H Kolts and D W Setser, J. Chem. Phys., **65**, 3468 (1976).

139. K Tamagake, D W Setser and J H Kolts., J. Chem. Phys., **74**, 4286 (1981).

140. D Lin, Y C Yu and D W Setser, J. Chem. Phys., **81**, 5830 (1984).

141. P Venkateswarlu, Can. J. Phys., **48**, 1055 (1970).

142. A B Callear, P Erman and J Kurepa, Chem. Phys. Lett., **44**, 599 (1976).

143. D L Rousseau, J. Mol. Spectrosc., **58**, 481 (1975).

144. T Ishiwata, A Tokunaga and I Tanaka, Chem. Phys. Lett., **112**, 356 (1984).

145. G Inoue, J K Ku and D W Setser, J. Chem. Phys., **80**, 6006 (1984).

146. H Hemmati and G J Collins, Chem. Phys. Lett., **67**, 5 (1979).

147. F A Cotton and G Wilkinson, "Advanced Inorganic Chemistry" (3rd Edition, Wiley Interscience, p. 438).

148. J G Calvert and J N Pitts., "Photochemistry" (Wiley, New York, 1966) p. 439.

149. C I M Beenakker, P J F Verbeek, G R Mohlmann and F J De Heer, J. Quant. Spectrosc. Radiat. Transfer, **15**, 333 (1975).

150. M Schmidt, H A Gillis and M Clerk, J. Phys. Chem., **79**, 2531 (1975).

151. R Ch Baas and C I M Beenakker, Comp. Phys. Comm., **8**, 236 (1974).

152. M Ito, P-K C Huang and E M Kosower, J. Chem. Soc. Faraday Trans., **57**, 1662 (1961).

153. C J Ingold and G W King, J. Chem. Soc., 2725 (1953).

154. K K Innes, J. Chem. Phys., **22**, 863 (1954).

155. W C Walker and G L Weissler, J. Chem. Phys., **23**, 1547 (1955).

156. V H Dibeler, J A Walker and K E McCulloch, J. Chem. Phys., **59**, 2264 (1973).

157. P D Foo and K K Innes, Chem. Phys. Lett., **22**, 439 (1973).

158. R W B Pearse and A G Gaydon, "Identification of molecular spectra " (Chapman + Hall, London, 1965).

159. A J Harrison, B J Cederholm and M A Terwillinger, J. Chem. Phys., **30**, 355 (1959).

160. J S Lake and A J Harrison, J. Chem. Phys., **30**, 361 (1959).

161. A Gedanken and M D Rowe, Chem. Phys., **36**, 181 (1979).

162. P Pechukas and J C Light, J. Chem. Phys., **42**, 3281 (1965).

163. P Pechukas, C Rankin and L C Light, J. Chem. Phys., **44**, 794 (1966).

164. J C Light, Discuss. Faraday Soc., **44**, 14 (1967).

165. E E Nikitin, Theor. Exp. Chem., **1**, 144 (1965).

166. C E Klots, J. Phys. Chem., **75**, 1526 (1971).

167. J L Kinsey, J. Chem. Phys., **54**, 1206 (1970).

168. M Quack and J Troe, Ber. Bunsenges. Phys. Chem., **78**, 240 (1974).

169. M Quack and J Troe, Ber. Bunsenges. Phys. Chem., **79**, 170 (1975).

170. J R Beresford, G Hancock, A J MacRobert, J Catanzarite, G Radhakrishnan, H Reisler and C Wittig, Faraday Discuss. Chem. Soc., **75**, 211 (1983).

171. W M Jackson, J B Halpern and C S Lin, Chem. Phys. Lett., **55**, 254 (1978).

172. J Brzozowski, P Bunken, N Elander and P Erman, J Astrophys., **207**, 414 (1976).

173. H W Hermann and S R Leone, J. Chem. Phys., **76**, 4766 (1982).

174. M D Barry and P A Gorry, Mol. Phys., **52**, 461 (1984).

175. A M Quinton and J P Simons, Chem. Phys. Lett., **81**, 214 (1981).

176. J O Hirschfelder, C F Curtiss and R B Bird, "Molecular theory of gases and liquids", (John Wiley & Sons, 1954) - formula on page 1023.

177. K Bergmann, U Hefter and J Witt, J. Chem. Phys., **72**, 4777 (1980).

178. J Dufayard and O Nedelec, Chem. Phys., **71**, 279 (1982).

179. H P Broida and T Carrington, J. Chem. Phys., **38**, 136 (1963).

180. O Nedelec and J Dufayard, J. Chem. Phys., **76**, 378 (1982).

181. W Brennen and T Carrington, J. Chem. Phys., **46**, 7 (1967).

182. M Clerc and M Schmidt, Far. Discuss. Chem. Soc., **53**, 217 (1972).

183. H Brunet, IEEE- J Quantum Electron., **QE-6**, 678 (1970).

184. J C Polanyi and K B Woodall, J. Chem. Phys., **56**, 1563 (1972).

185. K H Becker, H H Brenig and T Tatarczyk, Chem. Phys. Lett., **71**, 242 (1980).

186. D A Lichtin, M R Berman and M C Lin, Chem. Phys. Lett., **108**, 18 (1984).

187. R J Donovan and D Husain, Chem. Rev., **70**, 489 (1970).

188. C J Nokes and R J Donovan, Chem. Phys., **90**, 167 (1984).